# DESIGN, FABRICATION, AND CHARACTERIZATION OF A MEMS DUAL-BACKPLATE CAPACITIVE MICROPHONE

By

DAVID THOMAS MARTIN

A DISSERTATION PRESENTED TO THE GRADUATE SCHOOL
OF THE UNIVERSITY OF FLORIDA IN PARTIAL FULFILLMENT
OF THE REQUIREMENTS FOR THE DEGREE OF
DOCTOR OF PHILOSOPHY

UNIVERSITY OF FLORIDA

2007

ACKNOWLEDGMENTS

Financial support for this work has been provided by a National Science Foundation grant and by Sandia National Laboratories. I thank my advisors, Toshi Nishida and Mark Sheplak, for their many helpful technical discussions, as well as their career and personal advice. I am also grateful to my committee members, Lou Cattafesta and Rob Fox, for their assistance in the success of this project.

I am especially grateful to my many colleagues in the Interdisciplinary Microsystems Group. Karthik Kadirval and Jian Liu worked closely with this project and each added their insight and helpful contributions. I am grateful to Robert Dieme, Ben Griffin, Stephen Horowitz, Brian Homeijer, and Todd Schultz, for their assistance in the experimental setups. I thank Brandon Bertolucci for his technical assistance, as well as his photographic and artistic assistance along with Tai-an Chen. I am also grateful to all of the students at IMG for their engaging technical discussions, friendship, and comradery.

I am particularly thankful for the excellent machining work performed by Ken Reed at TMR engineering. I also acknowledge Keck Pathammavong, of Engent, Inc., for his skill in wirebonding the packaged devices. Other technical assistance was provided at the University of Florida by Prof. Ho-Bun Chan and his student Corey Stambough with the supercritical release, Al Ogden with packaging, and Stephen Tedeschi in preparing the SEM images. Pete Loeppert, from Knowles Acoustics, is acknowledged for providing amplifiers used as part of this work. The Electrical and Computer Engineering departmental staff is thanked for their kind assistance.

I thank my parents, Ed and Norine Martin, for their support and guidance. They instilled in me a good work ethic and perseverance; without which, this project would not have been as successful. Above all, I am grateful to my wife, Erica, for her never-ending patience and support.

TABLE OF CONTENTS

LIST OF TABLES

LIST OF FIGURES

Abstract of Dissertation Presented to the Graduate School
of the University of Florida in Partial Fulfillment of the
Requirements for the Degree of Doctor of Philosophy

# DESIGN, FABRICATION, AND CHARACTERIZATION OF A MEMS DUAL-BACKPLATE CAPACITIVE MICROPHONE

By

David Thomas Martin

August 2007

Chair: Toshikazu Nishida
Cochair: Mark Sheplak
Major: Electrical and Computer Engineering

A microphone is an instrument that measures an acoustic signal and generates an electrical output. Microphones have many common applications ranging from use in cellular phones and computers to high quality studio microphones for music recording. However, there is a less familiar application for microphones: microphones are utilized by commercial aircraft manufacturers to assist in the development of quiet aircraft. Communities surrounding airports object to the loud noises produced by approaching and departing aircraft. Therefore, strict regulations exist to limit the noise radiated by commercial aircraft. To reduce the noise radiation of airframes and jet engines, aircraft manufacturers perform rigorous testing during the development and qualification of their products. The microphones used for these measurements have specifications that differ greatly from a common audio microphone.

The industry relies on expensive non-MEMS microphones for aeroacoustic measurements. To date, there have been many MEMS microphones developed; some are even successful commercial products. However, the majority are targeted for audio applications. The existing aeroacoustic MEMS microphones show promise; however, the performance must be improved to compete with existing non-MEMS microphones. The goal of this research is to design a MEMS-based

microphone suitable for aeroacoustic measurements, while improving on the performance of existing devices.

This study details a thorough review of previous MEMS microphones and identifies which are most suitable for aeroacoustic measurements. Furthermore, the specific opportunities for improvement are discussed. A thorough development of the theory of operation for capacitive microphones is presented. Using this theoretical framework, the design of an aeroacoustic capacitive MEMS microphone is presented. The microphone is fabricated using the SUMMiT V process at Sandia National Laboratories. Multiple microphones are tested and the results indicate the designed microphone compares favorably to previous aeroacoustic MEMS microphones.

# CHAPTER 1
# INTRODUCTION

In an effort to reduce the impact of airports and air travel on local communities, the Federal Aviation Administration (FAA) has regulated the level of noise that aircraft may radiate. The US Code of Federal Regulations specifies tests that a commercial aircraft must pass for its airworthiness certification. Requirements are specified for three general classes of aircraft and are broken down further by weight. The regulations for each class of aircraft specify the maximum allowable effective perceived noise level (EPNL). The EPNL is the measured noise level corrected for atmospheric conditions, the duration of the sounds, and the specific operating conditions of the jet engine(s). For example, for an aircraft weighing $617,200$ pounds or more, the most stringent requirement limits the noise during approach to 105 $EPNdB$ [1].

To meet these requirements, the noise radiation of an aircraft must be considered during its design. To design quieter aircraft, it is important to localize and understand the sources of noise generation. The behavior of airframes and jet engines can be studied by conducting measurements on scale models in a wind tunnel where conditions are well controlled [2]. Aeroacoustic measurements are performed to quantify the sound field and to provide insight into noise generation mechanisms so that the noise can be reduced to acceptable levels. A key component in any aeroacoustic measurement setup is the microphone. The performance characteristics of the selected microphone greatly impacts the success of the measurements and the quality of the results. Some of the characteristics of the microphone to consider are the dynamic range, sensitivity, bandwidth, stability, size, and cost [2].

## 1.1 Motivation

In this section, a motivation for this work is given. The requirements for aeroacoustic measurements are translated into a set of design goals for an aeroacoustic microphone.

A microphone must meet several requirements to be suitable for aeroacoustic measurements. Table 1-1 summarizes how the requirements for aeroacoustic measurements differ from audio measurements. The specifications for audio microphones are mainly driven by the capabilities of the human ear. This comparison is an example; in practice, the microphone specifications are driven by a particular application.

Table 1-1. Comparison of audio and aeroacoustic microphone specifications

| Property | Audio Microphone | Aeroacoustic Microphone |
|---|---|---|
| Max Pressure | 120 $dB$ | 160 $dB$ |
| Bandwidth | 20 $Hz$-20 $kHz$ | 20 $Hz$-100 $kHz$ |
| Noise Floor | 20 $dB$ | 26 $dB$ |
| Size | O(5 $mm$) | O(500 $\mu m$) |

First, the sound pressure level (SPL) to be measured can be very high; for example, near an aircraft jet engine. Thus, the microphone should be capable of measuring sound pressure levels up to 160 $dB$ (re. to 20 $\mu Pa$) or 2000 $Pa$. Second, the FAA requires certification over the frequency range of 45 $Hz < f \leq 11.2$ $kHz$ for full scale vehicles. However, aeroacoustic testing is often conducted on 1/8 scale models. Therefore the frequency range of interest is increased by this scale factor; so the acoustic testing must be conducted over the range of 360 $Hz < f \leq 89.6$ $kHz$ [2]. However, the microphone frequency response should extend down to at least 20 $Hz$ for general characterization. There are several commercial microphones currently available that meet some of the required specifications [3]. The specifications of these microphones are summarized in Table 1-2.

The bandwidth requirements have implications for the size of the microphone. When the wavelength of the incident pressure is large compared to the size of the microphone as shown in Figure 1-1(a), the presence of the microphone does not

Table 1-2. Specifications of several Brüel and Kjær microphones

| Specification | 4190 | 4939 | 4138 |
|---|---|---|---|
| Diameter | 12.7 $mm$ (1/2 $in$) | 6.35 $mm$ (1/4 $in$) | 3.18 $mm$ (1/8 $in$) |
| Max Pressure | 148 $dB$ | 164 $dB$ | 168 $dB$ |
| Bandwidth | 3 $Hz$-20 $kHz$ | 4 $Hz$-100 $kHz$ | 6.5 $Hz$-140 $kHz$ |
| Noise Floor | $-17$ $dB/\sqrt{Hz}$* | 1 $dB/\sqrt{Hz}$† | 18 $dB/\sqrt{Hz}$ |
| Capacitance | 16 $pF$ | 6.1 $pF$ | 3.5 $pF$ |

* Noise figure from B&K 4134 1/2 $in$. microphone.
† Noise figure from B&K 4135 1/4 $in$. microphone.

disturb the sound field. However, at higher frequencies, the wavelength, $\lambda$, of the acoustic wave becomes smaller according to the relation $\lambda = c/f$; where $c$ is the isentropic speed of sound. When the wavelength is on the order of the size of the microphone, the incident pressure is scattered (or reflected) off of the microphone, and a non-uniform sound pressure is created on the diaphragm [4]. This effect, known as *diffraction*, is shown schematically in Figure 1-1(b). The microphone measures the sum of the undisturbed pressure field and the additional pressure generated by diffraction due to the presence of the microphone.

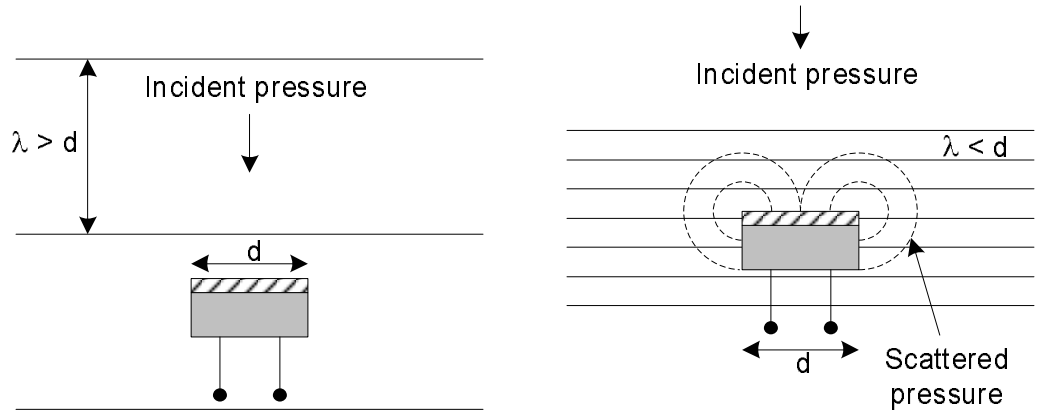


(a) Wavelength larger than the size of the microphone: minimal diffraction

(b) Wavelength smaller than the size of the microphone: diffraction

Figure 1-1. Relationship between the wavelength of the acoustic pressure, microphone size, and diffraction [5].

The degree to which the microphone disturbs the sound field depends on the angle of incidence of the sound wave. If the angle of incidence is known, then the microphone can be designed to compensate for the diffraction [6, 7]. Therefore, in order to have diffraction free-measurements in general,

$$ka << 1, \tag{1–1}$$

where $k$ is the wavenumber given by $k = \omega/c$, and $a$ is the microphone radius. The isentropic speed of sound is $c$, and $\omega$ is the angular frequency. For a maximum frequency of 89.6 $kHz$, $ka$ is equal to 1 with a microphone radius of 600 $\mu m$. Therefore, the microphone radius should be less than 600 $\mu m$ [4].

The lower limit of the input dynamic range is determined by the combined noise of the microphone and interface circuitry, and the overall sensitivity. It is desirable to have lower output noise and a high sensitivity for a low minimum detectable signal. In a sensor system, there are other considerations such as the resolution of the data acquisition system. If an analog-to-digital converter (ADC) is used, the dynamic range is approximately 6 $dB$ for each bit of resolution [8]. Thus a 16 bit ADC has a dynamic range of approximately 96 $dB$ and a 12 bit ADC has a dynamic range of 72 $dB$.

To localize the noise source, acoustic arrays are often used. An acoustic array consists of a large number of microphones arranged in a specific geometry. Through the use of beamforming signal processing, where appropriate weights and delays are applied to each microphone, a selective spatial response can be achieved. This allows the acoustic array to effectively listen to a particular region in space [2]. Due to the large numbers of microphones utilized in typical acoustic arrays, MEMS microphones are attractive due to the potential advantages of batch fabrication. This enables the possibility of a greatly reduced cost per microphone compared to traditional non-MEMS microphones; which can exceed $ 2000 per microphone [9].

A microphone should meet additional specifications for use in an acoustic array. The physical dimensions of two microphones in an acoustic array are shown in Figure 1-2. To avoid spatial aliasing in regularly spaced arrays, two adjacent sensors should be closer than one half of a wavelength. As seen in the figure, the dimensions of the package must be small enough to meet the microphone spacing requirements. Therefore, to avoid aliasing at 89.6 $kHz$, the microphones should be at most 1.9 $mm$ apart.

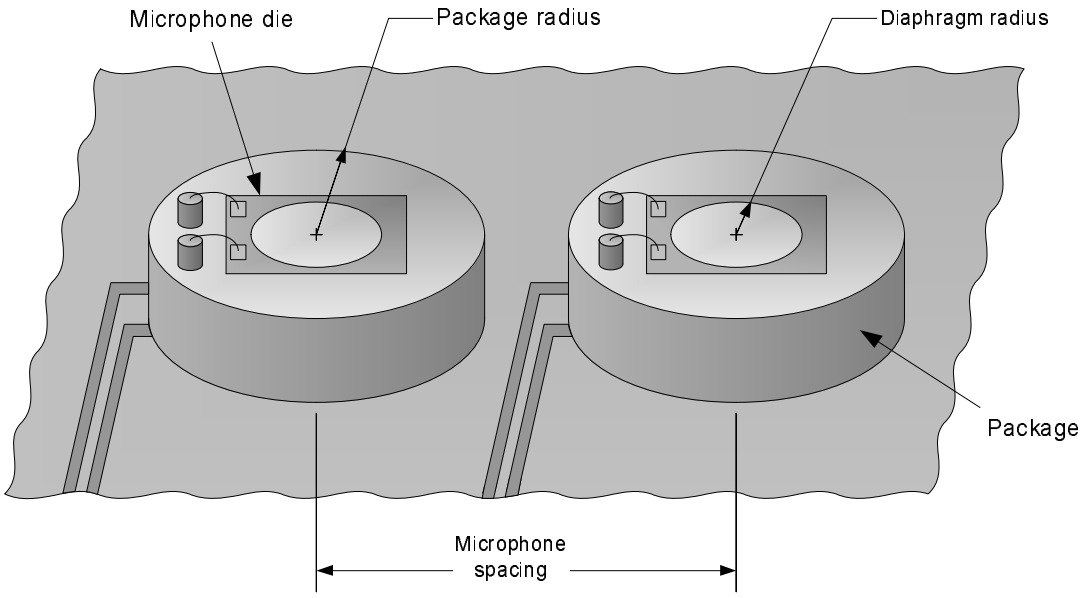


Figure 1-2. The important dimensions for acoustic arrays.

Another consideration for acoustic arrays is the phase and amplitude matching between microphones. The relative phase between channels is crucial information in beamforming algorithms. Mismatch between microphone channels can cause steering vector errors. Therefore it is advantageous to have microphones that are phase and amplitude matched. However it is important to note that even when the microphones are phase matched, other parts of the signal path may also have phase error, such as the interface circuitry and ADC [2, 10].

Microphone cost is another significant factor, especially because of the large number of sensors used in acoustic arrays, typically numbering in the $100s$ [11]. A

reduction in the "per channel" cost of an array can either significantly reduce the total cost of the array, or allow the use of additional sensors. The spatial resolution of the array is proportional to the diameter of the array; however, the minimum microphone spacing determines the upper frequency limit [2]. Therefore, it is advantageous to use a large number of microphones in an acoustic array. Thus, the microphone should also be designed such that its manufacturing and packaging result in a low cost.

Microelectromechanical systems (MEMS) technology has the potential to meet all of the above requirements. MEMS microphones are constructed using lithography based fabrication techniques similar to those used to fabricate integrated circuits [12]. Therefore a small device size is easily attainable. Obtaining phase and amplitude matching is also possible. However this also depends on specific characteristics of the device fabrication and packaging, such as a well controlled vent channel [10]. In addition, it is cost-effective to fabricate MEMS devices in large numbers. Multiple wafers are processed in each lot, and hundreds to thousands of devices are on each wafer. Therefore, MEMS sensors fabricated in sufficient volume have the potential for a greatly reduced cost over traditional sensors [9].

## 1.2 Research Objectives

The goal of this research is to develop a MEMS microphone for aeroacoustic measurements. The key requirements for aeroacoustic measurements have been previously discussed in Section 1.1 and are summarized in Table 1-3. The previous research in MEMS microphones is discussed in detail in Chapter 2. Several previous MEMS microphones have been designed for aeroacoustic applications. The most notable devices are the piezoresistive microphone presented by Arnold et al. [13], the piezoelectric microphone developed by Horowitz et al. [14], and the capacitive microphone developed by Scheeper et al. [15]. However, the benchmark

for aeroacoustic microphones is the conventional (non-MEMS) Brüel and Kjær 4138 condenser microphone.

Table 1-3. Design goals for an aeroacoustic microphone

| Property | Value |
|---|---|
| Maximum pressure | 160 $dB$ |
| Bandwidth | 20 $Hz$-90 $kHz$ |
| Noise floor | $\sim$ 26 $dB/\sqrt{Hz}$ |
| Nonlinearity | $<$ 3 % @ 160 $dB$ |
| Diaphragm radius | $<$ 600 $\mu m$ |

From a detailed literature review of previous MEMS microphones in Section 2.3, it is clear that capacitive microphones in general have shown high sensitivities and low noise floors. Single backplate microphones have limitations with regards to pull-in instability and linearity, further discussed in Chapter 3. However, the advantages of negative feedback can be leveraged with a dual-backplate capacitive microphone; giving the potential for increased stability, bandwidth, and linearity.

For this dissertation, a dual-backplate capacitive microphone has been designed, fabricated, and characterized. The microphone has been fabricated using the *SUMMiT V* process at Sandia National Laboratories [16]. A detailed lumped element model has been developed to model the microphone dynamics. It has also been extended to develop a noise model of the microphone and interface circuitry. A total of 10 microphones have been characterized; 7 with a voltage amplifier, and 3 with a charge amplifier. This work highlights the differences between these amplifier topologies with regards to a low-capacitance MEMS microphone.

The contributions of this work are as follows:

- Development of a MEMS based dual-backplate capacitive microphone suitable for aeroacoustic measurements.

- Novel use of the SUMMiT V process to fabricate a dual-backplate MEMS capacitive microphone.
- Development of a lumped element model and noise model for the dual-backplate microphone.
- Characterization of 10 devices in terms of linearity, bandwidth, and noise floor.
- Experimental comparison between a voltage amplifier and a charge amplifier for low-capacitance MEMS microphones.

## 1.3 Dissertation Overview

This dissertation is organized into seven chapters and four appendices. Chapter 1 introduced and motivated the topic of this dissertation. The background information relevant to this work is discussed in Chapter 2. The modeling is discussed in Chapter 3. This includes the formulation of a lumped element model for the dual-backplate microphone structure as well as a noise model. The design and theoretical performance of the microphone is presented in Chapter 4. Chapter 5 describes the details of the device fabrication. The experimental results are discussed in Chapter 6. Finally, concluding remarks and suggestions for future work are given in Chapter 7.

Supporting details for this dissertation are included in a set of appendices. Appendix A gives the details of of the lumped element model for a clamped circular plate. A detailed derivation of the predicted frequency response is given in Appendix B. The uncertainly analysis for the theoretical microphone performance is presented in Appendix C. Finally, the details of the SUMMiT V process are discussed in Appendix D.

# CHAPTER 2
# BACKGROUND

In this chapter, the basic principles of operation for a microphone are discussed. The key figures of merit are explained and defined. Next, the commonly used transduction mechanisms for MEMS microphones are presented, including the scaling relationships between device size and performance. Finally, a review of previous MEMS microphones is given.

## 2.1 Principles of Microphone Operation

A microphone is a transducer that converts an acoustic signal into an electrical signal. Figure 2-1 shows a schematic representation of a generic microphone. The acoustic energy exists in the form of an incident pressure wave. Information is contained in the amplitude, frequency, and phase of the pressure wave.

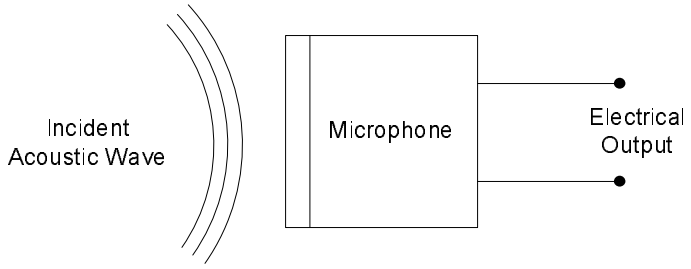


Figure 2-1. Schematic representation of a generic microphone.

Most microphones share some common traits with each other. They have a diaphragm, or cantilever beam, that is exposed to the incident sound pressure. The sound pressure acts on the diaphragm and causes it to deflect, as shown in Figure 2-2. The deflection is detected by a transduction mechanism and typically an electrical output is generated. Microphones also have a vent channel to provide pressure equalization to the cavity. It will be shown later, in Section 3.2, that this vent channel causes the microphone to only respond to time varying pressures. This distinguishes a microphone from an absolute pressure sensor that can measure static pressures.

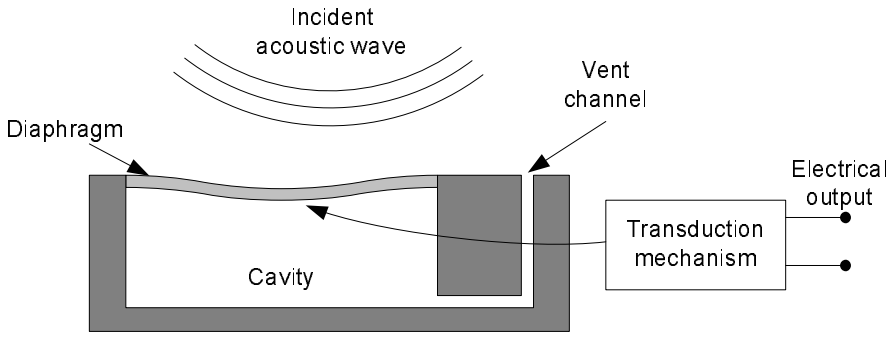


Figure 2-2. Illustration of the operation of a generic microphone. The incident pressure causes a diaphragm deflection which produces an output voltage.

A linear microphone subject to a sinusoidal incident pressure, $P_{in}(\omega)$, with amplitude $P_{in}$ and frequency $\omega$, has an output of the following form,

$$V_o(\omega) = H_{mic}(\omega)P_{in}(\omega); \tag{2–1}$$

where $V_o(\omega)$ and $P_{in}(\omega)$ are the Fourier transforms of the respective time series signals [17]. The term $H(\omega)$ is the frequency response function and is written in terms of its magnitude, $|H(j\omega)|$, and phase, $\angle H(\omega)$, as follows

$$H(\omega) = |H(\omega)|e^{j\angle H(\omega)}. \tag{2–2}$$

The magnitude of the transfer function describes the sensitivity, $S$, of the microphone as a function of frequency. Similarly, the phase of the frequency response is the phase shift, $\phi$, of the microphone as a function of frequency.

In order for the microphone output to accurately represent the spectral content of the acoustic input, it is necessary for a microphone to have a flat frequency response, such that the sensitivity does not vary with frequency. Furthermore, the ideal microphone has *zero* phase shift. A typical frequency response for an under-damped microphone is given in Figure 2-3. The range of frequencies for which the magnitude response of the microphone is flat to within a given tolerance, such as 3 $dB$, gives the usable frequency range of the microphone. This frequency

range is known as the flat band region of the frequency response or more simply the *bandwidth* of the microphone. When a sensitivity of a microphone is reported, it is implied that this is the sensitivity in the flat band region.

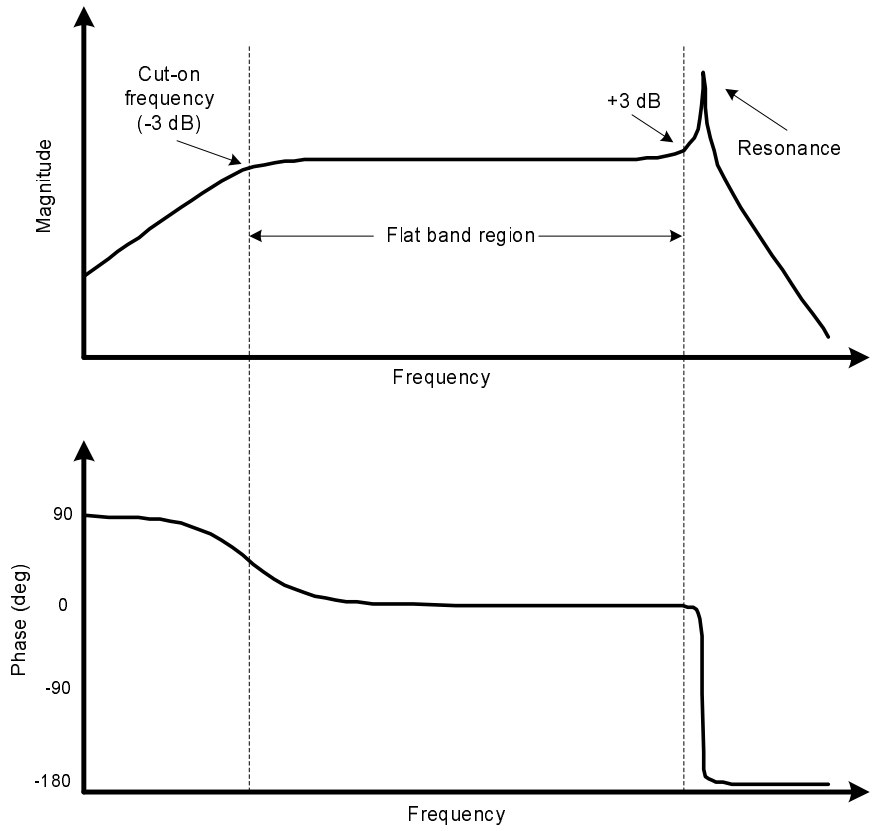


Figure 2-3. Typical frequency response of an under-damped microphone showing the key features.

Also shown in Figure 2-3 is the cut-on frequency and resonant frequency. The low-frequency response of the microphone is dominated by the vent channel and the cavity volume. These two elements of the microphone create a first order high-pass filter and a corresponding cut-on frequency. Below the cut-on frequency, the magnitude response has a slope of 20 $dB$ per decade. It is also possible for the low frequency response of the microphone to be dominated by the interface electronics. At high frequencies, the frequency response of the microphone is dominated by the resonant frequency and the damping of the microphone. The diaphragm has a mechanical resonance that is a function of its compliance and mass. The damping

in the microphone structure determines the shape of the frequency response near the resonance. An under-damped system will have a distinct resonant peak as shown in Figure 2-3, while an over-damped system will not have such a peak. However, in a free-field measurement, scattering effects of the microphone structure may affect the shape of the frequency response near the resonant frequency possibly extending the bandwidth. A microphone can be designed for a known acoustic field, i.e. pressure-field or free-field, to maximize the bandwidth [6]. A pressure-field is where the sound pressure has the same magnitude and phase at any point. Conversely, a free-field is where acoustic waves propagate freely; typically plane waves with a determined propagation direction are assumed [18]. Above the resonant frequency, the frequency response has a slope of $-40\ dB$ per decade .

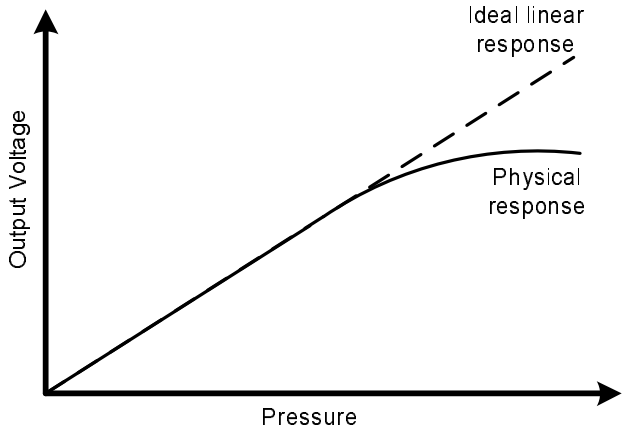


Figure 2-4. The typical actual(–) and ideal(- -) response of a microphone to varying incident pressure amplitudes.

As was previously discussed, the frequency response of the microphone describes how the sensitivity varies with frequency, similarly, the *linearity* of the microphone describes how the magnitude of the microphone output varies with the amplitude of the incident pressure. Shown in Figure 2-4 is the ideal(- -) and actual(–) response of a typical microphone to a single-tone pressure with a varying amplitude. Ideally, the output voltage varies linearly with the amplitude of the incident pressure. However, in practice, various sources of non-linearity

limit the useful maximum pressure. As seen in the figure, the actual response of a microphone deviates from the ideal linear response above a maximum pressure. Typically, the maximum pressure for which the microphone is considered linear is the pressure at which the nonlinear response differs from the ideal linear response by more than 3 %. Since a non-linear response results in distortions in the output, the non-linearity of the microphone can be expressed in terms of the total harmonic distortion (THD) in the frequency domain. The THD is defined as the ratio of the total power in all the higher harmonics ($n > 2$) to the power in the fundamental frequency as follows [17]

$$\text{THD} = \frac{\sum_{n=2}^{\infty} p^2(\omega_n)}{p^2(\omega_1)}. \tag{2–3}$$

Another parameter of interest for microphones is the noise floor. The microphone noise, along with the noise contributions from the interface circuitry, defines the lower end of the dynamic range since it is the output of the microphone when no input is applied [19]. This lower limit of the input dynamic range is the minimum detectable signal (MDS).

Noise is typically expressed in terms of a power spectral density (PSD); for example, it has the units of $V^2/Hz$ for electrical noise. Therefore the total noise power depends on the PSD integrated over the bandwidth of interest [19]. A typical noise PSD is shown in Figure 2-5. In this example, the output referred voltage noise of a microphone includes contributions from the microphone itself as well as the interface electronics.

Systems in thermodynamic equilibrium exhibit thermal noise proportional to the dissipation present in the system [20]. Thermal noise is also referred to as white noise because the PSD is flat for all frequencies. An additional source of noise is flicker noise, or more commonly referred to as 1/f noise because the noise PSD is inversely proportional to frequency. This noise source is only present when a DC

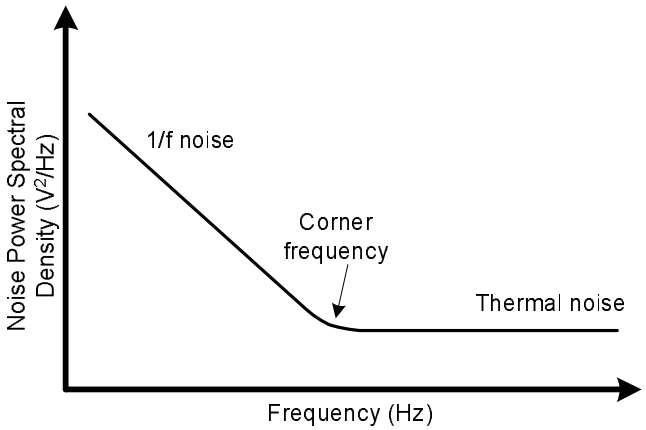


Figure 2-5. The typical power spectral density of the noise floor for a microphone.

current is flowing and is typically seen in piezoresistors and interface electronics. The flicker noise typically dominates at lower frequencies. The corner frequency is the frequency at which the noise PSD of the flicker noise equals the thermal noise [19]. The dynamic response of the microphone can shape the contribution of individual noise sources. This may result in the flat thermal noise of a resistor having a non-flat spectral shape at the output of the microphone.

As previously stated, the total noise power depends on the measurement bandwidth. Therefore, it is common for the noise floor of a microphone to be given for a particular bandwidth. For example, the noise can be given at a specific frequency for a narrow bandwidth, such as the noise at 1 $kHz$ in a 1 $Hz$ bandwidth. Conversely, the noise can be integrated over a specified bandwidth, such as 20 $Hz$ to 20 $kHz$ for audio microphones. Another common metric for audio microphones is the A-weighted noise, denoted $dBA$. Here, the noise spectrum is passed through a filter approximating the response of the human ear, then the noise spectrum is integrated and converted to dB [5]. This metric is not appropriate for aeroacoustic microphones, since both the bandwidth of this filter and the weighting are not relevant. A more useful noise figure of merit for aeroacoustic microphones is the noise in a narrow bandwidth, such as 1 $Hz$ or 1/3 octave, at a particular frequency

such as 1 $kHz$, because the microphone signals are often sampled and analyzed in the frequency domain. Thus the bandwidth $\Delta f$ for the noise power is the bin width in the frequency domain. Ideally, the noise spectrum over the full microphone bandwidth is given.

There are some general scaling relationships that the noise floor of a microphone exhibits. For example, as the resonant frequency and maximum pressure increase, the sensitivity tends to decrease. In general, as the resonant frequency increases, the noise floor will increase. Furthermore, as the maximum pressure increases, the noise floor will also increase. This will in turn increase the input refereed pressure noise of the microphone. These relationships will become evident by studying previous MEMS microphones in Section 2.3.

## 2.2 Transduction Mechanisms and Scaling

In this section, the various types of transduction schemes will be identified. Then, an introduction to the principles of operation for each type of transducer and its scaling will be discussed. A summary of the scaling for all of the microphone types will be given in Section 2.2.6. A detailed derivation of the operation of capacitive microphones will be given in Chapter 3. Before discussing the details of the four principle transduction schemes for MEMS microphones, the general properties of electromechanical transducers will be discussed.

### 2.2.1 Introduction to Electromechanical Transducers

A transducer is a device that converts a signal from one energy domain to a signal in an another domain. Microphones are an example of an electromechanical transducer where an acoustic sound field causes a mechanical response in the microphone which is coupled to an electrical output. There are several properties of electromechanical transducers that can be used to classify them and provide physical insight into their operation. These properties include linear vs. nonlinear,

conservative vs. non-conservative, reciprocal vs. non-reciprocal, and direct vs. indirect [21].

A linear transducer is desirable to ensure measurements have high spectral fidelity. There are various non-linearities that exist in transducers that can limit the dynamic range of the devices. For example, the pressure induced diaphragm deflection can become non-linear for large displacements [22]. Furthermore, the transduction from a mechanical displacement to an electrical output can also be non-linear. This is the case for capacitive transducers. However, the transducer can be linearized about a point for a small region of operation. For capacitive transducers, this can be accomplished via a bias voltage or charge [21].

Transducers can also be energy conserving, i.e. energy is not lost during the transduction from one energy domain to another. Examples of energy-conserving transducers include magnetic, piezoelectric, and capacitive. Optical and piezoresistive transducers are examples of non-energy conserving devices.

A reciprocal transducer is capable of bi-directional operation between two energy domains. For example, a reciprocal transducer converts a signal from one energy domain to the electrical domain; furthermore, it converts a signal from the electrical domain to the first energy domain. In the first mode of operation, the transducer is operating as a sensor; while in the second mode of operation, the transducer is operating as an actuator. An electrostatic microphone is an example of a reciprocal transducer. It can operate as a microphone and convert an acoustic signal to an electrical signal. Furthermore, it can operate as an actuator and convert an electrical signal into an acoustic signal [21].

Another property of electromechanical transducers is whether the transduction is direct or indirect. In a direct transducer, there is a direct relationship between one energy domain and another. An example is an electrodynamic transducer. The motion of a conductor in a magnetic field results in an induced voltage as given by

Lenz' Law [23]. Conversely, a current through a conductor in a magnetic field will result in a force on the conductor [23]. An electrostatic transducer, however, is an indirect transducer.

There are four common transduction schemes used for MEMS microphones. These are the piezoelectric, piezoresistive, optical, and capacitive transduction mechanisms. These are discussed in detail in sections Section 2.2.2 through Section 2.2.5.

### 2.2.2 Introduction to Piezoelectric Microphones

Certain materials generate an electric charge as a result of an applied mechanical stress; these materials are known as piezoelectric materials. Similarly, a mechanical strain is produced in these materials when an external electric field is applied. The generation of electric charge is known as the direct piezoelectric effect while the generation of a mechanical strain is known as the converse piezoelectric effect [24].

The linear piezoelectric constitutive equations expressed in terms of the stress and displacement are [25]

$$S_{ij} = s^E_{ijkl} T_{kl} + d_{kij} E_k \tag{2–4}$$

$$D_i = d_{ikl} T_{kl} + \varepsilon^T_{ik} E_k, \tag{2–5}$$

where $D_i$ and $E_k$ are the electric displacement and electric field whose units are $[C/m^2]$ and $[V/m]$, respectively. Similarly, $T_{kl}$ and $S_{ij}$ are the mechanical stress and strain with units of $[Pa]$ and $[m/m]$, respectively. The mechanical compliance for a constant electric field is $s^E_{ijkl}$, and $\varepsilon^T_{ik}$ is the electric permittivity for a constant stress. The piezoelectric coefficient, $d_{kp}$, quantifies the piezoelectric response for a given strain or applied electric field [24]. The subscripts denote the component of each variable in a particular direction. In a bending mode piezoelectric microphone, the relevant piezoelectric coefficient is $d_{31}$ where the electric displacement in the

'3' direction is related to a mechanical strain in the '1' direction. Conversely, a thickness mode transducer relies on the $d_{33}$ piezoelectric coefficient.

There are two basic configurations of piezoelectric microphones that have been developed in the past: (1) devices with thin diaphragms or (2) devices with a cantilever beam as illustrated in Figure 2-6. The top figure shows a typical piezoelectric microphone with a diaphragm. On top of this diaphragm is a stack consisting of a lower electrode, a piezoelectric film, and a top electrode. This is a simplified cross section in which insulation layers and the details of the electrode geometry are not shown. The bottom figure shows a cross section of a piezoelectric microphone that utilizes a cantilever beam. This type of microphone has a similar electrode/piezoelectric stack, however it is located at the clamped end of the beam because the stresses are concentrated in this region.

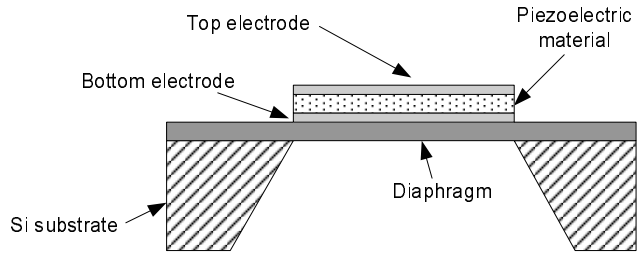


(a) Diaphragm configuration used in [26]

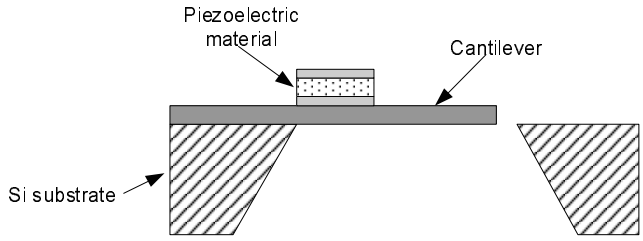


(b) Cantilever beam configuration used in [27]

Figure 2-6. Typical cross sections of piezoelectric microphones. The details of the electrode geometry and vent channel are not shown.

There are a variety of materials that can be used as the active piezoelectric element. The most commonly used piezoelectric thin film for microphones is zinc oxide, ZnO. Other materials that can be used are lead zirconate titanate,

PZT, aluminum nitride, AlN, and aromatic polyurea [14]. There are various tradeoffs when selecting the piezoelectric material such as the magnitude of the piezoelectric coefficient, the film stability, relative permittivity, and compatibility with other processes. For example, AlN is fully compatible with a complimentary metal oxide semiconductor (CMOS) process but has a relatively low piezoelectric coefficient compared to PZT, which cannot be used in a CMOS process [14]. Another parameter of interest for piezoelectric microphones is the $g*$ coefficient, which considers the behavior of piezoelectric composites [28].

Piezoelectric microphones can be operated in one of two ways: they can be operated in a voltage mode where the output voltage is amplified by a voltage amplifier; or they can be operated in a charge mode where the output charge is converted to a voltage by a charge amplifier. The advantage of using the charge mode is that the overall sensitivity is not affected by parasitic capacitance, for example by changing the cable length [29].

When discussing MEMS devices and comparing to traditional devices, it is important to study how the device performance scales as the device size is reduced. The sensitivity is proportional to the stress in the diaphragm, which is proportional to $(a/h)^2$ for a plate [30]. As seen from Equation 2–5, the stress creates an electric displacement. The voltage across the piezoelectric element is proportional to the thickness of the piezoelectric material, $h_{pe}$. Therefore, if the aspect ratio of the diaphragm remains fixed, the stress in the diaphragm will not change as the dimensions are reduced. However, if the piezoelectric thickness is reduced, the sensitivity will be lower; assuming the diaphragm stress is independent of the piezoelectric stress. The bandwidth of the microphone is dominated by the resonant frequency of the diaphragm which is proportional to $h/a^2$, therefore, as the size of the microphone is reduced, the bandwidth increases [21]; this assumes that the diaphragm is modeled as a plate. The microphone contributes to the

noise floor due to internal resistance which gives rise to $\sqrt{4kTR}$ noise [19], however dominant noise sources for piezoelectric devices are typically the interface circuitry and environmental interference from sources such as power lines [29].

### 2.2.3 Introduction to Piezoresistive Microphones

While the resistance of all resistors will change due to stress-induced deformation, certain materials exhibit a much higher change in resistance due to an applied stress. These materials undergo a fundamental electronic change in resistivity due to an applied stress; this is the piezoresistive effect. For semiconductor piezoresistive materials such as silicon, the change in resistivity is due to a change in the mobility. For a resistor with resistivity $\rho$, the change in resistivity, $\Delta\rho$, is given by

$$\frac{\Delta\rho_{ij}}{\rho_{ij}} = \Pi_{ijkl} T_{kl}, \tag{2–6}$$

where $\Pi$ is the piezoresistance tensor and $T$ is the stress tensor. This effect was first observed in silicon by Smith in 1954 [31].

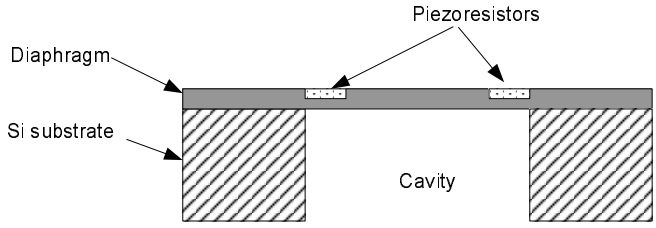


(a) Junction isolated piezoresistors used in [32]

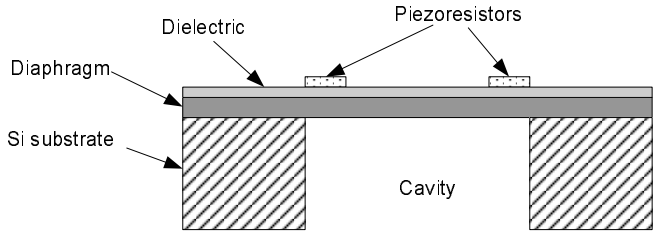


(b) Dielectrically isolated piezoresistors used in [33]

Figure 2-7. Typical cross sections of piezoresistive microphones.

The piezoresistance effect of silicon can be leveraged to create a microphone. Figure 2-7 shows a cross section of typical configurations for piezoresistive microphones. The structure of the piezoresistive microphone is similar to that of the piezoelectric microphone in Figure 2-6(a) in that they both have a diaphragm, substrate, and a cavity. The unique feature of a piezoresistive microphone is that it has one or more piezoresistors that are stressed when the diaphragm deflects. These are typically located near the edge of the diaphragm because the stresses are concentrated in this region. As the incident pressure deflects the diaphragm, stresses cause the resistivity of the piezoresistor to change. The piezoresistors can be embedded in the diaphragm as in Figure 2-7(a); in this case, the piezoresistors are isolated from the diaphragm by a reverse biased pn junction. An alternative is to dielectrically isolate the piezoresistors from the diaphragm as is shown in Figure 2-7(b).

There are several ways to arrange the piezoresistors. The most common is to use four active resistors connected in a Wheatstone bridge configuration, as shown in Figure 2-8. Here, the four resistors all have the same nominal value, $R$. They are arranged and sized such that when the diaphragm deflects, two resistors increase by $\Delta R$ and two decrease by $\Delta R$. The output of the microphone is a differential voltage that is given by

$$V_{out} = V_o^+ - V_o^- = \frac{\Delta R}{R} V_B. \tag{2–7}$$

The sensitivity scaling of the piezoresistive microphone is similar to that of a piezoelectric microphone. The stress in the diaphragm is proportional to $(a/h)^2$ [30]. This stress creates a change in resistance through the piezoresistive transduction coefficients. Thus, the sensitivity will not be reduced as the area is reduced as long as the aspect ratio remains the same. The sensitivity also scales with bias voltage, thus a high bias voltage is desirable. However, the maximum bias voltage is limited by power dissipation, heating, and electro-migration [34].

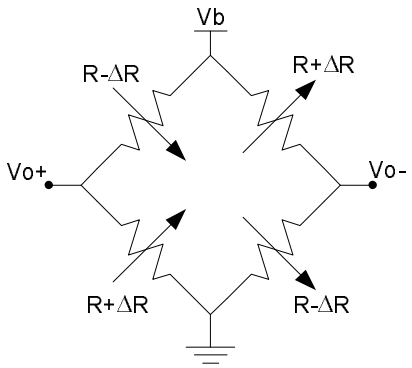


Figure 2-8. Equivalent circuit of a piezoresistive microphone with four active piezoresistors in a Wheatstone bridge configuration.

Furthermore, increasing the bias voltage increases the $1/f$ noise of the microphone. The thermal noise is proportional to $\sqrt{R}$ [19]. The bandwidth of the microphone is dominated by the resonant frequency of the diaphragm, which scales as $h/a^2$; thus as the diaphragm size is reduced, the bandwidth will increase [21].

The performance of piezoresistive microphones is affected by temperature. For example, as the temperature increases, thermal noise increases. Furthermore, at higher temperatures, the leakage current in junction isolated devices increases. As the operating temperature of the device varies, the sensitivity can exhibit temperature drift. The $\Pi$ coefficients are a function of temperature, which impacts the sensitivity. However this can be compensated through the use of circuitry [35].

Piezoresistive microphones have the advantage of not being affected by parasitic capacitance. The relatively low output resistance that is typical of piezoresistive microphones allows the use of instrumentation amplifiers, as used by Arnold et al. [13], without great concern for the input capacitance of the amplifier. Due to mismatch in the nominal values of the piezoresistors, the differential output of a full-bridge device is typically passed through a high pass filter before amplification.

### 2.2.4 Introduction to Optical Microphones

An optical microphone is a device that modulates a light signal based on an incident acoustic wave and then converts the light signal to an electrical signal. There is a wide variety of modulation schemes that can be used for optical microphones, however they can be broadly grouped into three categories: (1) intensity modulation, (2) phase modulation, and (3) polarization modulation. The intensity modulation scheme is typically used by MEMS microphones [36].

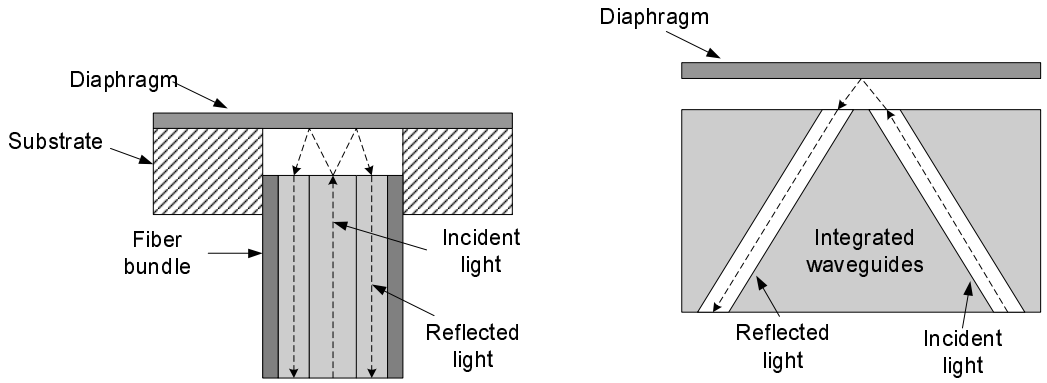


(a) Single fiber bundle for incident and reflected light [37]

(b) Two separate waveguides for incident and reflected light [38]

Figure 2-9. Typical cross sections of fiber-optic lever microphones.

There are two configurations of intensity modulation based microphones that have been used in MEMS based optical microphones. Schematics of fiber-optic lever configurations are shown in Figure 2-9. In each case, a light source is arranged such that it is incident on a diaphragm. As the diaphragm moves, the amount of recovered light is modulated. Figure 2-9(a) shows a configuration where the incident and reflected light are in the same fiber bundle. These devices are typically comprised of a fiber bundle that is used in conjunction with a microfabricated diaphragm. Microphones of the type shown in Figure 2-9(b) have separate paths for the incident and reflected light. They typically have a microfabricated waveguide that is placed in close proximity to a diaphragm.

There are some advantages to using an optical microphone. First, electronics are not needed at the measurement location, thus optical microphones are insensitive to electromagnetic interference and do not emit electromagnetic radiation. Furthermore, optical microphones can be deployed in harsh environments that are not suitable for electronics [38].

However, there are several drawbacks to the optical microphone. Optical microphones require an external reference light source. Furthermore, the output voltage of the microphone may be sensitive to fluctuations in the reference light source. Thus, a very stable reference light source is necessary or additional circuitry must be included to compensate for fluctuations in the reference light source. The packaging is difficult because the waveguides and the diaphragm must be carefully aligned. Furthermore, the packaging must protect the alignment from environmental vibrations [39].

To convert the optical signal to an electrical signal, optoelectronics are a necessary component of an optical microphone setup; typically a photodiode is used. The photodiode can be a significant source of noise due to shot noise [19]. Other noise sources include thermal radiation of the membrane and optical fibers, as well as random pressure fluctuations on the diaphragm; however, these noise sources are typically not dominant for optical microphones [40].

The sensitivity of an optical microphone is proportional to the diaphragm deflection, rather than the bending stress as was the case for the piezoelectric and piezoresistive microphones. The deflection of a clamped circular plate is proportional to $a^4/h^3$ [30]. This can be factored into two terms, $(a/h)^2 \cdot (A/h)$; where $A$ is the surface area of the diaphragm. The first term remains constant if the aspect ratio is fixed, while second term will decrease as the microphone dimensions are reduced. Therefore, if the aspect ratio remains constant, the sensitivity will be reduced as the device size is reduced. The bandwidth will be

limited by the resonant frequency of the diaphragm, which scales as $h/a^2$ for a plate [21]. Thus, the bandwidth will increase as the radius is reduced.

### 2.2.5 Introduction to Capacitive Microphones

The fourth type of microphone is based on the capacitive transduction scheme. Representative cross sections of single backplate MEMS capacitive microphones are shown in Figure 2-10(a) – Figure 2-10(f). Capacitive microphones share some common features with the previous types of microphones, such as a diaphragm and cavity, however there are several distinct features that are unique to capacitive microphones. In addition to a diaphragm, the capacitive microphone also has a porous backplate separated from the diaphragm by an air gap. The backplate holes allow the incident pressure to pass through the backplate and deflect the diaphragm. Sufficient backplate holes must be used or the bandwidth of the microphone will suffer because the microphone will become over-damped. The backplate holes may also be used to tune the damping to maximize the bandwidth for free-field microphones [18].

There are many possible configurations for the backplate in MEMS capacitive microphones. For example, the backplate can be perforated with a large number of holes and be located above the diaphragm as shown in Figure 2-10(b), or the backplate can be located beneath the diaphragm and have a small number of holes as shown in Figure 2-10(a).

The single-backplate MEMS capacitive microphone can be modified by the addition of another plate as shown in Figure 2-11(a). The dual-backplate microphone has two backplates, one on either side of a diaphragm. Historically, this type of differential electrostatic transducer was known as a push-pull device [49]. The earliest uses of this topology was for electrostatic loudspeakers dating back to a 1924 German patent issued to H. Riegger [50].

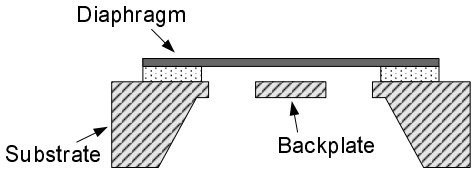


(a) Microphone with a backplate containing a small number of large holes below the diaphragm [41]

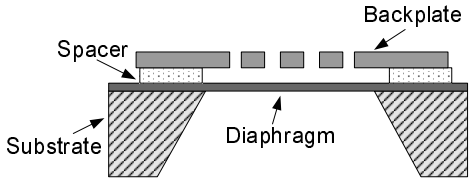


(b) Microphone with a highly perforated backplate above the diaphragm [42]

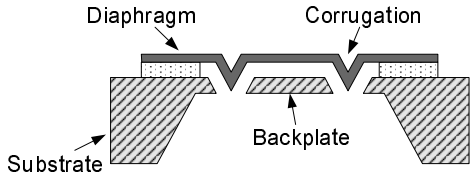


(c) Microphone with a corrugated diaphragm [43]

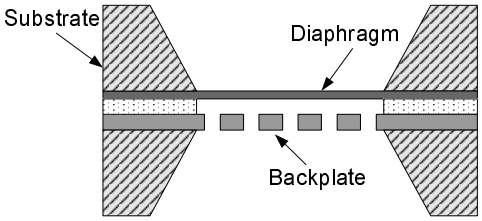


(d) Microphone with the backplate below the diaphragm and a patterned substrate above the diaphragm [44].

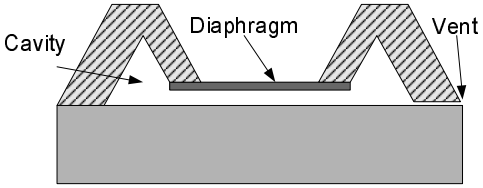


(e) Microphone with a solid backplate and small cavity [45]

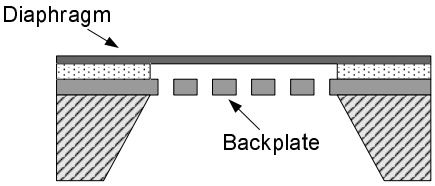


(f) Microphone with a highly perforated backplate below the diaphragm [46]

Figure 2-10. Typical cross sections of single-backplate capacitive MEMS microphones.

This type of device was proposed for MEMS microphones by Bay et al. [51] and developed by Rombach et al. [47, 52, 53] and Martin et al. [54]. The dual-backplate microphone has several advantages over the single-backplate structure. It has the potential for up to twice the sensitivity, a higher bias voltage further increasing the sensitivity, and increased linearity assuming comparable materials and geometry to a corresponding single-backplate microphone. The dual-backplate microphone can also be operated in closed loop with symmetric electrostatic forces acting on the diaphragm. Similarly, the dual diaphragm microphone has one backplate with a diaphragm on either side, as shown in Figure 2-11(b). This

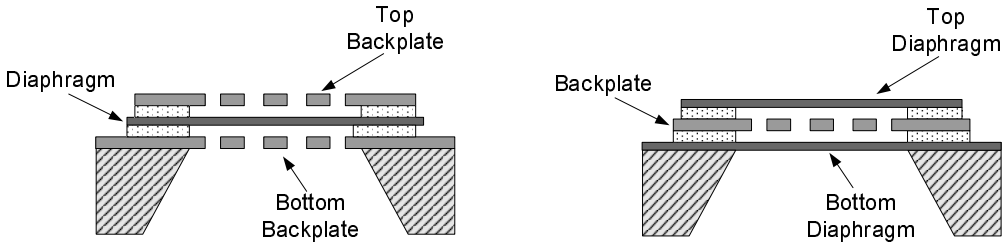


(a) Dual-backplate capacitive MEMS microphone [47].

(b) Dual-diaphragm capacitive MEMS microphone [48].

Figure 2-11. Cross sections of a differential MEMS capacitive microphone.

type of microphone was proposed by Bay et al. [48]. While this structure is not well suited to force feedback applications, it does offer the potential for increased sensitivity and linearity. This structure can also be hermetically sealed to reduce the impacts of the environment on the device performance.

The plates in a capacitive microphone are conductive, thus one or two capacitors are formed depending on the type of capacitive microphone. The capacitors can be approximated by a parallel plate capacitor, which has a capacitance of

$$C = \frac{\epsilon_0 A}{d}, \tag{2–8}$$

where $A$ is the surface area, $\epsilon_0$ is the permittivity, and $d$ is the distance between the plates [23]. In air, the permittivity is assumed to be the permittivity of free space in a vacuum. When the microphone is exposed to an incident sound pressure, the diaphragm deflects. This deflection causes the magnitude of the capacitance to change. Various types of interface circuitry can be used to detect the capacitance change [12].

There are two general classes of capacitive microphones: *condenser* and *electret*. Condenser microphones are biased with an external voltage source, while electrets are biased with a fixed permanent charge. The fixed charge is typically implanted into a thin dielectric layer on the backplate [55]. Electret microphones have the advantage of not being susceptible to electrostatic pull-in. However, the

fabrication is more difficult because a stable embedded charge must be produced. Electret microphones are typically used in low-power and portable applications such as sound level meters [18].

The performance of the capacitive microphone does not scale as favorably as some of the other types of microphones. The derivation of the background material used for the scaling analysis will be given in Chapter 3. The sensitivity depends on both the compliance of the diaphragm and the electric field in the air gap [55]. Therefore, the sensitivity is proportional to the electric field, $V_B/g$, the aspect ratio of the diaphragm, $(a/h)^2$, and the ratio of the diaphragm area to the diaphragm thickness, $(A/h)$. The surface area of the diaphragm with radius $a$ is given by $A$, $h$ is the diaphragm thickness, $V_B$ is the bias voltage, and $g$ is the gap thickness. Therefore, the sensitivity will be reduced as the area is reduced, even if the aspect ratio is kept constant. If the electric field, $V_B/g$, remains constant, this component of the sensitivity will not be affected by scaling. However, there is an upper limit to the bias voltage that can be used with capacitive microphones due to electrostatic collapse of the diaphragm. This pull-in voltage[1] is proportional to $g^{3/2}$ [12]. Thus, electric field will scale as $g^{1/2}$ and will be negatively affected by a reduction in microphone size.

Another issue for capacitive microphones is the magnitude of the capacitance. As the device is scaled down, the capacitance decreases, this can lead to losses due to parasitic capacitances. In addition, the $kT/C$ noise, the total noise across the capacitor integrated for all frequencies, will increase [19]. However, this is not a significant issue if the microphone is operated in a small bandwidth; as is the case when the microphone is sampled and analyzed in the frequency domain. The

[1] The pull-in voltage, including the assumptions and limitations of the model, are discussed in more detail in Section 3.2.7

bandwidth, however, has the potential to increase as the microphone dimensions are reduced. The resonant frequency is proportional to $h/a^2$. However, the acoustic resistance of the backplate holes is proportional to $1/g^3$ and $1/N_h$, where $N_h$ is the number of holes. Thus, the resistance will increase; if it is large enough to excessively damp the microphone, the overall bandwidth could be reduced [21].

The noise floor for capacitive microphones contains contributions from the thermomechanical noise of the sensor and noise sources from the interface electronics [6]. In capacitive microphones, the vent resistance has the potential to dominate the low frequency noise; especially in high-sensitivity devices [18]. Noise contributions from the interface circuit also depend on the type of interface circuit chosen; this will be discussed further in Section 3.3.

### 2.2.6 Scaling Summary

A summary of the scaling properties for MEMS microphones is given in Table 2-1. The scaling of the sensitivity, bandwidth, and the gain-bandwidth (GBW) product are given for piezoelectric, piezoresistive, optical, and capacitive microphones. The GBW product comparison illustrates how the overall microphone performance scales. Assuming the diaphragm aspect ratio and the piezoelectric thickness to diaphragm thickness ratio both remain constant, the sensitivity of the piezoelectric microphone will decrease as the microphone dimensions are reduced while the bandwidth will increase. The GBW product will remain unchanged. Similarly, the GBW product of the optical microphone will also remain unchanged as the microphone dimensions are reduced. The overall performance of the piezoresistive microphone will increase while the performance of the capacitive microphone will decrease.

There are several issues as the sensors become very small. As the diaphragm radius is reduced, the thickness must become very small to maintain the aspect ratio; this could pose fabrication problems. Additionally, as the diaphragm thickness

is reduced, the thickness of the piezoresistors becomes very small. This limits how the minimum value of each resistor, which affects noise performance. Capacitive microphones also have additional issues at small scales; the backplate resistance can become large, effectively lowering the bandwidth, and the capacitance of the device is reduced which can cause losses due to parasitic capacitances.

Table 2-1. Scaling properties of MEMS microphones.

| Microphone type | Sensitivity | Bandwidth | GBW | Summary |
|---|---|---|---|---|
| Piezoelectric | $\frac{a^2}{h^2} \cdot h_{pe}$ | $\frac{h}{a^2}$ | $\frac{h_{pe}}{h_d}$ | S ↓, BW ↑, GBW – |
| Piezoresistive | $V_B \cdot \frac{a^2}{h^2}$ | $\frac{h}{a^2}$ | $\frac{V_B}{h}$ | S – , BW ↑, GBW ↑ |
| Optical | $\frac{A}{h} \cdot \frac{a^2}{h^2}$ | $\frac{h}{a^2}$ | $\frac{a^2}{h^2}$ | S ↓, BW ↑, GBW – |
| Capacitive | $\frac{V_B}{g} \cdot \frac{A}{h} \cdot \frac{a^2}{h^2}$ | $\frac{h}{a^2}$ | $\frac{V_B}{g} \cdot \frac{a^2}{h^2}$ | S ↓, BW ↑, GBW ↓ |

## 2.3 Previous MEMS Microphones

A review of previous research in the field of MEMS microphones is given in this section. This review is divided in terms of transduction mechanism and discusses the significant contributions as well as relevant performance metrics.

### 2.3.1 Literature Review of Piezoelectric Microphones

A review of previous work on the development of piezoelectric MEMS microphones is given in this section. Table 2-2 shows a summary of published piezoelectric MEMS microphones. A timeline of milestones in the development of piezoelectric MEMS microphones is given in Figure 2-12.

The first microfabricated microphone was presented by Royer et al. [26] in 1983. This device used a 3 $\mu m$ thick layer of ZnO sputtered on top of a 30 $\mu m$ thick circular diaphragm with a radius of 1.5 $mm$. Aluminum was used for the electrodes. A sensitivity of 250 $\mu V/Pa$ and a bandwidth from 10 $Hz$ to 10 $kHz$ was reported. The sensitivity varied by 5 $dB$ over this range. The noise floor was measured to be 73 $dBA$.

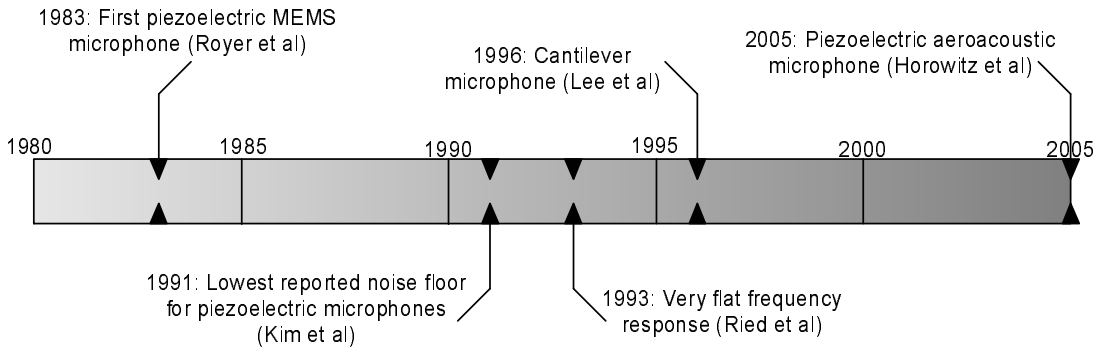


Figure 2-12. Timeline showing milestones in piezoelectric MEMS microphone development.

The Berkeley Sensor and Actuator Center has been active in piezoelectric MEMS microphone research. Their first effort was published by Kim et al. [56] in 1987. This device comprised of a 2 $\mu m$ thick 2 $mm \times 2$ $mm$ square diaphragm with a ZnO piezoelectric film. Later devices were reported in 1989 [57] and 1991 [58]. Both of these devices also used a ZnO piezoelectric layer atop a silicon nitride diaphragm. However, for these devices, a CMOS voltage amplifier was fabricated on the same die as the microphones. In an effort to improve the performance over the first device, an improved process to control the diaphragm stress was used, as well as a larger diaphragm and active area. However, neither of these microphones exhibited a flat frequency response, although the second generation microphone has the lowest reported noise floor for piezoelectric MEMS microphones.

In 1992, Schellin et al. [59] reported a piezoelectric microphone utilizing a polymer film for the active material. Polyurea was used for the piezoelectric material because it has a larger piezoelectric coefficient than aluminum nitride and zinc oxide. A $d_{31}$ piezoelectric coefficient of 5.7 $pC/N - 7.0$ $pC/N$ was reported by the authors. Although a material with a higher piezoelectric coefficient was used, the sensitivity was much lower than that reported previously by Kim et al [58]. Furthermore, the bandwidth was not flat; it varied by about 12 $dB$ over the bandwidth of the microphone.

Table 2-2. Summary of the specifications of piezoelectric MEMS microphones.

| Author | Diaphragm Dimensions | Piezoelectric material | Sensitivity | Dynamic Range | Bandwidth (Predicted) |
|---|---|---|---|---|---|
| Royer et al. 1983 [26] | 1.5 $mm^*$ × 30 $\mu m$ | ZnO | 250 $\mu V/Pa$ | 73 $dBA$ - N/R | 10 $Hz$-10 $kHz$ (0.1 $Hz$-10 $kHz$) |
| Kim et al. 1987 [56] | 2 $mm^\dagger$ × 2 $\mu m$ | ZnO | 0.5 $mV/Pa$ | N/R | 20 $Hz$-5 $kHz$ |
| Kim et al. 1989 [57] | 2 $mm^\dagger$ × 1.4 $\mu m$ | ZnO | 80 $\mu V/Pa$ | N/R | 3 $kHz$-30 $kHz$ |
| Kim et al. 1991 [58] | 3.04 $mm^\dagger$ × 2.0 $\mu m$ | ZnO | 1000 $\mu V/Pa$ | 50 $dBA$ - N/R | 200 $Hz$-16 $kHz$ |
| Schellin et al. 1992 [59] | 0.8 $mm^\dagger$ × 1.0 $\mu m$ | Polyurea | 4000 $\mu V/Pa$ - 30 $\mu V/Pa$ | N/R | 100 $Hz$-20 $kHz$ |
| Ried et al. 1993 [60] | 2.5 $mm^\dagger$ × 3.5 $\mu m$ | ZnO | 920 $\mu V/Pa$ | 57 $dBA$ - N/R | 100 $Hz$-18 $kHz$ |
| Lee et al. 1996 [27] | 2 $mm^\ddagger$ × 4.5 $\mu m$ | ZnO | 38 $mV/Pa$ | N/R | 100 $Hz$-890 $Hz$ |
| Lee et al. 1998 [61] | 2 $mm^\ddagger$ × 1.5 $\mu m$ | ZnO | 30 $mV/Pa$ | N/R | 50 $Hz$-1.8 $kHz$ |
| Ko et al. 2003 [62] | 3 $mm^\dagger$ × 3.0 $\mu m$ | ZnO | 30 $\mu V/Pa$ | N/R | 1 $kHz$-7.3 $kHz$ |
| Niu et al. 2003 [63] | 3 $mm^\dagger$ × 3.2 $\mu m$ | ZnO | 520 $\mu V/Pa$ | N/R | 100 $Hz$-3 $kHz$ |
| Zhao et al. 2003 [64] | 1 $mm^\dagger$ × N/R | PZT | 38 $mV/Pa$ | N/R | 10 $Hz$-20 $kHz$ |
| Hillenbrand et 2004 [65] | 0.3 $cm^2$ area × 55 $\mu m$ | VHD40 | 2.2 $mV/Pa$ | 37 $dBA$-164 $dB$ | 140 $kHz$ |
| | 0.3 $cm^2$ area × 275 $\mu m$ | VHD40 | 10.5 $mV/Pa$ | 26 $dBA$-N/R | 28 $kHz$ |
| Horowitz et al. 2005 [14] | 900 $\mu m^*$ × 3.0 $\mu m$ | PZT | 0.75 $\mu V/Pa$ | 47.8 $dB^\S$ - 169 $dB$ | 100 $Hz$-6.7 $kHz$ (100 $Hz$-50 $kHz$) |

$^*$ Radius of circular diaphragm. $^\dagger$ Side length of square diaphragm.
$^\ddagger$ Side length of cantilever. $^\S$ 1 $Hz$ bin.

Ried et al. published results for another piezoelectric microphone in 1993 [60]. This microphone has much better performance than the previous piezoelectric microphones. Again, a square silicon nitride diaphragm was used with ZnO. Further improvements to the process were made to control the stress in the nitride layer. ZnO was used for the piezoelectric material. This microphone demonstrated a flat frequency response from 100 $Hz$ up to near the resonant frequency of 18.3 $kHz$. In 1996, Lee et al. [27] of the same research group reported

work on a cantilever microphone. This device has a cross section as shown in Figure 2-6(b). An important requirement for a cantilever microphone is that the stresses must be controlled so that the cantilever will not curl. To avoid curling, a low stress silicon nitride layer is sandwiched between two layers of silicon nitride with 150 $MPa$ of tensile stress. While this device had a high sensitivity of 38 $mV/Pa$, the bandwidth was limited to 890 $Hz$. This device can also be used as a microspeaker; at resonance, a sound pressure level of 100 $dB$ was produced into a coupler with a volume of 2 $cm^3$ from a 6 $V$ peak ($V_p$) input at 4.8 $kHz$. An improved device was published by Lee et al. in 1998 [61] with a sensitivity of 30 $mV/Pa$ and a bandwidth of 1.8 $kHz$.

In 2003, piezoelectric microphones were reported by Ko et al. [62], and Niu and Kim [63]. The device developed by Ko et al. is a piezoelectric microphone/microspeaker. Operated as a microphone, it has a low sensitivity and fairly low bandwidth extending to 7.3 $kHz$. When operated as a speaker, a sound pressure of 284 $mPa$ was achieved at a distance of 1 $cm$ at the second resonant frequency of 13.3 $kHz$ with a drive voltage of 15 $V_p$. Niu and Kim utilized parylene-D, a material with low stress and stiffness compared to silicon nitride, in a bimorph configuration in an attempt to create a microphone with a high sensitivity. The device displayed a sensitivity of about 520 $\mu V/Pa$ and a bandwidth limited to 3 $kHz$. Another device was presented by Zhao et al. [64] in 2003. This microphone utilized PZT for the piezoelectric material. A sensitivity of 38 $mV/Pa$ was achieved over a bandwidth extending to 20 $kHz$.

In 2004, Hillenbrand et al. published results for two piezoelectric microphone designs that have several specifications that are attractive for aeroacoustic measurements [65]. This device uses a cellular polypropylene (VHD40) film for the piezoelectric layer. Devices were fabricated with a single 55 $\mu m$ film and five films connected in series. The single film device achieved a dynamic range of 37 $dBA$ to

164 $dB$ with a theoretical resonant frequency of 140 $kHz$. The authors, however, did not discuss the potential aeroacoustic applications of the microphone.

The only piezoelectric MEMS microphone developed to meet the specifications for aeroacoustic measurements was presented by Horowitz et al. in 2005 [14]. This device uses the piezoelectric material PZT atop a silicon diaphragm. The measured dynamic range extends from 47.8 $dB/\sqrt{Hz}$ at 1 $kHz$ to 169 $dB$. While the bandwidth was measured only to 6.7 $kHz$, the resonant frequency was measured to be 50.8 $kHz$, thus the device should have a flat bandwidth up to near this frequency.

There has been good progress in the development of piezoelectric microphones. Early devices suffered from poor stress control in the diaphragms which resulted in non-flat frequency responses. Later devices improved in this respect, however, some had very small bandwidths. The microphone developed by Ried et al. [60] was the first to show a flat frequency response. For all of the microphones, except the work of Horowitz et al. and Hillenbrand et al., the dynamic range was not quantified. Due to its smaller size, Horowitz et al. report the most suitable piezoelectric microphone for aeroacoustic measurements. .

### 2.3.2 Literature Review of Piezoresistive Microphones

A review of piezoresistive MEMS microphones is given in this section. Table 2-3 shows a summary of the key specifications for piezoresistive MEMS microphones. A timeline of milestones in the development of piezoresistive MEMS microphones is given in Figure 2-13.

The first use of a piezoresistive material to create a microphone was in 1957 by Burns [76]. It was constructed of a macro-scale aluminum square diaphragm with an 8 $in.$ side length. A cantilever transferred the diaphragm motion to a piezoresistive bimorph cantilever that consists of two 0.016 $in.$ thick slabs of n-type

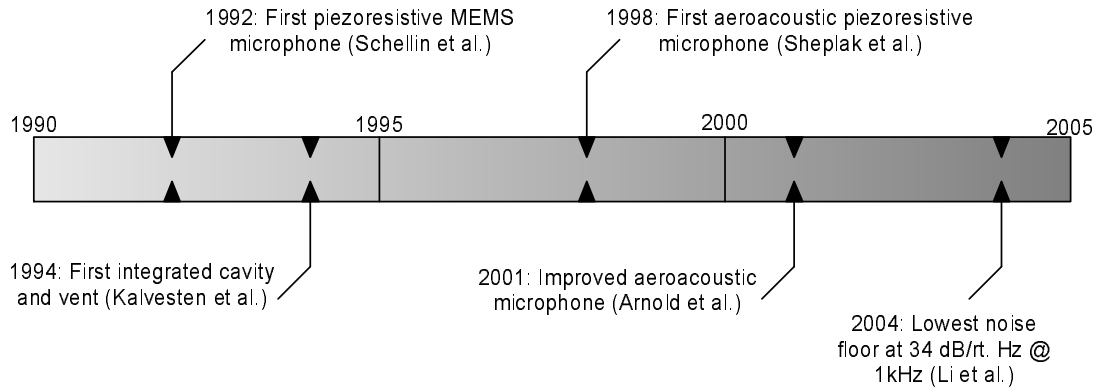


Figure 2-13. Timeline showing milestones in piezoresistive MEMS microphone development.

germanium. While this device was not a MEMS microphone, it demonstrated that semiconductor piezoresistive materials can be used to create transducers.

In 1969, silicon was leveraged to create a MEMS microphone with single crystalline p-type silicon piezoresistors junction isolated from the n-type substrate [66]. This device uses two piezoresistors as part of RC-oscillators. As the resistance changes due to the incident pressure, the oscillation frequency is modulated. The authors noted the need to passivity the surface of the device to avoid drift due to humidity. A layer of silicon nitride was used for this purpose.

A piezoresistive MEMS microphone was presented in 1992 by Schellin et al. [33]. This microphone consists of a square diaphragm with four p-type polysilicon piezoresistors dielectrically isolated from a silicon diaphragm. Several devices were made with varying doping concentrations; the resistance of these devices varied from 300 $\Omega$ to 21 $k\Omega$. With a bias voltage of 6 $V$, the sensitivity was 4.2 $\mu V/Pa \cdot V$. The frequency response between 100 $Hz$ and 5 $kHz$ varied by $\pm 3$ $dB$, with a resonant frequency at 10 $kHz$.

In 1994, Kälvesen et al. [67] presented a microphone for measurements in turbulent gas flows. This device uses two active p-type polysilicon piezoresistors dielectrically isolated from a square polysilicon diaphragm with a 100 $\mu m$ side length. Two additional polysilicon resistors are created on-die to complete the

Table 2-3. Summary of piezoresistive MEMS microphones

| Author | Diaphragm Dimensions | Sensitivity | Dynamic Range | Bandwidth (Predicted) |
|---|---|---|---|---|
| Peake et al 1967 [66] | N/R† | N/R | N/R | N/R |
| Schellin et al 1992 [33] | 1.0 $mm^*$ × 1 $\mu m$ | 4.2 $\mu V/Pa \cdot V$ | N/R | 100 $Hz$-5 $kHz$ |
| Kälvestin et al 1994 [67] | 100 $\mu m^*$ × 0.4 $\mu m$ | 0.09 $\mu V/Pa \cdot V$ | 96 $dBA$ - N/R | 10 $Hz$-10 $kHz$ (2 $mHz$-1 $MHz$) |
| Kälvestin et al 1995 [68, 69] | 300 $\mu m^*$ × 0.4 $\mu m$ | 0.03 $\mu V/Pa \cdot V$ | 90 $dBA$ - N/R | 10 $Hz$-10 $kHz$ (10 $Hz$-0.9 $MHz$) |
| Schellin et al 1995 [32] | 1 $mm^*$ × 1.3 $\mu m$ | 3.8 $\mu V/Pa \cdot V$ | 61 $dBA$ - 128 $dB$ | 50 $Hz$-10 $kHz$ |
| Sheplak et al 1998 [70, 71] | 105 $\mu m^\dagger$ × 0.15 $\mu m$ | 2.24 $\mu V/Pa \cdot V$ | 92 $dB^\ddagger$ - 155 $dB$ | 300 $Hz$-6 $kHz$ (100 $Hz$-300 $kHz$) |
| Naguib et al 1999 [72, 73] | 510 $\mu m^*$ × 0.4 $\mu m$ | .18 $\mu V/Pa \cdot V$ - 1.0 $\mu V/Pa \cdot V$ | N/R | 1 $kHz$-5.5 $kHz$ |
| | 710 $\mu m^*$ × 0.4 $\mu m$ | 1.0 $\mu V/Pa \cdot V$ | N/R | 1 $kHz$-5.5 $kHz$ |
| Arnold et al 2001 [13] | 500 $\mu m^\dagger$ × 1.0 $\mu m$ | 0.6 $\mu V/Pa \cdot V$ | 52 $dB^\ddagger$ - 160 $dB$ | 1 $kHz$-20 $kHz$ (10 $Hz$-40 $kHz$) |
| Huang et al 2002 [74] | 710 $\mu m^*$ × 0.38 $\mu m$ | 1.1 $\mu V/Pa \cdot V$ | 54 $dB^\ddagger$ - 174 $dB$ | 100 $Hz$-10 $kHz$ |
| Li et al 2004 [75] | N/R× 1.0 $\mu m$ | 10 $\mu V/Pa \cdot V$ | 34 $dB^\ddagger$ - N/R | 100 $Hz$-8 $kHz$ |

* Side length of square diaphragm. † Radius of circular diaphragm.
‡ 1 $Hz$ bin.

Wheatstone bridge. This device had a high noise floor of 96 $dBA$. This device was also the first with an integrated cavity and vent channel. Results for a second generation device were presented in 1995 [68, 69]. This device again uses dielectrically isolated polysilicon piezoresistors, however the diaphragm size was increased to 300 $\mu m$ in side length. While this device has a 6 $dB$ lower noise floor than the first device, it also has a lower sensitivity. In fact, both microphones, with sensitivities of 0.09 $\mu V/Pa \cdot V$ and 0.03 $\mu V/Pa \cdot V$ respectively, have low sensitivities. This was attributed to the small cavity beneath the diaphragm which acoustically stiffened the diaphragm. In addition, the resonant frequency of these devices was near 1 $MHz$. This is too high for turbulent gas flow measurements, which the authors

report as having negligible frequency content above 10 $kHz$. A lower resonant frequency through a more compliant diaphragm would increase the sensitivity.

In 1995, Schellin et al. [32] reported on a second piezoresistive microphone. This device has four active p-type piezoresistors created by implanting an n-well with boron. The diaphragm thickness was increased to 1.3 $\mu m$ and with a bias voltage of 8 $V$, the sensitivity was 3.8 $\mu V/Pa \cdot V$. The noise floor of the microphone is 61 $dBA$, while the upper upper limit of the dynamic range is 128 $dB$. The authors concluded that the sensitivity could be increased by reducing the in-plane stress in the diaphragm and by an improved piezoresistor design.

The Interdisciplinary Microsystems Group at the University of Florida has been active in the development of aeroacoustic microphones, including piezoresistive microphones. Their first device, published by Sheplak et al. [70, 71], has a 1500 Å thick circular diaphragm with 210 $\mu m$ diameter. The device uses four p-type single-crystalline silicon piezoresistors dielectrically isolated from the diaphragm. A compact integrated winding vent channel and cavity was used to give a well defined cut on frequency, which is estimated to be 100 $Hz$. The predicted bandwidth extends up to 300 $kHz$, and it is experimentally verified to be flat up to 6 $kHz$. The device has a dynamic range of 92 $dB/\sqrt{Hz}$ at 250 $Hz$ to 155 $dB$. An improved device was presented by Arnold et al. [13]. Differences between this microphone and the previous microphone include a larger diaphragm, lower resistance piezoresistors, and a silicon nitride passivation layer to minimize drift. This device achieved 40 $dB$ reduction in noise floor; however, it has a lower sensitivity and predicted resonant frequency (150 $kHz$). This microphone also demonstrates the potential for excellent matching between devices that MEMS technology offers; the sensitivity and phase response of eight devices varied by $\pm 0.1$ $dB$ and 0.2°, respectively.

Another group of researchers from Michigan State University, Illinois Institute of Technology, and the University of Michigan have been collaborating on the

development of piezoresistive MEMS microphones. In 1999, Naguib et al. [72, 73] presented results for two microphone designs with two diaphragm sizes. These devices have four dielectrically isolated single-crystalline silicon p-type piezoresistors. Limited results for these microphones were presented; they had a sensitivity up to 10 $\mu V/Pa$. A third microphone was reported by Huang et al. [74] in 2002. This device has a similar geometry to the previous microphone, however an improved process to fabricate the piezoresistors was used to lower the noise floor. This device uses dielectrically isolated poly-crystalline silicon piezoresistors. The dynamic range is from 54 $dB/\sqrt{Hz}$ to 174 $dB$ at 2% nonlinearity. While this device has a large dynamic range, with a bandwidth of 10 $kHz$, it does not have the bandwidth required for aeroacoustic measurements.

In 2004, Li et al. [75] presented a piezoresistive microphone with electronics integrated on the same die. Four polysilicon resistors were placed at the edge of a 1 $\mu m$ thick silicon nitride diaphragm. The diaphragm area was not reported. The amplified sensitivity is 10 $\mu V/Pa \cdot V$ with a bias voltage of 5 $V$ and the noise floor is approximately 34 $dB/\sqrt{Hz}$ at 1 $kHz$. The upper limit of the dynamic range was not reported. The bandwidth extends up to 8 $kHz$.

There have been several piezoresistive microphone designs that meet one or more of the requirements for aeroacoustic measurements. The microphone presented by Arnold et al. [13] is the best piezoresistive microphone for aeroacoustic measurements to date. It has sufficient bandwidth and dynamic range. Other devices, such as the work by Sheplak et al. [71] and Huang et al. [74] showed a linear response up to sound pressure levels approaching or exceeding 160 $dB$, however they suffered from a high noise floor or insufficient bandwidth, respectively. Early piezoresistive devices in general were plagued by high noise floors. However, more recent devices have shown that it is possible to fabricate piezoresistive microphones

with lower noise floors. These improvements are mainly due to improved resistor geometry design and improved process flows.

### 2.3.3 Literature Review of Optical Microphones

This section gives a review of previous work in optical MEMS microphones. A timeline of milestones in the development of optical MEMS microphones is given in Figure 2-14 and the reported specifications of the optical microphones are given in Table 2-4.

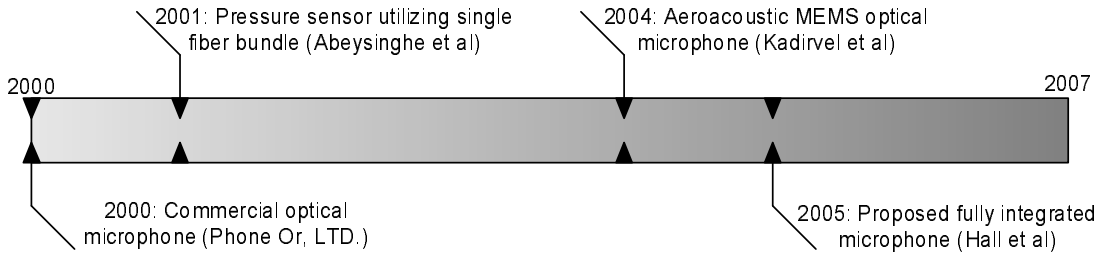


Figure 2-14. Timeline showing milestones in optical MEMS microphone development.

Table 2-4. Summary of optical MEMS microphones

| Author | Diaphragm Dimensions | Sensitivity | Dynamic Range | Bandwidth (Predicted) |
|---|---|---|---|---|
| Abeysinghe et al 2001 [77] | N/R | 0.017 $\mu V/Pa$ | N/R - 347 $kPa$ | N/R |
| Kadirvel et al 2004 [37] | 500 $\mu m^*$ × 1.0 $\mu m$ | 0.5 $mV/Pa$ | 70 $dB^\dagger$ - 132 $dB$ | 300 $Hz$-6.4 $kHz$ (100 $kHz$) |
| Lee et al 2004 [78] | 100 $\mu m^*$ × 1.0 $\mu m$ | 0.5 $\AA/Pa$ | $2\times10^{-4}$ $\AA^\dagger$ - N/R | N/R |
| Hall et al 2005 [79] | 2.1 $mm^\ddagger$ × 3.3 $\mu m$ | 44 $\AA/Pa$ | $2.4\times10^{-2}$ $\AA$ - N/R | N/R-4 $kHz$ |
| Bucaro et al 2005 [80] | 800 $\mu m^*$ × 1.5 $\mu m$ | 25 $mV/Pa$ | 30.6 $dB^\dagger$ - N/R | N/R-20 $kHz$ |
| Song et al 2005 [81] | 800 $\mu m^\ddagger$ × 5 $\mu m$ | N/R | N/R | N/R-2 $kHz$ |

$^*$ Radius of circular diaphragm. $^\dagger$ 1 $Hz$ bin.
$^\ddagger$ Side length of square diaphragm.

In 1985 (and again in later years), Garthe et al. proposed using micromachining technology in the development of integrated optical microphones [38, 82, 83].

The 1985 device has an integrated waveguide chip fabricated using polymethyl methacrylate (PMMA) placed in close proximity to a diaphragm, as shown in Figure 2-9(b). For this first device, rather than using a membrane, a movable mirror was used. The mirror's position was controlled by a micro-positioning device. The coupling ratio, a measure of the recovered light, varied as expected versus the mirror's distance; however, there are no results in terms of microphone specifications. In addition, results were presented for a non-MEMS optical microphone. This device utilized a backplate with a variable air-gap to control the damping. The frequency response extends from 50 $Hz$ to 18 $kHz$. A noise floor of 38 $dBA$ was achieved with a reference optical signal.

Theoretical work on an integrated optical microphone was published by Greywall [84] in 1999. A microphone structure similar to Figure 2-9(a) was discussed. Greywall focused on a theoretical comparison of a condenser microphone and an optical microphone. The author concludes that the optical microphone can have a sensitivity comparable to the condenser microphone.

In 2001, Abeysinghe et al. [77] presented results for an optical MEMS pressure sensor. This device has a structure similar to that shown in Figure 2-9(a). The diaphragm is silicon, to which a borosilicate multimode fiber was anodically bonded. Before the bond, a cavity was created in the fiber bundle by etching the fiber core. The sensitivity of this microphone is 0.017 $\mu V/Pa$ and it has a linear response up to 347 $kPa$, or 204 $dB$. The bandwidth and noise floor were not reported, however. With its very low sensitivity and high operating pressures, the pressure sensor is not well suited for use as a microphone.

An aeroacoustic optical MEMS microphone was presented by Kadirvel et al. [37] in 2004. This device has a structure as shown in Figure 2-9(a). The microphone consists of a 1 $\mu m$ thick silicon nitride circular diaphragm, 500 $\mu m$ in radius, that is deposited on top of a silicon substrate. Aluminum is deposited on

top of the silicon nitride to increase the diaphragm's reflectivity. A fiber bundle was positioned in the cavity beneath the diaphragm. The device shows an overall sensitivity of 0.5 $mV/Pa$, a noise floor of 70 $dB/\sqrt{Hz}$ at 1 $kHz$, and a linear response up to 132 $dB$. The theoretical bandwidth extends to 100 $kHz$, however the frequency response was measured over the range from 300 $Hz$ to 6.7 $kHz$. Over this range, the magnitude varied by approximately 0.5 $dB$.

In 2004, Lee et al. [78] published results for an optical microphone with integrated photodetectors. This device has a 200 $\mu m$ diameter 1 $\mu m$ thick circular aluminum diaphragm. The sensitivity of this microphone is 0.5 $\mathring{A}/Pa$. A second device is reported by Hall et al. in 2005 [79]. This device is unique, in that a fully integrated optical microphone is proposed. A vertical cavity surface emitting laser (VCSEL) is used for the light source; however for this paper, the light source was not integrated with the microphone. The laser shines through a substrate that contains a hole for the laser to pass through and the photodetectors. The photodetectors receive the reflected light from a diaphragm on a third substrate. Furthermore, a diffraction grating is fabricated under the diaphragm. The fabricated device contained a square diaphragm with a side length of 2.1 $mm$ and a thickness 3.3 $\mu m$. Although the resonant frequency was measured to be 44.8 $kHz$ in a vacuum, the bandwidth is limited to 4 $kHz$ due to acoustic damping. The diaphragm has a sensitivity of 44 $\mathring{A}/Pa$ and an A-weighted noise floor of $2.4\times10^{-2}$ $\mathring{A}$. The sensitivities and noise floors for these devices were not reported in terms of an incident pressure; rather they are reported with respect to the diaphragm displacement.

Also in 2005, Bucaro et al. [80] discussed their work on an optical microphone design. The device has a diameter of 1.6 $mm$ and a thickness of 1.5 $\mu m$. The MEMS diaphragm is constructed using bulk micromachining on an SOI wafer with a 1.5 $\mu m$ thick device layer. The device has a sensitivity of approximately

25 $mV/Pa$ and a resonant frequency of approximately 20 $kHz$. The noise floor of this microphone is 30.6 $dB/\sqrt{Hz}$ at 1 $kHz$.

Song et al. reported on their work on an optical microphone in 2005 [81, 85]. This device consists of a 800 $um$ × 800 $\mu m$, 5 $\mu m$ square reflective plate and a multi-mode fiber. This microphone has a usable bandwidth up to 2 $kHz$, however the dynamic range and noise floor were not investigated.

A commercial optical microphone is produced by Optoacoustics, Ltd., for use in MRI machines. The optical microphone is well suited for use near MRI equipment because of the high magnetic fields present. The microphone can be designed without any metal components. Thus, it is not influenced by the magnetic field. This device operates up to a frequency a 15 $kHz$ and a sound pressure level of 140 $dB$. It has a sensitivity of 1.5 $mV/Pa$.

### 2.3.4 Literature Review of Capacitive Microphones

A review of previous work in capacitive MEMS microphones is presented in this section. A summary of the specifications of previously developed MEMS capacitive microphones is given in Table 2-5 and a timeline of milestones in the development of capacitive MEMS microphones is given in Figure 2-15.

Table 2-5. Summary of previous capacitive MEMS microphones.

| Author | Diaphragm Dimensions | Air Gap | Capacitance | $V_{Bias}$ | Sensitivity | Dynamic Range | Bandwidth (Predicted) |
|---|---|---|---|---|---|---|---|
| Hohm et al. 1984 [41] | 8.0 $mm^*$ × 13 $\mu m$ | 20 $\mu m$ | 9 $pF$ | *350 V*† | 3 $mV/Pa$ | N/R | 100 $Hz$-7.5 $kHz$ |
| Sprenkels et al. 1989 [86, 87] | 3.0 $mm^*$ × 2.5 $\mu m$ | 20 $\mu m$ | N/R | *300 V*† | 25 $mV/Pa$ | N/R | 100 $Hz$-15 $kHz$ |
| Murphy et al. 1989 [88] | N/R× 1.5 $\mu m$ | 25-95 $\mu m$ | N/R | *200 V*† | 4-8 $mV/Pa$ | N/R | 100 $Hz$-15 $kHz$ |
| Hohm et al. 1989 [89] | 0.8 $mm^*$ × .25 $\mu m$ | 2 $\mu m$ | 6 $pF$ | 28 $V$ | 0.2 $mV/Pa$-4.3 $mV/Pa$ | N/R | 200 $Hz$-20 $kHz$ |
| Bergqvist et al. 1990 [44] | 2 $mm^*$ × 5 $\mu m$ | 4 $\mu m$ | 3.5 $pF$ | N/R | 13 $mV/Pa$ | N/R | 500 $Hz$-2 $kHz$ |
| | 2 $mm^*$ × 6 $\mu m$ | 4 $\mu m$ | 3.5 $pF$ | N/R | 6.1 $mV/Pa$ | N/R | 100 $Hz$-5 $kHz$ |

* Side length of square diaphragm. † Effective bias voltage for electret.
‡ Radius of circular diaphragm. § Frequency modulation. ¶ 1 $Hz$ bin.

Table 2-5. Continued

| Author | Diaphragm Dimensions | Air Gap | Capacitance | $V_{Bias}$ | Sensitivity | Dynamic Range | Bandwidth (Predicted) |
|---|---|---|---|---|---|---|---|
| | 2 $mm^*$ × 8 $\mu m$ | 4 $\mu m$ | 3.5 $pF$ | N/R | 1.4 $mV/Pa$ | N/R | 500 $Hz$-20 $kHz$ |
| Bergqvist et al. 1991 [90] | 2 $mm^*$ × 5.1 $\mu m$ | 2 $\mu m$ | 5 $pF$ | 5 $V$ | 1.8 $mV/Pa$ | 37 $dBA$-120 $dB$ | 2 $Hz$-20 $kHz$ |
| Scheeper et al. 1991 [91] | 2 $mm^*$ × 1 $\mu m$ | 1 $\mu m$ | 20 $pF$ | 2 $V$ | 1.4 $mV/Pa$ | N/R | 40 $Hz$ |
| Scheeper et al. 1992 [92] | 2 $mm^*$ × 1 $\mu m$ | 3.3 $\mu m$ | 5-7 $pF$ | 16 $V$ | 2 $mV/Pa$ | 35 $dBA$-N/R | 100 $Hz$-10 $kHz$ |
| Kühnel et al. 1992 [93] | 0.8 $mm^*$ × .25 $\mu m$ | 2 $\mu m$ | 1 $pF$ | 28 $V$ | 1.8 $mV/Pa$ | N/R | 100 $Hz$-20 $kHz$ |
| Bourouina et al 1992 [45] | 500 $\mu m^*$ × 1 $\mu m$ | 5 $\mu m$ | N/R | N/R | 0.4 $mV/Pa$ | N/R | N/R-20 $kHz$ |
| | 707 $\mu m^*$ × 1 $\mu m$ | 5 $\mu m$ | N/R | N/R | 2 $mV/Pa$ | N/R | N/R-7 $kHz$ |
| | 1 $mm^*$ × 1 $\mu m$ | 5 $\mu m$ | N/R | N/R | 3.5 $mV/Pa$ | N/R | N/R-2.5 $kHz$ |
| | 1$mm^*$ × 1 $\mu m$ | 7.5 $\mu m$ | N/R | N/R | 2.4 $mV/Pa$ | N/R | N/R-10 $kHz$ |
| Bergqvist et al. 1994 [42] | 1.8 $mm^*$ × 8 $\mu m$ | 3 $\mu m$ | 5.4 $pF$ | 28 $V$ | 1.4 $mV/Pa$ | 43 $dBA$-N/R | 300 $Hz$-13 $kHz$ |
| Bernstein et al. 1996 [94] | 1.8 $mm^*$ ×N/R | N/R | N/R | 5-10 $V$ | 16 $mV/Pa$ | 25 $dBA$-114 $dB$ | 300 $Hz$-15 $kHz$ |
| | 1.0 $mm^*$ ×N/R | N/R | N/R | 5-10 $V$ | 16 $mV/Pa$ | 25 $dBA$-114 $dB$ | 70 $Hz$-15 $kHz$ |
| Zou et al. 1996 [43, 95] | 1 $mm^*$ × 1.2 $\mu m$ | 2.6 $\mu m$ | 3.6 $pF$ | 10 $V$ | 14.2 $mV/Pa$ | 39 $dBA$-N/R | 100 $Hz$-9 $kHz$ |
| Ning et al. 1996 [96] | 2 $mm^*$ × 0.5 $\mu m$ | 3 $\mu m$ | 9.1 $pF$ | 6 $V$ | 3 $mV/Pa$ | N/R | 100 $Hz$-10 $kHz$ |
| Cunningham et 1997 [97] | 1 $mm^{\ddagger}$ × 0.5 $\mu m$ | 2 $\mu m$ | 5.1 $pF$ | 8 $V$ | 2.1 $mV/Pa$ | N/R | 200 $Hz$-10 $kHz$ |
| Pedersen et al. 1997 [98] | 1.6 $mm^*$ × 0.9 $\mu m$ | 1.5 $\mu m$ | 14.9 $pF$ | 15 $V$ | 5.1 $mV/Pa$ | 35 $dBA$-N/R | 100 $Hz$-15 $kHz$ |
| | 2.1 $mm^*$ × 0.9 $\mu m$ | 1.5 $\mu m$ | 18.5 $pF$ | 15 $V$ | 8.1 $mV/Pa$ | 34 $dBA$-N/R | 100 $Hz$-15 $kHz$ |
| Pedersen et al. 1998 [99] | 2.2 $mm^*$ × 1.1 $\mu m$ | 3.6 $\mu m$ | 10.1 $pF$ | N/A | 234 $Hz/Pa^{\S}$ | 60 $dBA$-120 $dB$ | 100 $Hz$-15 $kHz$ |
| Hsu et al. 1998 [46] | 2.6 $mm^*$ × 2 $\mu m$ | 4 $\mu m$ | 16.2 $pF$ | 10 $V$ | 20 $mV/Pa$ | N/R | 100 $Hz$-10 $kHz$ |
| Pedersen et al. 1998 [100] | 2.2 $mm^*$ × 1.1 $\mu m$ | 3.6 $\mu m$ | 10.1 $pF$ | 14 $V$ | 10 $mV/Pa$ | 27 $dBA$-120 $dB$ | 100 $Hz$-8 $kHz$ |
| Schafer et al. 1998 [101] | 0.4 $mm^{\ddagger}$ × 0.75 $\mu m$ | 4 $\mu m$ | 0.2 $pF$ | 12 $V$ | 14 $mV/Pa$ | 27 $dBA$-N/R | 150 $Hz$-10 $kHz$ |

$^*$ Side length of square diaphragm. $^{\dagger}$ Effective bias voltage for electret.

$^{\ddagger}$ Radius of circular diaphragm. $^{\S}$ Frequency modulation. $^{\P}$ 1 $Hz$ bin.

Table 2-5. Continued

| Author | Diaphragm Dimensions | Air Gap | Capacitance | $V_{Bias}$ | Sensitivity | Dynamic Range | Bandwidth (Predicted) |
|---|---|---|---|---|---|---|---|
| Torkkeli et al. 2000 [102] | 1 $mm^*$ × 0.8 $\mu m$ | 1.3 $\mu m$ | 11 $pF$ | 2 $V$ | 4 $mV/Pa$ | 33.5 $dB$, N/R | 10 $Hz$-12 $kHz$ |
| Rombach et al. 2000 [47, 52, 53] | 2 $mm^*$ × 0.49 $\mu m$ | 0.9 $\mu m$ | N/R | 1.5 $V$ | 13 $mV/Pa$ | 23 $dBA$-118 $dB$ | 10 $Hz$-20 $kHz$ |
| Li et al. 2001 [103] | 1 $mm^*$ × 1.2 $\mu m$ | 2.6 $\mu m$ | 1.64 $pF$ | 5 $V$ | 9.4 $mV/Pa$ | N/R | 100 $Hz$-19 $kHz$ |
| Brauer et al. 2001 [104] | 1.2 $mm^*$ × 0.4 $\mu m$ | N/R | 10 $pF$ | 4.5 $V$ | 3.16 $mV/Pa$ | 4 $dB$¶ | 100 $Hz$-10 $kHz$ |
| Kressmann et a 2002 [105] | 1 $mm^*$ × 620 $nm$ | 2 $\mu m$ | 2 $pF$ | 4 $V$† | 3 $mV/Pa$ | 39 $dBA$-123 $dB$ | 10 $Hz$-50 $kHz$ |
| Scheeper et al. 2003 [15] | 1.95 $mm$‡ × 0.5 $\mu m$ | 20 $\mu m$ | 3.5 $pF$ | 200 $V$ | 22 $mV/Pa$ | 23 $dBA$-141 $dB$ | 251 $Hz$-20 $kHz$ |
| Neumann et al. 2003 [106] | 320 $\mu m^*$ × N/R | N/R | 1 $pF$ | N/A | 1.4 $kHz/Pa$§ | 46 $dBA$-N/R | 100 $Hz$-6 $kHz$ |
| Hansen et al. 2004 [107] | (70 $\mu m$ × 190 $\mu m$) × 0.4 $\mu m$ | 1 $\mu m$ | 3.56 $pF$ | N/A | 7.3 $mV/Pa$ | 64 $dBA$-N/R | 0.1 $Hz$-100 $kHz$ |
| Martin et al. 2005 [54] | 0.23 $mm$‡ × 2.0 $\mu m$ | 2 $\mu m$ | 0.74 $pF$ | 9 $V$ | 0.28 $mV/Pa$ | 42 $dB$¶-160 $dB$ | 300 $Hz$-20 $kHz$ |

* Side length of square diaphragm. † Effective bias voltage for electret.
‡ Radius of circular diaphragm. § Frequency modulation. ¶ 1 $Hz$ bin.

The early capacitive MEMS microphones were all electret microphones. The first silicon based capacitive microphone was published by Hohm et al. [41] in 1984. This microphone has a Mylar diaphragm suspended above a backplate with one large hole, similar to Figure 2-10(a). This device uses silicon dioxide deposited on the backplate for the charged layer, charged to about $-350\ V$; the charge density was not reported. Limited characterization indicates a bandwidth from 100 $Hz$ to 7 $kHz$ within 3 $dB$.

Later, two other electret MEMS microphones were developed. In 1989, Sprenkels et al. [86, 87] published results for an electret microphone. The geometry of this device is similar to Figure 2-10(a), however, the backplate makes contact with the center of the diaphragm. This device exhibited a flat bandwidth to 15 $kHz$ with a 5 % variation between devices. Also, in 1989, Murphy et al. [88]

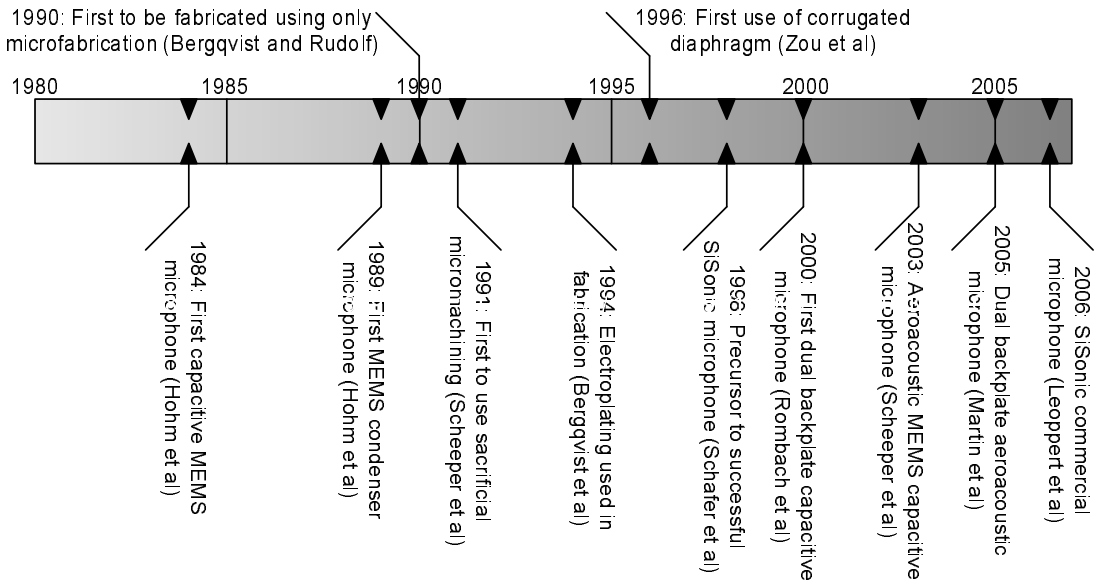


Figure 2-15. Timeline showing milestones in capacitive MEMS microphone development.

published results for another electret microphone with a resonant frequency of about 15 $kHz$. The charge densities were not reported for either of these two microphones.

The early capacitive MEMS microphones, while utilizing micromachining technology, still required manual assembly steps. The microphone developed by Hohm et al. [89] in 1989 improved on previous designs by fabricating the diaphragm and backplate using only micromachining. This device was the first MEMS condenser microphone. However, the backplate and diaphragm components still were joined together by hand. Two wafers were used for the fabrication of the diaphragm and backplate, and the two parts were glued together. The structure of this microphone is similar to Figure 2-10(d), with a patterned substrate above the diaphragm. While these devices were functioning microphones, the patterned substrate above the diaphragm has the potential to cause negative scattering effects. It is better to have a flush mounted diaphragm. Hohm et al. fabricated microphones with varying diaphragm stress by controlling by the ion-implantation dose. For a bias voltage of 28 $V$, the sensitivities ranged from 0.2 $mV/Pa$ to

4.3 $mV/Pa$ and the bandwidths ranged from 2 $kHz$ for the most sensitive device, and to 20 $kHz$ for the least sensitive device. These devices were characterized with voltage amplifiers.

Bergqvist and Rudolf [44] published the first capacitive microphone to be fabricated without hand assembly, using only micromachining, in 1990. Two wafers are used for the fabrication of the diaphragm and backplate, then they are joined together with an anodic bond. In the same year, a second device was published [90]. Both of these microphones have a structure similar to Figure 2-10(d) and both used voltage amplifiers. The second device improved on the performance of the first by reducing the air gap, thus increasing the sensitivity and capacitance, and increasing the number of acoustic holes, which increased the bandwidth. This was the first MEMS capacitive microphone with a highly perforated backplate.

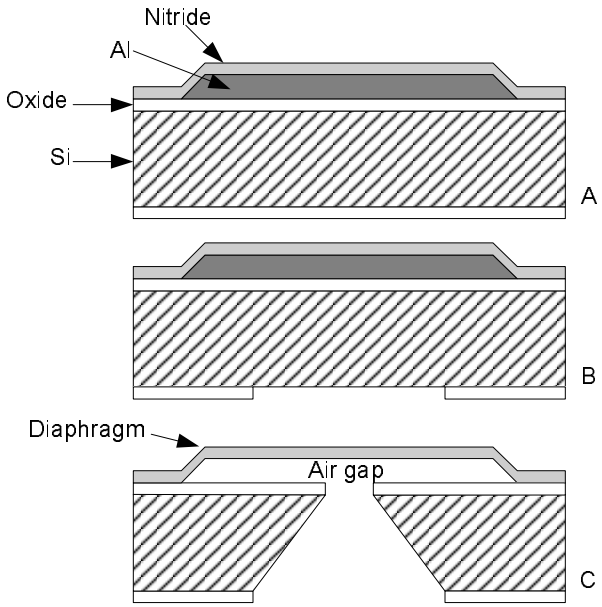


Figure 2-16. Sacrificial micromachining process flow used by Scheeper et al. [91].

The previous MEMS capacitive microphones have been fabricated such that the diaphragm and backplate are formed on separated wafers and then joined together. In 1991, Scheeper et al. [91] presented a condenser microphone fabricated using sacrificial micromachining. The microphone fabrication, shown in Figure 2-16,

uses aluminum as the sacrificial layer which supports the diaphragm and is then subsequently etched. While this device was the first to use sacrificial processing to fabricate a condenser microphone, the microphone itself has limited use because of the limited bandwidth. In 1992, Scheeper et al. [92] improved on the previous design. This device again used sacrificial micromachining. To improve on the previous device, a large number of backplate holes were used; the structure of the microphone now resembles Figure 2-10(b). Furthermore, the air gap thickness was increased to reduce the acoustic damping. This microphone had a flat bandwidth out to 10 $kHz$.

Due to the negative aspects of capacitive microphone scaling, several innovative microphone geometries have been developed. These either focus on reducing the acoustic resistance of the air gap, or reducing the in-plane stress of the diaphragm to increase the sensitivity of the microphone.

In 1992, Kühnel and Hess [93] published results for a condenser microphone with a structured backplate. A cross-section of this device is shown in Figure 2-17. This microphone achieved a bandwidth up to 20 $kHz$. Groves were placed in the backplate to reduce the resistance in the air gap. Therfore, in addition to reducing the backplate resistance by increasing the number of holes [92], this device demonstrates that a structured backplate can also be used to reduce the backplate resistance. However, the structured backplate results in a non-uniform air gap; this will affect the electrostatic behavior of the microphone. However the authors did not discuss this behavior.

A technique used to increase the diaphragm compliance, and thus the sensitivity, is to relieve diaphragm stress using a corrugated diaphragm. Scheeper et al. [108] produced the first MEMS corrugated diaphragm in 1994. The first microphone to utilize a corrugated diaphragm was published by Zou et al. [43, 95]

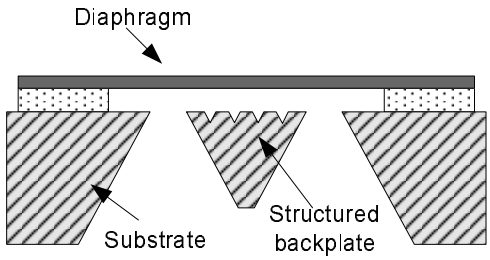


Figure 2-17. Cross section of the microphone developed by Kühnel and Hess [93].

in 1996. Corrugated microphones have a cross section similar to that in Figure 2-10(c). This device has a 0.4 $\mu m$ thick diaphragm with 8 $\mu m$ deep corrugations.

Other devices that used a corrugated diaphragm include the work of Cunningham and Bernstein [97] in 1997, Li et al. [103] in 2001, and Kressman et al. [105] in 2002. The microphone designed by Cunningham and Bernstein has a 0.5 $\mu m$ thick diaphragm with 1 $\mu m$ deep corrugations, while the device designed by Li et al. has a 1.2 $\mu m$ thick diaphragm with a single 300 $\mu m$ deep corrugation. The device reported by Kressman et al. has a 0.62 $\mu m$ thick diaphragm with 1.2 $\mu m$ deep corrugations. This device is also the first corrugated electret microphone. While the corrugations increase the compliance of the diaphragm, which increases the sensitivity; the fabrication process becomes more complex.

A series of microphones with various diaphragm areas and air gap thicknesses were fabricated by Bourouina et al. [45]. This work demonstrates the scaling attributes of capacitive microphones. These microphones all have the geometry shown in Figure 2-10(e) with a solid backplate and a small cavity. The edge length of the square diaphragm ranged from 500 $\mu m$ to 1$\mu m$ and the air gap thickness ranged from 5 $\mu m$ to 7.5 $\mu m$. From their results, it is clearly seen that increasing the diaphragm size increases sensitivity and decreases bandwidth. In addition, increasing the air gap thickness lowers the sensitivity and increases the bandwidth.

In 1994, Bergqvist and Gobet [42] reported on a capacitive microphone fabricated using surface micromachining and electroplating. To fabricate the device,

first a sacrificial layer of photoresist is deposited. Copper is then electroplated on top of the resist to form the backplate. The silicon wafer is etched from the backside; the etch is timed such that 8 $\mu m$ of the wafer remains when the etch is completed. This silicon layer forms the diaphragm. This device has a cross section similar to Figure 2-10(b). Both the capacitance and sensitivity were lower than expected. This was attributed to the buckling of the backplate which increased the air gap to about 5 $\mu m$.

The first capacitive microphone with on-chip circuitry was presented by Bernstein and Borenstein [94] in 1996. This device utilized electroplating to fabricate the backplate, similar to the process flow used by Bergqvist and Gobet [42]. The on-chip interface circuitry was a JFET buffer with an effective input capacitance of 0.5 $pF$.

Pedersen et al. published results for several microphones with on-chip interface circuitry. Their first device, published in 1997 [98], did not include on-chip circuitry. However, this microphone was the basis for their future work. It used polyimide for both the diaphragm and backplate and the microphone geometry is similar to that of Figure 2-10(b). A metallization consisting of chromium and gold was used to produce an electrically conductive diaphragm and backplate. This device exhibited a bandwidth up to 15 $kHz$ and a noise floor of 34 $dB$. In 1998, Pedersen et al. reported on a new microphone with integrated electronics. The microphone geometry was similar to the previous design, however it has larger dimensions. A schematic of the interface circuit is shown in Figure 2-18. The microphone is a variable capacitor in an oscillator; as the capacitance value changes, the frequency of oscillation changes. While this device used a unique detection scheme, it had a high noise level for an audio microphone of 60 $dBA$.

Pedersen et al. [100], in 1998, improved the performance of their previous microphone design [99] by integrating the same microphone with a different

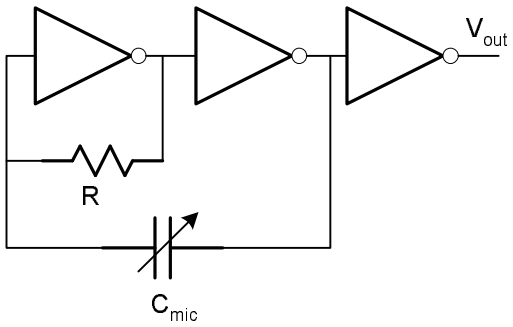


Figure 2-18. Integrated circuitry used by Pedersen et al. [99].

interface circuit than previously used. For this device, an integrated DC-DC converter generates the bias voltage for the microphone and the microphone output is buffered by an integrated source follower. This device had the lowest noise floor of the three microphones developed by Pedersen et al.; it was 27 $dBA$.

Schafer et al. [101], of Knowles Acoustics, developed a condenser microphone for hearing aid use in 1998. This device is unique in that it uses a diaphragm that is supported in the middle, rather than clamped at the perimeter. This yields a compliance nearly five times larger than an edge clamped diaphragm of the same dimensions. Corrugations are used to relieve the in-plane stress of the diaphragm. This microphone also features an integrated charge pump to generate the bias voltage as well as an integrated CMOS buffer. The sensitivity of the microphone is 14 $mV/Pa$ for a bias voltage of 12 $V$. The bandwidth is flat from about 150 $Hz$ to 10 $kHz$ and the resonant frequency is around 17 $kHz$. The A-weighted noise is as low as 28 $dBA$. This device used a unique diaphragm arrangement and is well suited for a hearing aid.

Knowles Acoustics produces several commercial MEMS capacitive microphones. Rather that the on-chip buffer described in the 1988 paper [101], these are hybrid packaged with off-chip voltage buffers for a lower overall manufacturing cost. Configurations are available with either unity gain or a gain of 20 $dB$. An example is the SP0101 [109], which has a sensitivity of 7.9 $mV/Pa$, a bandwidth of 10 $kHz$,

and a noise floor of 35 $dBA$. All of these microphones, with 10 % distortion at 115 $dB$, are for high volume, low cost audio applications. The commercial SiSonic microphones were also reported in 2006 by Leoppert and Lee [110].

In 2000, Torkkeli et al. [102] published results for a condenser microphone that used polysilicon doped with boron at a level of $10^{19}$ $cm^{-3}$ for both the diaphragm and the backplate. The annealing temperature was adjusted for each layer to achieve the desired stress. The bandwidth is flat from 10 $Hz$ to 12 $kHz$, and the noise floor is 33.5 $dBA$. Initially, the sensitivity was lower and the noise floor was higher; an increase in the cavity volume from 0.8 $mm^3$ to 110 $mm^3$ improved these parameters. This device used a charge amplifier for the interface circuitry.

The majority of the previous MEMS capacitive microphones have been designed for audio applications, e.g. hearing aids. In 2003, Scheeper et al. [15], of Brüel and Kjær, developed a MEMS-based measurement microphone that can be used for sound pressure levels well in excess of 120 $dB$. This device has a 0.5 $\mu m$ thick diaphragm with a radius of 1.95 $mm$; the octagonal diaphragm is approximated as being circular. The diaphragm is joined to the backplate wafer with an air gap of 20 $\mu m$. This microphone is packaged in a robust metal shell, however, due to the geometry and fabrication of the microphone, the diaphragm is not flush with the top surface of the sensor. The cross section is similar to Figure 2-10(d), however the backside is enclosed by the package. With a bias voltage of 200 $V$, a sensitivity of 22 $mV/Pa$ was achieved. The microphone has a bandwidth up to 20 $kHz$; the lower limit of the bandwidth was not reported, however the frequency response extends to as low as 251 $Hz$. The most distinguishing feature of the microphone is its dynamic range, which extends from 23 $dBA$ to 141 $dB$. A comparison of this device to other Brüel and Kjær microphones is given in Table 2-6.

Table 2-6. Comparison of the Brüel and Kjær MEMS microphone to non-MEMS Brüel and Kjær microphones

| Specification | 4134 | 4135 | 4138 | MEMS |
|---|---|---|---|---|
| Diameter | 12.7 $mm$ (1/2 $in$) | 6.35 $mm$ (1/4 $in$) | 3.18 $mm$ (1/8 $in$) | 3.9 $mm$ |
| Max Pressure | 160 $dB$ | 164 $dB$ | 168 $dB$ | 141 $dB$ |
| Bandwidth | 4 $Hz$-20 $kHz$ | 4 $Hz$-100 $kHz$ | 6.5 $Hz$-140 $kHz$ | 251-20 $kHz$ |
| Noise Floor | 18 $dBA$ | 29.5 $dBA$ | 55 $dBA$ | 23 $dBA$ |

In 2003, Neumann et al. [106] developed a microphone fabricated using a standard CMOS process. The diaphragm was fabricated using an array of six 320 $\mu m$ × 320 $\mu m$ square diaphragms. Each diaphragm consists of a winding pattern of metal and oxide to create a mesh membrane. The substrate is used as the backplate. The geometry of each microphone is similar to Figure 2-10(a). A frequency modulation type of interface circuitry is used where the microphone is the variable capacitor in an oscillator. The signal is transmitted off-chip via an FM signal and is recovered with an FM receiver. The sensitivity is 1.4 $kHz/Pa$ and the bandwidth was flat to within 3 $dB$ over the range from 100 $Hz$ to 6 $kHz$. Both the bandwidth and the sensitivity of this device were not close to the predicted values. This was primarily due to the uncertainties of the mechanical properties in a CMOS process.

Hansen et al. [107] published results for a wide bandwidth capacitive microphone in 2004. This is a unique device that is based on a RF detection scheme. Rather than using the typical single-backplate structure, a small sealed structure was used as shown in Figure 2-10(e), with no vent. A diaphragm was suspended over the substrate creating a small sealed volume. A large number of these devices were connected in a line to form a transmission line. As the capacitance changed, the phase speed of the transmission line changed. The device structure

and equivalent circuit are shown in Figure 2-19. Each 0.4 $\mu m$ thick diaphragm is 70 $\mu m \times 190$ $\mu m$ in area; 45 of the devices are connected in a RF transmission line with a total active capacitance of 3.56 $pF$. A sensitivity of 7.3 $mV/Pa$ was achieved over a bandwidth of 0.1 $Hz$ to 100 $kHz$. One drawback of this device is its relatively high noise floor at 63.6 $dBA$. This device has the advantage of being sealed to protect it from the environment. The large bandwidth of this microphone is well suited to aeroacoustic measurements. However, no information is given regarding the the microphone's maximum pressure or linearity.

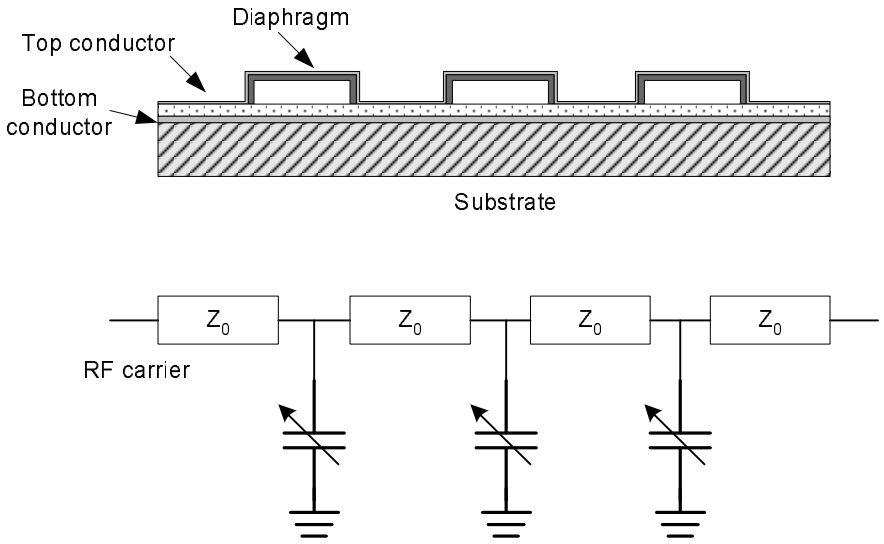


Figure 2-19. Schematic and equivalent circuit of the microphone designed by Hansen et al. [107].

In 2006, Pedersen [111] presented results for a capacitive microphone designed for high frequency applications. This microphone is derived from the Knowles SiSonic$^{TM}$microphone; however the design is modified to extend the bandwidth. The microphone has a sensitivity of 398 $\mu V/Pa$ and an input referred noise floor of 22 $dB/\sqrt{Hz}$ at 1 $kHz$. The bandwidth extends to 100 $kHz$; however, the upper limit of the dynamic range is limited to 140 $dB$.

**Differential capacitive microphones**. As previously discussed, there are several other possibilities for capacitive microphones than the traditional single-backplate design. Figure 2-11 shows two possible configurations for a differential capacitive microphone. There has been a limited amount of previous research into these types of condenser microphones.

In 1996, Bay et al. [48] investigated a dual-diaphragm capacitive microphone. A theoretical analysis of the dual-diaphragm microphone was discussed. In addition, a suggested process flow was given. According to the authors, the advantages of this type of microphone are an increased sensitivity and an immunity to dust and moisture since it is hermetically sealed. In 1999, Bay et al. [51] published a theoretical discussion on a dual-backplate microphone. Due to several problems that were foreseen with the double diaphragm microphone, such as complicated processing and sensitivity to barometric pressure, the authors focused their efforts on a dual-backplate microphone. The dependence of the sensitivity of the microphone to bias voltage, in-plane diaphragm stress, diaphragm thickness, and air gap thickness were investigated. For implementation of force-feedback, the use of a sigma-delta converter was suggested as it provides a digital output; however a comparison of force feedback interface circuit topologies was not given. While these two studies by Bay et al. provide some useful insight into the advantages and disadvantages of differential capacitive microphones, actual devices have yet to be fabricated.

The first dual-backplate microphone to be fabricated and successfully tested was presented by Rombach et al. [47, 52, 53] in 1999. The lower backplate is a composite consisting of a 0.85 $\mu m$ thick layer of silicon nitride and 0.4 $\mu m$ thick layer of boron doped polysilicon. The lower backplate has a total stress of 180 $MPa$. A 0.9 $\mu m$ layer of silicon dioxide is deposited as the first sacrificial layer. Then a stack of 0.045 $\mu m$ of silicon nitride, 0.4 $\mu m$ of polysilicon, and

0.045 $\mu m$ of silicon nitride are deposited to create a diaphragm with a stress of 45 $MPa$. A second 0.9 $\mu m$ layer of silicon dioxide is deposited to form the second sacrificial layer. The top backplate consists of 3 $\mu m$ of polysilicon with a stress of 220 $MPa$. The top backplate is patterned from the top of the wafer using traditional photolithography. The bottom backplate is patterned after all of the upper layers have been deposited by etching from the backside. This removes the need for chemical mechanical polishing because there are no features in the lower backplate when the diaphragm is deposited. The diaphragm is a square with a 2 $mm$ side length. The characterization was conducted on the wafer-scale with the microphones actuated from the backside of the wafer. A low noise voltage amplifier was used for the interface circuitry. With a bias voltage of 1.5 $V$, a sensitivity of 13 $mV/Pa$ was achieved. The frequency response is flat from 10 $Hz$ to about 20 $kHz$. The noise floor is 22.5 $dBA$ and the upper limit of the dynamic range is 118 $dB$. This device was the first successful dual-backplate microphone. Its performance is well matched to audio applications, however further development is needed to produce a device suitable for aeroacoustic measurements.

### 2.3.5 Literature Review Summary

A wide range of MEMS microphones have been developed in the past. These can be grouped into four general transduction techniques: piezoelectric, piezoresistive, optical, and capacitive. The majority of MEMS microphone research has been focused on audio applications. However, at least one microphone targeted for aeroacoustic measurements using each of the four discussed transduction schemes has been designed and fabricated. Table 2-7 summarizes the results for the highest performing aeroacoustic microphones reported to date for each transduction scheme (excluding the dual-backplate aeroacoustic microphone).

The piezoelectric microphone developed by Horowitz et al. [14] can measure the highest maximum pressure. Furthermore, based on this table it has the largest

Table 2-7. Comparison of previous aeroacoustic MEMS microphones and the Brüel and Kjær 4138 traditional condenser microphone.

| Microphone | Type | Radius | Max Pressure | Noise Floor | Bandwidth |
|---|---|---|---|---|---|
| B&K 4138 [3] | Capacitive | 1.6 $mm$ | 168 $dB$ | 20 $dB^*$ | 6.5 $Hz$–140 $kHz$ |
| Arnold et al. [13] | Piezoresistive | 500 $\mu m$ | 160 $dB$ | 52 $dB^*$ | 10 $Hz$–100 $kHz^\dagger$ |
| Scheeper et al. [15] | Capacitive | 1.95 $mm$ | 141 $dB$ | 23 $dBA$ | 251 $Hz$–20 $kHz$ |
| Horowitz et al. [112] | Piezoelectric | 900 $\mu m$ | 169 $dB$ | 48 $dB^*$ | 100 $Hz$–50.8 $kHz^\ddagger$ |
| Pedersen [111] | Capacitive | 180 $\mu m$ | 140 $dB$ | 22 $dB^*$ | 50 $Hz$–75 $kHz^\ddagger$ |

$^*$ 1 $Hz$ bin at 1 $kHz$. $^\dagger$ Predicted bandwidth. $^\ddagger$ Resonant frequency.

dynamic range; however, the noise floor for the capacitive microphone is reported in $dBA$, which has a higher value than $dB/\sqrt{Hz}$. Assuming a flat noise spectrum, the 23 $dBA$ noise figure is equivalent to a noise level of $-18$ $dB/\sqrt{Hz}$. Thus, the capacitive microphone has both the lowest noise floor and largest dynamic range. However, the capacitive microphone is physically too large and has too small of a bandwidth for aeroacoustic measurements.

# CHAPTER 3
# MICROPHONE MODELING

In this chapter, a detailed model of a capacitive microphone is presented. The analysis is broken into three major sections.

In Section 3.1, the quasi-static behavior of the microphone is discussed. This includes the diaphragm behavior, electrostatic behavior, and finally, a discussion on the non-linear properties of the microphone.

In Section 3.2, the dynamic behavior of the microphone is studied. This is facilitated using the lumped element modeling technique. An equivalent circuit model of the microphone is developed. This is used to predict the frequency response and identify key features that impact the microphone response. This is followed by a discussion of electrostatic pull-in; a phenomenon of particular interest for capacitive microphones.

Finally, in Section 3.3, a noise model is developed. First, the derived lumped element model is used to estimate the noise generated by the microphone itself. This is followed by an investigation of the noise due to interface circuitry.

## 3.1 Quasi-Static Modeling

In this section, the quasi-static model of the capacitive microphone is developed; this is treated in three steps. First, the diaphragm model is developed and discussed. This is followed by the electrostatic analysis of a capacitive microphone. This includes an introduction to the electromechanical model of a capacitive transducer. This general model is then applied to specific implementations of the capacitive microphone. Finally, the detailed analysis of the condenser microphone is given.

A cross section of the dual-backplate microphone is shown in Figure 3-1. The major elements of the microphone are the diaphragm, top backplate, bottom backplate, air gaps, backplate holes, cavity, and vent channel. The diaphragm is located between the two backplates and they are separated by two air gaps. The

backplates have holes to allow the acoustic pressure to deflect the diaphragm. A cavity is created beneath the microphone structure. The vent channel equalizes the pressure in the cavity to the ambient pressure.

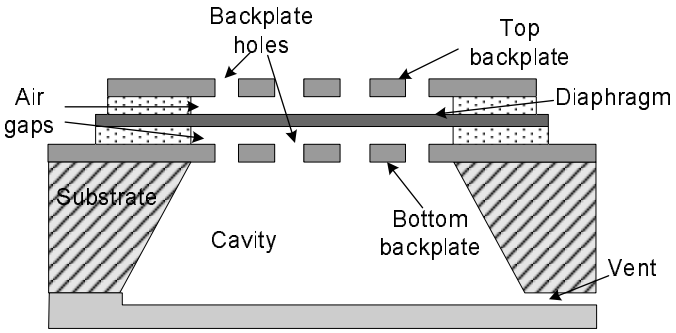


Figure 3-1. Cross section of the dual-backplate capacitive microphone showing the key components.

### 3.1.1 Diaphragm Model

The analysis of the microphone operation begins with the behavior of the diaphragm. The diaphragm deflects when it is exposed to an incident pressure. For microphones, the incident acoustic pressure is a perturbation, $p$, about the ambient pressure, $p_0$; the total pressure $P$ is written as [4]

$$P = p_0 + p. \tag{3–1}$$

The microphone is constructed such that the pressure in the cavity remains constant and is equal to the ambient pressure. [1] Thus the pressure below the diaphragm equals $p_0$, while the pressure above the diaphragm will equal $P$. Therefore, the net pressure acting on the diaphragm is equal to the acoustic pressure perturbation, $p$.

[1] This assumption is valid above a certain frequency and is discussed further in Section 3.2.

A schematic of the diaphragm is shown in Figure 3-2. For this analysis, the diaphragm is assumed to be homogeneous, axisymmetric, and linearly elastic. Furthermore, the diaphragm is assumed to have a perfectly clamped boundary condition around the perimeter of the diaphragm and to have zero residual in-plane stress. The diaphragm has a radius $a$ and a thickness $h$. It is assumed that the Young's Modulus, $E$, and Poisson's ratio, $\nu$, are both known and the diaphragm is loaded with a uniform pressure, $p$.

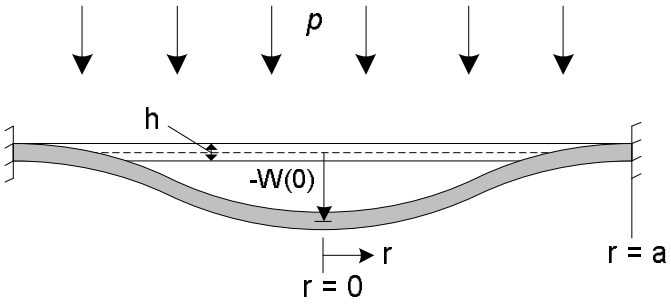


Figure 3-2. Schematic of the idealized circular diaphragm.

#### 3.1.1.1 Small deflection theory

The diaphragm is modeled as having zero in-plane stress while at rest [16]. As the magnitude of the diaphragm deflection increases, the strain in the neutral axis will increase. However, for small deflections, the neutral axis strain can be neglected.

The general governing differential equation for the small displacement solution for a clamped circular plate is given by [22]

$$\nabla^4 w = \frac{-p}{D}, \tag{3–2}$$

where $w$ is the transverse deflection of the plate and $D$ is the flexural rigidity of the plate; which is given by

$$D = \frac{Eh^3}{12\left(1-\nu^2\right)}. \tag{3–3}$$

By assuming an axisymmetric solution where the deflection only depends on the radial coordinate $r$, Equation 3–2 can be simplified to

$$\frac{1}{r}\frac{d}{dr}\left\{r\frac{d}{dr}\left[\frac{1}{r}\frac{d}{dr}\left(r\frac{dw}{dr}\right)\right]\right\} = \frac{-p}{D}. \tag{3–4}$$

The deflection of the clamped circular plate is subject to four boundary conditions. First, the center deflection is finite; second, the deflection at the clamped boundary is zero; third, the slope of the plate at the clamped boundary is zero; and forth, the slope of the plate is zero at the center. Respectively, these can be written mathematically as

$$\begin{aligned} BC\ 1: &\quad w(0) < \infty, \\ BC\ 2: &\quad w(a) = 0, \\ BC\ 3: &\quad \frac{dw}{dr}(0) = 0, \\ \text{and } BC\ 4: &\quad \frac{dw}{dr}(a) = 0. \end{aligned} \tag{3–5}$$

By solving Equation 3–4 with the boundary conditions given in Equation 3–5, the following expression for the plate deflection is obtained:

$$w(r) = \frac{-pa^4}{64D}\left[1 - \left(\frac{r}{a}\right)^2\right]^2. \tag{3–6}$$

Substituting the expression for the flexural rigidity from Equation 3–3 into Equation 3–6 gives an expression for the deflection completely in terms of the plate geometry and material parameters,

$$w(r) = \frac{-3pa^4(1-\nu^2)}{16Eh^3}\left[1 - \left(\frac{r}{a}\right)^2\right]^2. \tag{3–7}$$

This gives the deflection of the diaphragm for small displacements. The deflection shape is given by the term $\left[1-(r/a)^2\right]^2$, while the center displacement of the plate is given by

$$w_L(0) = \frac{-pa^4}{64D}. \tag{3–8}$$

The normalized diaphragm deflection is shown in Figure 3-3. The maximum deflection is in the center of the diaphragm and has a magnitude given by Equation 3–8. The slope of the deflection is zero at the diaphragm center and at the clamped boundaries.

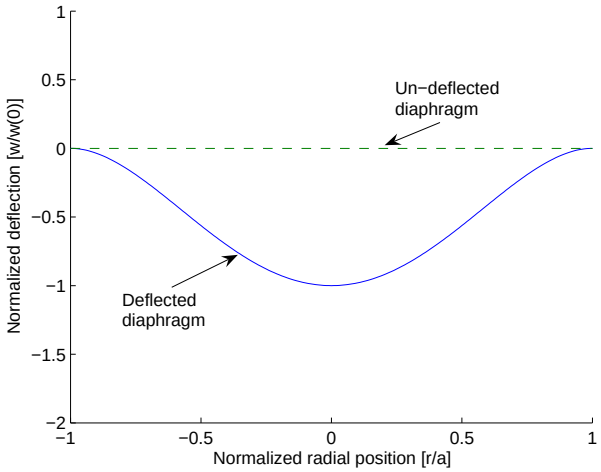


Figure 3-3. Normalized deflection of a clamped circular plate.

#### 3.1.1.2 Large deflection theory

When the deflection becomes large enough to be approximately the same magnitude as the thickness of the plate, the internal strain cannot be neglected. The derivation of the large displacement formulation is not given here; rather, the reader is referred to the following reference [22].

The large deflection of the plate is approximated by [22]

$$w_{NL}(0) = \frac{-pa^4}{64D} \frac{1}{1 + 0.488\frac{w(0)^2}{h^2}}. \tag{3–9}$$

Thus the large deflection is essentially the small deflection, given by Equation 3–8, scaled by the factor $\left(1 + 0.488\frac{w(0)^2}{h^2}\right)^{-1}$. The large deflection of the diaphragm is assumed to have the same mode shape as the small deflection. The behavior of the plate under large displacements is significant because this introduces a cubic

nonlinearity into the diaphragm deflection when the microphone is exposed to high incident pressures.

The behavior of the nonlinear deflection of a clamped circular plate is shown in Figure 3-4. For small pressures, up to the dotted line in the figure, the ideal linear deflection and non-linear deflection are approximately equal. However, at higher pressures, the cubic nonlinearity effectively stiffens the diaphragm and the nonlinear deflection is smaller than the ideal deflection. Furthermore, in the frequency domain, the nonlinearity produces harmonic distortion.

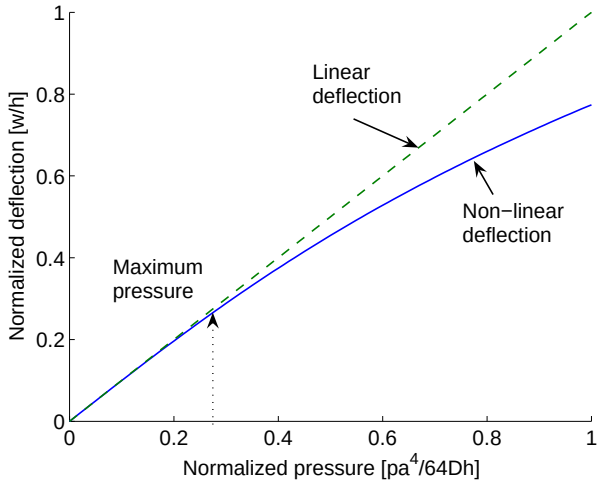


Figure 3-4. Non-linear diaphragm deflection compared to linear deflection.

### 3.1.2 Electrostatic Model

In the previous section, the deflection of the diaphragm due to an incident pressure was found. In this section, the electrical properties of the microphone are investigated. First, an overview of electrostatic transducer fundamentals is given; this is then extended to physical microphone implementations. Next detailed derivations for the electrostatic behavior of condenser microphones with interface circuitry are developed. This includes the output voltage, electrostatic force, and the effect of parasitic capacitance.

#### 3.1.2.1 Introduction to electrostatic transducers

The capacitive microphone is an example of an electrostatic transducer. In general, electrostatic transducers consist of at least two electrodes spaced a prescribed distance apart. At least one of the electrodes is free to move when subjected to an input signal. This results in one or more variable capacitors. Discussions of electrostatic transducers can in found in textbooks by Hunt [49], and more recently by Rossi [21], among others. Before discussing the detailed derivations of the electrostatic microphone in Section 3.1.2.2 and Section 3.1.2.3, a brief overview is given first without derivation.

**Background**. A model of a two plate electrostatic transducer is shown in Figure 3-5. This device consists of two parallel conducting plates. One is assumed to be fixed, and the other is movable. A capacitance exists between the two plates, given by $C = \epsilon_0 A/x$; where $A$ is the surface area and $x$ is the distance between the two plates. As indicated in Figure 3-5, the plates are a distance $x_0$ apart when the system is at rest. The moveable plate moves a distance $x'$ as a result of the net force applied to the plate. The equilibruim capacitance is $C = \epsilon_0 A/x_0$ and the time-varying capacitance is given by

$$C(t) = C_0 \left[1 - \frac{x'(t)}{x_0}\right]^{-1}. \tag{3–10}$$

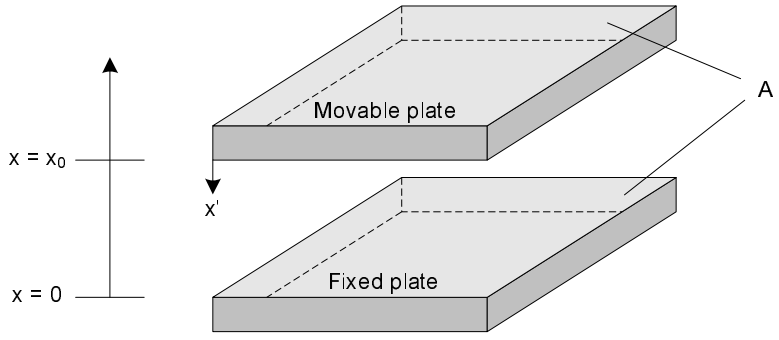


Figure 3-5. Model of a two plate electrostatic transducer.

The voltage between the terminals of the capacitor is given by V(t) = Q(t)/C(t), where $Q(t)$ is the charge on the plate. Substituting in Equation 3–10, the voltage is written as

$$V(t) = \frac{Q(t)}{C_0}\left[1 - \frac{x'(t)}{x_0}\right]. \tag{3–11}$$

The voltage between the plates results in an electrostatic force given by [21]

$$F_e(t) = -\frac{1}{2}\frac{\epsilon_0 A}{\left(x_0 - x'(t)\right)^2}V^2(t) = -\frac{1}{2}\frac{Q^2(t)}{\epsilon_0 A}. \tag{3–12}$$

At this point, no assumptions have been made regarding the method of applying the voltage or charge to the capacitor. The force may be written either in terms of the voltage $V(t)$ or the charge $Q(t)$, as they are equivalent. The electrostatic force is attractive between the two plates and is negative for the sign convention shown in Figure 3-5.

In a physical transducer, a mechanical restoring force is present. As the moveable plate deflects, an associated spring provides a force to oppose the deflection [21]. Written in terms of the mechanical compliance, $C_m$, the force is

$$F_m(t) = \frac{x'(t)}{C_m}. \tag{3–13}$$

The characteristic electrostatic equations governing this system are written as [21]

$$V(t) = \frac{Q(t)}{C_0} - \frac{x'(t)}{x_0}\frac{Q(t)}{C_0}, \tag{3–14}$$

and

$$\begin{aligned} F(t) &= \frac{x'(t)}{C_m} - \frac{1}{2}\frac{\epsilon_0 A}{\left(x_0 - x'(t)\right)^2}V^2(t) \\ &= \frac{x'(t)}{C_m} - \frac{1}{2}\frac{Q^2(t)}{\epsilon_0 A}. \end{aligned} \tag{3–15}$$

These general equations describe the behavior of a parallel plate electrostatic transducer. It is evident that the voltage and force are coupled; that is, they are

dependent on each other. Furthermore, both the voltage and force are non-linear, in general. The voltage is proportional to $x'(t) \cdot Q(t)$ and the force is proportional to $V^2(t)$. In addition, there is a potential singularity in the force as $x'(t)$ approaches $x_0$.

At this point, Rossi linearized Equation 3–14 and Equation 3–15 by assuming small perturbations via polarization [21]. The voltage and charge were assumed to be composed of a mean and time varying component. The small perturbation assumption implies that $x'(t) \ll x_0$, $v'(t) \ll V_0$, and $q'(t) \ll Q_0$. However, for the microphone designer, it is useful to consider physical implementations of a capacitive microphone and the constraints they impose on the coupled electromechanical equations (Equation 3–14 and Equation 3–15).

**Capacitive microphone implementations**. In a physical device, the microphone is biased in a manner such that either the voltage or the charge is approximately constant (neglecting modulation or feed-back schemes). This is accomplished via an external bias voltage or a permanent stored charge for condenser and electret microphones, respectively. The details of how the external bias voltage is applied is discussed later in this section. With this assumption, Equation 3–14 and Equation 3–15 can be simplified.

First, the constant voltage case is considered. In this case, $V(t)$ becomes $V_0$. Furthermore, $Q(t)$ is expressed as $V_0 \cdot C(t)$. For a microphone with constant voltage, Equation 3–14 is rewritten such that the output is the charge $Q(t)$. Thus the coupled electrostatic equations become

$$Q(t) = V_0 C_0 + V_0 \frac{x'(t)}{x_0} \frac{\epsilon_0 A}{x_0 - x'(t)}, \tag{3–16}$$

and

$$F(t) = \frac{x'(t)}{C_m} - \frac{1}{2} \frac{\epsilon_0 A}{\left(x_0 - x'(t)\right)^2} V_0^2. \tag{3–17}$$

Hence, the output charge is non-linear in terms of $x'(t)$. Furthermore, the force has a singularity at $x'(t) = x_0$, resulting in an pull-in instability [49]. Electrostatic pull-in is caused by the increasing net force as the diaphragm approaches the backplate; it is examined in more detail in Section 3.2.7. Physically, this limits the maximum bias voltage, $V_0$, that may be applied to the microphone.

The behavior described by Equation 3–16 and Equation 3–17 applies to condenser microphones in two regimes. The first is when the bias voltage is directly applied to a condenser microphone, as is the case when a charge amplifier is used. The amplifier converts the output charge to a voltage and maintains a constant potential across the capacitor. The second regime occurs when a condenser microphone is biased through a large resistor, such as with a voltage amplifier, and the DC behavior of the microphone is considered. The large resistor prevents the charge from changing due to AC inputs. The DC bias point of the microphone is set by the external bias voltage. In this bias condition, the microphone is susceptible to pull-in caused by the external bias voltage [49].

The second general case of a constant charge is now considered. This occurs for an electret microphone with an embedded charge [21] and for a condenser microphone biased through a large resistor when subject to AC inputs [49]. In this case, the output is the voltage, $V(t)$, across the terminals of the microphone. Thus the characteristic electrostatic equations become

$$V(t) = \frac{Q_0}{C_0} - \frac{x'(t)}{x_0}\frac{Q_0}{C_0}, \tag{3–18}$$

and

$$F(t) = \frac{x'(t)}{C_m} - \frac{1}{2}\frac{Q_0^2}{\epsilon_0 A}. \tag{3–19}$$

For the constant charge case, the output voltage is linear with respect to $x'(t)$. Additionally, the force is also linear with $x'(t)$ and there is not a singularity in the force. Thus, as long as the charge remains constant, pull-in will not occur [49].

This introduction presented the basic principles of modeling electrostatic transducers. The classical representation in Rossi [21] was applied to physical microphone implementations. Several key issues were identified, such as pull-in instability and non-linearities. To further analyze the electrostatic behavior of capacitive microphones, they are now examined in a design-oriented methodology giving key physical insight. Integral to this analysis is the consideration and implications of the interface circuitry. This analysis is limited to condenser microphones, although the constant charge results can be applied to electret microphones. First, the single-backplate condenser microphone is discussed. Then, the results are applied to the dual-backplate condenser microphone. Each microphone type is considered with both a charge amplifier and a voltage amplifier.

For each of the four cases, the analysis follows the methodology listed below:

1. Define the geometry.
2. Derive the capacitance, charge, and voltage on the capacitor(s).
3. Introduce details pertaining to the interface circuitry.
4. Derive the output voltage of the microphone.
5. Derive the electrostatic force between the diaphragm and backplate(s).

Each capacitor is treated as a parallel plate capacitor. For the initial discussion, the area of each capacitor is simply assumed to be the physical area of the plates. The effects of the diaphragm curvature on the electrostatic behavior are investigated in Section 3.1.3. In addition to the electroacoustics textbooks by Hunt [49] and Rossi [21], additional background on condenser microphones is available in the literature [113–115].

#### 3.1.2.2 Single-backplate condenser microphone

The electrostatic behavior of a single-backplate condenser microphone is treated for two cases. First, the bias voltage is directly applied to the capacitor, resulting in a constant voltage across the two plates. Then, the bias voltage is applied through a large resistor, giving the capacitor a constant charge. The first case is physically realized when the microphone is biased with a DC voltage and a

charge amplifier is used for the interface circuitry. A voltage amplifier is typically used with the the second case.

**Constant voltage**. A schematic of a single-backplate condenser microphone with the bias voltage directly applied is shown in Figure 3-6. The single-backplate condenser microphone consists of a fixed backplate separated from a movable diaphragm by a nominal gap distance $g_0$. As shown in the figure, the diaphragm moves by a distance $g'$; thus the air gap between the backplate and the diaphragm, $g$, is given by

$$g = g_0 - g'. \tag{3–20}$$

The backplate and diaphragm are both circular with a radius $a$ and a surface area of $A = \pi a^2$. The diaphragm is assumed to move as a rigid piston with a displacement equal to the center deflection, $w(0)$. Therefore, the capacitor is always treated as a parallel plate capacitor.

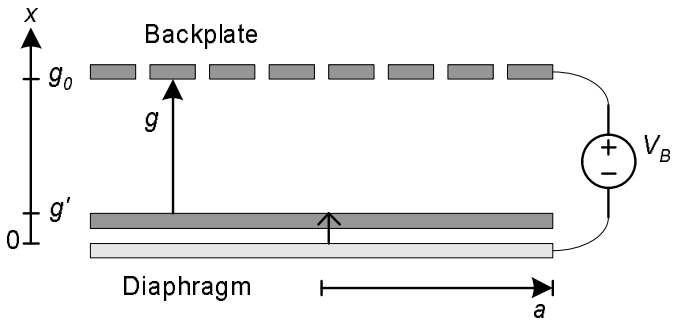


Figure 3-6. Electrical model of a single-backplate condenser microphone with a constant voltage.

A voltage, $V_B$, is applied between the diaphragm and backplate and the capacitance of the parallel plate capacitor is given by [23]

$$C_1 = \frac{\epsilon_0 A}{g}. \tag{3–21}$$

Substituting Equation 3–20 into Equation 3–21 results in the following expression for the capacitance

$$C_1 = \frac{\epsilon_0 A}{g_0 - g'}. \tag{3–22}$$

The change in capacitance due to the gap change is the physical phenomenon that results in the microphone output. The capacitance may also be expressed in terms of a mean capacitance, $C_{1_0}$, and a change in capacitance, $\Delta C_1$, as

$$C_1 = C_{1_0} + \Delta C_1, \tag{3–23}$$

where $C_{1_0}$ is

$$C_{1_0} = \frac{\epsilon_0 A}{g_0}. \tag{3–24}$$

To find $\Delta C_1$, first the expression for the total capacitance, given by Equation 3–22, and the mean capacitance, given by Equation 3–24, are substituted into Equation 3–23; thus

$$\frac{\epsilon_0 A}{g_0 - g'} = \frac{\epsilon_0 A}{g_0} + \Delta C_1. \tag{3–25}$$

Solving for $\Delta C_1$ results in

$$\Delta C_1 = \frac{g'}{g_0}\frac{\epsilon_0 A}{g_0 - g'}. \tag{3–26}$$

The change in capacitance is simply the capacitance $C_1$, given by Equation 3–22, scaled by the factor $(g'/g_0)$.

The change in capacitance, given by Equation 3–26, is non-linear in terms of the gap change. However, if $g'$ is assumed to be small compared to $g_0$, a linear expression for $\Delta C_1$ can be found. The linearization of Equation 3–26 begins with

$$\Delta C_1 = \frac{g'}{g_0}\frac{\epsilon_0 A}{g_0 - g'} \cdot \frac{g_0 + g'}{g_0 + g'}, \tag{3–27}$$

which is rewritten as

$$\Delta C_1 = \frac{\epsilon_0 A}{g_0}\frac{\left(g_0 \cdot g' + g'^2\right)}{{g_0}^2 - {g'}^2}. \tag{3–28}$$

The $g'^2$ terms are negligible and therefore dropped. Thus, Equation 3–28 is simplified to

$$\Delta C_1 = \frac{g'}{g_0}\frac{\epsilon_0 A}{g_0}. \tag{3–29}$$

This expression is now linear in terms of $g'$. Comparing Equation 3–29 to Equation 3–26, the factor $(g'/g_0)$ now scales the mean capacitance, $C_{1_0}$. The linearized capacitance becomes

$$C_1 = \frac{\epsilon_0 A}{g_0}\left(1 + \frac{g'}{g_0}\right). \tag{3–30}$$

The charge on the capacitor, $Q_1$, given by $Q_1 = C_1 V_B$, is expanded to

$$Q_1 = \frac{\epsilon_0 A}{g_0 - g'} V_B. \tag{3–31}$$

The charge may also be expressed in terms of $\Delta C_1$,

$$Q_1 = V_B\left(C_{1_0} + \Delta C_1\right). \tag{3–32}$$

From Equation 3–32, a mean charge, $Q_{1_0}$ and a change in change, $\Delta Q_1$ are defined;

$$Q_{1_0} = \frac{\epsilon_0 A}{g_0} V_B \tag{3–33}$$

and

$$\Delta Q_1 = \Delta C_1 V_B. \tag{3–34}$$

Substituting Equation 3–24 and Equation 3–29 into Equation 3–32, the final expression for the linearized charge on the capacitor is

$$Q_1 = V_B C_{1_0}\left(1 + \frac{g'}{g_0}\right). \tag{3–35}$$

To find the output voltage of a single-backplate condenser microphone with a constant voltage, the interface circuity must also be considered. Shown in Figure 3-7 is a single backplate microphone connected to a charge amplifier. The details of the DC bias circuitry are not shown. One plate of the microphone is biased with

a DC voltage $V_B$, while the other plate is connected to the inverting input of an operational amplifier. The non-inverting input is grounded. A feedback capacitor, $C_f$, is placed in the feedback path from the output to the negative input. Due to negative feedback, the other plate of the microphone is held at small signal ground [116].

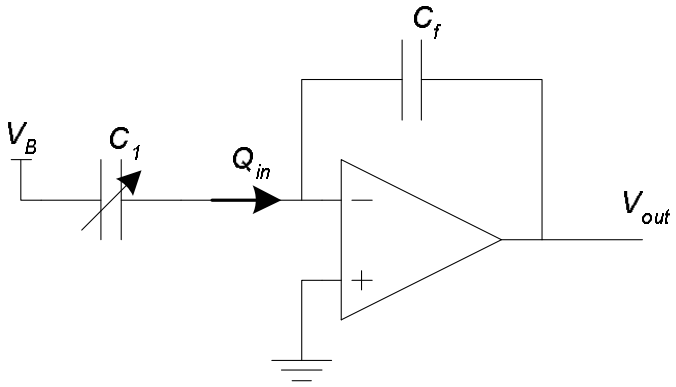


Figure 3-7. Simplified circuit of a single-backplate condenser microphone and a charge amplifier.

The charge amplifier stores the input charge, $Q_{in}$, on the feedback capacitor to generate an output voltage equal to

$$V_{out} = \frac{Q_{in}}{C_f}. \tag{3–36}$$

The input charge is the time varying component of the charge on the capacitor, $\Delta Q_1$, given by Equation 3–34. Therefore, the output voltage of the microphone is written as

$$V_{out} = \frac{\Delta C_1}{C_f} V_B. \tag{3–37}$$

Substituting Equation 3–29 into Equation 3–37 gives the linearized output voltage,

$$V_{out} = \frac{V_B}{g_0} \frac{C_{1_0}}{C_f} g'. \tag{3–38}$$

To find the final expression for the output voltage, the center deflection of the diaphragm given by Equation 3–8 is substituted for $g'$. Therefore the output

voltage of the single backplate capacitive microphone with a constant voltage is given by

$$V_{out}\Big|_{CV} = -p\frac{V_B}{g_0}\frac{C_{1_0}}{C_f}\frac{a^4}{64D}. \tag{3–39}$$

However, it is noted that this expression for the output voltage does not consider the effects of the rest of the microphone structure including the cavity. This is further investigated in Section 3.2.

It is also useful to study the electrostatic force on the diaphragm. As shown in Figure 3-6, the backplate and diaphragm are directly biased with a constant voltage. This voltage creates an electrostatic force that tends to move the diaphragm towards the backplate as indicated in the figure.

The electric field in the air gap between the diaphragm and backplate is given by [23]

$$E = \frac{V_B}{g}. \tag{3–40}$$

The electrostatic energy density, $u_e$ $[J/m^3]$, in the air gap is given by

$$u_e = \tfrac{1}{2}\epsilon_0 E^2, \tag{3–41}$$

therefore, the total energy is

$$U_e = \int_{\forall} u_e dV, \tag{3–42}$$

where $\forall$ is the integration volume between the two plates. Assuming a parallel plate capacitor and neglecting fringing fields, this volume is equal to $A{\cdot}g$; thus $u_e$ is constant over the volume. Substituting Equation 3–40 and Equation 3–41 into Equation 3–42 gives [23]

$$U_e = \frac{\epsilon_0 A {V_B}^2}{2g}, \tag{3–43}$$

which is rewritten as

$$U_e = \frac{1}{2}C_1 {V_B}^2. \tag{3–44}$$

For two parallel plates biased with a constant voltage, the electrostatic force is given by

$$F_e = + \left( \frac{dU_e}{dg} \right)_{V_B = const} \tag{3–45}$$

By substituting Equation 3–44 into Equation 3–45 and recalling that $C_1$ is a function of $g'$ as given in Equation 3–22, the electrostatic force is written as

$$F_e = \tfrac{1}{2} {V_B}^2 \frac{dC_1}{dg'}. \tag{3–46}$$

Thus the final equation for the electrostatic force for a constant voltage is given by

$$F_e\Big|_{CV} = \tfrac{1}{2} {V_B}^2 \frac{\epsilon_0 A}{(g_0 - g')^2}. \tag{3–47}$$

The electrostatic force given in Equation 3–47 is in the positive $x$ direction, which causes the diaphragm to deflect up towards the backplate. Furthermore, the electrostatic force increases as the diaphragm moves closer to the backplate, approaching infinity as the gap becomes very small. Without a restoring force, the diaphragm would always collapse into the backplate. In Section 3.2.7, the relationship between the restoring force of the diaphragm and the electrostatic force is investigated. In addition, the force is proportional to $1/g_0 - {g'}^2$, which introduces a nonlinearity if the deflection, $g'$ is large. However, at large deflections, the accuracy of this model would suffer because the two plates are no longer parallel. A more general model accounting for a non-parallel plate capacitor is investigated by Pedersen [117]

**Constant charge**. The single-backplate capacitive microphone is now considered with a voltage bias applied through a large resistor. This applies a charge $Q_B$ on the capacitor that is approximately constant. The resistor, $R_b$, and device capacitor determine a time constant with an associated high-pass filter corner frequency that is typically chosen to be below the lowest frequency of interest. For inputs above this corner frequency, the charge on the capacitor is

essentially constant [49]. A model of the microphone in this configuration is shown in Figure 3-8.

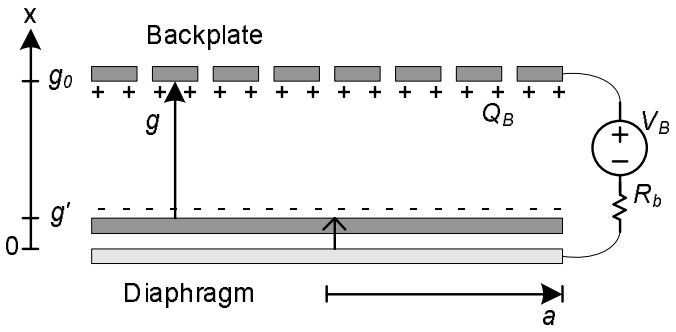


Figure 3-8. Electrical model of a single-backplate condenser microphone with voltage source applied through a large resistor.

The gap and capacitance are given by Equation 3–20 and Equation 3–22, respectively. The voltage across the capacitor, $V_1$, is given by $V_1 = Q_B/C_1$. Thus, $V_1$ is

$$V_1 = \frac{g_0 - g'}{\epsilon_0 A} Q_B. \tag{3–48}$$

Unlike the nonlinear charge from the constant voltage analysis, given in Equation 3–31, the voltage across the capacitor biased with a constant charge is linear with respect to $g'$. Equation 3–48 may be defined in terms of the nominal capacitance, $C_{1_0}$, and the change in capacitance, $\Delta C_1$, such that

$$V_1 = \frac{Q_B}{C_{1_0} + \Delta C_1}. \tag{3–49}$$

Figure 3-9 shows the microphone connected to a voltage buffer. One plate of the microphone is connected to the voltage source, while the other is connected to the amplifier. This second plate is also connected to ground through a large resistor. The high pass filter formed by $R_b$ and $C_1$ forces the DC voltage on the second plate to equal zero, but for frequencies above $1/\left(2\pi R_b C_{1_0}\right)$, the voltage on this plate is free to change.

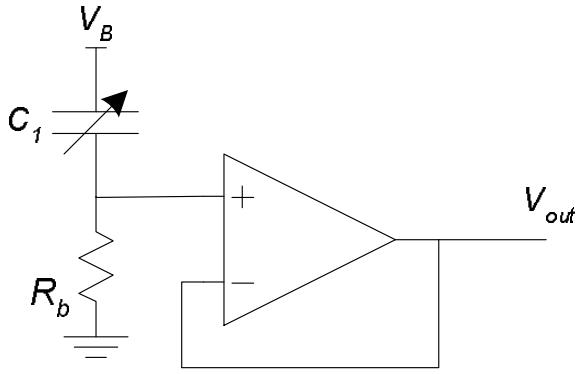


Figure 3-9. Simplified circuit of a single-backplate condenser microphone and a voltage amplifier.

This bias arrangement results in a fixed DC charge on the capacitor given by

$$Q_B = C_{1_0} V_B. \tag{3–50}$$

Therefore, the voltage across the capacitor, $V_1$, is given by

$$V_1 = \frac{C_{1_0} V_B}{C_{1_0} + \Delta C_1}. \tag{3–51}$$

By expressing $V_1$ as $V_1 = V_B - V_{out}$, where $V_{out}$ is the output voltage of the microphone (and the buffer amplifier), Equation 3–51 is rewritten as

$$C_{1_0} V_B = (C_{1_0} + \Delta C_1)(V_B - V_{out}). \tag{3–52}$$

By expanding and simplifying Equation 3–52, the following expression for the output voltage is obtained,

$$V_{out} = \frac{\Delta C_1}{C_1} V_B. \tag{3–53}$$

Substituting Equation 3–26 and Equation 3–22 into Equation 3–53 yields

$$V_{out} = \frac{g'}{g_0} V_B \tag{3–54}$$

for the output voltage. This expression is linear with $g'$ and linearization is not necessary. Substituting Equation 3–8 into Equation 3–54 results in the final

expression for the output voltage,

$$V_{out} = -p\frac{V_B}{g_0}\frac{a^4}{64D}. \tag{3–55}$$

However, in a physical implementation of a single-backplate condenser microphone and voltage amplifier, the effects of parasitic capacitance and the amplifier input capacitance must be considered. Figure 3-10 shows the single-backplate microphone with a bias resistor and voltage buffer as before; however, now a parasitic capacitance, $C_p$, and an input capacitance, $C_i$, have been added.

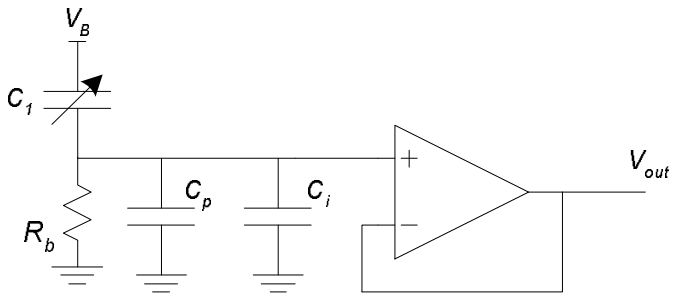


Figure 3-10. Circuit model of a single-backplate microphone and a voltage amplifier with parasitics.

For this configuration, the bias charge is still given by Equation 3–50. However, when the voltage at the input to the amplifier changes, there is charge sharing between the microphone capacitance and the parasitic and input capacitances. Therefore, Equation 3–52 becomes

$$\underbrace{C_{1_0}V_B}_{\substack{\text{initial}\\ \text{charge}}} = \underbrace{(C_{1_0}+\Delta C_1)\,(V_B - V_{out})}_{\substack{\text{charge on}\\ \text{microphone}}} + \underbrace{(C_p + C_i)\,(0 - V_{out})}_{\substack{\text{charge lost}\\ \text{to sharing}}}; \tag{3–56}$$

the initial charge, $Q_B$, the charge on the microphone capacitor and the charge lost due to charge sharing are shown. Solving Equation 3–56 for $V_{out}$ gives the output voltage for a constant bias charge,

$$V_{out}\Big|_{CC} = \frac{\Delta C_1}{C_1 + C_p + C_i}V_B. \tag{3–57}$$

Note that when $C_p$ and $C_i$ are present, the charge on the microphone capacitor is not constant. However, the total charge in the system is constant. Comparing Equation 3–57 to Equation 3–53 gives an attenuation factor, $H_C$, defined as

$$H_c = \frac{C_1}{C_1 + C_p + C_i}. \tag{3–58}$$

This result quantifies the signal loss due to the parasitic and input capacitances and agrees with previously published analysis [55]. The term, $H_c$, is a function of the top capacitance value, $C_1$. Therefore, $H_c$ is not constant as the pressure loading varies on the microphone. This introduces a non-linearity into the output voltage because the output voltage is no longer linearly proportional to the incident pressure. In general, as the total parasitic capacitance increases, the non-linearity increases. This behavior is further explored in Section 3.1.3.

Next, the electrostatic force between the backplate and diaphragm is considered. For this analysis, the effects of the parasitic and input capacitances are assumed to be negligible so that the charge on the capacitor remains constant. The electric field between the backplate and the diaphragm when biased with a constant charge is given by [23]

$$E = \frac{Q_B}{\epsilon_0 A}. \tag{3–59}$$

The electrostatic energy density, $u_e$, is given by Equation 3–41 for this case as well. By substituting Equation 3–59 into Equation 3–41 and Equation 3–42, the following expression for the electrostatic energy is obtained,

$$U_e = \int_{\forall = A \cdot g} = \frac{{Q_B}^2}{2\epsilon_0 A^2} dV. \tag{3–60}$$

The integration volume, $\forall$, is the region where the electric field exists and is equal to $A{\cdot}g$. Assuming the backplate and diaphragm are parallel, the electrostatic

energy is given by [23]

$$U_e = \frac{{Q_B}^2}{2C_1}. \tag{3–61}$$

The electrostatic force between two conductors with a constant charge is given by [23]

$$F_e = -\left(\frac{dU_e}{dg}\right)_{Q_B=const} \tag{3–62}$$

By substituting Equation 3–61 into Equation 3–62, the following expression for the electrostatic force is found,

$$F_e = -\frac{{Q_B}^2}{2}\frac{d}{dg'}\left(\frac{1}{C_1}\right); \tag{3–63}$$

where, $dg' = -dg$. Solving this expression gives the final result for the electrostatic force between two parallel plates with a constant charge,

$$F_e\Big|_{CC} = \frac{{Q_B}^2}{2\epsilon_0 A}. \tag{3–64}$$

Unlike the electrostatic force with a constant voltage, this force is constant regardless of the diaphragm's position.

#### 3.1.2.3 Dual-backplate condenser microphone

The previously derived results for the output voltage and electrostatic force are applied to the dual-backplate condenser microphone. Similar to the treatment of the single-backplate microphone, the dual-backplate capacitive microphone is considered with DC voltage applied directly to the microphone and applied through a large resistor. Furthermore, for the dual-backplate microphone, bias voltages of equal magnitude and opposite sign are applied to the two backplates.

**Constant voltage**. A dual-backplate capacitive microphone biased with two voltage sources connected directly is shown in Figure 3-11. It is assumed that all three plates have the same radius, $a$, and surface area given by $A = \pi a^2$. Furthermore, the nominal air gap between the diaphragm and each backplate is assumed to be equal to $g_0$. The diaphragm is perturbed a distance $g'$, which causes

the top air gap to be reduced and the bottom air gap to be increased; the air gaps are given by

$$g_1 = g_0 - g', \tag{3–65}$$

and

$$g_2 = g_0 + g'. \tag{3–66}$$

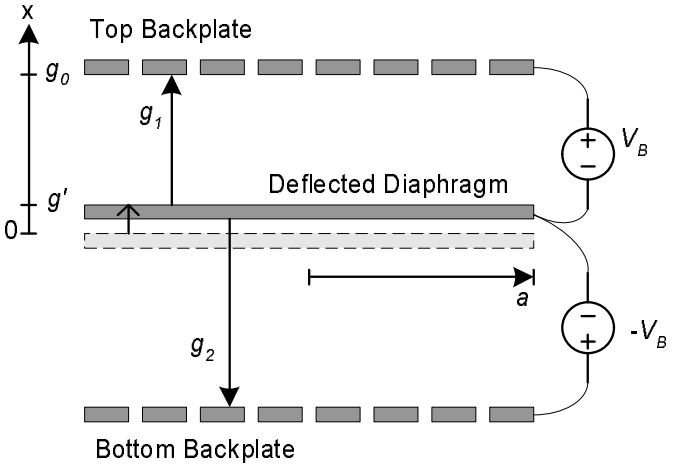


Figure 3-11. Dual-backplate condenser microphone with directly connected bias voltages .

The derivation of the output voltage of the dual-backplate capacitive microphone with a constant voltage follows the method used for the single-backplate microphone. The top and bottom capacitances, respectively, are

$$C_1 = \frac{\epsilon_0 A}{g_0 - g'}, \tag{3–67}$$

and

$$C_2 = \frac{\epsilon_0 A}{g_0 + g'}. \tag{3–68}$$

Similar to $C_1$, $C_2$ is expressed in terms of a mean capacitance, $C_{2_0}$, and a change in capacitance, $\Delta C_2$, such that

$$C_2 = C_{2_0} + \Delta C_2. \tag{3–69}$$

The change in the bottom capacitance is found in the same manner as that for the top capacitance. Equation 3–69 is rewritten as

$$\frac{\epsilon_0 A}{g_0 + g'} = \frac{\epsilon_0 A}{g_0} + \Delta C_2. \tag{3–70}$$

Solving this for $\Delta C_2$ results in

$$\Delta C_2 = -\frac{g'}{g_0}\frac{\epsilon_0 A}{g_0 + g'}. \tag{3–71}$$

Similar to $\Delta C_1$, Equation 3–71 is the change in capacitance $C_2$, scaled by the factor $(g'/g_0)$. However, the change in $C_2$ has the opposite sign of the change in $C_1$. This differential capacitance change is a key feature of the dual-backplate microphone. Furthermore, the linearized change in bottom capacitance is

$$\Delta C_2 = -\frac{g'}{g_0}\frac{\epsilon_0 A}{g_0}. \tag{3–72}$$

The charge on the two capacitors, $C_1$ and $C_2$, is

$$Q_1 = V_B \left(C_{1_0} + \Delta C_1\right), \tag{3–73}$$

and

$$Q_2 = -V_B \left(C_{2_0} + \Delta C_2\right). \tag{3–74}$$

The dual-backplate condenser microphone is now considered with a charge amplifier as shown in Figure 3-12. The top backplate is biased with $+V_B$ and the bottom backplate is biased with $-V_B$. The diaphragm is connected to the input of the charge amplifier and is held at small signal ground. The DC voltage level of the diaphragm is set by a bias resistor not shown in the figure.

As before, the gain of the charge amplifier is given by Equation 3–36. There are two components to the output voltage; one from each capacitor. The input charge, $\Delta Q$, is the sum of $\Delta Q_1$ and $\Delta Q_2$. These are found from Equation 3–73 and Equation 3–74, using the linearized form of the capacitance changes; and are given

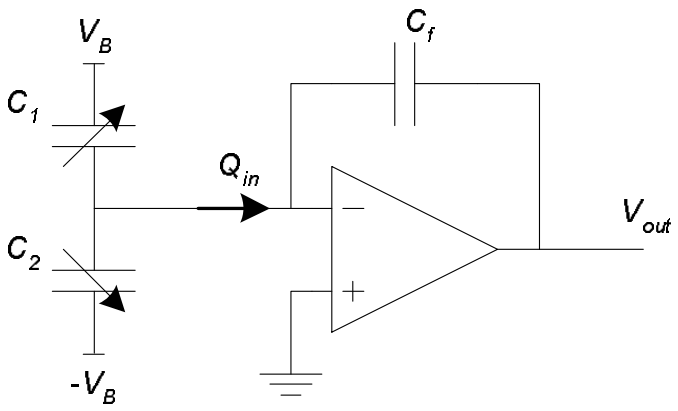


Figure 3-12. Electrical model of a dual-backplate capacitive microphone with a charge amplifier.

by

$$\Delta Q_1 = V_B C_{1_0} \frac{g'}{g_0}, \tag{3–75}$$

and

$$\Delta Q_2 = V_B C_{2_0} \frac{g'}{g_0}. \tag{3–76}$$

Assuming that the areas and nominal gaps are the same for each capacitor, $C_{1_0} = C_{2_0}$ and $\Delta C_1 = \Delta C_2$. Thus, the total input charge is twice that of the single-backplate capacitive microphone. Furthermore, the output voltage, which is given by

$$V_{out} = 2\frac{V_B}{g_0}\frac{C_{1_0}}{C_f} g', \tag{3–77}$$

is also twice that of the single-backplate capacitive microphone ( Equation 3–38). By substituting the diaphragm deflection, given by Equation 3–8, for $g'$, the final expression for the output voltage of a dual-backplate capacitive microphone biased with a constant voltage is determined;

$$V_{out}\Big|_{CV} = -2p\frac{V_B}{g_0}\frac{C_{1_0}}{C_f}\frac{a^4}{64D}. \tag{3–78}$$

Next, the electrostatic force acting on the diaphragm is considered. There are two components to the force, one from the top backplate and one from the bottom

backplate. The electrostatic force due to the top backplate, $F_{e_1}$, and the force due to the bottom backplate, $F_{e_2}$, are found in the same manner used to derive Equation 3–46 as follows,

$$F_{e_1} = \tfrac{1}{2} {V_B}^2 \frac{dC_1}{dg'} \tag{3–79}$$

and

$$F_{e_2} = \tfrac{1}{2} {V_B}^2 \frac{dC_2}{dg'}. \tag{3–80}$$

Evaluating these expressions using Equation 3–67 and Equation 3–68 gives

$$F_{e_1} = \tfrac{1}{2} {V_B}^2 \frac{\epsilon_0 A}{(g_0 - g')^2} \tag{3–81}$$

and

$$F_{e_2} = -\tfrac{1}{2} {V_B}^2 \frac{\epsilon_0 A}{(g_0 + g')^2}. \tag{3–82}$$

The two electrostatic forces act in opposite directions. This arises because the electrostatic force between the diaphragm and each backplate is attractive; thus the diaphragm is pulled towards the backplate. Therefore, $F_{e_1}$ is directed in the positive $x$ direction, and $F_{e_2}$ is directed in the negative $x$ direction. The total electrostatic force acting on the diaphragm is equal to $F_{e_1} + F_{e_2}$,

$$F_e\Big|_{V_B} = \tfrac{1}{2} {V_B}^2 \frac{\epsilon_0 A}{(g_0 - g')^2} - \tfrac{1}{2} {V_B}^2 \frac{\epsilon_0 A}{(g_0 + g')^2}; \tag{3–83}$$

further simplification yields

$$F_e\Big|_{V_B} = 2 {V_B}^2 \frac{\epsilon_0 A g_0 g'}{\left({g_0}^2 - {g'}^2\right)^2}. \tag{3–84}$$

The electrostatic force for the dual-backplate capacitive microphone with a constant voltage is less than that of the single-backplate microphone, although the force still approaches infinity as the diaphragm moves towards either backplate. When the diaphragm is in the rest position, the magnitude of the electrostatic force is equal to zero. When the diaphragm is perturbed, the electrostatic force is

directed towards the nearest backplate; thus if $g'$ is positive, $F_e$ is directed in the positive $x$ direction and if $g'$ is negative, $F_e$ is directed in the negative $x$ direction.

**Constant charge**. The final electrostatic case is a dual-backplate condenser microphone biased with voltage sources applied through a large resistor. Similar to the single-backplate case, this sets up an approximately constant charge on the microphone capacitors. As shown in Figure 3-13, a positive voltage is applied to the top backplate and a negative voltage is applied to the bottom backplate. This results in opposite charges on the two capacitors.

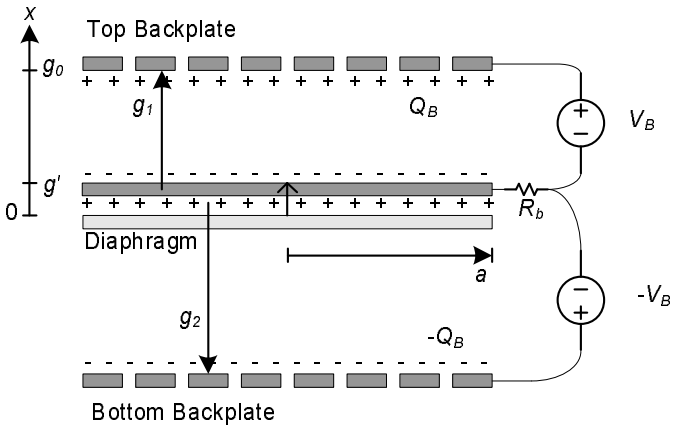


Figure 3-13. Dual-backplate condenser microphone biased with voltage sources connected through a large resistor.

The top and bottom air gap distances are given by Equation 3–65 and Equation 3–66, and the top and bottom capacitances are given by Equation 3–67 and Equation 3–68, respectively. The voltages across each capacitor are

$$V_1 = \frac{g_0 - g'}{\epsilon_0 A} Q_B, \tag{3–85}$$

and

$$V_2 = -\frac{g_0 + g'}{\epsilon_0 A} Q_B. \tag{3–86}$$

As was the case with the single-backplate capacitive microphone, the voltages given in Equation 3–85 and Equation 3–86 vary linearly with $g'$.

Similar to the analysis of the single-backplate microphone with constant charge, the capacitances are defined in terms of a nominal capacitance and a change in capacitance. Thus, Equation 3–85 and Equation 3–86 become

$$V_1 = \frac{Q_B}{C_{1_0} + \Delta C_1}, \tag{3–87}$$

and

$$V_2 = \frac{-Q_B}{C_{1_0} + \Delta C_2}; \tag{3–88}$$

where $\Delta C_1$ is given by Equation 3–26 and $\Delta C_2$ is given by Equation 3–71.

The microphone is considered with a voltage amplifier as shown in Figure 3-14; the microphone is represented by $C_1$ and $C_2$. The top and bottom backplates are biased with voltages $V_B$ and $-V_B$, respectively. The bias resistor, $R_b$ holds the DC voltage of the diaphragm at 0 $V$. However, for frequencies above the cut-on frequency, $1/2\pi R_b\,(C_{1_0} + C_{2_0})$, the voltage of the middle plate is free to change while the charge on each microphone capacitor remains constant (neglecting the effect of the parasitic and input capacitances).

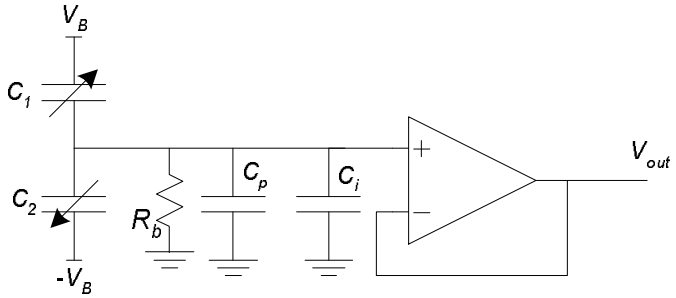


Figure 3-14. Simplified circuit of a dual-backplate microphone and a voltage amplifier.

The charge stored on each capacitor due to the bias voltage is $Q = C_0 V_B$, thus the voltage, $V_1$, across the top capacitor and the voltage, $V_2$, across the bottom capacitor are

$$V_1 = \frac{C_{1_0} V_B}{C_{1_0} + \Delta C_1}, \tag{3–89}$$

and

$$V_2 = \frac{C_{2_0} V_B}{C_{2_0} + \Delta C_2}. \tag{3–90}$$

To find the output voltage, the initial and final charge on each capacitor is analyzed. The principle of superposition is used, where each voltage source is considered individually. Thus there are two components to the output voltage. Therefore, only one of the capacitors has an initial charge for each component.

For the dual-backplate microphone, one device capacitor acts as a parasitic capacitor for the other device capacitor. Therefore, there is charge sharing between the two capacitors, even without considering the effects of parasitic and input capacitances. While the charge on each capacitor may not be strictly constant, the total charge in the system is constant. Generally, the initial and final charge for each capacitor is not the same. However, for the case of equal mean capacitances, equal capacitance changes, and no parasitic and input capacitance, the charge on each capacitor is constant.

For now, the effects of the parasitic and input capacitances are neglected. First the initial charge from the top capacitor is analyzed; thus, the voltage source for $C_2$, $(-V_B)$, is set to 0. The initial charge is equal to $Q_{1_0} = C_{1_0} V_B$ and is equated to the final charge as shown

$$C_{1_0} V_B = C_1 V_1 + C_2 V_2, \tag{3–91}$$

where the voltage $V_2$ is equal to $0 - V_{out}$. Note, that the charge from $C_1$ is free to move to $C_2$. Indeed, it must to satisfy the relation $Q = CV$ for each capacitor. Therefore, Equation 3–91 can be expanded to

$$C_{1_0} V_B = (C_{1_0} + \Delta C_1)(V_B - V_{out}) - C_2 V_{out}, \tag{3–92}$$

and solving for $V_{out}$ due to $C_1$ gives

$$V_{out_{C_1}} = \frac{\Delta C_1}{C_1 + C_2} V_B. \tag{3–93}$$

Similarly, the initial charge on the bottom capacitor, $Q_2 = -C_{2_0}V_B$, is equated to the final charge with the voltage source for $C_1$ set to 0,

$$-C_{2_0}V_B = C_2V_2 + C_1V_1, \tag{3–94}$$

where the voltage $V_1 = 0 - V_{out}$. Equation 3–94 is re-written as

$$-C_{2_0}V_B = (C_{2_0} + \Delta C_2)(-V_B - V_{out}) - C_1V_{out}. \tag{3–95}$$

The output voltage due to $C_2$ is

$$V_{out_{C_2}} = \frac{-\Delta C_2}{C_1 + C_2}V_B. \tag{3–96}$$

The total output voltage is the sum of Equation 3–93 and Equation 3–96,

$$V_{out} = \frac{\Delta C_1 - \Delta C_2}{C_1 + C_2}V_B. \tag{3–97}$$

By substituting Equation 3–26, Equation 3–71, Equation 3–67, and Equation 3–68 into Equation 3–97, the output voltage is simplified to

$$V_{out} = \frac{g'}{g_0}V_B. \tag{3–98}$$

The final expression for the output voltage is found by substituting Equation 3–8 into Equation 3–98,

$$V_{out} = -p\frac{V_B}{g_0}\frac{a^4}{64D}. \tag{3–99}$$

Considering the effects of the parasitic capacitance, $C_p$, and the input capacitance, $C_i$, Equation 3–97 becomes

$$V_{out}\Big|_{CC} = \frac{\Delta C_1 - \Delta C_2}{C_1 + C_2 + C_p + C_i}V_B. \tag{3–100}$$

Comparing the output voltage given in Equation 3–100 to that in Equation 3–97, gives the attenuation factor, $H_c$, for the dual-backplate microphone as

$$H_c = \frac{C_1 + C_2}{C_1 + C_2 + C_p + C_i}. \tag{3–101}$$

Similar to the single-backplate microphone with a voltage amplifier, the output of the dual-backplate microphone packaged with a voltage amplifier is linear when the effects of parasitic capacitances are not considered. The impact of $H_c$ on the linearity is investigated in Section 3.1.3.

Now the electrostatic force acting on the diaphragm is considered. There are again two components to the electrostatic force; one from the top backplate and a second from the bottom backplate. The two electrostatic forces,

$$F_{e_1} = \frac{{Q_B}^2}{2\epsilon_0 A}, \tag{3–102}$$

and

$$F_{e_2} = -\frac{{Q_B}^2}{2\epsilon_0 A}, \tag{3–103}$$

are found using the same method used to derive Equation 3–64. These two forces are equal in magnitude and opposite in sign. The force due to the top backplate, $F_{e_1}$, is directed in the positive $x$ direction and the force due to the bottom backplate is directed in the negative $x$ direction. The total force acting on the diaphragm is the sum of the forces given in Equation 3–102 and Equation 3–103, thus the total electrostatic force is *zero* as long as the charge remains constant,

$$F_e\Big|_{V_B} = \frac{{Q_B}^2}{2\epsilon_0 A} - \frac{{Q_B}^2}{2\epsilon_0 A} = 0. \tag{3–104}$$

#### 3.1.2.4 Linear electrostatic analysis summary

Several observations can be made by comparing the results of the four cases. Table 3-1 lists the sensitivities of both the single-backplate and dual-backplate

microphones biased with a constant charge and a constant voltage, assuming parallel plate motion. The sensitivity of the dual-backplate condenser microphone is twice that of the single-backplate microphone when the bias voltage is applied directly.

However, for condenser microphones biased through a large resistor, as is the case when the microphone is used with a voltage amplifier, the sensitivity of the single-backplate and dual-backplate microphones are the same. This can be understood physically by comparing Equation 3–53 to Equation 3–93 and Equation 3–96. All three equations have the same basic form; the ratio of a change in capacitance to the full capacitance value, scaled by a bias voltage. The output of the dual-backplate microphone is the sum of two components: Equation 3–93 and Equation 3–96. Assuming that the geometry of the top and bottom capacitors are the same, these two components of the output voltage are half of the value of the output voltage of the single-backplate microphone, given in Equation 3–53. This is because the denominator for the dual-backplate microphone, $C_1 + C_2$, is twice as big as the denominator of the single-backplate microphone, $C_1$. Thus the output of the dual-backplate microphone is the sum of two components, each one half the magnitude of that of the single backplate microphone.

Table 3-1. Summary of theoretical linear sensitivity of condenser microphones.

| | Direct biasing (constant voltage) | Bias resistor (constant charge) |
|---|---|---|
| Single backplate | $-\frac{V_B}{g_0}\frac{C_{1_0}}{C_f}\frac{a^4}{64D}$ | $-\frac{V_B}{g_0}\frac{a^4}{64D}$ |
| Dual backplate | $-2\frac{V_B}{g_0}\frac{C_{1_0}}{C_f}\frac{a^4}{64D}$ | $-\frac{V_B}{g_0}\frac{a^4}{64D}$ |

A summary of the electrostatic forces is given in Table 3-2. The electrostatic force acting on the diaphragm is similar for both the single-backplate microphone

and dual-backplate microphone directly connected voltage sources. While the magnitude is less for the dual-backplate microphone, both forces approach infinity as the diaphragm nears a backplate. For the constant charge case, the force is constant for the single-backplate microphone and it is equal to zero for the dual-backplate microphone.

Table 3-2. Summary of the electrostatic force acting on the diaphragm of capacitive microphones.

| | Direct biasing (constant voltage) | Bias resistor (constant charge) |
|---|---|---|
| Single backplate | $\frac{1}{2}{V_B}^2\frac{\epsilon_0 A}{(g_0-g')^2}$ | $\frac{{Q_B}^2}{2\epsilon_0 A}$ |
| Dual backplate | $2{V_B}^2\frac{\epsilon_0 A g_0 g'}{\left({g_0}^2-{g'}^2\right)^2}$ | 0 |

Theoretically, this implies that the condenser microphones biased through a large resistor never experiences dynamic electrostatic collapse of the diaphragm. This agrees with the analysis presented by Hunt, where he concludes that the electric field produced by the constant charge is essentially constant as the diaphragm moves [49]. This is not the case physically because the derivation of the electrostatic force assumed parallel plate capacitors; this assumption is not valid as the diaphragm approaches a backplate. The dynamic, non-linear pull-in analysis is beyond the scope of this discussion, further discussion can be found in [118].

### 3.1.3 Non-linear Static Electromechanical Analysis

In this section, the non-linear behavior of condenser microphones is explored. First, a capacitance model will be developed that considers the effect of the non-uniform gap. Then the electrostatic and mechanical non-linearities are examined to show the impact of the electrostatic non-linearity for the four cases previously

discussed. This was previously investigated by Warren et al. [113, 114] and Donk et al. [115]. The following analysis expands on their work.

#### 3.1.3.1 Non-uniform gap capacitor

The previously developed expressions for the sensitivity assumed that the capacitance between each backplate and the diaphragm was a parallel plate capacitor. This approximation was useful to provide physical insight into the behavior of the microphone as well as scaling information. However, to more accurately predict the sensitivity, a more accurate model of the capacitance is needed.

Consider the geometry shown in Figure 3-15; now the air gap is no longer assumed to be uniform. The deflection is assumed to be small such that the charge density on the surface of the plates is constant; furthermore, the backplate holes are neglected.

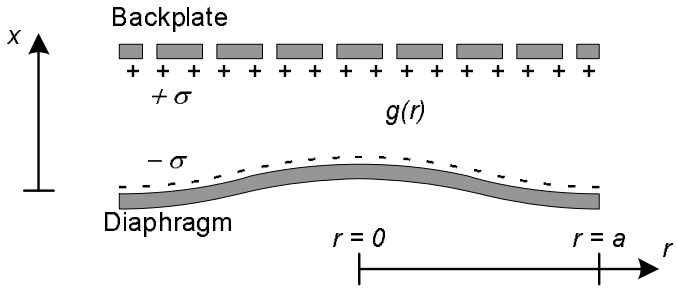


Figure 3-15. Model of the top capacitor with a non-uniform air gap.

The capacitance is directly found from the following [23],

$$\int_{+}^{-} \mathbf{E}\cdot d\mathbf{s} = \frac{Q}{C}. \tag{3–105}$$

For two conductors with an infinitesimal area of $dA$ and with opposite surface charge densities of magnitude $\sigma$, the electric field, $\mathbf{E}$, between the two conductors is

$-\hat{\mathbf{x}}\sigma/\epsilon_0$. A capacitance, $dC$, exists and is given by

$$\begin{aligned} dC &= \frac{dQ}{-\frac{\sigma}{\epsilon_0}\int_{g(r)}^{0} d\mathbf{s}} \\ &= \frac{dQ}{\frac{\sigma}{\epsilon_0} g(r)} \end{aligned} . \tag{3–106}$$

By noting that $dQ = \sigma dA$, Equation 3–106 is rewritten as

$$dC = \frac{\epsilon_0\, dA}{g(r)}. \tag{3–107}$$

The total capacitance is found by integrating over the entire area of the conductors. The gap distance, $g(r)$, is equal to the nominal gap distance, $g_0$, minus the plate deflection given by Equation 3–7. Therefore, the capacitance is found by evaluating the following integral,

$$C = \int_0^a \frac{2\pi\epsilon_0 r}{g_0 - w(0)\left[1 - \left(\frac{r}{a}\right)^2\right]^2}\, dr. \tag{3–108}$$

This integral was solved numerically using MathCad; it has two solutions: one for a positive diaphragm deflection and one for a negative deflection,

$$C = \begin{cases} \dfrac{\operatorname{arctanh}\left(\sqrt{\frac{w(0)}{g_0}}\right)}{\sqrt{\frac{w(0)}{g_0}}} \dfrac{\epsilon_0 \pi a^2}{g_0} & : \quad w(0) \geq 0 \\ \dfrac{\arctan\left(\sqrt{\frac{-w(0)}{g_0}}\right)}{\sqrt{\frac{-w(0)}{g_0}}} \dfrac{\epsilon_0 \pi a^2}{g_0} & : \quad w(0) \leq 0 \end{cases} . \tag{3–109}$$

The capacitance given in Equation 3–109 is the mean capacitance multiplied by a scale factor. When the diaphragm deflection is zero, the scale factor is one; therefore the capacitance is exactly that predicted by the simple parallel plate model. For this condition of zero deflection, the plates are indeed parallel. The non-uniform gap and the parallel plate capacitances are plotted in Figure 3-16

versus the diaphragm deflection. The change in capacitance for the non-uniform gap capacitance model is less than that predicted by the parallel plate model.

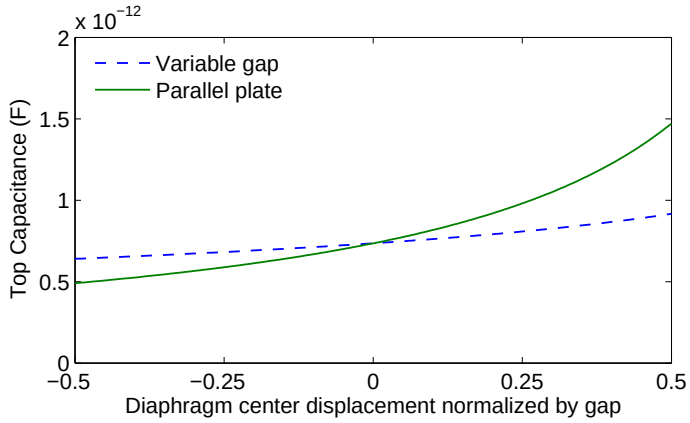


Figure 3-16. Capacitance of the top backplate as predicted by the non-uniform gap model and the parallel plate model as a function of diaphragm displacement.

The behavior of the non-linear capacitance is of particular interest for small displacements, as this is related to the nominal sensitivity of the capacitive microphone. The expression for the capacitance given in Equation 3–109 is simplified using a Taylor series expansion, assuming the deflection is small [119]. The quantity $\sqrt{w(0)/g_0}$ is replaced by $x$. The functions $\operatorname{arctanh} x$ and $\arctan x$ are simplified to

$$\operatorname{arctanh} x = x + \frac{x^3}{3}, \tag{3–110}$$

and

$$\arctan x = x - \frac{x^3}{3}. \tag{3–111}$$

respectively. This Taylor approximation has less than 1 % error when the diaphragm center displacement is less than 21 % of the nominal gap. The $x^3$ term appears in both Equation 3–110 and Equation 3–111 with opposite signs, therefore a single expression for the capacitance is found that is valid for both positive and negative diaphragm deflection. Using Equation 3–110, Equation 3–111, and

Equation 3–109, and by writing $w(0)$ as $g'$, the capacitance is approximated as

$$C_{eff} = \frac{\epsilon_0 A}{g_0}\left(1 + \frac{1}{3}\frac{g'}{g_0}\right). \tag{3–112}$$

By comparing Equation 3–112 to Equation 3–30, the change in capacitance is one third of that predicted by the parallel plate model. Therefore, the changes in the top and bottom capacitance, given by Equation 3–26 and Equation 3–71 respectively, are rewritten as

$$\Delta C_{1_{eff}} = \frac{1}{3}\frac{g'}{g_0}\frac{\epsilon_0 A}{g_0 - g'}. \tag{3–113}$$

and

$$\Delta C_{2_{eff}} = -\frac{1}{3}\frac{g'}{g_0}\frac{\epsilon_0 A}{g_0 + g'}. \tag{3–114}$$

Furthermore, the total capacitance of the top and bottom capacitors becomes

$$C_{1_{eff}} = \frac{\epsilon_0 A}{g_0} + \frac{1}{3}\frac{g'}{g_0}\frac{\epsilon_0 A}{g_0 - g'}. \tag{3–115}$$

and

$$C_{2_{eff}} = \frac{\epsilon_0 A}{g_0} - \frac{1}{3}\frac{g'}{g_0}\frac{\epsilon_0 A}{g_0 + g'}. \tag{3–116}$$

Linear approximations of Equation 3–115 and Equation 3–116 are

$$C_{1_{eff_L}} = C_{1_0}\left(1 + \frac{1}{3}\frac{g'}{g_0}\right). \tag{3–117}$$

and

$$C_{2_{eff_L}} = C_{2_0}\left(1 - \frac{1}{3}\frac{g'}{g_0}\right). \tag{3–118}$$

Furthermore, the linear changes in capacitance are

$$\Delta C_{1_{eff_L}} = \frac{1}{3}\frac{g'}{g_0}\frac{\epsilon_0 A}{g_0}. \tag{3–119}$$

and

$$\Delta C_{2_{eff_L}} = -\frac{1}{3}\frac{g'}{g_0}\frac{\epsilon_0 A}{g_0}. \tag{3–120}$$

The one third factor is also present in the effective area (Equation 3–137 developed in Section 3.2.1); thus the capacitances given in Equation 3–119 and Equation 3–120 are rewritten as

$$\Delta C_{1_{eff_L}} = \frac{g'}{g_0}\frac{\epsilon_0 A_{eff}}{g_0} \tag{3–121}$$

and

$$\Delta C_{2_{eff_L}} = -\frac{g'}{g_0}\frac{\epsilon_0 A_{eff}}{g_0}. \tag{3–122}$$

The previously derived results for the capacitive microphone sensitivity are accurate if the effective area is used rather than the physical area. This agrees with the results obtained by [115].

In Figure 3-17, the top capacitance predicted by the non-uniform gap model (Equation 3–109) is compared to the capacitance predicted by the non-linear uniform-gap model (Equation 3–115) and the linear uniform-gap model (Equation 3–117). Both uniform-gap models are used with the effective area.

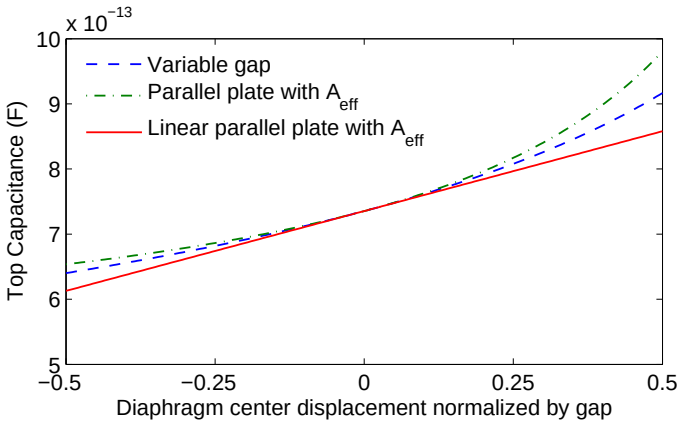


Figure 3-17. Capacitance of the top backplate as predicted by the non-uniform gap model and effective area approximation model.

The effective area model bridges the parallel plate model and the non-uniform gap model. It may be achieved by either assuming small deflection for the full non-uniform gap model or by using the effective area, $A_{eff}$, in the parallel plate model. All models are well matched for small deflections. Therefore, the linear capacitance

with the effective area is used to accurately predict the microphone behavior for small deflections. In addition, it has the advantage of a simple expression that provides scaling information.

#### 3.1.3.2 Condenser microphone non-linearity

In the section, the effect of the mechanical non-linearity, as well as the non-linear capacitance on the performance of condenser microphones is examined. Previous work by Pedersen et al. has studied the non-linear behavior of single backplate condenser microphones with square diaphragms [120].

As part of the previous electrostatic discussion, the sources of electrostatic non-linearity were identified. For microphones biased directly with a voltage source, a non-linearity is introduced into the $\Delta C$ quantities by the $g_o \pm g'$ term in the denominator; as shown in Equation 3–26 and Equation 3–71. It was also shown that microphones biased through a large resistor did not have non-linearity, in the absence of parasitic capacitance.

However, when the models are modified to include the effective area, non-linearities are introduced into the voltage amplifier cases. Consider the single-backplate capacitive microphone biased with a constant charge. The output voltage is given by Equation 3–53. Substituting Equation 3–113 and Equation 3–115 into Equation 3–53, the output voltage becomes

$$V_{out}\Big|_{SBP_{CC}} = \frac{\frac{1}{3}\frac{g'}{g_0}\frac{\epsilon_0 A}{g_0 - g'}}{\frac{\epsilon_0 A}{g_0} + \frac{1}{3}\frac{g'}{g_0}\frac{\epsilon_0 A}{g_0 - g'}} V_B. \tag{3–123}$$

This is simplified to

$$V_{out}\Big|_{sbp_{cc}} = \frac{\frac{1}{3}\frac{g'}{g_0}}{1 - \frac{2}{3}\frac{g'}{g_0}} V_B. \tag{3–124}$$

Therefore, the output voltage is no longer linearly proportional to $g'$. The non-linearity in the output voltage is defined as

$$\%NL = \frac{V_{out_L} - V_{out_{NL}}}{V_{out_L}} \times 100. \tag{3–125}$$

The impact of the non-uniform gap on the output voltage non-linearity can be seen by comparing Figure 3-18(b) to Figure 3-18(a). The non-linearity for the charge amplifier cases is unchanged by the non-uniform gap model. Conversely, the non-linearity for the voltage amplifier cases is increased.

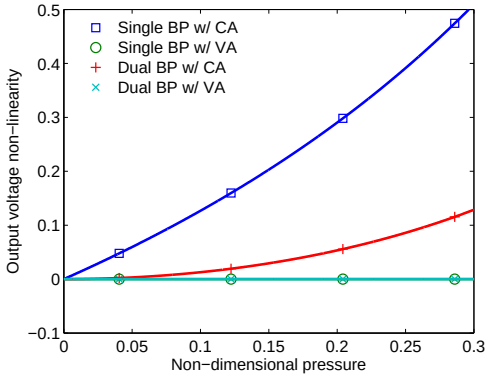


(a) Ideal parallel plate model.

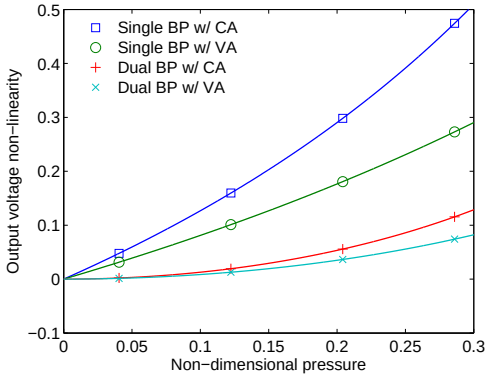


(b) Parallel plate model with $A_{eff}$

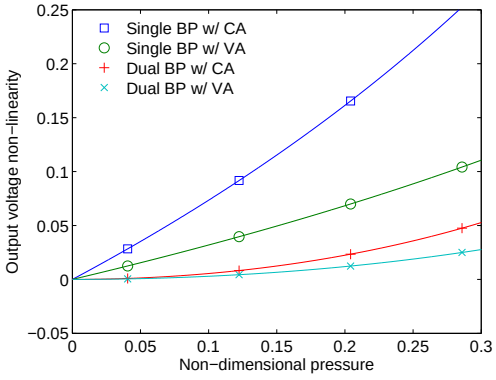


(c) Full non-uniform gap model.

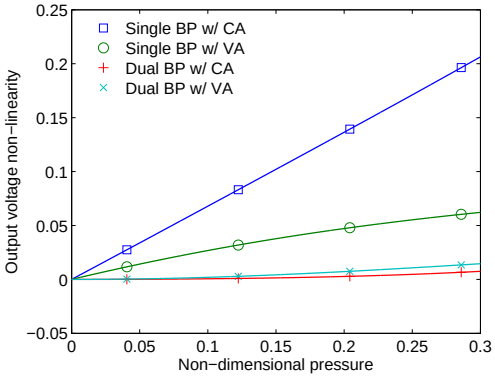


(d) Non-uniform gap with non-linear deflection

Figure 3-18. Non-linearity of the single-backplate and dual-backplate microphones with both a charge amplifier and a voltage amplifier. Four different levels of modeling are compared.

As shown in Figure 3-17, the effective area parallel plate model over-predicts the capacitance change compared to the non-uniform gap model. Furthermore, the non-linearity is less for the four microphone cases when the non-uniform gap model is used to predict the microphone output, as shown in Figure 3-18(c). The effect of the electrical non-linearity is to cause the change in capacitance to become greater for higher incident pressures. However, the mechanical non-linearity causes the diaphragm deflection to be less at higher pressures. These two non-linearities oppose one another; thus the non-linearity for the four microphone cases is lowest when the effect of the mechanical non-linearity is considered, as shown in Figure 3-18(d).

Another point of interest is that the non-linearity of the dual-backplate microphone is much lower than the single-backplate microphone, regardless of the type of interface circuitry used. Physically, this is due to the differential nature of the dual backplate microphone. The ideal capacitance changes are of opposite sign. Furthermore, the non-linearities for the capacitance changes are of opposite sign; thus they oppose each other.

Ideally, both the single-backplate microphone and the dual-backplate microphone do not have any electrostatic non-linearity when used with a voltage amplifier. However, previously it was shown that the non-uniform gap introduces a non-linearity. Another source of electrostatic non-linearity for microphones used with voltage amplifiers is the parasitic capacitance. The output voltage vs. pressure non-linearity of a single-backplate microphone and dual-backplate microphone are shown in Figure 3-19(a) and Figure 3-19(b), respectively. The effects of the non-linear deflection are neglected to isolate the effect of the parasitic capacitance. Without a parasitic capacitance, the non-linearity of the voltage amplifier is less than that of the charge amplifier. As the parasitic capacitance becomes larger, the non-linearity approaches that of the charge amplifier cases.

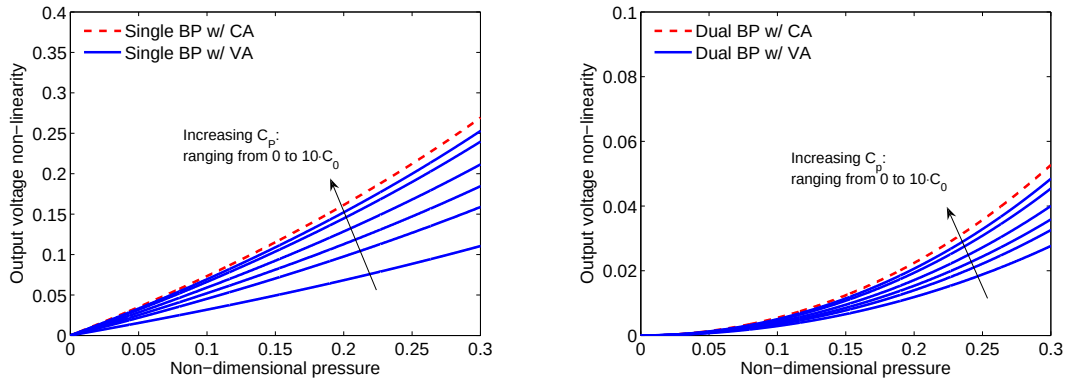


(a) Non-linearity for the single-backplate microphone.

(b) Non-linearity for the dual-backplate microphone.

Figure 3-19. Non-linearity of both the single-backplate and dual-backplate microphones for varying values of parasitic capacitance

## 3.2 Lumped Element Modeling

To further study the theoretical behavior of the microphone, a lumped element model (LEM) is developed. The microphone is a complex three dimensional structure. By utilizing a lumped element model, the distributed properties of the microphone are represented by a set of lumped elements. However, for a lumped element model to be a valid representation of the system, the wavelength of interest must be much larger than the length scale of the device. For the microphone, this means that the wavelength of the incident acoustic wave must be much larger than the diameter of the diaphragm [21].

To construct the lumped element model, the mechanical and acoustic properties of the microphone are represented by equivalent circuit elements. Each energy domain is represented by a pair of conjugate power variables; which in general are effort and flow. An impedance analogy is used, such that the impedance relates the effort, $e$, to the flow, $f$, via $e = Z \cdot f$. For example, in the electrical domain, the effort variable is voltage and the flow variable is current. In each energy domain, the product of the effort and flow variables is power. A summary of the conjugate

power variables for the mechanical, acoustic, and electrical domains are given in Table 3-3.

Table 3-3. Lumped element modeling conjugate power variables.

| Energy Domain | Effort | Flow | Displacement |
|---|---|---|---|
| Mechanical | Force $[N]$ | Velocity $\left[\frac{m}{s}\right]$ | Position $[m]$ |
| Acoustic | Pressure $\left[\frac{N}{m^2}\right]$ | Volumetric Flow $\left[\frac{m^3}{s}\right]$ | Volume $\left[m^3\right]$ |
| Electrical | Voltage $[V]$ | Current $[A]$ | Charge $[C]$ |

There are several types of elements that comprise a lumped element model. Energy is supplied to the system through effort and flow sources. Transduction between energy domains is represented by controlled sources or transformers. There are three passive elements: the generalized resistor, the generalized capacitor, and the generalized inductor. The generalized resistor represents energy lost through dissipation. The generalized capacitor represents the storage of potential energy, while the generalized inductor represents the storage of kinetic energy. Each of the lumped elements in an LEM can be in any energy domain; the lumped elements for the mechanical, acoustic, and electrical energy domains are listed in Table 3-4. For example, in the electrical domain, potential energy is stored in a capacitor; while in the mechanical domain, potential energy is stored in a spring. However, it is common to refer to the mechanical generalized capacitance in terms of a compliance rather than a spring; the compliance is given by $1/k$.

Table 3-4. Lumped elements for various energy domains.

| Energy Domain | Generalized Resistance | Generalized Capacitance | Generalized Inductance |
|---|---|---|---|
| Mechanical | $R_m$ $\left[\frac{N \cdot s}{m}\right]$ | $C_m$ $\left[\frac{m}{N}\right]$ | $M_m$ $[kg]$ |
| Acoustic | $R_a$ $\left[\frac{N \cdot s}{m^5}\right]$ | $C_a$ $\left[\frac{m^5}{N}\right]$ | $M_a$ $\left[\frac{kg}{m^4}\right]$ |
| Electrical | $R$ $[\Omega]$ | $C$ $[F]$ | $L$ $[H]$ |

A relationship between a mechanical impedance and an equivalent acoustic impedance may be found. A general impedance, $Z$, is defined as

$$Z = \frac{e}{f}, \tag{3–126}$$

where $e$ and $f$ are generalized effort and flow, respectively. In the mechanical domain, force, F, is the effort variable and velocity, v, is the flow variable. Therefore the mechanical impedance is

$$Z_m = \frac{F}{v}. \tag{3–127}$$

Similarly, in the acoustic domain the effort variable is pressure, P, and the flow variable is volumetric flow, Q; thus

$$Z_a = \frac{P}{Q}. \tag{3–128}$$

An effective area, $A_{eff}$ can be defined such that $P = F/A_{eff}$ and $Q = vA_{eff}$. Physically, the effective area maintains continuity of volume velocity between the acoustic and mechanical domain. By substituting these expressions for $P$ and $Q$ into Equation 3–128, the acoustic impedance is written as

$$Z_a = \frac{F}{v{A_{eff}}^2} = \frac{Z_m}{{A_{eff}}^2}. \tag{3–129}$$

To model the transduction between energy domains, an ideal transformer is used. The circuit model of a transformer is shown in Figure 3-20. The ideal transformer transforms power from one energy domain to a second energy domain. The relationship between the effort and flow for the two energy domains is described by [21]

$$\begin{pmatrix} e_2 \\ f_2 \end{pmatrix} = \begin{bmatrix} n & 0 \\ 0 & -\frac{1}{n} \end{bmatrix} \begin{pmatrix} e_1 \\ f_1 \end{pmatrix}, \tag{3–130}$$

where $n$ is the *turns ratio* of the transformer. The orientation of positive polarities and direction of positive flows are shown in Figure 3-20.

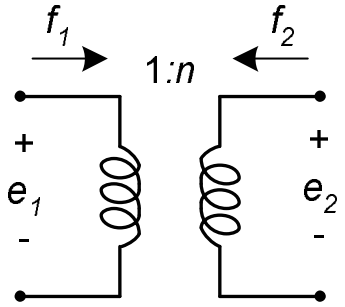


Figure 3-20. Symbol for the transformer LEM element.

The lumped elements for the microphone are found by isolating various aspects of the microphone and analyzing energy storage and dissipation. First, each element is found and then assembled to construct the complete equivalent circuit model of the microphone. Analysis of the equivalent circuit yields closed-form estimates of various performance metrics, including the bandwidth and pull-in voltage. These closed-form solutions provide insight into the scaling of the microphone performance metrics as well as providing a set of design equations.

A naming convention is used for the lumped elements throughout this dissertation. A lumped element is written as $Z_{m,n}$ where $Z$ is either a resistance, capacitance, or inductance, $m$ is the energy domain, and $n$ is an abbreviation for the element. For example, $C_{a,cav}$ is the acoustic cavity compliance.

### 3.2.1 Diaphragm

To find the lumped element representation for the diaphragm, the distributed diaphragm is modeled as a clamped circular plate and lumped to a piston of mass, $M_{m,p}$, and a spring with compliance, $C_{m,p}$ as shown in Figure 3-21[2] . The area

[2] The general parameters $M_{m,p}$ and $C_{m,p}$ are used and can be applied to the diaphragm as well as the two backplates.

of the piston is not the area of the diaphragm, rather it is chosen to maintain continuity of volume velocity between the physical diaphragm and piston model. The pressure on the piston is assumed to be uniform and the lumped elements will be found such that the piston deflection for a given pressure is equal to the center deflection of the diaphragm for the same pressure.

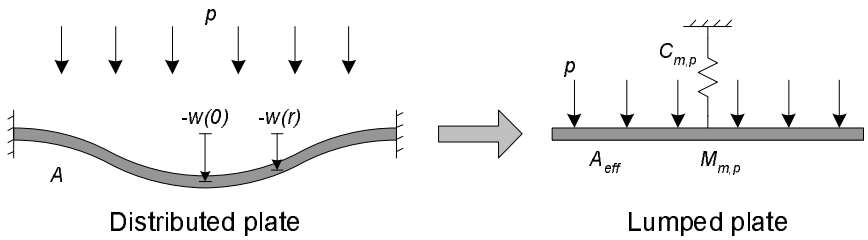


Figure 3-21. Spring and piston model for a distributed diaphragm.

#### 3.2.1.1 Mechanical lumped parameters

The storage of potential energy as the plate deflects is represented by a lumped compliance. The derivation is given in Appendix A. The lumped mechanical compliance of the plate, $C_{m,p}$, is given in Equation A–11 and repeated here

$$C_{m,p} = \frac{3a^2}{64\pi D}. \tag{3–131}$$

The storage of kinetic energy associated with the plate motion is represented by a lumped mass. The lumped mechanical mass of the plate, $M_{m,p}$, is given in Equation A–17 and repeated here

$$M_{m,p} = \frac{\pi a^2 \rho'}{5} = \frac{\pi a^2 \rho h}{5}. \tag{3–132}$$

#### 3.2.1.2 Effective area

In this section, the effective area, $A_{eff}$, of the plate is found. The effective area ensures that the volume velocity of the distributed diaphragm is the same as that for the lumped piston [21]. In general, the volume velocity, $Q$, is given by

$$Q = \int v \, dA. \tag{3–133}$$

For a piston with uniform velocity, the volume velocity is equal to

$$Q = v(0)A_{eff}. \tag{3–134}$$

Substituting Equation A–14 into Equation 3–133 gives the following expression for the volume velocity of the diaphragm,

$$Q = 2\pi v(0) \int_0^a \left[1 - \left(\frac{r}{a}\right)^2\right]^2 r\, dr, \tag{3–135}$$

which is evaluated to

$$Q = \frac{\pi a^2}{3} v(0). \tag{3–136}$$

Comparing Equation 3–136 to Equation 3–134, the effective area of the clamped circular plate is

$$A_{eff} = \frac{\pi a^2}{3}, \tag{3–137}$$

which is one third of the physical area of the plate.

The effective area is used to relate the mechanical lumped elements of the plate to the acoustic equivalent. It is also used to model the electrostatic behavior of the microphone. As discussed in Section 3.1.3, the use of the effective area to estimate the change in capacitance as the diaphragm deflects results in a more accurate model.

#### 3.2.1.3 Acoustic lumped parameters

With the effective area, the acoustic lumped parameters for the plate are found using Equation 3–129. The lumped acoustic compliance of the plate is

$$C_{a,p} = \frac{\pi a^6 (1 - \nu^2)}{16 E h^3}, \tag{3–138}$$

while the lumped acoustic mass is

$$M_{a,p} = \frac{9\rho h}{5\pi a^2}. \tag{3–139}$$

### 3.2.2 Microphone Structure

In this section, the acoustic properties of the microphone structure are considered. Figure 3-22 shows the microphone structure and how various aspects are modeled. The vent geometry in the figure is for discussion only; there are many possible vent channel configurations. There are resistive losses due to the air gaps [121] and the backplate holes [122]. The cavities formed between the diaphragm and each backplate and the large cavity beneath the three plates act as an acoustic compliance. In addition, the mass of the cavity air may be significant [4]. The vent channel is modeled as a fluidic resistance [123]. Each of these elements are first discussed in further detail; then the complete lumped element model of the microphone is constructed.

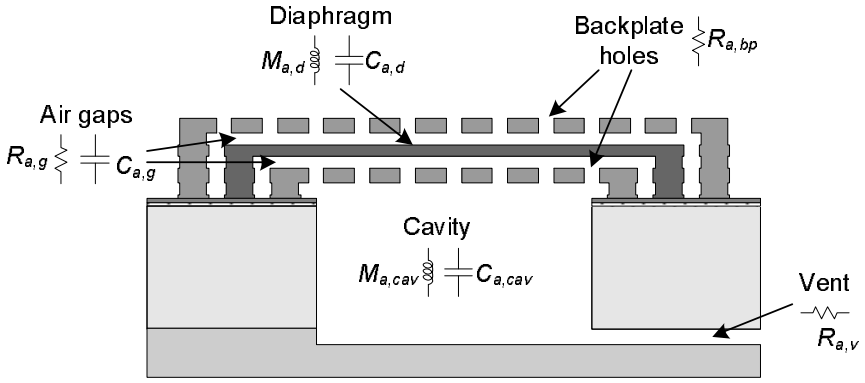


Figure 3-22. Schematic diaphragm of the dual-backplate microphone showing how various features of the structure are modeled.

#### 3.2.2.1 Backplate resistance

As the diaphragm moves, air flows between the diaphragm and each backplate and is forced to pass through the backplate holes as well. The first component of the resistance, squeeze-film damping, is given by [121]

$$R_{a,g} = \frac{12\mu_{air}}{\pi n_h g_0^3} B(A_r), \tag{3–140}$$

where $n_h$ is the number of backplate holes and $\mu_{air}$ is the viscosity of air. The term $A_r$ is the ratio of the total area of the backplate holes to the area of the backplate

and $B(A_r)$ is defined as

$$B(A_r) = \frac{1}{4} ln \left( \frac{1}{A_r} \right) - \frac{3}{8} + \frac{1}{2} A_r - \frac{1}{8} {A_r}^2. \tag{3–141}$$

The second component of the backplate resistance is due to viscous losses as air passes through the backplate holes. The acoustic resistance modeling this effect is [122]

$$R_{a,h} = \frac{72 \mu_{air} h_{bp} n_h}{\pi a_{bp}^4 A_r^2}, \tag{3–142}$$

where $a_{bp}$ and $h_{bp}$ are the radius and thickness of the backplate, respectively. This expression for the resistance is simplified by substituting $n_h \pi a_h^2 / \pi a_{bp}^2$ for $A_r$ as follows,

$$R_{a,h} = \frac{72 \mu_{air} h_{bp}}{\pi a_h^4 n_h}, \tag{3–143}$$

where $a_h$ is the radius of each backplate hole.

The total resistance introduced by the backplate and air gap is the sum of Equation 3–140 and Equation 3–143. Both resistances are proportional to the viscosity of air and inversely proportional to the number of backplate holes. The resistance given in Equation 3–140 is also inversely proportion to the air gap cubed, $g_0^3$. This resistance is significant as the device dimensions are reduced to the MEMS scale. The second resistance given in Equation 3–143 is inversely proportional to the radius of each backplate hole raised to the fourth power, $a_h^4$. This suggests that the resistance is less with a smaller number of larger holes; however, this type of backplate design negatively effects the electrostatic performance of the device.

#### 3.2.2.2 Cavity impedance

A cavity of air stores potential energy as the gas is compressed. Therefore, the cavities in the microphone structure are modeled as acoustic compliances. The value of the compliance is given by [4]

$$C_{a,cav} = \frac{V}{\rho_0 c_0^2}. \tag{3–144}$$

The cavity compliance is proportional to the volume of the cavity. Therefore, for the shallow cavities between the diaphragm and the two backplates, the compliance here is negligible; i.e. the air does not compress in these small cavities. This is desirable for the dual-backplate microphone so that the full incident pressure deflects the diaphragm.

The motion of the air in the cavity also has kinetic energy that is represented by an acoustic mass, given by [4]

$$M_{a,cav} = \frac{\rho_0 V}{3A_{cav}^2}, \tag{3–145}$$

where $A_{cav}$ is the cross sectional area of the cavity.

#### 3.2.2.3 Vent resistance

The final element to be considered is the effect of the vent channel. Modeling the flow in the channel as fully developed laminar flow, then the acoustic resistance through the channel is [123]

$$R_{a,v} = \frac{128\mu L_{eff}}{\pi D^4}, \tag{3–146}$$

where $L_{eff}$ is the effective length of the channel and $D$ is the hydraulic diameter. The effective channel length considers features of the channel such as bends, which make the channel behave as though it is longer than the physical length.

### 3.2.3 Electrostatic Transduction

To construct the transduction portion of the lumped element model, the relationship between a pressure acting on the diaphragm and the electrical output is considered. This behavior was explored in detail in Section 3.1.2, where the behavior of the single-backplate and dual-backplate condenser microphone was discussed for two bias conditions. Separate equations for the output were needed for each case. In this section, the transformer model is derived for the single-backplate microphone for both biasing conditions. It is shown that the model is the same for both cases. Then, the transformer model is extended to the dual-backplate

microphone. The derivations for the transformer parameters utilize previous derived results from Section 3.1.2.

#### 3.2.3.1 Single-backplate condenser microphone

A schematic cross section of a single-backplate capacitive microphone is shown in Figure 3-23. The diaphragm is represented by its compliance, $C_{a,d}$, and the nominal capacitance between the diaphragm and backplate is $C_{1_0}$. The mean capacitance is used because a linear circuit model is being developed.

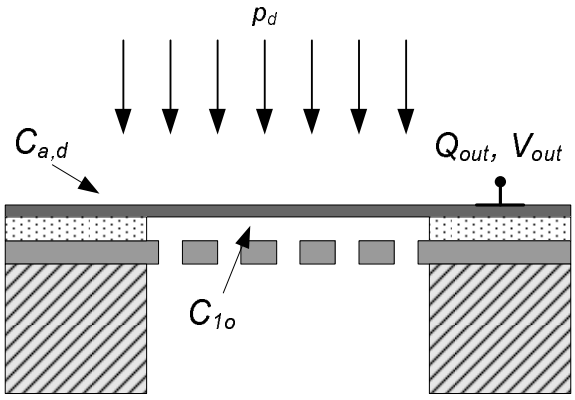


Figure 3-23. Cross-section of the single-backplate capacitive microphone showing relevant parameters for the transformer discussion. The output is either the charge or voltage on the diaphragm.

**Constant voltage**. First, the case of the bias voltage directly connected to the microphone is considered. The small-signal circuit model this case is shown in Figure 3-24. The input pressure results in a pressure, $p_d$, that acts on the diaphragm. This pressure results in an output charge, $\Delta Q_1$. The transformer converts the pressure across the diaphragm, $p_d$, to a voltage, $v_o$. This voltage is not a physical voltage on the microphone; rather, it represents the transduction. The final electrical output is the change in charge on the capacitor $C_{1_0}$. For the constant voltage case, the right terminal of $C_{1_0}$ is connected to small signal ground. However, it could have a non-zero DC voltage level that would be considered in the net bias voltage on the microphone.

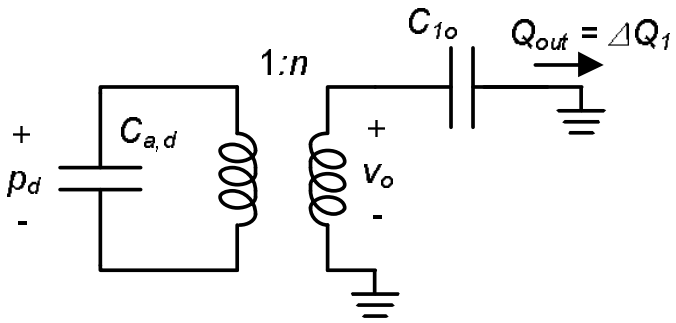


Figure 3-24. Transformer modeling the transduction from the acoustic domain to the electrical domain for a single capacitor biased with a constant voltage.

From Equation 3–130, the voltage, $v_o$, is

$$v_o = n \cdot p_d. \tag{3–147}$$

The charge on the capacitor due to the small signal voltage $v_o$ is the change in charge, $\Delta Q_1$, from the nominal charge. This change in charge is the output charge for the capacitive microphone biased with a constant voltage. Thus,

$$\Delta Q_1 = C_{1_0} v_o \tag{3–148}$$

Equating the $\Delta Q$ from Equation 3–34, using the change in capacitance given in Equation 3–119, to Equation 3–148 results in

$$C_{1_0} v_o = \frac{1}{3} \frac{g'}{g_0} C_{1_0} V_B; \tag{3–149}$$

which is simplified to

$$v_o = \frac{1}{3} \frac{g'}{g_0} V_B. \tag{3–150}$$

Substituting Equation 3–147 for $v_0$ and Equation 3–8 for $g'$, the turns ratio, $n$, becomes

$$n = -\frac{1}{3} \frac{V_B}{g_0} \frac{a_d^4}{64D}. \tag{3–151}$$

The 1/3 factor accounts for the diaphragm curvature and the physical diaphragm radius, $a_d$, is used in this model.

**Constant charge**. The condenser microphone is now considered with the bias voltage applied through a large resistor. The small-signal model of this case is shown in Figure 3-25. The output is now the voltage at the right terminal of the capacitor $C_{1_0}$. The microphone is loaded by the parallel combination of $C_p$ and $C_i$.

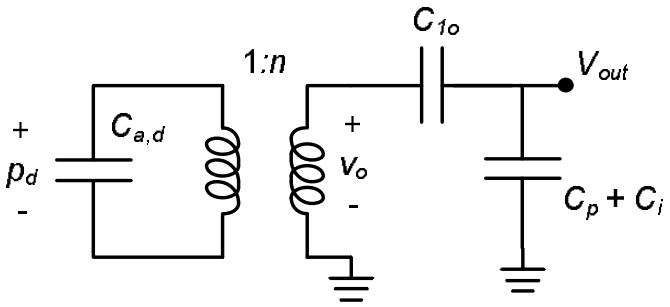


Figure 3-25. Transformer modeling the transduction from the acoustic domain to the electrical domain for a single capacitor biased with a constant charge.

The output voltage in Figure 3-25 is

$$V_{out} = v_o \frac{C_{1_0}}{C_{1_0} + C_p + C_i}. \tag{3–152}$$

The output voltage for a single-backplate microphone with a constant charge bias was previously given in Equation 3–57, which is rewritten as

$$V_{out} = \frac{\Delta C_1 V_B}{C_{1_0}} \frac{C_{1_0}}{C_{1_0} + C_p + C_i} \tag{3–153}$$

using the mean capacitance value $C_{1_0}$ to linearize the expression. Substituting Equation 3–147 for $v_o$ and Equation 3–119 for $\Delta C_1$ and equating Equation 3–152 and Equation 3–153 yields

$$np_d = \frac{1}{3}\frac{g'}{g_0} V_B. \tag{3–154}$$

Substituting Equation 3–8 for $g'$, the turns ratio for the condenser microphone biased through a large resistor is

$$n = -\frac{1}{3}\frac{V_B}{g_0}\frac{a_d^4}{64D}. \tag{3–155}$$

This is identical to the turns ratio for the constant voltage case, given in Equation 3–151; thus the same transformer model is used for either biasing scheme.

#### 3.2.3.2 Dual-backplate condenser microphone

A schematic cross-section of a dual-backplate condenser microphone is shown in Figure 3-26. The diaphragm is represented by its compliance, $C_{a,d}$. The nominal capacitance between the diaphragm and top backplate is $C_{1_0}$ and the nominal capacitance between the bottom backplate and the diaphragm is $C_{2_0}$. The mean capacitances are used because a linear circuit model is being developed.

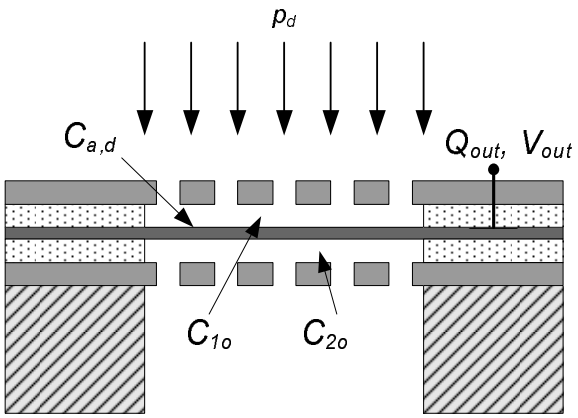


Figure 3-26. Cross-section of the dual-backplate capacitive microphone showing relevant parameters for the transformer discussion. The output is either the charge or voltage on the diaphragm.

**Constant voltage bias**. The small-signal circuit model for the dual-backplate condenser microphone biased directly is shown in Figure 3-27. This model differs from historical transformer models for differential electrostatic transducers in that two transformers are used. Previous models have used a single center-tapped transformer [49]. However, this model presented here is preferred because it

clearly identifies the contribution of the second active capacitor and is suitable for both methods of applying the bias voltage to the microphone. The center-tapped transformer model was only used with the voltage bias applied through a resistor. Furthermore, the double-transformer model gives physical insight into the relationship between single-backplate and double-backplate electrostatic transducers.

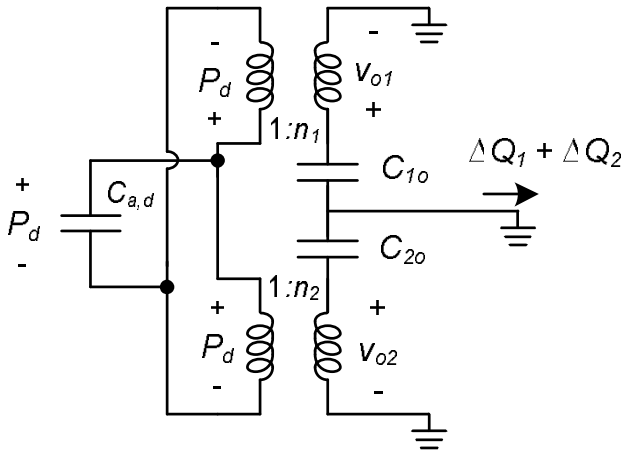


Figure 3-27. Transformer model for the dual-backplate capacitive microphone biased with a constant voltage.

Two transformers are included in this model to represent the transduction of both the top and bottom capacitors. They both are connected across $C_p$, thus the pressure $p_d$ is on the acoustic side of the two transformers. The pressure $p_d$ is converted to the voltages $v_{o1}$ and $v_{o2}$ through the two transformers. To complete the transformer model for the dual-backplate condenser microphone, $n_1$ and $n_2$ must be determined.

The output of the dual-backplate capacitive microphone biased with a constant voltage is $\Delta Q_1 + \Delta Q_1$, as shown in Figure 3-27. These charges were found in Section 3.1.2.3 to be $\Delta C \cdot V_B$, where the capacitance changes are given by Equation 3–119 and Equation 3–120, respectively. By substituting Equation 3–8 for

$g'$, the charges $\Delta Q_1$ and $\Delta Q_1$ are written as

$$\Delta Q_1 = -\frac{p_d}{3} C_{1_0} \frac{V_B}{g_0} \frac{a_d^4}{64D} \tag{3–156}$$

and

$$\Delta Q_2 = -\frac{p_d}{3} C_{2_0} \frac{V_B}{g_0} \frac{a_d^4}{64D}. \tag{3–157}$$

To find $n_1$ and $n_2$, the charge resulting from $v_{o1}$ and $v_{o2}$ is considered. The charge due to $v_{o1}$ is

$$\Delta Q_1 = C_{1_0} n_1 p_d; \tag{3–158}$$

similarly, the charge due to $v_{o2}$ is

$$\Delta Q_2 = C_{1_0} n_2 p_d. \tag{3–159}$$

Comparing Equation 3–158 to Equation 3–156 and Equation 3–159 to Equation 3–157, it can be seen that $n_1$ is equal to $n_2$; furthermore,

$$n_1 = n_2 = -\frac{1}{3} \frac{V_B}{g_0} \frac{a_d^4}{64D}. \tag{3–160}$$

Again, the diaphragm curvature is factored into this model.

**Constant charge bias**. The final case to consider is the dual-backplate condenser microphone biased through a large resistor. The small signal model for this case is shown in Figure 3-28. As was the case for the single-backplate microphone, the output is loaded by the parallel combination of $C_p$ and $C_i$.

The output due to $v_{o1}$ and $v_{o2}$ is

$$V_{out} = n_1 p_d \frac{C_{1_0}}{C_{1_0} + C_{2_0} + C_p + C_i} \tag{3–161}$$

and

$$V_{out} = n_2 p_d \frac{C_{2_0}}{C_{1_0} + C_{2_0} + C_p + C_i}, \tag{3–162}$$

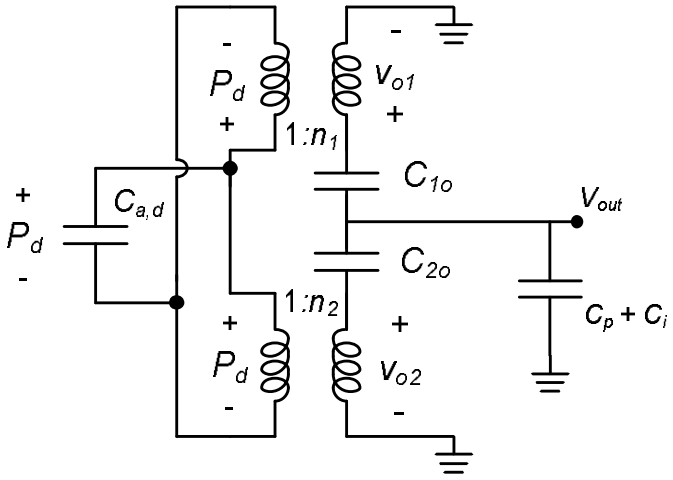


Figure 3-28. Transformer model for the dual-backplate capacitive microphone biased with a constant charge.

respectively. The output contributions from the top and bottom capacitors found using electrostatic analysis, given in Equation 3–93 and Equation 3–96, can be expressed as

$$V_{out} = -\frac{p_d}{3}\frac{V_B}{g_0}\frac{a_d^4}{64D}\frac{C_1}{C_1 + C_2 + C_p + C_i}V_B \tag{3–163}$$

and

$$V_{out} = -\frac{p_d}{3}\frac{V_B}{g_0}\frac{a_d^4}{64D}\frac{C_2}{C_1 + C_2 + C_p + C_i}V_B. \tag{3–164}$$

Comparing Equation 3–163 to Equation 3–161 and Equation 3–164 to Equation 3–162, the turns ratios for the dual-backplate microphone are equal to those for the single-backplate microphone.

#### 3.2.3.3 Summary

The turns ratio is the same for all the condenser microphone cases, given by

$$n = -\frac{1}{3}\frac{V_B}{g_0}\frac{a_d^4}{64D}. \tag{3–165}$$

The curvature of the diaphragm deflection is represented in this model by the 1/3 factor. This accounts for the effective area of the diaphragm. A single model is used to model any condenser microphone. If the microphone is a dual-backplate device, two transformers are simply included in the model. It is also noted that the

turns ratio for the transformer is not directly related to the device capacitances. Rather, the turns ratio is a function of the nominal gap distance, $g_0$, and the diaphragm properties including the radius, $a_d$.

### 3.2.4 Electrostatic Compliance

In this section, the effect of the electrostatic forces present in the condenser microphone is approximated as a compliance. The electrostatic force is attractive between the diaphragm and backplates. This results in a force the pulls the diaphragm towards the backplates. The restoring force due to the mechanical compliance pulls the diaphragm back towards the rest position. Thus, the electrostatic compliance has the effect of reducing the stiffness of the diaphragm [12].

The electrostatic compliance is relevant for the discussion of the microphone dynamics. The constant voltage case corresponds to condenser microphones biased directly with a voltage source. The constant charge case corresponds to condenser microphones biased through a large resistor. For high frequency diaphragm motions, the charge on the condenser microphone is constant.

To find the electrostatic compliance, first, the electrostatic force is identified. The electrostatic compliance is given by

$$\frac{1}{C_{m,el}} = \frac{dF_e}{dx}. \tag{3–166}$$

This compliance is found for the single-backplate and dual-backplate condenser microphones.

#### 3.2.4.1 Single-backplate condenser microphone

The single-backplate microphone is considered for both a constant voltage bias and a constant charge bias. The electrostatic forces for both cases were previously derived in Section 3.1.2.2. These results are used to determine the electrostatic compliance.

**Constant voltage**. The electrostatic force for a single-backplate condenser microphone with a constant voltage is given by Equation 3–47. Thus the electrostatic compliance is

$$\frac{1}{C_{m,el}} = \frac{d}{dg'}\left[\frac{1}{2}{V_B}^2\frac{\epsilon_0 A_{eff}}{(g_0 - g')^2}\right] = {V_B}^2\frac{\epsilon_0 A_{eff}}{(g_0 - g')^3}. \tag{3–167}$$

To have a linear circuit element, the compliance must not depend on the position of the diaphragm, $g'$. A linear approximation of Equation 3–167 is found assuming $g'$ is small. This results in the mechanical electrostatic compliance,

$$C_{m,el} = \frac{g_o^3}{V_B^2 \epsilon_0 A_{eff}}, \tag{3–168}$$

where $g_0$ is the equilibrium gap of the biased single backplate condenser microphone. Therefore, the acoustic electrostatic compliance of a single-backplate condenser microphone with a constant voltage is

$$C_{a,el} = \frac{g_o^3 A_{eff}}{V_B^2 \epsilon_0}. \tag{3–169}$$

**Constant charge**. For a single-backplate condenser microphone with a constant charge, the electrostatic force is given by Equation 3–64. Thus, the electrostatic compliance is

$$\frac{1}{C_{m,el}} = \frac{d}{dg'}\left[\frac{{Q_B}^2}{2\epsilon_0 A_{eff}}\right]. \tag{3–170}$$

The electrostatic force does not depend on $g'$, thus the stiffness is zero, and the compliance is

$$C_{a,el} = \infty. \tag{3–171}$$

Physically, this means the electrostatic compliance does not impact the dynamic response of a single-backplate condenser microphone with a constant charge.

#### 3.2.4.2 Dual-backplate condenser microphone

The dual-backplate condenser microphone is now analyzed to find the electrostatic compliance for both a constant voltage and a constant charge.

**Constant voltage**. The electrostatic force for a dual-backplate microphone with constant voltage is given by Equation 3–84. This yields an electrostatic compliance as follows,

$$\frac{1}{C_{m,el}} = \frac{d}{dg'}\left[2{V_B}^2\frac{\epsilon_0 A_{eff} g_0 g'}{\left({g_0}^2 - {g'}^2\right)^2}\right]. \tag{3–172}$$

Evaluating Equation 3–172 and assuming $g'$ is small, yields

$$C_{a,el} = \frac{g_o^3 A_{eff}}{2V_B^2 \epsilon_0} \tag{3–173}$$

for the acoustic electrostatic compliance. This compliance is one-half of the value for an equivalent single-backplate condenser microphone. Thus the softening impact on the dynamic behavior is larger for a single-backplate condenser microphone.

**Constant charge**. As was the case for the single-backplate condenser microphone with a constant charge, the electrostatic force for the dual-backplate microphone (Equation 3–104) is equal to zero. Thus the electrostatic compliance is

$$C_{a,el} = \infty \tag{3–174}$$

and does not affect the dynamic behavior of the dual-backplate condenser microphone with a constant charge.

#### 3.2.4.3 Summary

The electrostatic force of the single-backplate and dual-backplate condenser microphones with a constant voltage bias are compared to the mechanical restoring force of the diaphragm in Figure 3-29. Linear approximations of the electrostatic force are given as dashed lines. It is this linearized force that is represented by the electrostatic compliance. Due to the non-linear nature of the electrostatic force, the

electrostatic compliance is a reasonable approximation for small deviations from the equilibrium point.

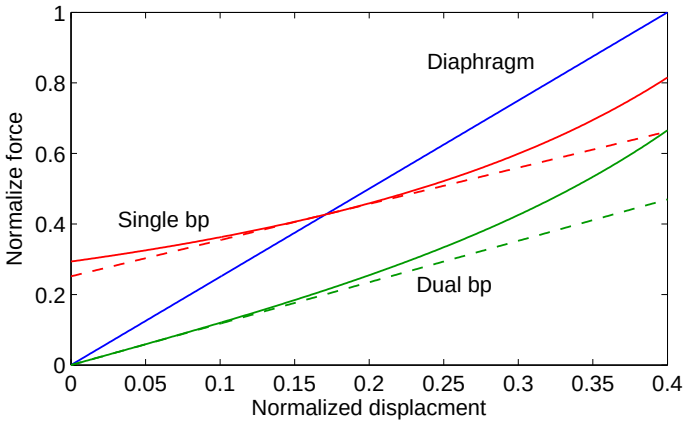


Figure 3-29. Comparison of the diaphragm restoring force to the electrostatic force.

### 3.2.5 Complete Lumped Element Model

Now that each of the lumped elements have been discussed, the final lumped element model is constructed. The microphone is modeled in the acoustic energy domain. The individual elements are arranged by analyzing the flow of volume velocity through the microphone structure. Using an impedance analogy, elements that share the same volume velocity are connected in series; conversely, elements that see the same pressure are connected in parallel.

By referring to Figure 3-30 to visualize the flow through the microphone structure, the final simplified lumped element model is constructed; it is shown in Figure 3-31. The output is either $\Delta Q$ or $V_{out}$ depending on if the bias voltage is applied directly or through a bias resistor. The LEM is the same for either case, and the interface circuitry forces the desired bias condition.

The incident pressure first sees the top backplate and the vent channel. The flow through the backplate may either pass through the backplate holes or deflect the backplate; therefore the backplate compliance and resistance are connected in parallel. Because the cavities between the diaphragm and backplates are very

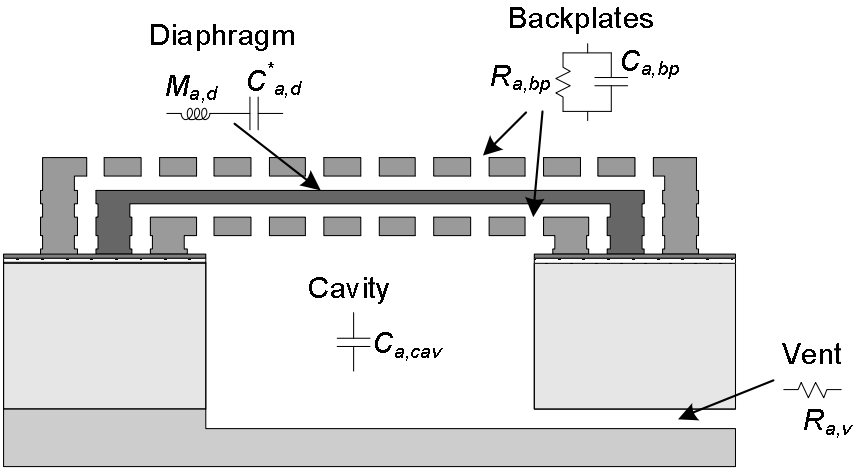


Figure 3-30. Schematic diaphragm of the dual-backplate microphone showing lumped elements included in the LEM.

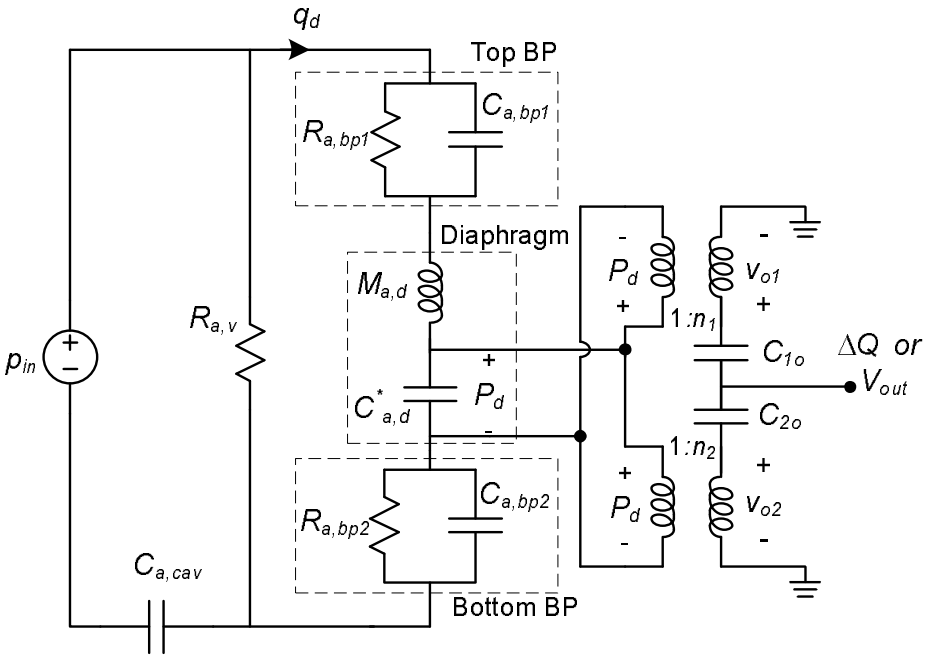


Figure 3-31. Lumped element model of the dual-backplate condenser microphone.

small, the compliance of these cavities is neglected. The flow then deflects the diaphragm; thus the diaphragm mass and diaphragm compliance are connected in series with the backplate impedance. The same model that was used for the top backplate is used for the bottom backplate; this is connected in series with the top backplate and diaphragm because all three elements have the same flow. After

passing through the bottom backplate, the volume velocity may either compress the air in the cavity or pass through the vent channel. The vent channel is in parallel to the series combination of the top backplate, diaphragm, and bottom backplate; finally the cavity compliance is connected such that it can be fed from the vent channel or the flow through the bottom backplate. For the designed microphone, the cavity mass is much less than the diaphragm mass, thus this term is neglected.

A summary of the lumped elements used is given in Table 3-5. The compliance $C_{a,p}$ is used for $C_{a,bp1}$, $C_{a,d}$, and $C_{a,bp2}$. Similarly, the plate mass is used for $M_{a,d}$. The resistance of each backplate, $R_{a,bp1}$ and $R_{a,bp2}$, is given by $R_{a,g} + R_{a,h}$. The turns ratios of the top and bottom transformers, $n_1$ and $n_2$ respectively, are both given by $n$.

Table 3-5. Expressions for the acoustic lumped elements of the microphone.

| Symbol | Element | Expression |
|---|---|---|
| $C_{a,p}$ | Plate compliance | $\frac{\pi a^6 \left(1-\nu^2\right)}{16Eh^3}$ |
| $M_{a,p}$ | Plate mass | $\frac{9\rho h}{5\pi a^2}$ |
| $R_{a,g}$ | Air gap resistance | $\frac{12\,\mu_{air}}{\pi n_h\, g_0^3} B(A_r)$ |
| $R_{a,h}$ | Backplate hole resistance | $\frac{72\,\mu_{air} h_{bp}}{\pi a_h^4 n_h}$ |
| $C_{a,cav}$ | Cavity compliance | $\frac{V}{\rho_0 c_0^2}$ |
| $R_{a,v}$ | Vent resistance | $\frac{128\mu L_{eff}}{\pi D^4}$ |
| $n$ | Turns ratio | $-\frac{1}{3}\frac{a^4}{64D}\frac{V_B}{g_0}$ |

In Figure 3-31, the diaphragm is represented by the acoustic compliance $C_{a,d}^*$. This represents the diaphragm compliance and the electrostatic compliance, if

present; and is given by

$$C^*_{a,d} = \frac{C_{a,d}C_{a,el}}{C_{a,d} + C_{a,el}}. \tag{3–175}$$

The acoustic diaphragm compliance, $C_{a,d}$, and the electrostatic compliance, $C_{a,el}$, share the same flow. Therefore, they are in series, as represented by $C^*_{a,d}$. For cases where the electrostatic compliance is negligible, $C^*_{a,d}$ simply becomes $C_{a,d}$.

### 3.2.6 Theoretical Frequency Response

Using the lumped element model, the theoretical frequency response of the microphone is investigated. First, the transfer function from the incident pressure to the pressure across the diaphragm is studied. Then, the impact of the backplate compliance on the frequency response is considered. The details of the microphone frequency response derivation are given in Appendix B.

The frequency response of the equivalent circuit model shown in Figure 3-31 is given in Equation B–12; repeated here for convenience,

$$H_{mic} = \frac{sC_{a,cav}R_v}{sC^*_{a,d}\left(1 + sC_{a,cav}R_{a,v}\right)Z_p + sC^*_{a,d}R_{a,v}}, \tag{3–176}$$

where $Z_p$ is the impedance of the series combination of the diaphragm and both backplates. Neglecting the compliance of the backplates, the simplified frequency response can be approximated by Equation B–15; repeated here,

$$H^s_{mic} = \frac{sC_{a,cav}R_{a,v}}{\left\{\begin{array}{l} s^3M_{a,d}C^*_{a,d}C_{a,cav}R_{a,v} \\ + s^2\left[M_{a,d}C^*_{a,d} + C^*_{a,d}C_{a,cav}\left(R_{a,bp1} + R_{a,bp2}\right)R_{a,v}\right] \\ + s\left[C^*_{a,d}\left(R_{a,bp1} + R_{a,bp2}\right) + \left(C_{a,cav} + C^*_{a,d}\right)R_{a,v}\right] + 1 \end{array}\right\}}. \tag{3–177}$$

In Figure 3-32, the frequency response of $p_d/p_{in}$ given in Equation B–15 is plotted. The values used for this example are chosen to accentuate the notable features of the frequency response. The diaphragm mass ($7\times10^4$ $[kg/m^4]$) and compliance ($1.5\times10^{-16}$ $[m^5/N]$) were selected to give a resonant frequency near

20 $kHz$. The total damping of $14{\times}10^{8}$ $[Ns/m^5]$ was chosen to give an underdamped response. Finally, the cavity compliance ($60{\times}10^{-16}$ $[m^5/N]$) and vent resistance ($1{\times}10^{13}$ $[Ns/m^5]$) were chosen to give a cut-on frequency near 10 $Hz$.

As shown in Figure 3-32(a), the flat band of the frequency response is between the cut-on frequency, $f_{cut}$, and the resonant frequency, $f_0$. The loading of the electrical domain through the transformers is neglected here. This effect depends on how the microphone is biased and is discussed further in Section 3.2.4. The dynamics of the microphone structure without bias are given below.

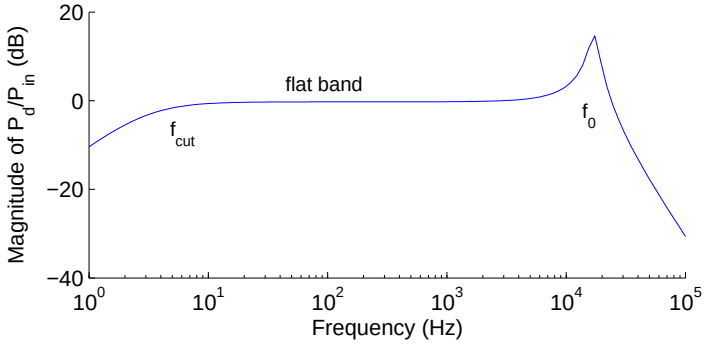


(a) Magnitude response of $p_d/p_{in}$ for an example microphone.

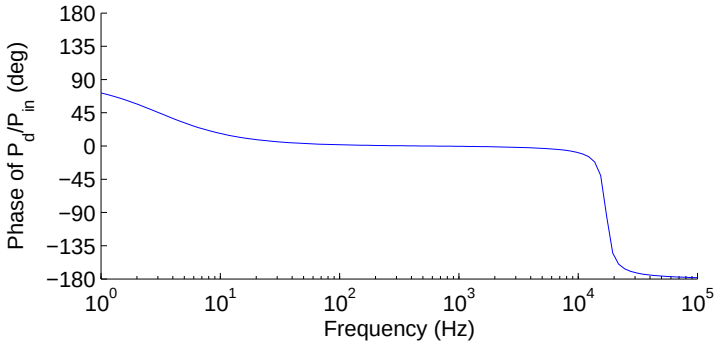


(b) Phase response of $p_d/p_{in}$ for an example microphone.

Figure 3-32. Frequency response of a dual-backplate microphone example in terms of $p_d/p_{in}$ as predicted by the LEM.

**Cut-on frequency**. To find an expression for the cut-on frequency, $f_{cut}$, a low frequency circuit approximation is considered. When the frequency is far below the resonant frequency, the diaphragm mass can be approximated as a short circuit.

For proper microphone operation, the backplate resistances must be much smaller than the vent resistance, thus they can also be neglected. The low frequency equivalent circuit is shown in Figure 3-33.

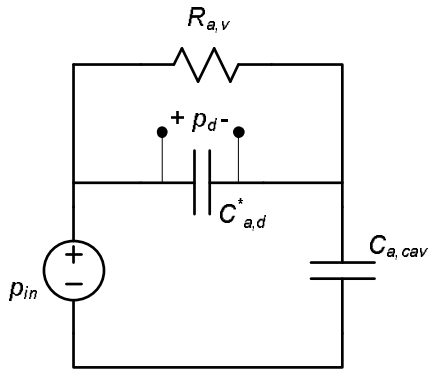


Figure 3-33. Low frequency equivalent circuit of the dual-backplate microphone.

The expression for $p_d/p_{in}$ for this simplified circuit is given by

$$\frac{p_d}{p_{in}} = \frac{sC_{a,cav}R_{a,v}}{1 + sR_{a,v}\left(C_{a,cav} + C^*_{a,d}\right)}. \tag{3–178}$$

This is a single-pole high pass function with a cut-on frequency of

$$f_{cut} = \frac{1}{2\pi R_{a,v}\left(C_{a,cav} + C^*_{a,d}\right)}, \tag{3–179}$$

and a slope of +20 $dB$/decade below $f_{cut}$ [124].

**Resonant frequency**. The lumped element model simplifies to the equivalent circuit shown in Figure 3-34 for frequencies near the resonant frequency. At higher frequencies, the vent resistance is effectively an open circuit, compared to the other impedances. Thus, the microphone is approximately a simple second order system with a mass of $M_{a,d}$, a compliance of $\left(C^{*-1}_{a,d} + C^{-1}_{a,cav}\right)^{-1}$, and a resistance of $R_{a,bp1} + R_{a,Rbp2}$.

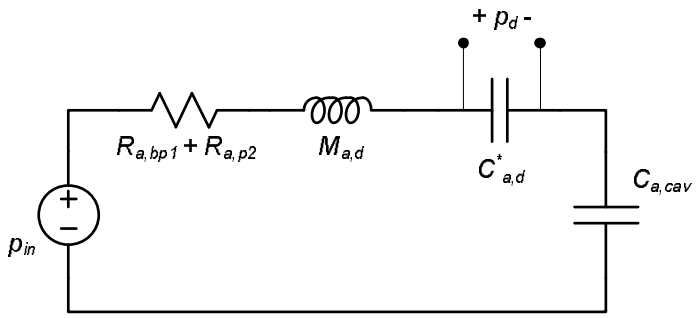


Figure 3-34. High frequency equivalent circuit of the dual-backplate microphone.

The transfer function, $p_d/p_{in}$, for frequencies near the resonance of the microphone is given by

$$\frac{p_d}{p_{in}} = \frac{1}{s^2 M_{a,d} C^*_{a,d} + s\left(R_{a,bp1} + R_{a,bp2}\right) C^*_{a,d} + \left(1 + \frac{C^*_{a,d}}{C_{a,cav}}\right)}. \tag{3–180}$$

The microphone is characterized in terms of its natural frequency, $\omega_0$, and damping ratio, $\zeta$ [124]. The natural frequency is

$$\omega_0 = \frac{1}{\sqrt{M_{a,d}\left(\frac{C^*_{a,d} C_{a,cav}}{C^*_{a,d} + C_{a,cav}}\right)}}, \tag{3–181}$$

while the damping ratio is given by

$$\zeta = \frac{R_{a,bp1} + R_{a,bp2}}{2}\sqrt{\frac{\frac{C^*_{a,d} C_{a,cav}}{C^*_{a,d} + C_{a,cav}}}{M_{a,d}}}. \tag{3–182}$$

If the microphone is lightly damped, or $\zeta$ is much less than one, the frequency response has a maximum at $\omega_0$. However, as $\zeta$ approaches one, the peak in the magnitude response moves away from $\omega_0$ to

$$\omega_p = \omega_0\sqrt{1 - 2\zeta^2}. \tag{3–183}$$

If $\zeta$ is greater than one, then the microphone is overdamped, and the frequency response does not have a peak.

**Flat band response**. For frequencies between the cut-on frequency and the resonant frequency, the equivalent circuit is further simplified. Above the cut-on frequency, the vent resistance can be approximated as an open circuit; below the resonant frequency, the diaphragm mass and backplate resistances may also be neglected. The equivalent circuit for these mid-range frequencies is shown in Figure 3-35.

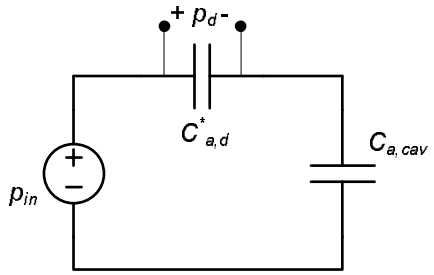


Figure 3-35. Equivalent circuit of the dual-backplate microphone for mid-range frequencies.

In the flat band region of the frequency response, the equivalent circuit of the microphone is reduced to a capacitive pressure divider. The microphone response in the flat band is

$$\frac{p_d}{p_{in}} = \frac{C_{a,cav}}{C_{a,cav} + C^*_{a,d}}. \tag{3–184}$$

Thus, the incident pressure is attenuated by the cavity compliance. To avoid attenuation, the cavity should be large such that $C_{a,cav} >> C^*_{a,d}$. This allows the full incident pressure to act on the diaphragm.

**Compliant backplate implications**. In the previous sections, an expression for $p_d/p_{in}$ has been found for various frequency ranges. However, this does not yet give the frequency response of the microphone in terms of a ratio of the output voltage to the incident pressure. To find this, the pressure across the diaphragm must be related to the output voltage. For the dual-backplate microphone, the output voltage of the microphone was shown to be given by Equation 3–78 or Equation 3–99 with a constant voltage bias or a constant charge bias, respectively.

In these expressions for the output voltage, the pressure $p$ is the pressure across the diaphragm, $p_d$.

In deriving the expressions for the microphone output voltage, it was assumed that the relationship between the pressure incident on the diaphragm and the diaphragm deflection is linear, as given by Equation 3–8. Furthermore, a parallel plate capacitor was assumed in which the change in the air gap was solely due to the diaphragm deflection. However, if there is a significant pressure differential across the backplates, and if the backplates are sufficiently compliant, the backplates will have a non-negligible deflection. Shown in Figure 3-36 is a situation where the air gap changes both due to diaphragm and backplate motion. The air gaps of a dual-backplate microphone can be expressed as

$$g_1 = g_o - g'_d + g'_{bp1}, \tag{3–185}$$

and

$$g_2 = g_o + g'_d - g'_{bp2}; \tag{3–186}$$

where $g'_d$, $g'_{bp1}$, and $g'_{bp2}$ are the deflection of the diaphragm, top backplate, and bottom backplate, respectively.

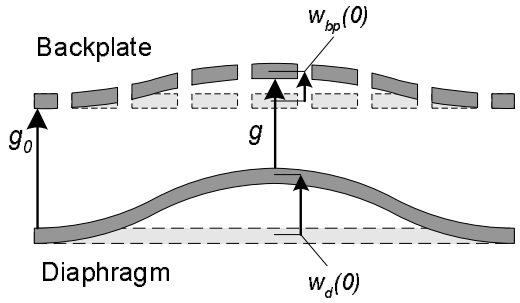


Figure 3-36. Schematic of an air gap changing due to both diaphragm motion and backplate motion.

The frequency response for $p_d/p_{in}$ given in Equation B–12 factors in the effect of the backplate compliances; it is repeated here,

$$H_{mic} = \frac{sC_{a,cav}R_{a,v}}{sC^*_{a,d}\left(1 + sC_{a,cav}R_{a,v}\right)Z_p + sC^*_{a,d}R_{a,v}}. \tag{3–187}$$

This expression for $p_d/p_{in}$ is similar to that given in Equation B–15, except that $Z_p$ is now a general impedance that includes the effects of the backplate compliance. A similar expression for $p_{bp1}/p_{in}$ and $p_{bp2}/p_{in}$ can also be found using Equation B–16 and Equation B–17. After the frequency response has been determined for the pressure across the diaphragm and each backplate, the frequency response for the total change in the air gaps can be found.

The deflection of a plate with compliance $C$ can be found if the pressure across the compliance is known. In the electrical domain, the charge on a capacitor is given by $Q_e = CV$. Similarly in the acoustic domain, the acoustic displacement, $q_a$ is

$$q_a = wA_{eff} = C_aP. \tag{3–188}$$

Therefore, the deflection is given by

$$w = \frac{C_aP}{A_{eff}}. \tag{3–189}$$

Using Equation 3–189, Equation 3–185, and Equation 3–185, the frequency response for the change in the two air gaps is

$$H_{g'_1} = H_{bp1}\frac{C_{a,bp1}}{A_{eff_{bp1}}} - H_{mic}\frac{C^*_{a,d}}{A_{eff}}, \tag{3–190}$$

and

$$H_{g'_2} = H_{mic}\frac{C^*_{a,d}}{A_{eff}} - H_{bp2}\frac{C_{a,bp2}}{A_{eff_{bp2}}}. \tag{3–191}$$

The frequency response of $g'$ for the top capacitor of a dual backplate microphone is shown in Figure 3-37 for two cases: (1) an ideal backplate with zero compliance; and (2) a backplate with finite compliance. The compliance of the

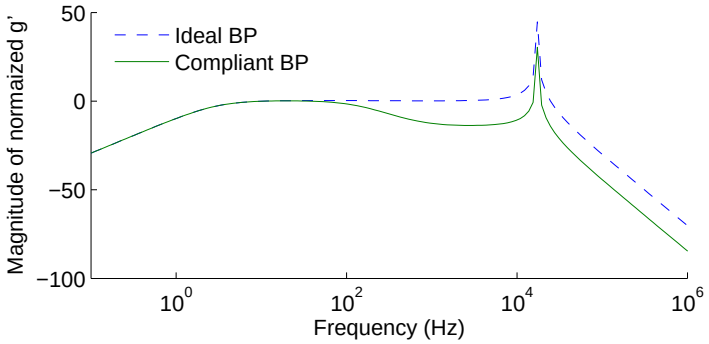


(a) Magnitude response of the normalized change in the air gap distance.

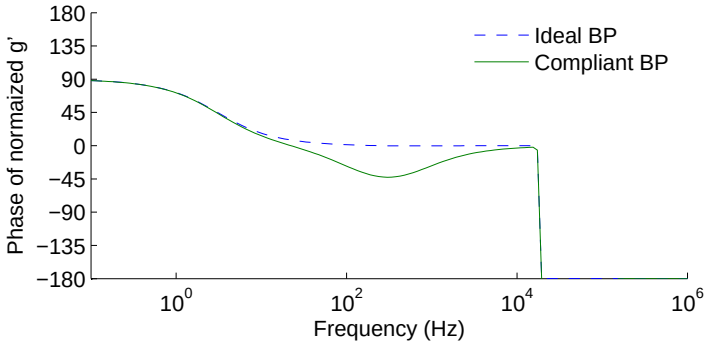


(b) Phase response of the normalized change in the air gap distance.

Figure 3-37. Frequency response of the normalized air gap distance showing the effects of a compliant backplate.

backplate for this example was chosen to make the backplate corner frequency approximately 100 $Hz$ so that the effect is clear. Using the values used for the example microphone in Section 3.2.6, a backplate compliance that is 1000× the diaphragm compliance is needed to observe the effect of finite backplate compliance.

At low frequencies, the two frequency response curves are the same, however at higher frequencies they diverge. The magnitude of the total gap change, $g'$, is less when the compliance of the backplate is significant; this reduces the sensitivity at higher frequencies. There are also anomalies in the phase response at higher frequencies. It is clearly desirable to design the microphone such that the effect of the backplate compliance on the microphone's response to an incident pressure

is negligible. However, the compliant backplate still deflects due to electrostatic forces.

### 3.2.7 Quasi-Static Pull-In

As was mentioned in Section 3.1.2, the electrostatic force acting on the diaphragm has the potential to cause the diaphragm to collapse into the backplate [12]. This phenomenon is known as *pull-in*. An understanding of the pull-in behavior of a microphone is necessary to determine its stability and allowable operating conditions. The study of the pull-in of a microphone can be divided into two classes: (1) quasi-static pull-in, where the diaphragm is initially at rest, the incident pressure is zero, and the electrical bias is constant; and (2) dynamic pull-in, where the diaphragm motion, incident pressure, and time varying electrical bias conditions are considered [125]. Only quasi-static pull-in is considered here; this gives the limits for the maximum DC bias values that can be used. Further discussion on dynamic pull-in for condenser microphones can be found in [118]. During use of the microphone, however, a lower electrical bias must be used to ensure stability. The quasi-static pull-in is examined for both single-backplate and dual-backplate condenser microphones.

For electrostatic pull-in to occur, the electrostatic force must increase as the diaphragm approaches the backplate. Because static pull-in is only being considered here, this analysis is valid regardless of how the bias voltage is applied.

As shown in Figure 3-38, there are two forces acting on the diaphragm. The mechanical force, $F_m$, is the restoring force of the diaphragm and the electrical force, $F_e$, is the electrostatic force due to the applied bias. For single-backplate microphones, this force has one component; while, for dual-backplate microphones, this force is the sum of two electrostatic forces. For all cases, the mechanical force is

$$F_m = -\left(1/C_{m,d}\right) g'. \tag{3–192}$$

This is re-written in terms of the air gap distance, $g$,

$$F_m = -\frac{1}{C_{m,d}}\left(g_0 - g\right); \tag{3–193}$$

The analysis of the quasi-static pull-in follows the work of Senturia [12].

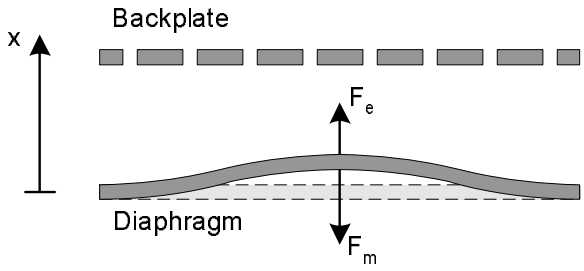


Figure 3-38. Single-backplate capacitive microphone schematic showing the relevant forces for quasi-static pull-in.

#### 3.2.7.1 Single-backplate condenser microphone

The electrostatic force for a single-backplate condenser microphone with an external bias voltage is given by Equation 3–47. This is expressed in terms of $g$, the instantaneous air gap distance,

$$F_e = \tfrac{1}{2}{V_B}^2\frac{\epsilon_0 A}{g^2}. \tag{3–194}$$

As can be seen from Equation 3–193 and Equation 3–194, the mechanical and electrostatic forces oppose each other. The electrostatic force is directed towards the backplate in the positive $x$ direction. The mechanical force is always directed towards the diaphragm rest position; assuming a positive diaphragm deflection, the mechanical force is directed in the negative $x$ direction.

The net force acting on the diaphragm is

$$F_{net} = \tfrac{1}{2}{V_B}^2\frac{\epsilon_0 A}{g^2} - \frac{1}{C_{m,d}}\left(g_0 - g\right). \tag{3–195}$$

When the bias voltage is initially applied to the microphone, the electrostatic force is greater that the mechanical restoring force. At equilibrium, the two

forces balance each other, thus $F_{net}$ is zero. The stability of the equilibrium point is determined by whether a small perturbation of the diaphragm towards the backplate causes an increase in the net force or a decrease. Using the coordinate system in Figure 3-38, an increase in $F_{net}$ causes the diaphragm to accelerate towards the backplate; thus the equilibrium point is unstable. However, if $F_{net}$ decreases, then the equilibrium point is stable.

For the single-backplate condenser microphone, $\partial F_{net}$ is given by

$$\partial F_{net} = \left( \frac{1}{C_{m,d}} - \frac{\epsilon_0 A {V_B}^2}{g^3} \right) \partial g. \tag{3–196}$$

Therefore, if the diaphragm is perturbed towards the backplate, $\partial g < 0$, then the quantity in parenthesis must be positive such that $\partial F_{net} < 0$. Thus,

$$\frac{1}{C_{m,d}} > \frac{\epsilon_0 A {V_B}^2}{g^3}. \tag{3–197}$$

A gap distance, $g_{PI}$, is defined at which the equilibrium transitions from stable to unstable. The bias voltage that results in this equilibrium position is $V_{PI}$, which is the *pull-in voltage*. At this critical condition, Equation 3–197 becomes

$$\frac{1}{C_{m,d}} = \frac{\epsilon_0 A {V_{PI}}^2}{{g_{PI}}^3}. \tag{3–198}$$

By substituting Equation 3–198 into Equation 3–195 and evaluating at $g_{PI}$ and $V_{PI}$, the critical gap distance where the stable-to-unstable transition occurs is found to be

$$g_{PI} = \frac{2}{3} g_0. \tag{3–199}$$

From Equation 3–199 and Equation 3–198 the pull-in voltage is

$$V_{PI} = \sqrt{\frac{8 {g_0}^3}{27 C_{m,d} \epsilon_0 A}}. \tag{3–200}$$

The bias voltage must be less than $V_{PI}$ to avoid quasi-static pull-in.

#### 3.2.7.2 Dual-backplate condenser microphone

The analysis of a dual-backplate condenser microphone with an external bias voltage is very similar to that of the single-backplate microphone. The mechanical force is given by Equation 3–193 and the electrostatic force is given by Equation 3–84. However, the forces are written in terms of $g'$ rather than the gap distance $g$ because there are now two gaps. The electrostatic force has been defined such that a positive $g'$ decreases the top air gap and increases the bottom air gap.

The net force acting on the diaphragm is

$$F_{net} = 2{V_B}^2 \frac{\epsilon_0 A g_0 g'}{\left({g_0}^2 - {g'}^2\right)^2} - \frac{g'}{C_{m,d}}. \tag{3–201}$$

Now, the change in $F_{net}$ due to a change in $g'$ is examined. To have a stable system, a positive $\partial g'$ must produce a negative $\partial F_{net}$. The differential of Equation 3–201 with respect to $g'$ is

$$\partial F_{net} = \left[\left(\frac{2{V_B}^2 \epsilon_0 A g_0}{\left(g_0^2 - {g'}^2\right)^2}\right)\left(\frac{g_0^2 + 3{g'}^2}{g_0^2 - {g'}^2}\right) - \frac{1}{C_{m,d}}\right] \partial g'. \tag{3–202}$$

The quantity in the brackets must be negative to have a stable microphone, thus

$$\frac{1}{C_{m,d}} > \left(\frac{2{V_B}^2 \epsilon_0 A g_0}{\left(g_0^2 - {g'}^2\right)^2}\right)\left(\frac{g_0^2 + 3{g'}^2}{g_0^2 - {g'}^2}\right). \tag{3–203}$$

At the verge of pull-in, with an applied voltage of $V_{PI}$ and an equilibrium position of $g'_{PI}$, Equation 3–202 is re-written as

$$\frac{1}{C_{m,d}} = \left(\frac{2{V_{PI}}^2 \epsilon_0 A g_0}{\left(g_0^2 - {g'_{PI}}^2\right)^2}\right)\left(\frac{g_0^2 + 3{g'_{PI}}^2}{g_0^2 - {g'_{PI}}^2}\right). \tag{3–204}$$

Substituting Equation 3–204 into Equation 3–201 and evaluating at $g'_{PI}$ and $V_{PI}$ results in

$$\begin{aligned} \cancel{g'_{PI}\left[\frac{2{V_{PI}}^2\epsilon_0 A g_0}{\left({g_0}^2-{g'_{PI}}^2\right)^2}\right]}\left[\frac{g_0^2+3{g'_{PI}}^2}{g_0^2-{g'_{PI}}^2}\right] &= \cancel{g'_{PI}\left[\frac{2{V_{PI}}^2\epsilon_0 A g_0}{\left({g_0}^2-{g'_{PI}}^2\right)^2}\right]} \\ {g_0}^2+3{g'_{PI}}^2 &= {g_0}^2-{g'_{PI}}^2 \\ 2{g'_{PI}}^2 &= 0\,. \end{aligned} \tag{3–205}$$

Therefore, the equilibrium position is at $g' = 0$; substituting this into Equation 3–204 results in the expression for the pull-in voltage,

$$V_{PI} = \sqrt{\frac{{g_0}^3}{2C_{m,d}\epsilon_0 A}}. \tag{3–206}$$

#### 3.2.7.3 Pull-in summary

The dual-backplate microphone has a pull-in voltage that is approximately 30 % higher than the single-backplate microphone. The results for the equilibrium position of the diaphragm show a distinct difference between single-backplate microphones and dual backplate microphones. The diaphragm of the single-backplate microphone moves towards the backplate until the pull-in voltage is reached, at which point it jumps to the backplate. For the dual-backplate microphone, however, the diaphragm remains centered as the bias voltages are increased; when the pull-in voltage is reached, the diaphragm jumps to one of the backplates.

The results are obtained through this analysis using several assumptions. The diaphragm deflection is assumed to be linear. Furthermore, the capacitor formed by the diaphragm and backplate is assumed to remain parallel as the diaphragm deflects; this is clearly not the case as the diaphragm approaches the backplate. Finally, the backplate is assumed to be rigid and for the dual backplate microphones, the two capacitors are assumed to be identical; this may not be the case in the physical microphone. Therefore, these predictions may not match

experimentally determined values of the pull-in voltage. However, these results do provide physical insight into the pull-in phenomenon as well as scaling information. The pull-in problem is investigated further by Liu et al. [118].

## 3.3 Noise Model

The minimum detectable signal of the microphone is determined by the noise floor of the microphone and interface circuitry. In this section, the thermomechanical noise generated in the microphone structure is discussed. This is followed by a discussion on the electronic noise considering both a charge amplifier and a voltage amplifier circuit.

To derive the noise behavior of the microphone, various noise sources are analyzed. Each of these is modeled as a power spectral density (PSD) having the units of power per $Hz$; i.e $[V^2/Hz]$ or $[Pa^2/Hz]$. The noise PSD from each noise source is referred to a common point and the respective PSDs are summed.

### 3.3.1 Microphone Noise

A simplified lumped element model of the dual-backplate microphone including noise sources is shown in Figure 3-39. In this model, the compliance of the backplates has been neglected. Furthermore, the damping of the backplates as well as any internal structural damping of the diaphragm have been combined into a single equivalent acoustic resistor, $R_{a,eff}$. Each resistor in Figure 3-39 has a thermomechanical noise source which may be represented by either a volume velocity noise or a pressure noise[3] . The noise due to resistor $R_{a,eff}$ is represented by a pressure noise PSD, $S_{P,R_{eff}}$. The noise due to $R_{a,v}$, however, is represented by a current noise PSD, $S_{Q,R_v}$. The PSD of these sources is $4kTR_{a,eff}$ and $4kT/R_{a,v}$, respectively [20].

[3] The choice of using a current noise or voltage noise to model a resistor is made solely on the ease of solving for the output noise.

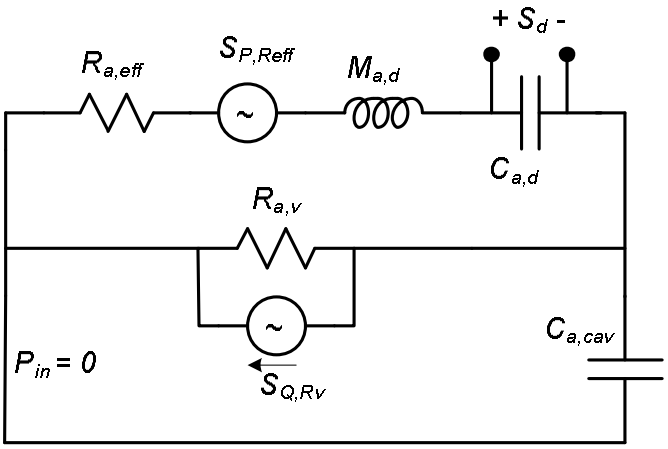


Figure 3-39. Acoustic noise model of the microphone.

To find the noise contributions of the acoustic damping within the microphone, the noise from each of the sources is referred to the port labeled $S_d$. The pressure at this location forces the diaphragm and generates the output voltage of the microphone. For the noise analysis, the incident pressure is set to zero and replaced with a short circuit. The noise from each resistor is found individually and the total noise PSD at $S_d$ is the sum of the two noise contributions.

The circuit shown in Figure 3-39 reduces to the noise model shown in Figure 3-40 when only $S_{P,R_{eff}}$ is considered. The current noise source $S_{Q,R_v}$ is replaced with an open circuit. To pressure noise PSD referred to the diaphragm is found using a pressure divider. The magnitude squared of the pressure gain from $S_{P,R_{eff}}$ to $S_d$ is used because the phase information is irrelevant for uncorrelated noise sources.

$$S_{d_{R_{eff}}} = \left| \frac{\dfrac{1}{sC_{a,d}}}{R_{a,eff} + sM_{a,d} + \dfrac{1}{sC_{a,d}} + R_{a,v} /\!/ \dfrac{1}{sC_{a,cav}}} \right|^2 \cdot S_{R_{eff}}. \tag{3–207}$$

This can be rewritten as

$$S_{d_{R_{eff}}} = \frac{\left|sR_{a,v}C_{a,cav}+1\right|^2}{\left|\begin{array}{l} s^3M_{a,d}C_{a,d}C_{a,cav}R_{a,v} \\ +s^2\left[M_{a,d}C_{a,d}+C_{a,d}C_{a,cav}R_{a,eff}R_{a,v}\right] \\ +s\left[C_{a,d}R_{a,eff}+C_{a,cav}R_{a,v}\right]+1 \end{array}\right|^2} \cdot S_{R_{eff}}, \tag{3–208}$$

which gives an expression for the noise PSD due to the resistor $R_{eff}$ referred to the diaphragm.

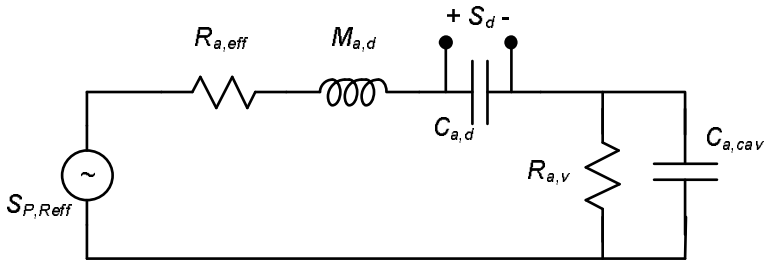


Figure 3-40. Acoustic noise model for $R_{eff}$.

Considering only the noise due to the vent resistor, the noise model is drawn as in Figure 3-41. The volume velocity PSD through the diaphragm due to $S_{Q_{R_v}}$ is found using a volume velocity divider,

$$S_{Q_d} = \left|\frac{R_{a,v}\,//\,C_{a,cav}\,//\,Z_d}{Z_d}\right|^2 \cdot S_{Q,R_v}, \tag{3–209}$$

where $Z_d$ is the series impedance of the diaphragm mass, diaphragm compliance, and effective resistance. Solving for the parallel impedance in the numerator and simplifying, Equation 3–209 becomes

$$S_{Q_d} = \left|\frac{R_{a,v}}{R_{a,v}+Z_d+sR_{a,v}C_{a,cav}}\right|^2 \cdot S_{Q,R_v}, \tag{3–210}$$

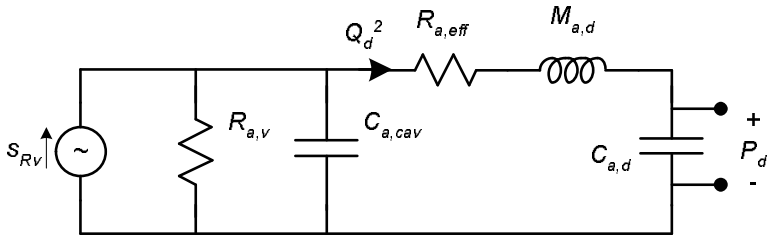


Figure 3-41. Acoustic noise model for $R_v$.

The pressure noise across the diaphragm capacitance due to the volume velocity noise given in Equation 3–210 is $S_{P,d_{R_v}} = \left|Q_d/sC_{a,d}\right|^2$,

$$S_{d_{R_v}} = \frac{R_{a,v}^2}{\left| \begin{array}{l} s^3 M_{a,d} C_{a,d} C_{a,cav} R_{a,v} \\ +s^2 \left[ M_{a,d} C_{a,d} + C_{a,d} C_{a,cav} R_{a,eff} R_{a,v} \right] \\ +s \left[ R_{a,eff} C_{a,d} + R_{a,v} \left( C_{a,cav} + C_{a,d} \right) \right] + 1 \end{array} \right|^2} \cdot S_{Q,R_v} \quad . \tag{3–211}$$

The two noise quantities given in Equation 3–208 and Equation 3–211 are plotted in Figure 3-42 for an example microphone. When referring the noise sources to the diaphragm, the noise sources are shaped by the dynamics of the microphone, as represented by the LEM. The noise due to $R_{a,eff}$ is flat between the cut-on frequency and resonant frequency of the microphone. However, the noise PSD due to the vent resistor is proportional to $1/f^2$ in the same frequency range. Thus, the vent resistor has the potential to be the dominant acoustic noise source for low frequencies.

At low frequencies, the pressure noise PSD due to $R_{a,eff}$ approaches $S_{P,R_{eff}}$; meaning that the total noise due to effective resistance appears across the diaphragm. Similarly, at low frequencies, the volume velocity noise PSD due to $R_{a,v}$ approaches the value of $R_{a,v}^2 \cdot S_{Q,R_v}$. At high frequencies both of the noise sources are shaped by the resonant peak and roll off after the resonance.

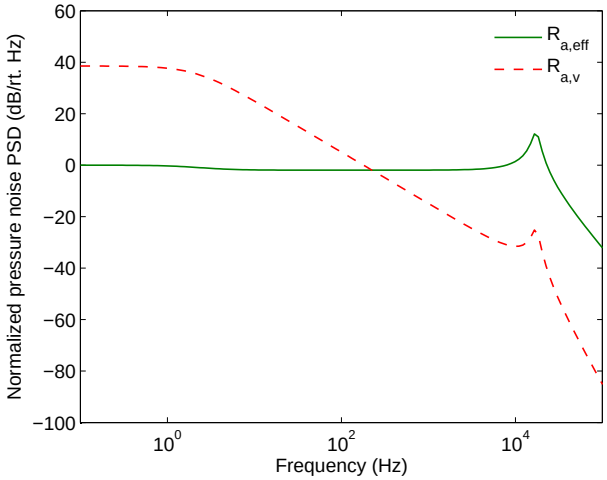


Figure 3-42. Theoretical noise contributions of a microphone example referred to the pressure across the diaphragm.

### 3.3.2 Interface Circuit Noise

As was discussed in Section 3.1.2, capacitive microphones may be used with various types of interface circuitry; in particular, a charge amplifier or a voltage amplifier. In this section, the noise of both circuits is discussed.

#### 3.3.2.1 Charge amplifier

A model of the charge amplifier, including noise sources, is shown in Figure 3-43. The charge amplifier consists of an operational amplifier with resistor, $R_{fb}$, and a capacitor, $C_{fb}$, in the feedback loop. At the input of the amplifier is a bias resistor, $R_b$, and a capacitor, $C_{tot}$, that represents the total capacitance at the input to the amplifier. This includes the device capacitance as well as any parasitic capacitance. The internal amplifier is modeled by a voltage noise and a current noise, $S_{va}$ and $S_{ia}$, respectively. The bias resistor and feedback resistor are both modeled by current noise sources, $S_{i_{R_{fb}}}$ and $S_{i_{R_b}}$, respectively.

The total noise at the output is the sum of the contributions from each of the noise sources and is found using superposition. To simplify the expressions, the impedances $Z_{fb}$ and $Z_i$ are defined. These are the feedback impedance and input

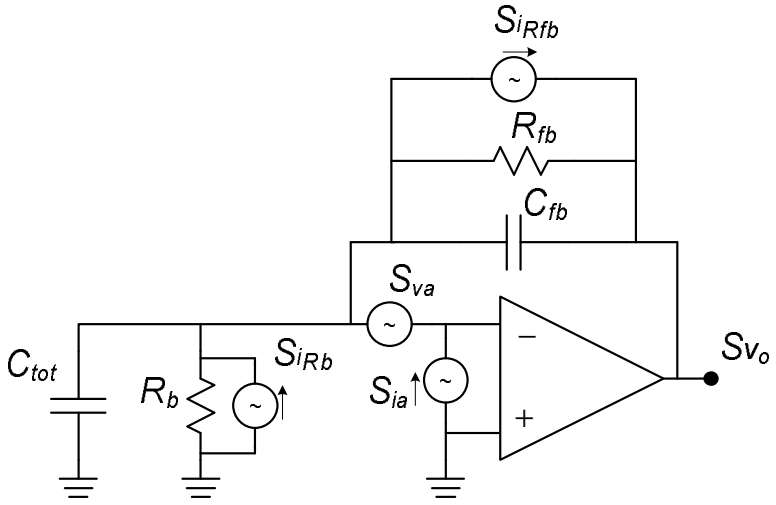


Figure 3-43. Noise model of the charge amplifier coupled to the microphone.

impedance and are given by

$$Z_{fb} = R_{fb} \Big/\!\Big/ C_{fb} = \frac{R_{fb}}{1 + sC_{fb}R_{fb}}, \tag{3–212}$$

and

$$Z_i = R_b \Big/\!\Big/ C_{tot} = \frac{R_b}{1 + sC_{tot}R_b}, \tag{3–213}$$

respectively.

The output noise PSD of the charge amplifier due to the electrical noise sources is

$$S_{v_{oCA}} = S_{va}\left|1 + \frac{Z_{fb}}{Z_i}\right|^2 + |Z_{fb}|^2\left[S_{ia} + S_{i_{R_{fb}}} + S_{i_{R_b}}\right]. \tag{3–214}$$

The voltage noise PSD of the amplifier scaled by the factor $|1 + Z_{fb}/Z_i|^2$. The current noise PSD of the amplifier and the two resistors added together are all scaled by the magnitude of the feedback impedance squared. At frequencies above $1/2\pi C_{fb}R_{fb}$ and $1/2\pi C_{tot}R_b$, which is the typically the frequency range of interest for a charge amplifier, Equation 3–214 is simplified to

$$S_{v_{oCA}} = S_{va}\left(1 + \frac{C_{tot}}{C_{fb}}\right)^2 + \left|\frac{1}{sC_{fb}}\right|^2\left[S_{ia} + S_{i_{R_{fb}}} + S_{i_{R_b}}\right]. \tag{3–215}$$

The higher the capacitance $C_{tot}$, the higher the contribution due to $S_{va}$. While a high device capacitance is beneficial for sensitivity, parasitic capacitance increases the noise at the output of the charge amplifier. The current noise PSD is scaled by a factor of $|1/sC_{fb}|^2$. This frequency-shapes the current noise spectrum such that the noise PSD at the output is proportional to $1/f^2$. Furthermore, this is twice the slope of electronic flicker (1/f) noise [19]. Therefore, the current noise is dominant at low frequencies.

#### 3.3.2.2 Voltage amplifier

The noise model for a voltage amplifier is shown in Figure 3-44. The noise sources include the amplifier and bias resistor. Similar to the charge amplifier, the total impedance at the input to the amplifier is $Z_i$, given by Equation 3–213.

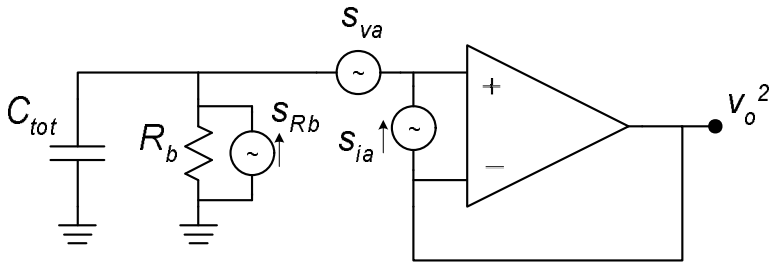


Figure 3-44. Noise model of the voltage amplifier coupled to the microphone.

The voltage noise PSD at the output is

$$S_{v_{o_{VA}}} = S_{va} + |Z_i|^2 \left[ S_{ia} + S_{i_{R_b}} \right]. \tag{3–216}$$

As was the case with the charge amplifier, the current noise PSD from the amplifier and bias resistor add and are scaled by the magnitude of the input impedance squared. A high frequency approximation to Equation 3–214 is

$$S_{v_{o_{VA}}} = S_{va} + \left| \frac{1}{sC_{tot}} \right|^2 \left[ S_{ia} + S_{i_{R_b}} \right]. \tag{3–217}$$

Therefore, the voltage amplifier has the potential to exhibit noise shaping due to the capacitance $C_{tot}$, similar to the $(1/f^2)$ noise seen in the charge amplifier. In this

case, a higher parasitic capacitance would reduce the contribution of the current noise sources by increasing $C_{tot}$. Furthermore, both the voltage noise and current noise must be considered when selecting a voltage amplifier.

# CHAPTER 4
# DESIGN AND THEORETICAL PERFORMANCE

In the previous chapter, the theory of operation of the microphone was discussed. Using the developed theory, the design of the dual backplate capacitive microphone is presented. This is followed by the theoretical microphone performance.

## 4.1 Microphone Design

The dual-backplate microphone was designed to meet the specifications given in Table 1-1 for an aeroacoustic microphone. The microphone was designed specifically to be fabricated using the SUMMiT V process at Sandia National Laboratories [16]; this process is described in detail in Appendix D. The use of this process imposes several constraints on the design; specifically, the thickness and residual stress of each layer are not free to be specified. In this section, the use of the SUMMiT V process flow to create the dual-backplate microphone structure is discussed first. Then the design for the diaphragm and the backplates is presented.

### 4.1.1 Microphone Structure

The layers that are available in the SUMMiT V process are shown in Figure D-1. The polysilicon layers must be patterned to create a device similar in structure to that shown in Figure 3-1. The sacrificial oxide layers are used to support the polysilicon layers during fabrication, but are then removed at the end of the process; thus they cannot be used as structural layers.

There are three polysilicon layers that are used for the microphone structure: Poly4 is used for the top backplate; Poly3 is used for the diaphragm; and the Poly2/Poly1 laminate is used for the bottom backplate. The top air gap is created from SacOx4 and the bottom air gap is created from SacOx3. In the dual-backplate structure depicted in Figure 2-11(a), which is similar to the microphone developed by Rombach et al. [47], the diaphragm is separated from the backplates by insulating layers. This is not the best arrangement for the SUMMiT V process

because only silicon dioxide could be used for the insulating layers and the silicon dioxide is etched during release. Therefore, for this microphone, anchors are created such that both backplates and the diaphragm are supported as shown in Figure 4-1. In this arrangement, the backplates and diaphragm are essentially concentric shells.

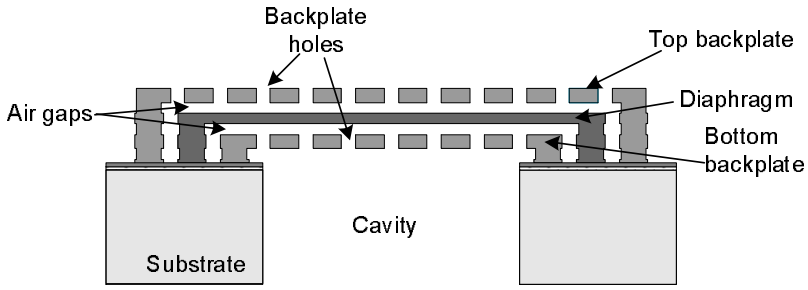


Figure 4-1. Cross section of the designed dual-backplate microphone.

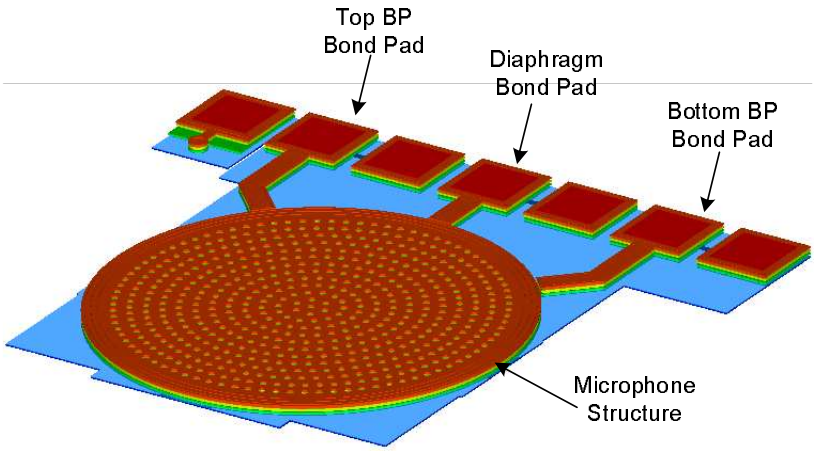


Figure 4-2. Microphone 3-D view.

The microphone is shown from the top in Figure 4-2. From this view, the diaphragm and bottom backplate are not visible. The bond pads for the diaphragm and both backplates are labeled. The other bond pads may be used to connect to the substrate and to null out the parasitic capacitance underneath the three connections to the diaphragm and backplates.

Additional details of the microphone structure are shown in Figure 4-3. The anchors for the bottom backplate, diaphragm, and top backplate are shown in

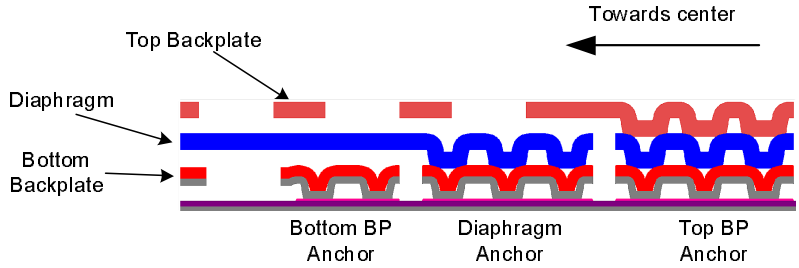


(a) Cross section showing the details of the anchor structure.

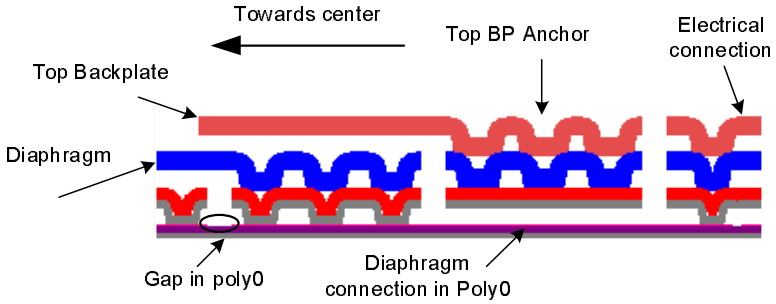


(b) Cross section showing the details of the electrical connection from the diaphragm to the bond pad.

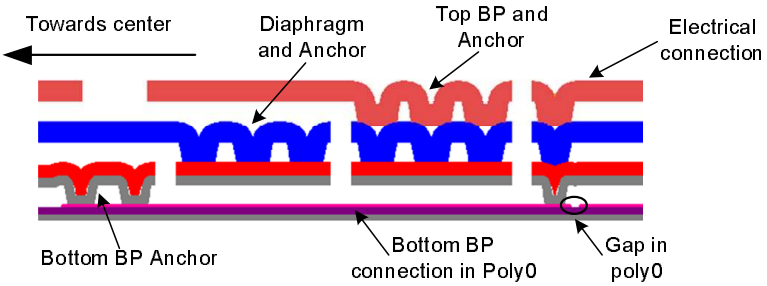


(c) Cross section showing the details of the electrical connection from the bottom backplate to the bond pad.

Figure 4-3. Details of the anchors and electrical connections are shown.

Figure 4-3(a). The polysilicon layers are stacked to construct the anchors for the diaphragm and backplate. To make electrical connections to the bottom backplate and diaphragm, tunnels are fabricated in the anchors. The electrical connection to the diaphragm is shown in Figure 4-3(b). The Poly0 layer of polysilicon connects the diaphragm anchor to the bond pad; above this connection, the top backplate anchor does not make contact with Poly0 in this region. A similar geometry was used for the connection to the bottom backplate as shown in Figure 4-3(c). Here,

the anchors for both the diaphragm and top backplate do not extend down to Poly0.

After the implementation strategy for the SUMMiT V process is developed, the specific dimensions of the microphone are then designed. Due to the constraints of the SUMMiT V process, the parameters that are free to be chosen are the diameter of the diaphragm and the backplate hole geometry.

### 4.1.2 Diaphragm Design

The diaphragm is designed such that deflection will be at most 3 % non-linear at an incident pressure of 2000 $Pa$. The previously derived results from Section 3.1.1 are used here.

The percent nonlinear deflection is defined as

$$\%NL = \frac{w_L(0) - w_{NL}(0)}{w_L(0)} \times 100, \tag{4–1}$$

where $w_L(0)$ is the linear center deflection of the diaphragm and $w_{NL}(0)$ is the nonlinear center deflection of the diaphragm. By substituting Equation 3–8 and Equation 3–9 into Equation 4–1 and setting the percent nonlinearity to 3 %, the following is obtained,

$$1 - \frac{1}{1 + 0.488\frac{w(0)^2}{h^2}} = 0.03. \tag{4–2}$$

Solving Equation 4–2 gives a constraint for the ratio of the center deflection to the diaphragm thickness,

$$\frac{w(0)}{h} = 0.25. \tag{4–3}$$

This result is general for a homogeneous, circular, stress-free plate; when the magnitude of the center deflection is equal to 25 % of the thickness of the plate, the deflection is 3 % nonlinear. Substituting Equation 4–3 into Equation 3–9 results in the following

$$\frac{w(0)}{h} = \frac{3pa^4(1-\nu^2)}{16Eh^4} = 0.25\,. \tag{4–4}$$

The material constants $\nu$ and $E$, and the diaphragm thickness $h$ are fixed; therefore, the diaphragm radius is found from Equation 4–4. Using the values given in Table 4-1 for $\nu$, $E$, and $h$, the diaphragm radius is chosen to be 230 $\mu m$; the aspect ratio of the diaphragm is 102.

### 4.1.3 Backplate Design

The design of the backplate holes is not as direct as the diaphragm design. There are many considerations and trade-offs for the backplate design:

- Low damping to limit backplate deflection due to acoustic pressure
- Reduced mechanical stiffness of the backplates due to holes
- Loss of electrical capacitance due to loss of backplate area
- Sufficient number of holes for the release etch

As was discussed in Section 3.2.6, if the backplate is too compliant, there are negative effects in the frequency response. A simplified model of the top backplate and the diaphragm is shown in Figure 4-4; this analysis is general for either backplate. The pressure drop across the backplate is compared to that across the diaphragm. For this analysis, only the impedance of the backplate and the diaphragm compliance are considered.

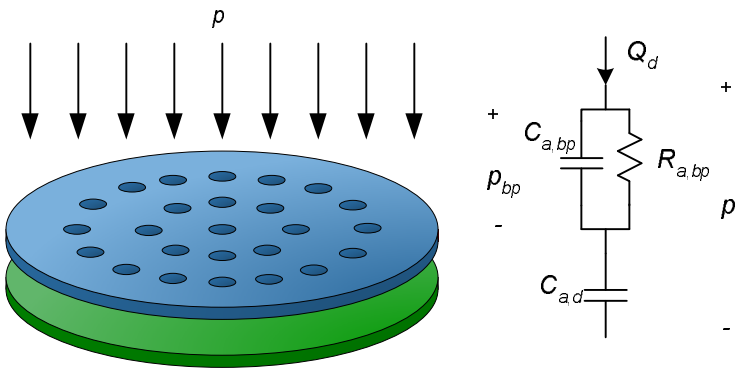


Figure 4-4. Simplified model of the diaphragm and top backplate

The backplate is represented by a compliance and a resistance in parallel; the backplate model is in series with the compliance of the diaphragm. As shown in the

figure, the uniform pressure loading, $p$, results in a volume velocity, $Q$, through the backplate and diaphragm. This equivalent circuit can be treated as a "pressure" divider, where the pressure across the backplate is given by

$$p_{bp} = p\frac{Z_{a,bp}}{Z_{a,bp} + Z_{a,d}}. \tag{4–5}$$

Similarly, the pressure across the diaphragm is given by

$$p_d = p\frac{Z_{a,d}}{Z_{a,bp} + Z_{a,d}}. \tag{4–6}$$

The deflection of a compliance due to a uniform pressure load is given in Equation 3–189; this deflection is proportional to the pressure across the compliance. It can be seen from Equation 4–5 that the pressure across the backplate is small as long as $Z_{a,bp}$ is much less than $Z_{a,d}$. Therefore, if this condition is met, the deflection of the backplate will be negligible. The impedance of the backplate is given by

$$Z_{a,bp} = \frac{R_{a,bp}}{1 + j\omega R_{a,bp}C_{a,bp}}. \tag{4–7}$$

As long as $\omega$ is less than $1/(R_{a,bp}C_{a,bp})$, the backplate impedance approximately equals $R_{a,bp}$. Therefore, the backplate deflection due to an acoustic pressure is negligible if the backplate resistance is less than the impedance of the diaphragm and if the frequency of operation is less than the critical frequency for each backplate,

$$f_{bp} = \frac{1}{2\pi R_{a,bp}C_{a,bp}}. \tag{4–8}$$

The backplates must be designed with a sufficient number of holes so that $f_{bp}$ for each backplate is well above the desired frequency range of operation.

However, as stated above, there are several other trade-offs. If there are too many backplate holes, the backplate compliance is greater than that predicted assuming there are not any backplate holes. Furthermore, as backplate area is lost due to the holes, the capacitance is reduced. However, if the hole radius is small

enough, fringing fields reduce the capacitance loss. Another consideration is that the backplate holes serve as the path for the etchant to remove the oxide from the air gaps; enough holes of sufficient radius must be provided for this etch.

The backplate geometry that was found to best balance these tradeoffs while providing a sufficiently small backplate resistance was to use backplate holes with a radius of 5 $\mu m$ with a total area of approximately 22 % of the backplate area. For the top backplate, 557 holes were used and 367 holes were used for the bottom backplate. This backplate hole configuration resulted in an $f_{bp}$ for the top and bottom backplates of 1.3 $MHz$ and 3.3 $MHz$, respectively.

### 4.1.4 Microphone Design Summary

The dual-backplate microphone was designed for the SUMMiT V process. It has been designed to operate linearly up to an incident pressure of 2000 $Pa$. The backplates were designed such that they would not have excessive deflection due to an acoustic pressure while not sacrificing too much capacitance due to the area lost by the holes. A summary of the physical properties of the microphone is given in Table 4-1.

## 4.2 Predicted Microphone Performance

Using the theory developed in Chapter 3 and the design parameters given in Table 4-1, the predicted microphone performance specifications are found, including the uncertainty in these estimates.

The uncertainty analysis for the sensitivity, resonant frequency, and noise floor is derived in Appendix C. The uncertainty values used for the thickness of the diaphragm and air gaps are taken from Table D-1. Sandia National Laboratories reports dimensional uncertainty of 0.1 $\mu m$ for line widths. This translates into the uncertainty in the diaphragm radius. Material parameters are assumed to have a 10 % variation.

Table 4-1. Microphone physical properties

| Symbol | Property | Value | Units |
|---|---|---|---|
| $E$ | Young's Modulus | 160 | $GPa$ |
| $\nu$ | Poisson's Ratio | 0.2 | - |
| $\rho$ | Density of polysilicon | 2330 | $kg/m^3$ |
| $\sigma_0$ | In-plane stress | 0 | $Pa$ |
| $a_d$ | Diaphragm radius | 230 | $\mu m$ |
| $h_d$ | Diaphragm thickness | 2.25 | $\mu m$ |
| $a_{bp1}$ | Top backplate radius | 256 | $\mu m$ |
| $h_{bp1}$ | Top backplate thickness | 2.25 | $\mu m$ |
| $a_{bp2}$ | Bottom backplate radius | 213 | $\mu m$ |
| $h_{bp2}$ | Bottom backplate thickness | 2.25 | $\mu m$ |
| $g$ | Gap distance | 2.0 | $\mu m$ |
| $a_h$ | Backplate hole radius | 5.0 | $\mu m$ |
| $N_1$ | Number of top backplate holes | 557 | - |
| $N_2$ | Number of bottom backplate holes | 367 | - |

### 4.2.1 Sensitivity

The predicted sensitivity of the dual-backplate condenser microphone is found for a directly applied bias and a bias applied through a resistor. The output voltage found in Section 3.1.2 gives the sensitivity from the pressure on the diaphragm, $p_d$, to an output voltage. However, the attenuation due to the cavity compliance also affects the sensitivity, as given by Equation 3–184. To simplify the expressions for the sensitivity, it is assumed that the nominal capacitances of the top and bottom capacitors are equal and the frequency of operation is in the flat-band region.

Therefore, the sensitivity for a dual-backplate capacitive microphone with a constant voltage bias is given by

$$S\Big|_{V_B} = \frac{2}{3}\frac{V_B}{g_0}\frac{C_{1_0}}{C_f}\frac{a^4}{64D}\frac{C_{a,cav}}{C_{a,cav}+C_{a,d}}. \tag{4–9}$$

Similarly, the sensitivity with a constant charge bias is

$$S\Big|_{Q_B} = \frac{1}{3} H_c \frac{V_B}{g_0} \frac{a^4}{64D} \frac{C_{a,cav}}{C_{a,cav} + C_{a,d}}. \tag{4–10}$$

The sensitivities may also be written in terms of the transformer turns ratios, $n_1$ and $n_2$, as

$$S\Big|_{V_B} = \frac{C_{a,cav}}{C_{a,cav} + C_{a,d}} (n_1 + n_2) \frac{C_{1_0}}{C_f}. \tag{4–11}$$

and

$$S\Big|_{Q_B} = \frac{C_{a,cav}}{C_{a,cav} + C_{a,d}} (n_1 + n_2) \frac{C_{1_0}}{C_{1_0} + C_{2_0} + C_p + C_i}. \tag{4–12}$$

The sensitivity for the designed microphone is found by evaluating these expressions with the values given in Table 4-1 and a bias voltage of 9.3 $V$ (the value used for experimentation). The predicted sensitivity for the designed dual-backplate capacitive microphone with a directly applied bias voltage and a 1.5 $pF$ feedback capacitor is

$$S\Big|_{V_B} = 370 \pm 190 \ \mu V/Pa, \tag{4–13}$$

where the uncertainty is calculated using Equation C–12. Similarly, for the same microphone with bias voltage applied through a large resistor and a total parasitic capacitance of 1 $pF$, the predicted sensitivity is

$$S\Big|_{Q_B} = 220 \pm 100 \ \mu V/Pa. \tag{4–14}$$

The large uncertainty in sensitivity is due to the use of chemical mechanical polishing in the SUMMiT V process. This gives a variation of up to 25 % in the thickness of the air gaps. This results in an uncertainty of close to 50 % in the sensitivity estimates.

### 4.2.2 Frequency Response

In this section, the frequency response of the designed microphone is discussed. The frequency response is plotted using the previously derived lumped element

model. The cut-on frequency, resonant frequency, damping ratio, and flat band attenuation are also found.

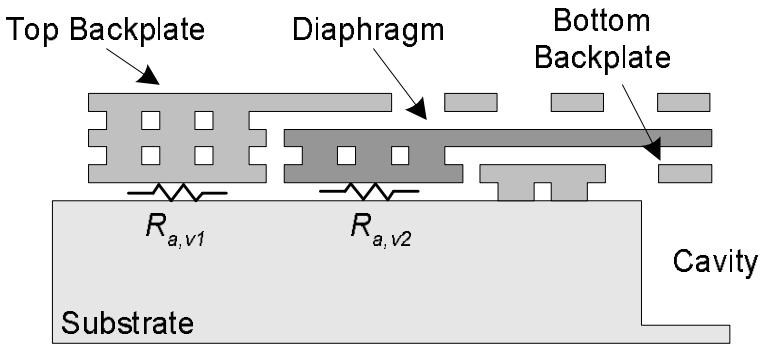


Figure 4-5. Cross section of the vent channel. There are two components: one is in parallel with the top backplate and the other connects to the cavity.

All of the lumped elements are computed using the parameters given in Table 4-1 except the vent resistance. The vent channel is created by the channel for electrical connections to the anchors for the diaphragm and bottom backplate. After the microphone is released, the sacrificial oxide is removed and the channel is opened. The geometry of the vent channel is shown in Figure 4-5. Two resistances are shown: $R_{a,v1}$ which connects the outside to a point between the top backplate and diaphragm; and $R_{a,v2}$ which connects to the cavity. The width of the vent channel is 42 $\mu m$ and the height is 2 $\mu m$. The hydraulic diameter of the channel is given by $4A/P$, where $A$ and $P$ are the cross-sectional area and perimeter of the channel, respectively [123]; for this geometry, the vent channel has a hydraulic diameter of 3.8 $\mu m$. There is not a significant resistance above the bottom backplate anchor because the restricted width of the vent channel extends only to the end of the diaphragm anchor. The length of the first part of the channel is 24 $\mu m$ and the length of the second part is 23 $\mu m$. The resistance $R_{a,v1}$ is in parallel with the top backplate, therefore it does not contribute significantly to the frequency response.

Table 4-2. Acoustic lumped element values for the designed microphone.

| Symbol | Description | Value | Units |
|---|---|---|---|
| $C_{a,d}$ | Diaphragm compliance | $1.53 \times 10^{-17}$ | $\frac{m^5}{N}$ |
| $M_{a,d}$ | Diaphragm mass | $5.68 \times 10^{4}$ | $\frac{kg}{m^4}$ |
| $C_{a,bp1}$ | Top backplate compliance | $2.91 \times 10^{-17}$ | $\frac{m^5}{N}$ |
| $R_{a,bp1}$ | Top backplate resistance | $4.19 \times 10^{9}$ | $\frac{Ns}{m^5}$ |
| $C_{a,bp2}$ | Bottom backplate compliance | $7.04 \times 10^{-18}$ | $\frac{m^5}{N}$ |
| $R_{a,bp2}$ | Bottom backplate resistance | $6.95 \times 10^{9}$ | $\frac{Ns}{m^5}$ |
| $C_{a,cav}$ | Cavity compliance | $5.06 \times 10^{-16}$ | $\frac{m^5}{N}$ |
| $R_{a,v}$ | Vent resistance | $7.54 \times 10^{13}$ | $\frac{Ns}{m^5}$ |
| $n_1$ | Top turns ratio | $-4.15 \times 10^{-4}$ | $\frac{V}{Pa}$ |
| $n_2$ | Bottom turns ratio | $-4.15 \times 10^{-4}$ | $\frac{V}{Pa}$ |

The predicted frequency response is found using the lumped element values given in Table 4-2 and is shown in Figure 4-6. It can be seen that the backplate compliance has a negligible effect on the microphone frequency response.

Finally, the values for the cut-on frequency, damping ratio, damped resonant frequency, and flat band attenuation are given in Table 4-3. The microphone has a predicted bandwidth from 4 $Hz$ to 173$\pm$9 $kHz$. It is lightly damped, with a damping ratio of 0.09. The low variation in the predicted resonant frequency is due to the fact that the resonant frequency does not depend on the air gap.

Table 4-3. Frequency response parameters

| Description | Value |
|---|---|
| Cut-on frequency | 4 $Hz$ |
| Damping ratio | 0.09 |
| Resonant frequency | 173 $kHz$ |
| Flat band attenuation | 0.97 |

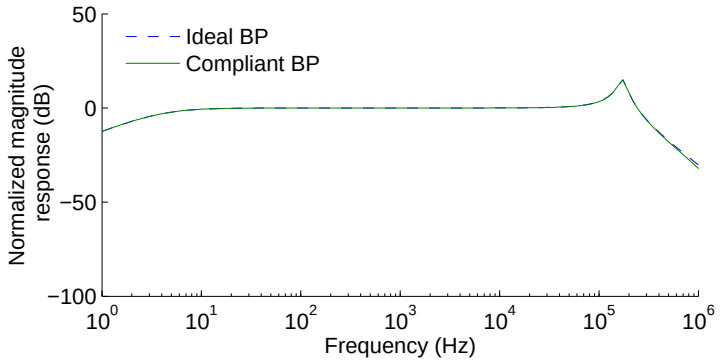


(a) Normalized magnitude response of the designed microphone.

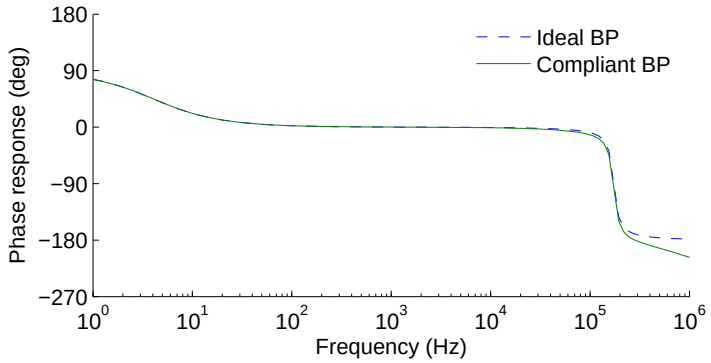


(b) Phase response of the designed microphone.

Figure 4-6. Frequency response of the designed dual-backplate microphone as predicted by the LEM.

### 4.2.3 Noise Floor

The noise floor of the microphone is predicted using the models developed in Section 3.3. There are two components to the noise floor, the thermomechanical noise of the microphone and the electrical noise of the interface circuitry.

The PSD of the acoustic noise source referred to the diaphragm is plotted in Figure 4-7. The noise due to $R_{a,eff}$ and $R_{a,v}$ is shown. Below approximately 400 $Hz$, the noise from the vent resistor is the larger of the two acoustic noise sources.

The theoretical output voltage noise PSD of the microphone packaged with a charge amplifier is shown in Figure 4-8. The contributions from the acoustic noise sources, bias resistor, and amplifier are shown. The charge amplifier considered

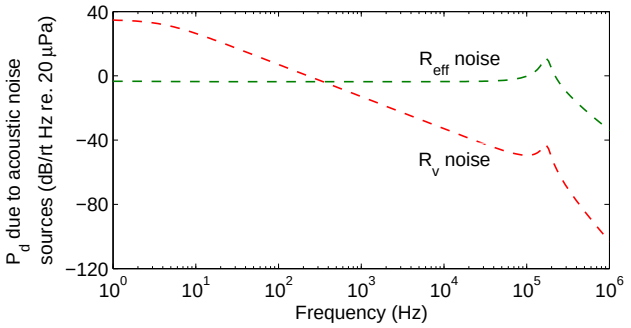


Figure 4-7. Theoretical noise contributions of the microphone referred to the pressure across the diaphragm.

here is based on the TLE2071 opamp manufactured by Texas Instruments. This amplifier is configured as a charge amplifier by placing a 1 $pF$ capacitor and a 2 $G\Omega$ resistor in the feedback path. Parasitic capacitance on the circuit board results in a net feedback capacitance of 1.5 $pF$. The input referred voltage noise of the amplifier is 17 $nV/\sqrt{Hz}$ and the input referred current noise is 2.8 $fA/\sqrt{Hz}$. Below 10 $kHz$, the noise spectrum is dominated by the current noise of the bias resistor. At 1 $kHz$, the predicted output PSD is $2.3 \times 10^{-13}$ $V^2/Hz$. This is equivalent to an input referred noise of 36 $dB/\sqrt{Hz}$ assuming a sensitivity of 370 $\mu V/Pa$. Considering the uncertainty in the sensitivity, the input referred noise floor is expected to vary by up to $\pm 3.5$ $dB/\sqrt{Hz}$.

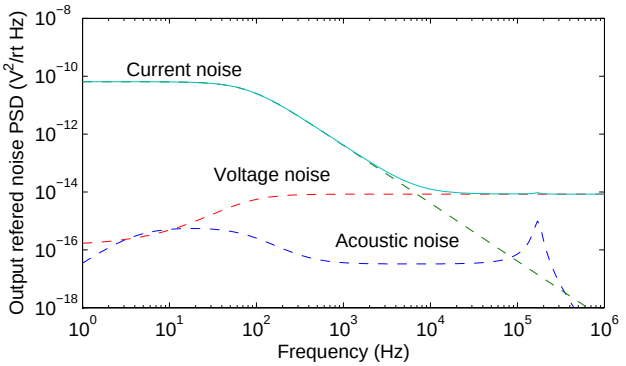


Figure 4-8. Theoretical output voltage noise PSD of the microphone with a charge amplifier.

The theoretical noise floor of the microphone packaged with a voltage amplifier is shown in Figure 4-9. The selected voltage amplifier is the SiSonic microphone amplifier, courtesy of Knowles Acoustics. A noise model was not provided, however, measurements of the voltage amplifier give a voltage noise density of $4 \times 10^{-16}\ V^2/Hz$ and a current noise density of $5 \times 10^{-31}\ A^2/Hz$. The acoustic noise is below the electrical noise for the majority of the frequency range, except near resonance; as can be seen from Figure 4-9. At 1 $kHz$, the predicted output voltage PSD for the microphone packaged with the voltage amplifier is $2.1 \times 10^{-15}\ V^2/Hz$. This is equivalent to an input referred noise of 20 $dB/\sqrt{Hz}$ assuming a sensitivity of 220 $\mu V/Pa$. The noise floor of the microphone with a voltage amplifier is expected to vary by as much as $\pm 4.0\ dB/\sqrt{Hz}$.

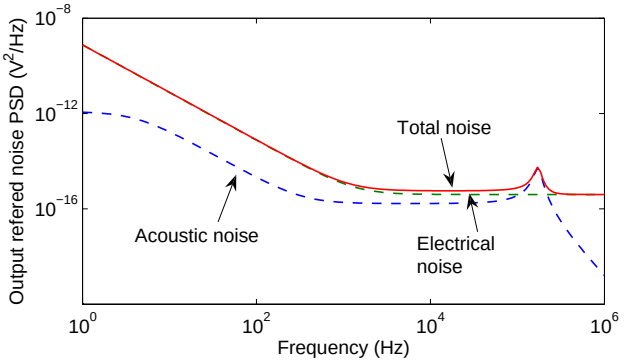


Figure 4-9. Theoretical output noise PSD of the microphone with a voltage amplifier.

### 4.2.4 Pull-in Voltage

The pull-in voltages for the designed dual-backplate microphone are found using the parameters given in Table 4-1 and the equations in Section 3.2.7. For comparison, the pull-in voltages of a single-backplate capacitive microphone with the same diaphragm and air gap dimensions are calculated.

The quasi-static pull-in voltage for the single-backplate condenser microphone is $V_{PI} = 31\ V$. The quasi-static pull-in voltage for the dual-backplate condenser

backplate microphone is

$$V_{PI} = 40\ V. \tag{4–15}$$

## 4.3 Summary

A dual-backplate microphone has been designed for aeroacoustic measurements. The target process flow is the SUMMiT V process at Sandia National Laboratories. The microphone has been designed to have a linear response up to 2000 $Pa$. The predicted sensitivity, frequency response, noise floor, and pull-in voltage have been found.

A summary of the specifications for the designed dual-backplate condenser microphone is given in Table 4-4 along with the predicted uncertainty.

Table 4-4. Summary of specifications for the designed microphone

| Specification | Value | Uncertainty |
|---|---|---|
| Sensitivity (CA) | 370 $\mu V/Pa$ | $\pm$ 190 $\mu V/Pa$ |
| Sensitivity (VA) | 220 $\mu V/Pa$ | $\pm$ 100 $\mu V/Pa$ |
| Resonant frequency | 173 $kHz$ | $\pm$ 9 $kHz$ |
| Noise floor (CA) | 36 $dB$ | $\pm$ 3.5 $dB$ |
| Noise floor (VA) | 20 $dB$ | $\pm$ 4.0 $dB$ |

# CHAPTER 5
# DEVICE FABRICATION

The fabrication of the dual-backplate capacitive microphone is presented in this chapter. The microphone fabrication utilized both the SUMMiT V process at Sandia National Laboratories and facilities at the University of Florida. The process flow is presented in two parts; the SUMMiT V fabrication and the post processing.

## 5.1 Process Flow

The SUMMiT V process at the Sandia National Laboratories was used to fabricate the structural layers of the microphone. This process, described in detail in Appendix D, mainly consists of the deposition and patterning of alternating layers of polysilicon and silicon dioxide. Polysilicon is used to form the microphone structure. Silicon dioxide is a temporary, or sacrificial, material to support the various layers of polysilicon during fabrication. After completion of the SUMMiT V process, a series of post processing steps are performed to release the device and complete the fabrication.

### 5.1.1 SUMMiT V Process Steps

The fabrication of the microphone through the completion of the SUMMiT V process is shown in Figure 5-1. The process flow is depicted as a series of schematic cross sections through the center of the microphone.

The SUMMiT V process begins with a 6 $in.$ silicon wafer. As shown in Figure 5-1(b), a layer of silicon dioxide and silicon nitride are then deposited. These insulate the polysilicon structure from the silicon substrate. In addition, the silicon nitride is used to provide adhesion for the polysilicon. The first layer of polysilicon, Poly0, is then deposited. This polysilicon layer is used to form a base for the anchors and for electrical interconnections.

The fabrication of the bottom air gap and diaphragm are shown in Figure 5-1(d) and Figure 5-1(e), respectively. A 2 $\mu m$ layer of sacrificial oxide forms a spacer


(a) Begin with 650 $\mu m$ thick silicon substrate.


(b) Deposit insulation layers of silicon dioxide and silicon nitride.

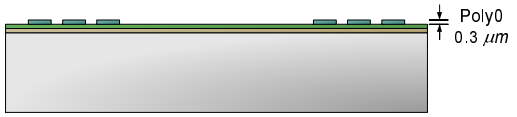


(c) Deposit the first polysilicon layer.

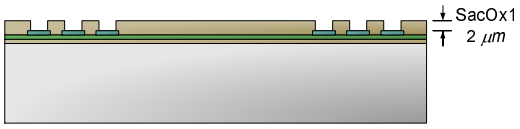


(d) Deposit and pattern a layer of sacrificial oxide.

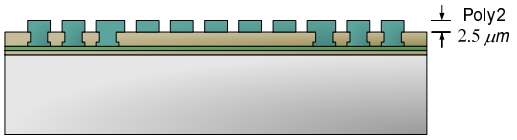


(e) Deposit polysilicon and pattern to form bottom backplate.

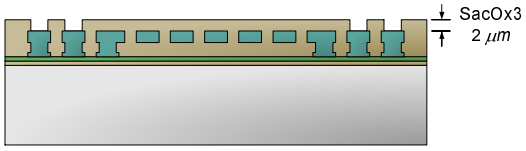


(f) Deposit and pattern sacrificial oxide that will create the bottom air gap.

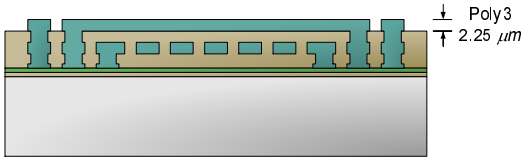


(g) Deposit polysilicon and pattern to form diaphragm.

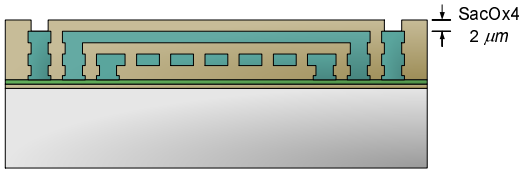


(h) Deposit and pattern sacrificial oxide for the top air gap.

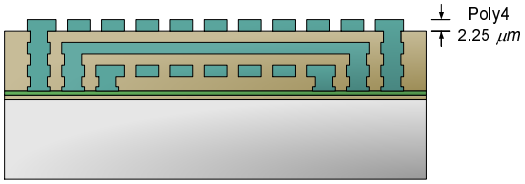


(i) Deposit polysilicon and pattern to form top backplate.

Figure 5-1. Process steps of the microphone fabrication through the completion of the SUMMiT V process.

between the Poly0 electrical connections and the next layer of polysilicon. The bottom backplate is formed by depositing and patterning Poly2. The bottom air gap space is held by the next sacrificial layer, Sacox3. The diaphragm is then formed from Poly3, as shown in Figure 5-1(g). The final steps of the SUMMiT V process create the top backplate, as shown in Figure 5-1(h) and Figure 5-1(i).

### 5.1.2 Post-SUMMiT V Process Steps

The remainder of the device fabrication after completion of the SUMMiT V process was conducted at the University of Florida. The key steps, represented by

schematic cross sections, are shown in Figure 5-2. To complete the fabrication of the microphone, the following steps are completed: deposit metal for bondpads; etch the silicon substrate; etch the oxide and nitride layers; and etch the sacrificial oxide. Although it was not shown in Figure 5-1 for simplicity, each of the layers that were deposited on the front surface of the silicon wafer during the SUMMiT V process were also deposited on the backside of the wafer. These layers are removed before the microphone cavity is formed.

The devices were returned from Sandia National Laboratories as unreleased die. To facilitate the post processing, a handle wafer is used to support the individual microphone die during processing. To construct the handle wafer, AZ9260 photoresist is spun on a 100 $mm$ Pyrex wafer at 4000 $RPM$, resulting in a thickness of approximately 4 $\mu m$. A 100 $mm$ silicon wafer is placed on the photoresist covered Pyrex wafer and pressure is applied by hand to join the two wafers together, as shown in Figure 5-2(a). The AZ9260 photoresist is then spun on the top of the silicon wafer at 2000 $RPM$, resulting in a thickness of approximately 9 $\mu m$. The photoresist is patterned and a cavity is etched via DRIE in the handle wafer to hold the microphone die, as depicted in Figure 5-2(b).

The microphone die is mounted in an inverted position into the handle wafer using Crystalbond 509, a thermoplastic polymer adhesive, as shown in Figure 5-2(c). The thermoplastic adhesive allows the microphone die to be inserted and removed by elevating the temperature of the adhesive, yet it provides a strong bond during handling. Mechanical lapping is performed to remove the backside layers. A slurry is created on the surface of a glass plate by mixing 5 $\mu m$ grit polishing powder with water. The microphone die, supported by the handle wafer, is lightly pressed onto the slurry coated plate and moved in a figure-8 pattern. This removes the backside of the microphone die until the surface of the die is flush with the surface of the handle wafer, at which point the lapping is complete. The remaining


(a) Begin by joining a silicon wafer to a Pyrex wafer with photoresist.

(b) Etch a cavity in the silicon to hold the microphone die using DRIE.

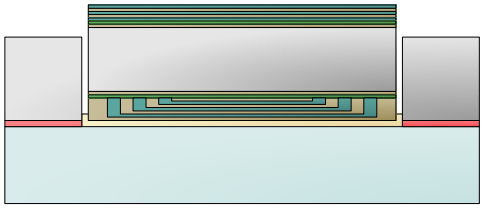

(c) Attach the microphone die to the handle wafer.

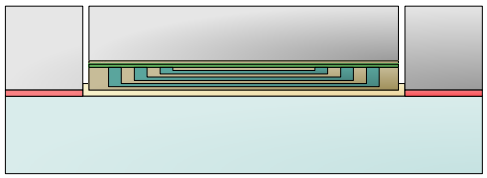

(d) Remove backside layers via mechanical lapping.

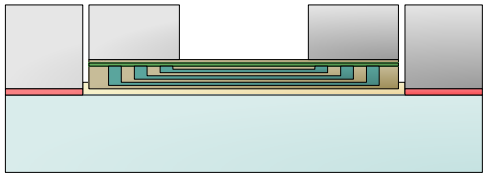

(e) Etch the silicon substrate of the microphone die using DRIE.

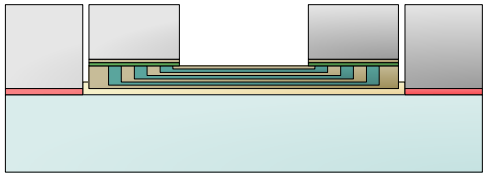

(f) Etch thin oxide layer using BOE and a silicon nitride etch using RIE.

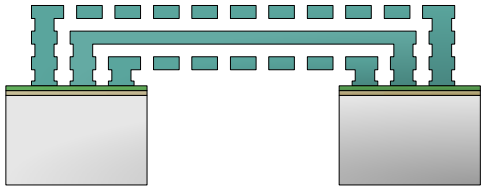

(g) Complete the device fabrication by etching the sacrificial oxide.

Figure 5-2. Fabrication steps performed after the completion of the SUMMiT V process.

thickness of the silicon substrate on the microphone die is approximately 600 $\mu m$ and the device now resembles Figure 5-2(d).

Photoresist is then spun on the top surface of the handle wafer. AZ9260 is used with a spin speed of 2000 $RPM$ for a time of 50 $s$. This results in a 9 $\mu m$ thick layer of photoresist. The photoresist is patterned to create a hole above each microphone structure using an EVG 620 mask aligner. Front-to-back alignment is used because the cavity is etched from the back side and must be aligned to the microphone features on the top side of the microphone die. The bottom portion of the handle wafer needs to be clear so that the patterned surface of the microphone die can be seen, therefore Pyrex is used. Then, the substrate of the microphone die is etched using DRIE. A schematic cross section of the device and handle wafer after the DRIE step is shown in Figure 5-2(e).

Figure 5-2(f) shows the device after the completion of the next two process steps. The 0.63 $\mu m$ layer of thermal oxide is etched using a 6:1 buffered oxide etch for 15 min. A mask is not needed for this etch because the silicon substrate acts as the mask. The nitride layer is etched using a UniAxis ICP RIE dry etch. The etch was performed at a pressure of 10 $mTorr$ and a power of 500 $W$; the gasses $SF_6$ and $O_2$ were used with flow rates of 50 $sccm$ and 10 $sccm$, respectively. Similar to the oxide etch, this etch does not require a mask; the substrate acts as a mask for the nitride layer. Although the nitride etch attacks the silicon substrate, the effect on the microphone structure is negligible.

After completion of the above steps, the microphone die is removed from the handle wafer by softening the adhesive by applying heat and the glue is removed by soaking the die in acetone. The microphone structure is released with a 40 $min.$ etch in a 49 % hydrofluoric acid solution; this is followed by a rinse in deionized water. If the microphone was simply removed from the water and left to dry, the

surface tension of the water would pull the diaphragm and backplates together, rendering the device useless; this phenomenon is termed *stiction*.

There are several techniques that have been developed in the past to avoid stiction during the release of MEMS structures. A chemical coating can be applied to the device surfaces to reduce adhesion [126]. Other approaches focus on avoiding the liquid evaporation through the use of freeze-drying [127] or a super critical phase transformation [128]. For this process, super critical drying is used with liquid $CO_2$ using a Bal-tec CPD 030 critical point dryer. First, the deionized water is substituted with methanol. Then, using the Bal-tec CPD, the methanol is substituted with liquid $CO_2$ at approximately a temperature of 12 $^{\circ}C$ and a pressure of 50 *bar*. The temperature is then slowly raised until the liquid $CO_2$ undergoes a supercritical phase change to a gas. This transition avoids the possibility of stiction. After the gaseous $CO_2$ is vented, the processing is finished. A schematic cross section of the finished device is shown in Figure 5-2(g).

## 5.2 Metallization and Wire Bonding Issues

The fabricated device has polysilicon bond pads. These are difficult to bond to using typical ball bonders with gold wire. Several attempts were made to metalize the bond pads. The process flow presents several challenges for bond pad metallization. The microphone must be released with an oxide etchant, thus the metal cannot be attacked by the release etchant. After release, the structure is very fragile; therefore, photolithography is not possible after the device is released. If a protective layer is used during the release process to cover the bond pad metal, it must be able to be removed with a wet chemical. Furthermore, it cannot leave residue on the structure.

The first metallization attempts utilized gold with a chromium adhesion layer because these metals are resistance to hydrofluoric acid etches [129]. However, devices with a Cr/Au metallization did not function. Further investigation showed

that the polysilicon was attacked during the release etch when exposed gold was present. A vulnerable 0.3 $\mu m$ polysilicon interconnect was damaged, severing the connection to the bottom backplate. This catalytic behavior of gold interacting with hydrofluoric acid to etch silicon has been previously reported [130, 131].

To avoid this issue, a process to release the microphone with aluminum bondpads was developed. This is somewhat challenging, as HF based etchants typically attack aluminum [129]. A commercial etchant manufactured by Transene, Inc., Silox Vapox III, was identified as a silicon etch that has a sufficient selectivity between silicon dioxide and aluminum. However, this etchant has a relatively slow etch rate, a 2 $hr$. etch was needed. Over this long etch time, it had a non-negligible reaction with aluminum. Bubbles formed on the surface of the aluminum, which lowered the yield of successfully released microphones. Furthermore, the aluminum surface was damaged during the etch, and it was not possible make a successful wire bond.

The final solution was to leave the bond pads without metallization. Engent, Inc. in Norcross, GA, an external company, was identified to successfully wire bond to bare polysilicon bond pads using a gold ball bonder. The process flow through release gives a high yield with approximately 90 % of the microphones releasing properly. The yield is reduced substantially during packaging. About 50 % of the microphones were successfully wire bonded. However, the yield was further reduced due to diaphragm buckling. This most likely occurred due to package-induced stress or electrostatic discharge. The final yield through packaging was approximately 33 %.

# CHAPTER 6
# RESULTS AND DISCUSSION

The key results obtained for the dual-backplate capacitive microphone described in Chapter 4 and Chapter 5 are presented in this chapter. First the fabricated microphone is described in detail. This is followed by a discussion of the microphone packaging developed for characterization. The experimental setup for each of the measurements is described and then the results are presented.

## 6.1 Realized MEMS Microphone

The dual-backplate capacitive microphone was fabricated using the process flow detailed in Chapter 5. A photograph of the die is shown in Figure 6-1. There are multiple devices on each die. These include two large dual-backplate microphones designed for audio applications. Results were not obtained from these devices due to fabrication issues and they are not referred to throughout the remainder of this dissertation. There are also two single-backplate microphone test structures consisting of the diaphragm and either the top or bottom backplate.

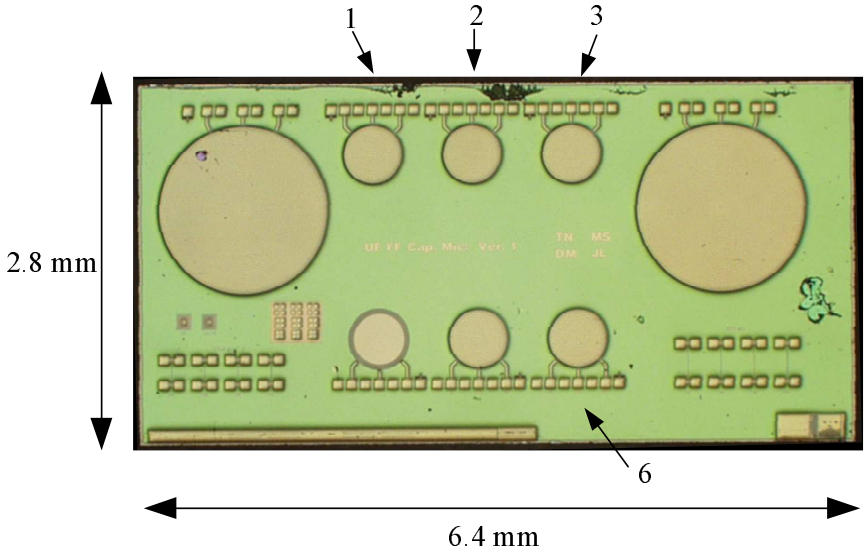


Figure 6-1. Photograph of the mic die with the individual microphones labeled.

On each die, there are four complete aeroacoustic dual-backplate microphones. In Figure 6-1, these are labeled *1*, *2*, *3*, and *6*, respectively. Throughout

this chapter, individual microphones are labeled by a letter corresponding to a particular die, and a number corresponding to the specific microphone on the die. For example, microphone Q1 is the microphone in position *1* on die Q.

A close-up view of one of the microphones is shown in Figure 6-2. The top backplate and backplate holes are visible. The bond pads connecting to the bottom backplate, diaphragm, and top backplate are labeled on the die in poly0. There are three additional bond pads that may be used as guard connections to minimize the effect of parasitic capacitance on the die, similar to those used on the SiSonic$^{TM}$microphone [110]. However, these were not used for the microphone characterization. The final bond pad on the top left of Figure 6-2 provides a connection to the substrate; this was also not used for the characterization.

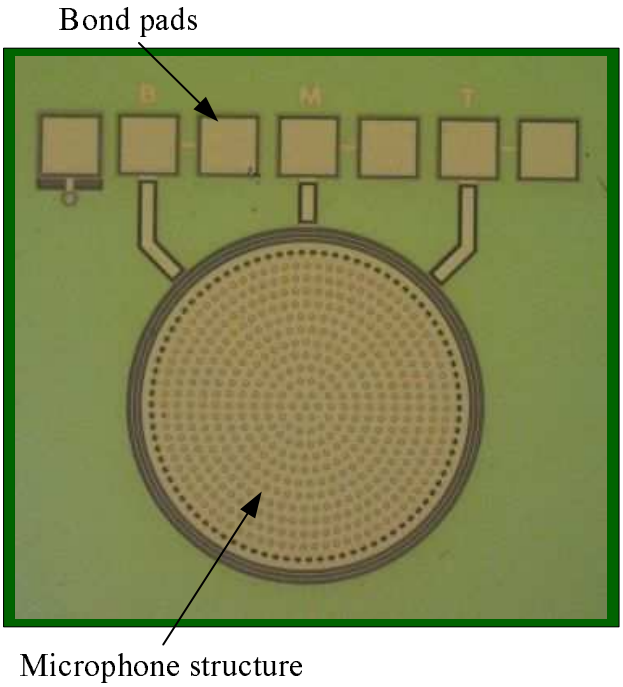


Figure 6-2. Photograph showing the top of the microphone.

The three layers of the microphone are visible in Figure 6-3. This figure is an scanning electron microscopy (SEM) image of a released microphone. The device

has been sectioned with a focused ion beam (FIB), revealing the diaphragm and bottom backplate.

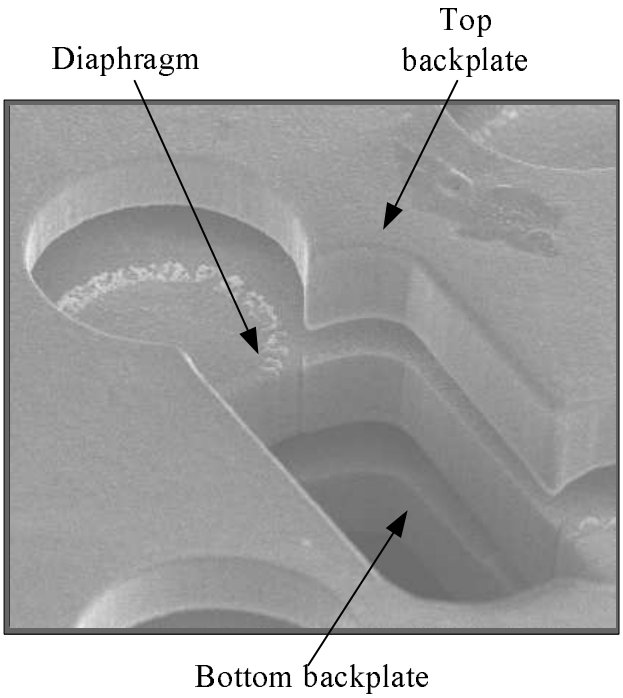


Figure 6-3. SEM image showing the three layers of the microphone.

Further details of the microphone structure are shown in Figure 6-4 and Figure 6-5. These figures are SEM images of an unreleased microphone. The die was sectioned using a dicing saw and a FIB was used to smooth the surface.

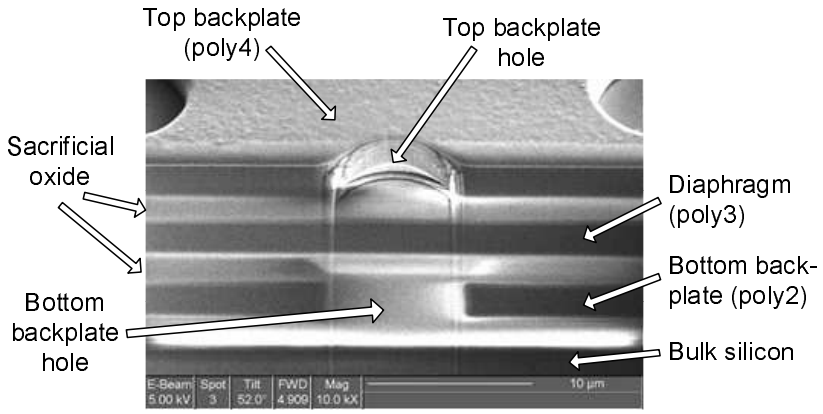


Figure 6-4. SEM image of a cross-section view of an unreleased microphone die.

Figure 6-4 is a cross-section view showing the top backplate, diaphragm, and bottom backplate. Figure 6-5 is a close-up view of the anchor cross-section that shows the details of the electrical connection to the diaphragm (shown schematically in Figure 4-3(b)).

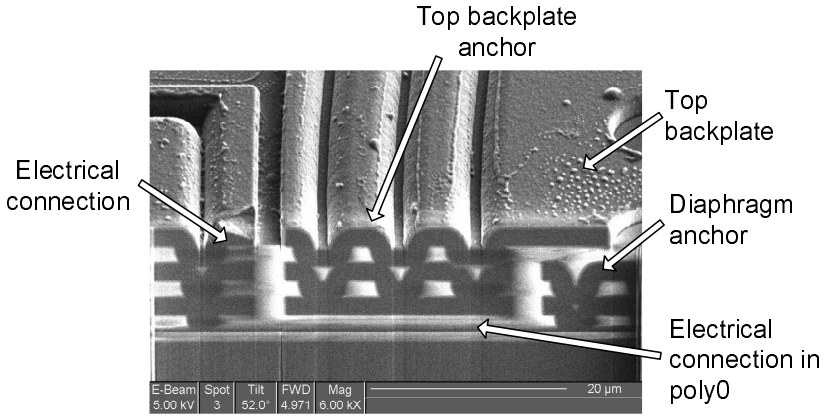


Figure 6-5. SEM image of the electrical connection to the diaphragm.

## 6.2 Microphone Packaging

The microphone packaging was designed to support laboratory acoustic testing. A schematic view of the designed package is shown in Figure 6-6.

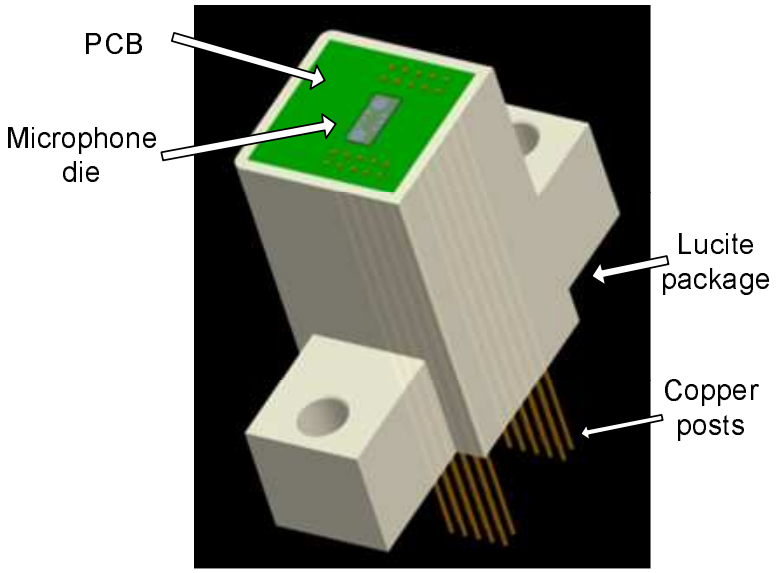


Figure 6-6. Schematic diagram of the microphone package.

The microphone package consists of a printed circuit board (PCB) that holds the microphone die. The PCB is placed in a Lucite plug. This plug is designed to fit into the acoustic test hardware and give a flush surface. Electrical connection to the microphone package is made via copper wires extending out of the package base.

### 6.2.1 Interface Circuits

The microphone is characterized with two distinct interface circuits, a voltage amplifier and a charge amplifier. The voltage amplifier is the SiSonic$^{TM}$microphone amplifier, courtesy of Knowles Acoustics. Figure 6-7 is a photograph of the amplifier die showing the required connections. This amplifier is interfaced to the microphone via the PCB discussed in Section 6.2.2.

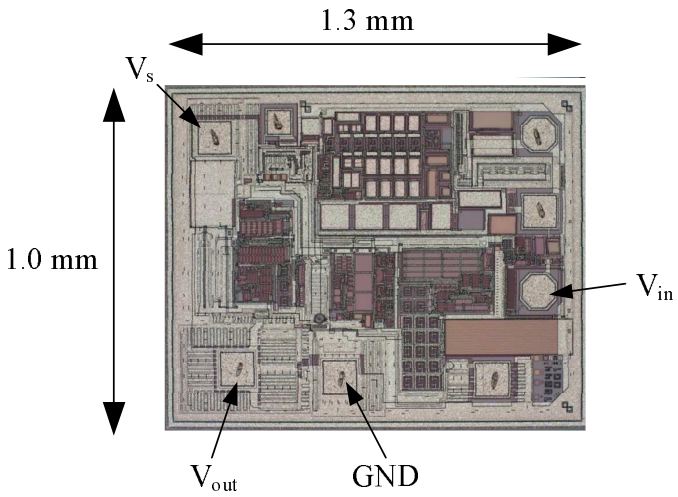


Figure 6-7. Photograph of the SiSonic$^{TM}$microphone amplifier.

The charge amplifier used is based on the TLE2071, manufactured by Texas Instruments. This circuit is realized on an external circuit board, shown in Figure 6-8. The board contains the amplifier circuit as well as BNC connectors for the microphone bias voltages. A 3-wire connection is made between the charge amplifier PCB and the microphone package that provides electrical contact for the top backplate, diaphragm, and bottom backplate.

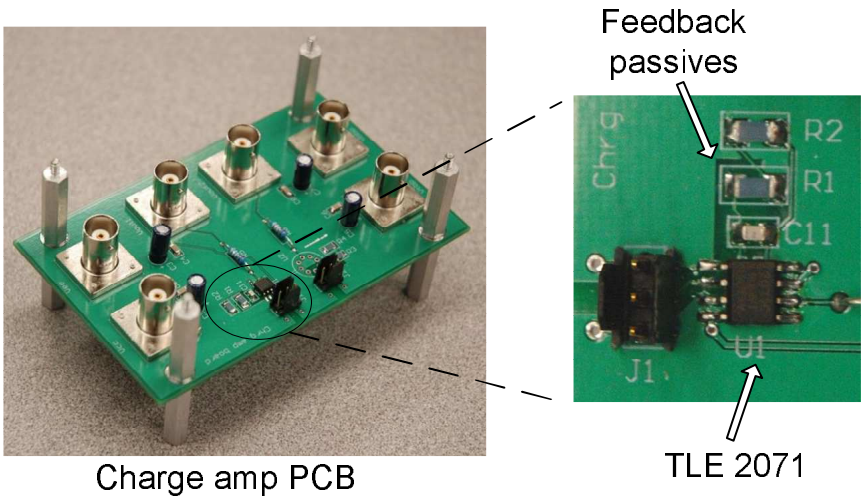


Figure 6-8. Photograph of the charge amplifier circuit board.

### 6.2.2 Printed Circuit Board

The printed circuit board contained in the microphone package serves three functions: (1) it supports the microphone die, (2) provides electrical connections to the microphone, and (3) it contains the supporting circuitry for the voltage amplifier. The top view of an un-populated PCB is shown in Figure 6-9(a). A recess has been cut into the PCB that allows the microphone to be flush with the PCB surface. A channel is provided around the perimeter of the cavity to contain excess epoxy when the microphone die is affixed to the PCB. Gold wire bonds are used to connect the microphone die to the circuit board. Electrical connection to the PCB is made via through-holes in which the copper wires are inserted and soldered.

The backside of the PCB can be configured in two ways to support either a voltage amplifier or a charge amplifier. For microphone die used with voltage amplifiers, the backside of the PCB is populated as shown in Figure 6-9(b). This includes affixing four amplifier die to the PCB using a conductive epoxy. The amplifier substrate is grounded to prevent drift which can result from stray charge. Wire bonds are used to connect the PCB to the amplifier die and are covered in

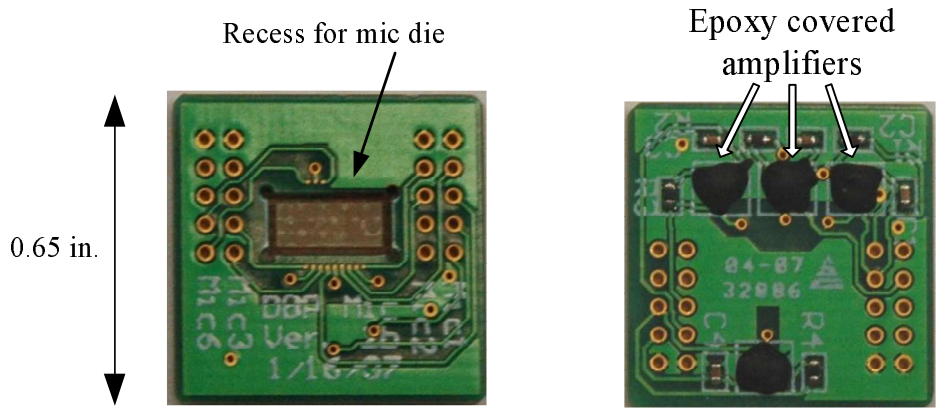


(a) Top view. (b) Bottom view.

Figure 6-9. Pictures of the printed circuit board used in the microphone package.

protective epoxy. Also included in the circuitry is a 50 Ω resistor in series with each amplifier output and a 0.1 $\mu F$ bypass capacitor for each amplifier's power supply. The trace from the diaphragm to the amplifier input is made as short as possible to minimize parasitic capacitance.

For microphone die used with a charge amplifier, the back-side of the PCB is not populated with the previously described voltage amplifier circuitry. In this case the diaphragm is directly connected to one of the copper posts. Rather than have this connection permanently on the PCB and load the voltage amplifier with additional parasitic capacitance, a wire bond is made to jumper the diaphragm trace to the PCB output.

### 6.2.3 Final Package

The populated PCB embedded in the Lucite package is shown in Figure 6-10. The microphone is flush with the PCB surface and the wire bonds are covered in epoxy. The copper posts are cut such that they terminate just below the surface of the PCB; thus the solder height is as low as possible.

The final package assembly is shown in Figure 6-11. The Lucite PCB holder has a dimension of 0.75 $in.$ × 0.75 $in.$ at the front surface.

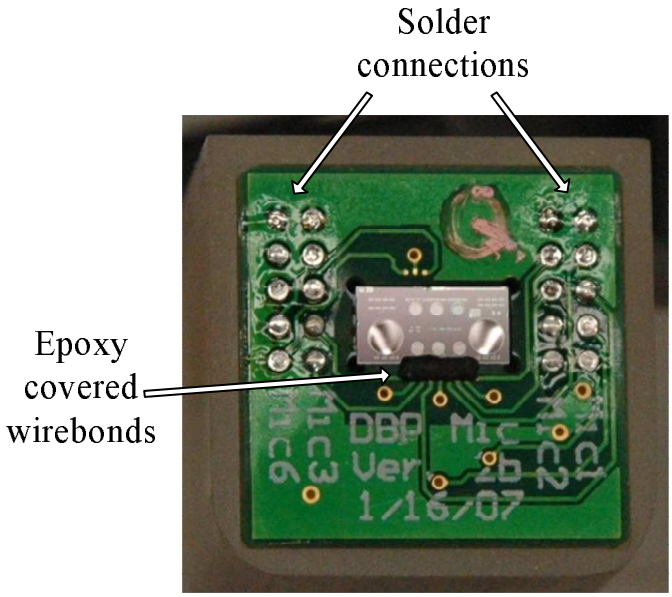


Figure 6-10. Photograph of the microphone embedded in the printed circuit board.

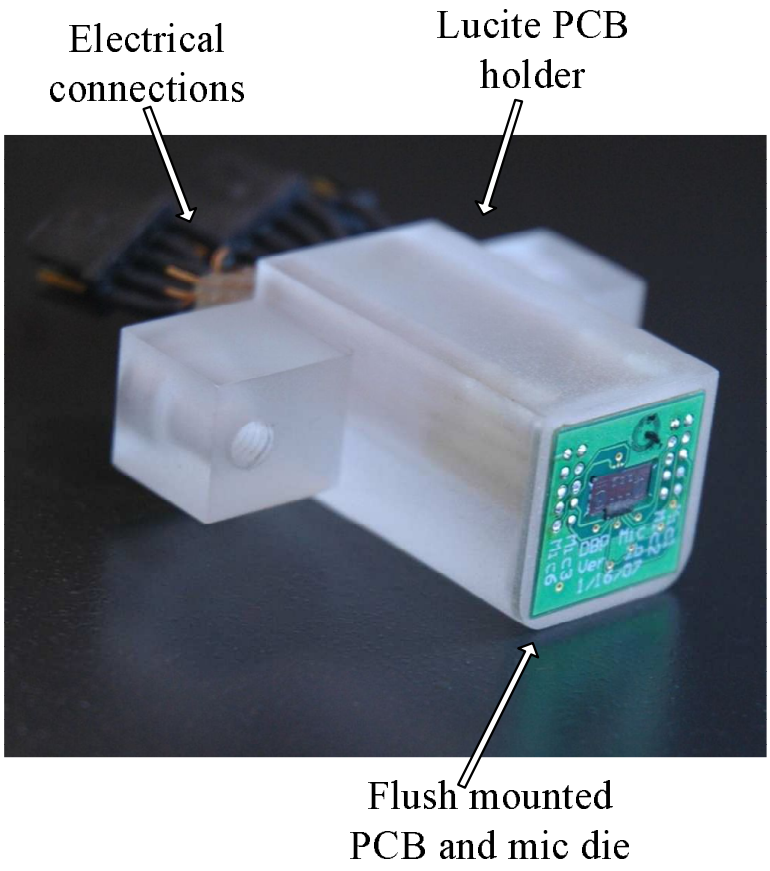


Figure 6-11. Photograph of the assembled microphone package.

## 6.3 Experimental Setup

In this section, the experimental setup for the microphone characterization is discussed. Three general types of experimental setups are used for the microphone characterization. For the frequency response and linearity experiments, a plane wave tube is used. A Faraday cage is used for the noise floor characterization. A laser vibrometer is used to measure the resonant frequency of the microphone.

### 6.3.1 Acoustic Experimental Setup

The microphones are characterized acoustically to determine the linearity of the microphone and measure the frequency response. The linearity is analyzed by plotting the microphone output voltage and sensitivity vs incident pressure, as well as estimating the total harmonic distortion.

#### 6.3.1.1 Plane Wave Tube

The plane wave tube (PWT) is a long rigid duct with a 1 $in.$ $\times$ 1 $in.$ square cross section. As shown in Figure 6-12, an acoustic driver is placed at one end of the tube. The device under test (DUT) and a reference microphone are placed at the other end such that they are at normal incidence to the incident pressure. Due to the geometry of the tube, there is a frequency below which only plane waves propagate; i.e. the pressure is uniform across the cross section of the PWT [4]. This allows the DUT and the reference microphone to be exposed to the same incident pressure. This frequency is 6.7 $kHz$ for air.

Also shown in Figure 6-12 is the supporting hardware for the plane wave tube experiments. The Brüel and Kjær Pulse multi-analyzer system provides a function generator to drive the acoustic driver and accepts the input signals from the DUT and reference microphone. The Pulse system also performs the data analysis functions and records the data. A PCB Piezoelectronics 377A51 condenser microphone is used for the reference microphone. This microphone is used due to its high maximum pressure. For consistency, it is used as the reference

microphone for all acoustic experiments. The signal sent to the acoustic driver is first amplified by a Crown K1 power amplifier. The sound field in the plane wave tube is produced by a BMS 4590P compression driver.

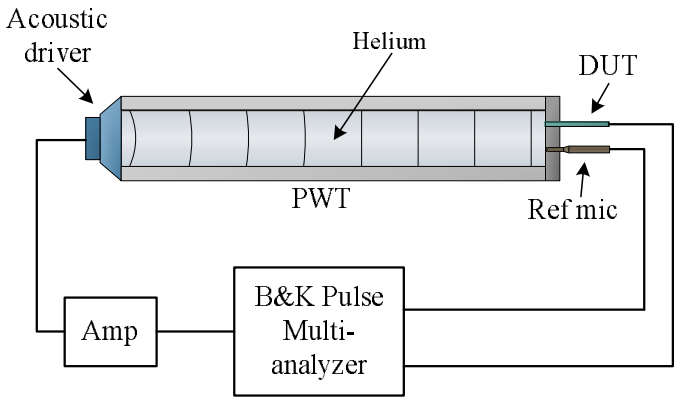


Figure 6-12. Large plane wave tube experimental setup.

However, the speed of sound in helium is approximately three times the speed of sound in air; thus only plane waves exist for frequencies up to approximately 20 $kHz$. Operating the microphone in helium has little impact on its performance. The cavity compliance decreases, thus the predicted sensitivity is reduced by 1 % and the resonant frequency is increased by less than 1 %. The predicted frequency response of the designed dual-backplate condenser microphone is shown in Figure 6-13 for operation in both air and helium.

The linearity experiments are conducted in air, and the frequency response measurements use helium. The magnitude response of two Brüel and Kjær condenser microphones in air and helium is shown in Figure 6-14 and Figure 6-15, respectively. The magnitude response is approximately 1 (0 $dB$) when only plane waves propagate. It can be seen that the use of helium extends this range to approximately 20 $kHz$.

The reference microphone and DUT are excited with a 1 $kHz$ tone for the linearity and THD measurements. The Pulse system is configured to compute a zoom-FFT of these signals with a 6.4 $kHz$ span and a center frequency of 3.4 $kHz$.

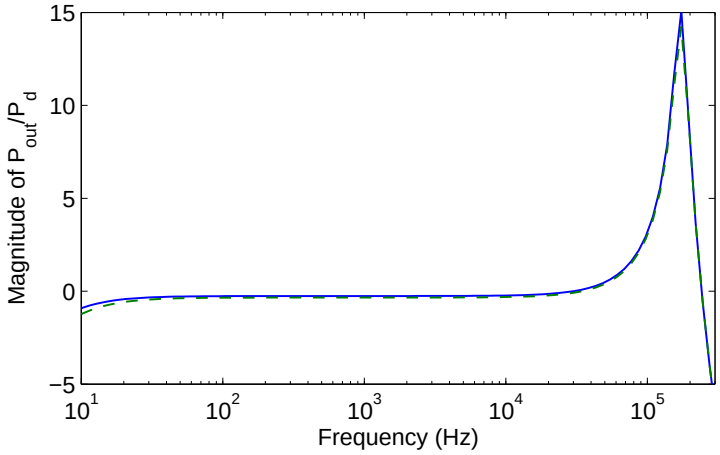


Figure 6-13. Theoretical magnitude response of the dual-backplate microphone in air(-) and helium (- -).

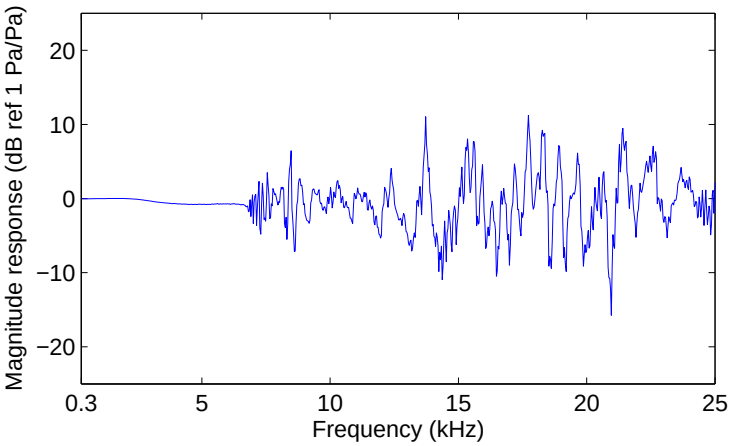


Figure 6-14. Magnitude response of two B&K 4138 condenser microphones in air.

This ensures that all harmonics up to 6 $kHz$ are captured. A 1600 line FFT is used giving a frequency resolution of 4 $Hz$. The amplitude of the incident pressure is incremented to characterize the microphones over a wide range of amplitudes; at each measurement point, 75 averages are taken with 0 %overlap.

For the frequency response tests, the generator is set to a periodic random signal with a span of 25.6 $kHz$. The FFT analyzer is configured accordingly to a span of 25.6 $kHz$ with a $\Delta f$ of 16 $Hz$. Each set of recorded data presented below is the result of 400 averages.

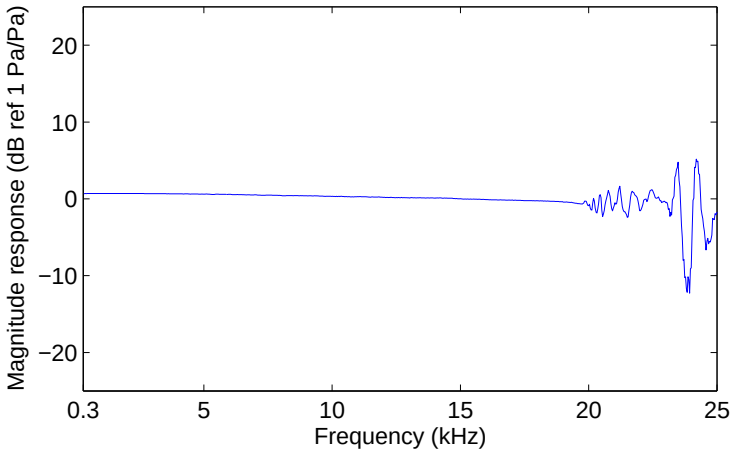


Figure 6-15. Magnitude response of two B&K 4138 condenser microphones in helium.

#### 6.3.1.2 THD Methodology

As the microphone transitions from linear to non-linear operation, the total harmonic distortion increases. To measure the THD in the microphones, a single-tone pressure is applied. Non-linearities in the microphone response result in the output having power at frequencies that are integer multiples of the fundamental frequency [21]. Thus the measured power in all the harmonics can be used to estimate the THD.

However, as the incident pressure becomes large, non-linearities are generated in the test setup. The acoustic driver outputs significant sound pressure at harmonic frequencies when driven with a single tone. Additionally, the acoustic wave propagation becomes non-linear at high sound pressure levels [4]. Therefore, the THD of the microphone must be estimated in the presence of external non-linearities.

To estimate the total harmonic distortion due to the DUT microphone, the harmonic components due to the experimental setup are subtracted from the DUT output signal. The reference microphone measures the total acoustic pressure including the harmonic components. The MEMS microphone sensitivity is used to

convert the harmonic pressure components measured by the reference microphone to a corresponding rms output voltage. This rms output voltage at each harmonic is subtracted from the measured voltage at each harmonic as depicted in Figure 6-16. Mathematically, this is described as

$$v_n^{eff} = v_n^{meas} - S{\cdot}p_n^{ref}, \tag{6–1}$$

where $v_n^{meas}$ is the measured rms voltage at the $n^{th}$ harmonic, $S$ is the microphone sensitivity, $p_n^{ref}$ is the rms pressure measured by the reference microphone at the $n^{th}$ harmonic, and $v_n^{eff}$ is the extracted rms voltage at the $n^{th}$ harmonic used to estimate the total harmonic distortion.

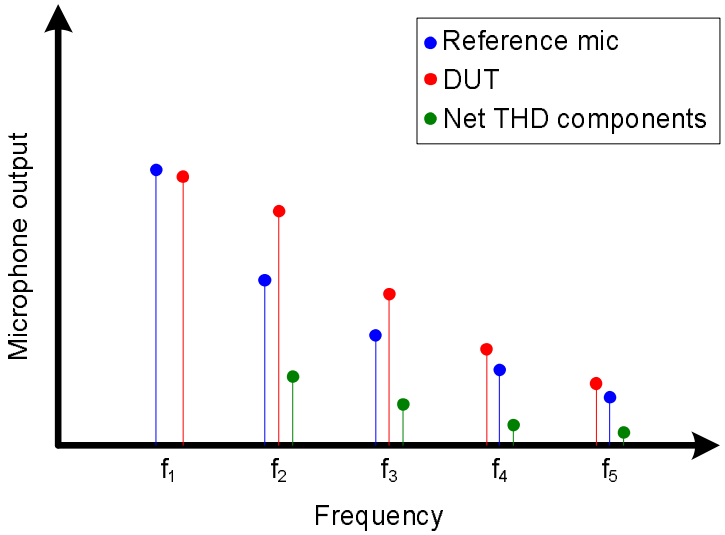


Figure 6-16. Graphic description of THD methodology.

Several assumptions are necessary for this analysis to be valid. First the reference microphone must not introduce any non-linearities in the system. The microphones are tested up to sound pressure levels approaching 170 $dB$; therefore, the choice of reference microphone is crucial. The PCB 377A51 condenser microphone has a 3 % distortion limit of 192 $dB$. Thus, the reference microphone is sufficient for these measurements. Additionally, the total pressure measured by the reference microphone must be the same as that sensed by the DUT microphone. A

1 $kHz$ tone is used for the THD measurements. Therefore, the first five harmonic components propagate as plane waves in the PWT. These five harmonics are used in the THD calculations. It is assumed the DUT generates negligible harmonic distortion above the $5^{th}$ harmonic.

### 6.3.2 Laser Vibrometer

The resonant frequency of the microphone is determined using a Polytec Scanning Doppler Laser Vibrometer (SLV). The microphone is placed on a microscope stage. A Polytec OFV 511 fiber interferometer generates a laser beam that is incident on the microphone diaphragm and receives the resulting interference optical signal through the microscope adapter. The laser must be positioned such that it passes through a top backplate hole, as shown in Figure 6-17. The center hole is used to maximize the measured velocity. The velocity is inferred from the returned optical signal by the vibrometer controller.

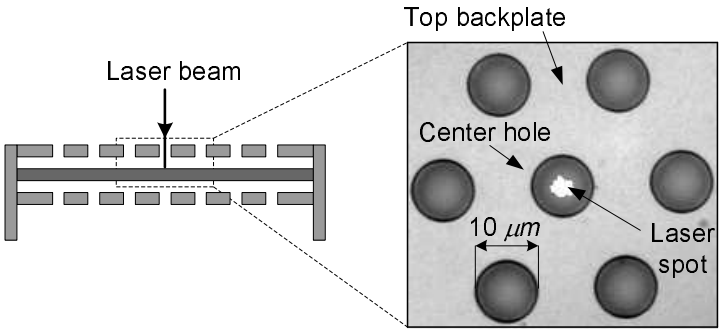


Figure 6-17. Experimental setup to determine the resonant frequency of the microphone.

The microphone is excited with an acoustic impulse generated by a cap gun. The pressure is recorded by a Brüel and Kjær 4138 reference microphone placed approximately 1 $in$ from the DUT microphone. A typical measured pressure is shown in Figure 6-18. The recorded pressure is shaped by a high pass filter with a 50 $kHz$ corner frequency that was used on both the reference channel and the velocity channel; the measured pressure near 170 $kHz$ is flat. The laser vibrometer

is configured to compute the FFT of the time series signals over a 500 $kHz$ bandwidth with a 156.25 $Hz$ bin width. Due to the nature of this experiment, averaging is not performed. While the test may be repeated multiple times and the resulting FFT's averaged, the source may not be repeatable. The data presented here is from single-shot measurements.

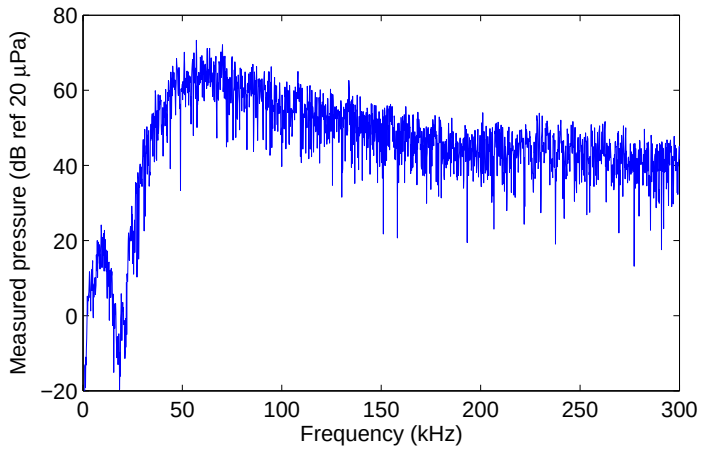


Figure 6-18. Typical pressure recorded by reference microphone for LV measurement.

### 6.3.3 Faraday Cage

The experimental setup for the noise experiments is shown in Figure 6-19. The microphone and interface circuitry are placed inside two concentric Faraday cages. A Faraday cage attenuates electromagnetic waves and reduces the amount of electromagnetic interference inside the box due to external sources. The use of two Faraday cages improves the electromagnetic interference reduction [132]. The output of the microphone is amplified and then sent to a Stanford Research Systems SR785 spectrum analyzer. The spectrum analyzer measures the output noise power spectral density. The input referred pressure noise is calculated using the measured microphone sensitivity.

The noise spectrum is measured from 10 $Hz$ to 102.4 $kHz$ by combining measurements of three separate frequency ranges. The first ranged from 20 $Hz$ to

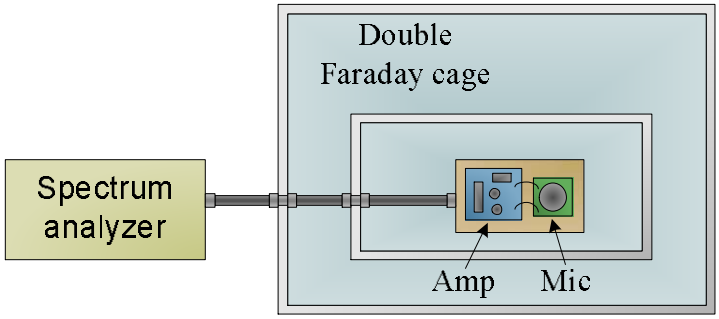


Figure 6-19. Faraday cage experimental setup for noise measurements.

200 $Hz$ with a bin width of 0.25 $Hz$ and 2300 averages. The second range spanned from 200 $Hz$ to 1.6 $kHz$ and had a bin width of 2 $Hz$ and 4000 averages. The final frequency range spanned from 1.6 $kHz$ to 102.4 $kHz$ with a 128 $Hz$ bin width and 30000 averages.

## 6.4 Experimental Results

In this section, the results of the microphone characterization are presented. First, the linearity and total harmonic distortion results are discussed. These are followed by the frequency response measurements and resonant frequency results. Finally, the measured noise floor is presented.

Microphones from four chips were packaged for the characterization. Three were packaged with voltage amplifiers yielding a total of seven devices with a voltage amplifier; these die are I, M, and Q. The forth die, O, was characterized with the charge amplifier; yielding three devices. Unless otherwise stated, all microphones were biased with $\pm 9.3\ V$ using alkaline batteries.

### 6.4.1 Linearity and Total Harmonic Distortion

The results of the linearity measurements for the microphones with voltage amplifiers are shown in Figure 6-20. The incident pressure was varied from as low as 43 $dB$ and increased to near 160 $dB$. As the incident pressure approaches

160 $dB$, the microphone output saturates. This is due to saturation of the voltage amplifier, which has a maximum input voltage of 500 $mV$. The measured sensitivities fall within the estimated sensitivity range.

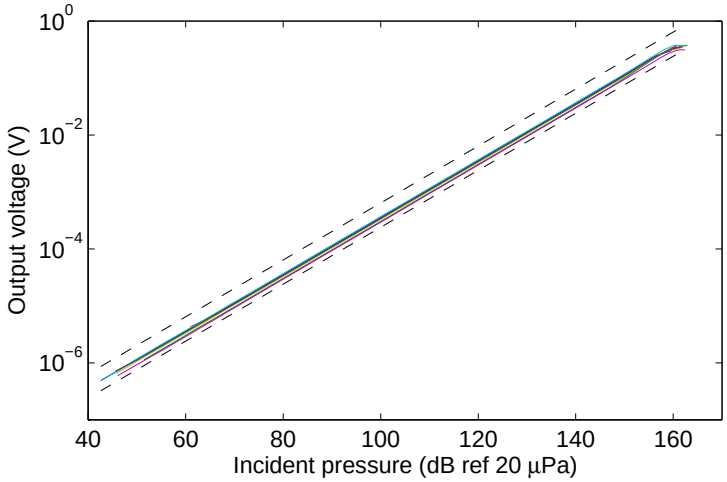


Figure 6-20. Output voltage vs. pressure for voltage amplifier microphones bounded by the theoretical sensitivity estimate.

To better visualize the extent of the linear range of operation, the measured sensitivity is plotted versus incident pressure in Figure 6-21. The sensitivities of the seven microphones are matched to within 2.1 $dB$. The average sensitivity of each microphone is given in Table 6-1 along with a 95 % confidence interval. The confidence interval for each microphone is computed using the methodology described in Section C.4.

To determine the maximum linear range of each microphone without influence from the input range of the voltage amplifier, the linearity measurements were repeated with a bias voltage of $\pm 2.0$ $V$. This lowers the sensitivity by a factor of 2/9.3; thus, the amplifier does not saturate at the highest sound pressure levels. The output voltage versus incident pressure for this case is plotted in Figure 6-22. These data are shown on a linear scale to accentuate the difference in sensitivity caused by the bias voltage reduction.

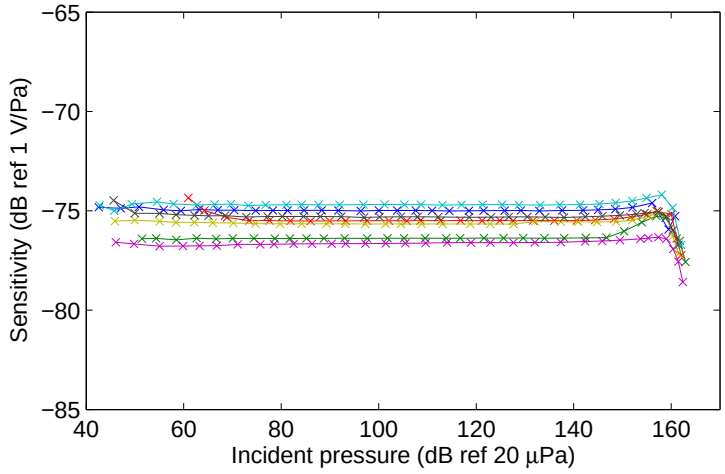


Figure 6-21. Sensitivity vs. pressure for voltage amplifier microphones.

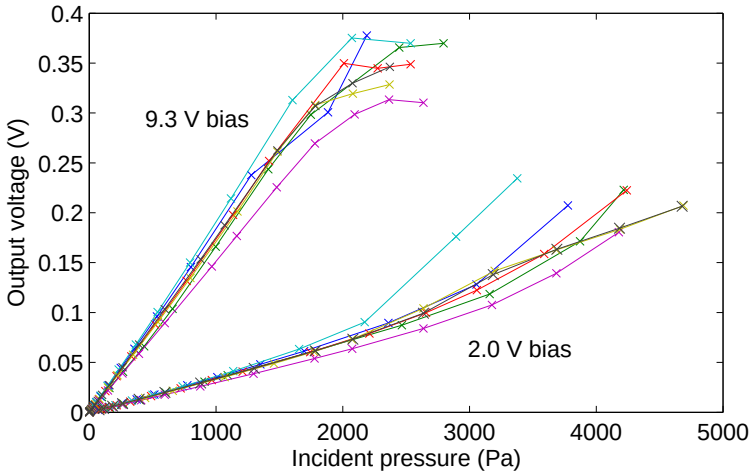


Figure 6-22. Output voltage vs. pressure for voltage amplifier microphones biased with $\pm 2.0\ V$.

The microphones are seen to deviate from the linear trend above 2000 $Pa$. The sensitivity is plotted versus incident pressure for the microphones biased with $\pm 2.0\ V$ in Figure 6-23. The increase in sensitivity at higher pressures is most likely due to the non-linear electrostatic behavior and agrees with the theoretical predications of the device non-linearity. The predicted non-linearity of a dual-backplate capacitive microphone for several conditions is shown in Figure 6-24. The worst-case non-linearity occurs for non-matched capacitors and when the

mechanical non-linearity is negligible. In the realized microphone, the capacitors do have mismatch. Furthermore, the onset of mechanical non-linearity could be delayed due to uncertainties in the mechanical model or if the air gaps are smaller than predicted.

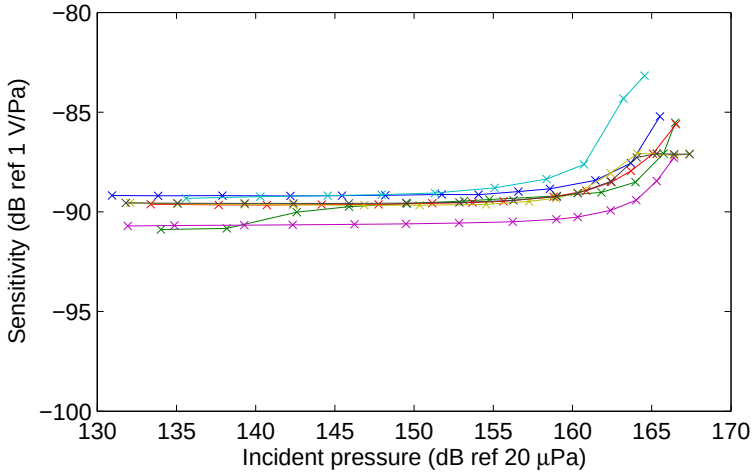


Figure 6-23. Sensitivity vs. pressure for voltage amplifier microphones biased with $\pm 2.0\ V$.

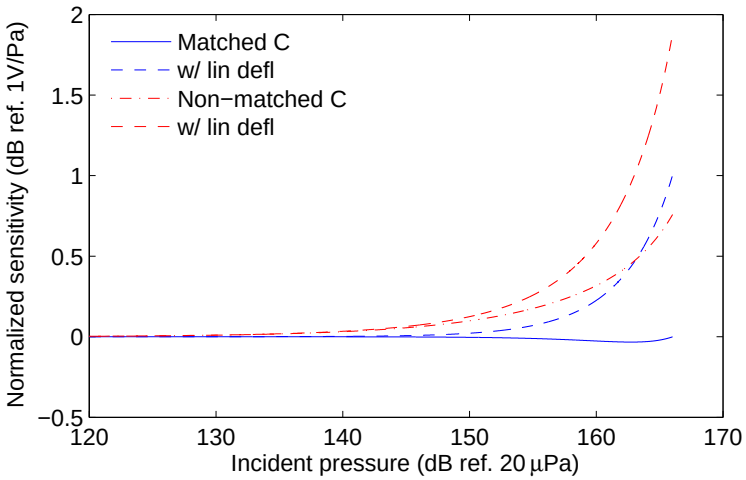


Figure 6-24. Theoretical non-linearity for a dual-backplate condenser microphone.

The estimated total harmonic distortion for the voltage amp microphones biased with $\pm 2.0\ V$ is given in Figure 6-25. Most microphones have between 3 % to 5 % THD near 164 $dB$. The specific results for each voltage amp microphone are

given in Table 6-1. The maximum pressure listed is the first data point for which the non-linearity is in the range of 3 % to 5 %; the corresponding THD is given.

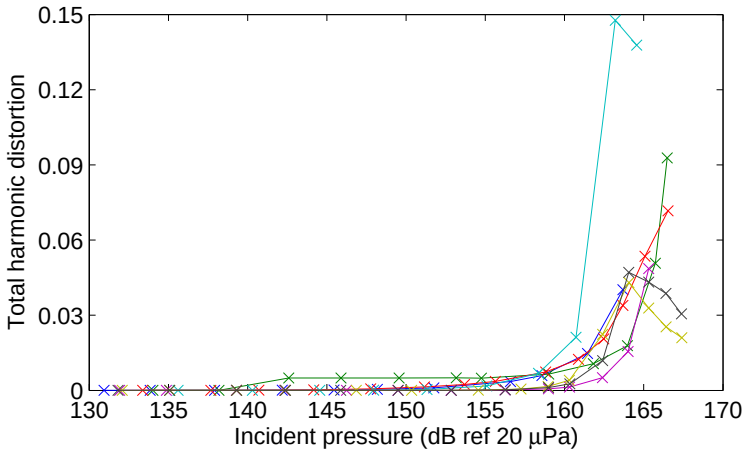


Figure 6-25. Total harmonic distortion for voltage amplifier microphones biased with $\pm 2.0\ V$.

Table 6-1. Summary of the linearity results for the microphones with voltage amplifiers

| Microphone | Measured sensitivity | Max Pressure | THD at Pmax |
|---|---|---|---|
| I2 | $178.3 \pm 0.3\ \mu V/Pa$ | 163.7 $dB$ | 4.0 % |
| I3 | $151.6 \pm 0.2\ \mu V/Pa$ | 165.7 $dB$ | 5.1 % |
| M1 | $168.1 \pm 0.3\ \mu V/Pa$ | 163.7 $dB$ | 3.4 % |
| M2 | $184.4 \pm 0.3\ \mu V/Pa$ | 160.7 $dB$ | 2.1 % |
| Q1 | $145.1 \pm 0.2\ \mu V/Pa$ | 165.3 $dB$ | 4.7 % |
| Q2 | $165.3 \pm 0.4\ \mu V/Pa$ | 164.1 $dB$ | 4.3 % |
| Q3 | $172.1 \pm 0.4\ \mu V/Pa$ | 164.1 $dB$ | 4.7 % |

The measured sensitivity and capacitance of the microphones may be used to estimate the air gaps and parasitic capacitance of each device. The results are listed in Table 6-2. The microphone parameter with the highest variability is the air gap distance. Therefore, the area of each capacitor is assumed to be the designed value. Each air gap is estimated from the measured capacitance as follows,

$$g_{est} = \frac{\epsilon_0 A}{C_{meas}}. \tag{6–2}$$

The air gaps may then be used to predict the microphone sensitivity. However, the parasitic capacitance is not known. Therefore, Equation 4–12 is used to estimate the parasitic capacitance, allowing for non-matched capacitors. The estimated parasitic capacitance ranges from 0.92 $pF$ to 2.23 $pF$. This includes the contribution of the amplifier input capacitance, estimated to be 0.3 $pF$.

Table 6-2. Summary of air gap and parasitic capacitance estimates for the microphones tested with voltage amplifiers.

| Microphone | Measured Capacitance (top, bottom) | Estimated gaps (top, bottom) | Estimated $C_p$ |
|---|---|---|---|
| I2 | 849.8 $fF$, 601.8 $fF$ | 2.14 $\mu m$, 2.44 $\mu m$ | 1.20 $pF$ |
| I3 | 871.0 $fF$, 580.7 $fF$ | 2.09 $\mu m$, 2.53 $\mu m$ | 1.65 $pF$ |
| M1 | 793.1 $fF$, 562.7 $fF$ | 2.30 $\mu m$, 2.61 $\mu m$ | 1.09 $pF$ |
| M2 | 808.2 $fF$, 567.0 $fF$ | 2.25 $\mu m$, 2.59 $\mu m$ | 0.92 $pF$ |
| Q1 | 915.1 $fF$, 656.9 $fF$ | 1.99 $\mu m$, 2.24 $\mu m$ | 2.23 $pF$ |
| Q2 | 960.2 $fF$, 603.3 $fF$ | 1.90 $\mu m$, 2.44 $\mu m$ | 1.74 $pF$ |
| Q3 | 867.3 $fF$, 632.1 $fF$ | 2.10 $\mu m$, 2.33 $\mu m$ | 1.42 $pF$ |

The linearity of the microphones tested with a charge amplifier is now examined. The output voltage versus pressure for the three tested microphones is plotted in Figure 6-26. The tested pressure range for these microphones extends from approximately 80 $dB$ to above 165 $dB$. Lower pressures were not used for the charge amplifier microphones because sufficient coherence ($> 0.9$) was not obtained for lower pressures. This is partially due to the higher noise floor of the charge amplifier circuit. However, the main cause is interference caused by 60 $Hz$ power line pick-up. The charge amplifier circuit is more susceptible to this interference because it is separated from the microphone by a 12 $in.$ length of cable.

The three charge amplifier microphones are matched to within 0.8 $dB$. The sensitivities of these microphones are plotted versus the incident pressure in Figure 6-27. The charge amplifier has a sufficient maximum input and output voltage range to not impact the dynamic range of the charge amplifier measurement. The

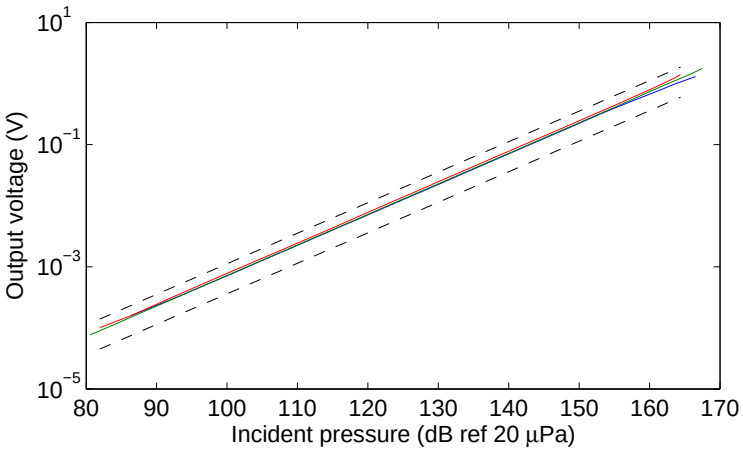


Figure 6-26. Output voltage vs. pressure for charge amplifier microphones, bounded by the theoretical estimate.

total harmonic distortion for the charge amplifier microphone measurements is given in Figure 6-28. Two of the microphones, O3 and O6, have distortion of less than 1 % at 164 $dB$. The third microphone, O1, has 3.3 % THD at 166.5 $dB$. However, a sufficient number of microphones has not been tested to statistically consider these results. The sensitivities with 95 % confidence intervals, as well as the THD results, are given in Table 6-3.

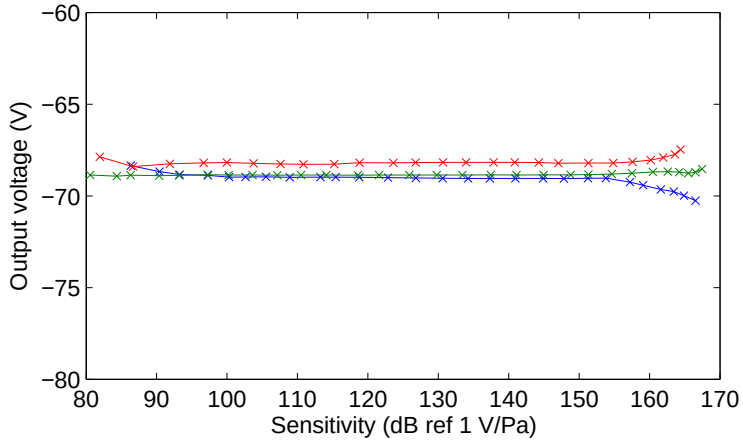


Figure 6-27. Sensitivity vs. pressure for charge amplifier microphones.

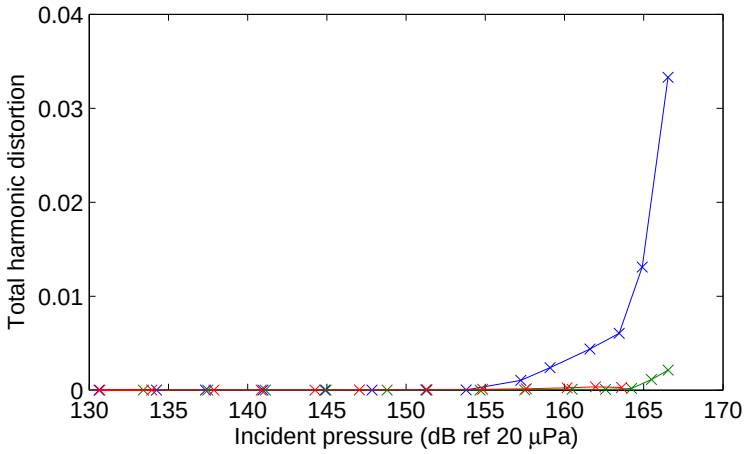


Figure 6-28. Total harmonic distortion for charge amplifier microphones.

Table 6-3. Summary of the linearity results for the microphones with charge amplifiers

| Microphone | Measured sensitivity | Max Pressure | THD at Pmax |
|---|---|---|---|
| O1 | $355 \pm 1\ \mu V/Pa$ | 166.5 $dB$ | 3.3 % |
| O3 | $360.4 \pm 0.2\ \mu V/Pa$ | 166.5 $dB$ | 0.2 % |
| O6 | $388.8 \pm 0.7\ \mu V/Pa$ | 163.6 $dB$ | 0.03 % |

### 6.4.2 Frequency Response

The frequency response of the seven microphones tested with voltage amplifiers has been measured. In Figure 6-29, the magnitude response is plotted over the range 300 $Hz$ to 25 $kHz$. While higher order modes propagate at frequencies above 20 $kHz$, the microphones qualitatively demonstrate a response up to 25 $kHz$. The theoretical sensitivity estimate for the microphone with a voltage amplifier is also included in this figure. The magnitude response is plotted up to 20 $kHz$ in Figure 6-30 to better show the matching between devices. The phase response for the seven microphones with voltage amplifiers is plotted in Figure 6-31.

The phase is centered around 180° because there is an inversion from pressure to voltage. The phase is matched to within 2° for most of the frequency range. The dip in phase around 10 $kHz$ coincides with reduced output from the acoustic

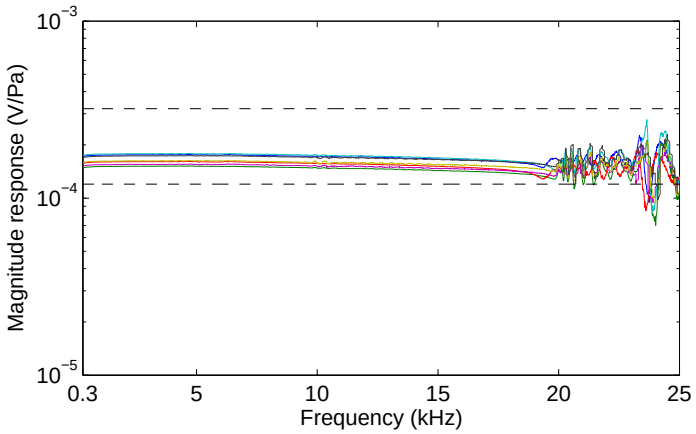


Figure 6-29. Magnitude response for voltage amplifier microphones extending to 25 $kHz$, bounded by the theoretical estimate.

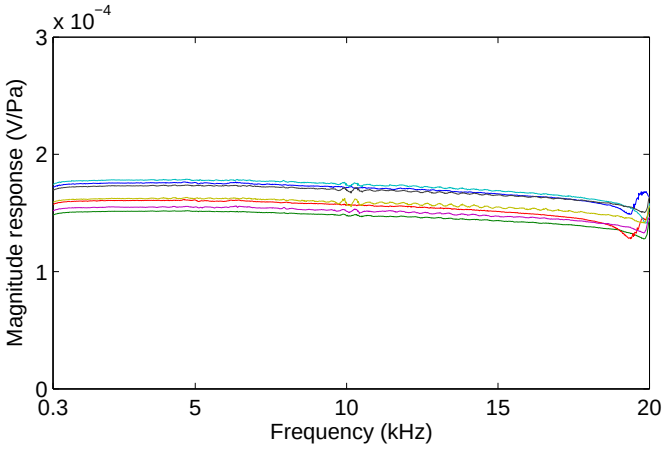


Figure 6-30. Magnitude response for voltage amplifier microphones up to 20 $kHz$.

driver. Above 19 $kHz$, the phase deviates from the nominal value of 180° as higher order modes begin to propagate.

The magnitude and phase response has been measured for the three microphones tested with a charge amplifier. While the charge amplifier does not lose sensitivity due to parasitic capacitance, this capacitance can affect the frequency response of the microphone. Vibrations in the cable result in a modulation of the parasitic capacitance and a corresponding charge injection into the amplifier. This phenomenon was observed in the charge amplifier measurements. It was partially mitigated by securing the cable as much as possible; however vibrations were not

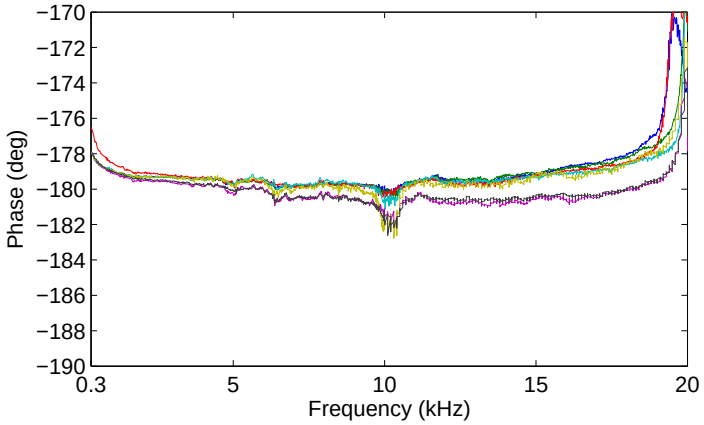


Figure 6-31. Phase response for voltage amplifier microphones.

completely eliminated. The magnitude and phase response for the charge amplifier with the flattest measured frequency response are shown in Figure 6-32 and Figure 6-33, respectively. This device responded best to securing the cabling.

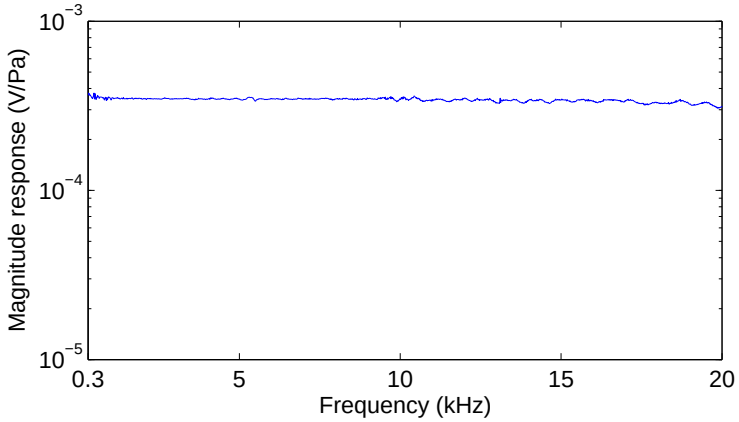


Figure 6-32. Magnitude response for charge amplifier microphones with minimal ripple.

The magnitude and phase response for all three charge amplifier microphones are given in Figure 6-34 and Figure 6-35, respectively. The cable and package vibration results in the ripple present in the frequency response measurements. The phase response for these microphones is centered around 0° because there is no inversion from incident pressure to output voltage.

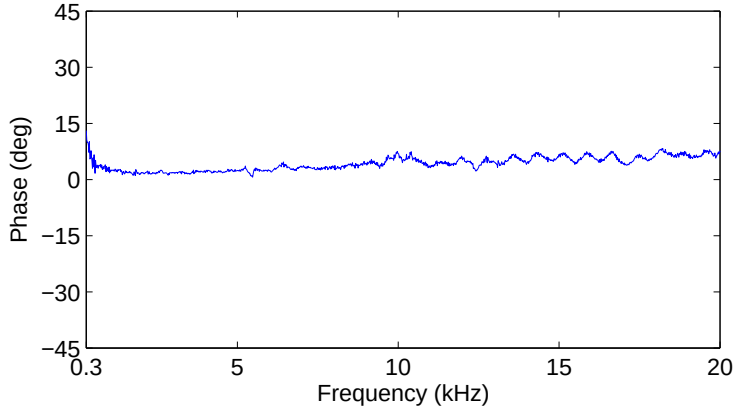


Figure 6-33. Phase response for charge amplifier microphones with minimal ripple.

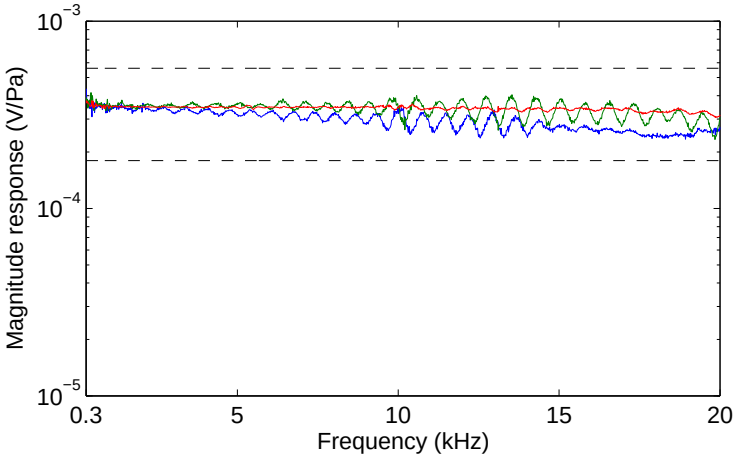


Figure 6-34. Magnitude response for all charge amplifier microphones, bounded by the theoretical estimate.

### 6.4.3 Resonant Frequency

While the highest measured frequency in the frequency response measurements is 25 $kHz$, the theoretical resonant frequency is 173 $kHz$. To determine the upper end of the microphone bandwidth, the frequency response is measured using the previously described experimental setup. This test was conducted for the three microphones on die O. Interface circuitry was not used for this measurement, because the diaphragm motion is measured optically. The FFT of the diaphragm velocity for the three microphones tested is given in Figure 6-36. The resonant frequency of the microphone is assumed to be the frequency at which the FFT is

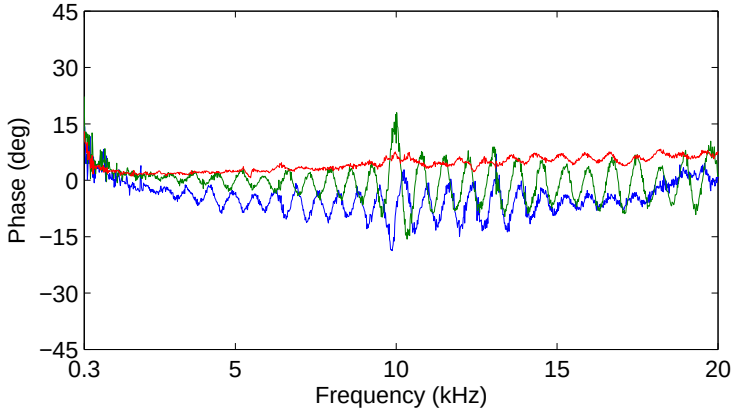


Figure 6-35. Phase response for all charge amplifier microphones.

maximum. The average resonant frequency is 158.0 $kHz$; the results for the three microphones are listed in Table 6-4.

Table 6-4. Summary of the resonant frequency results.

| Microphone | Measured resonant frequency |
|---|---|
| O1 | 158.0 $kHz$ |
| O3 | 159.1 $kHz$ |
| O6 | 157.0 $kHz$ |

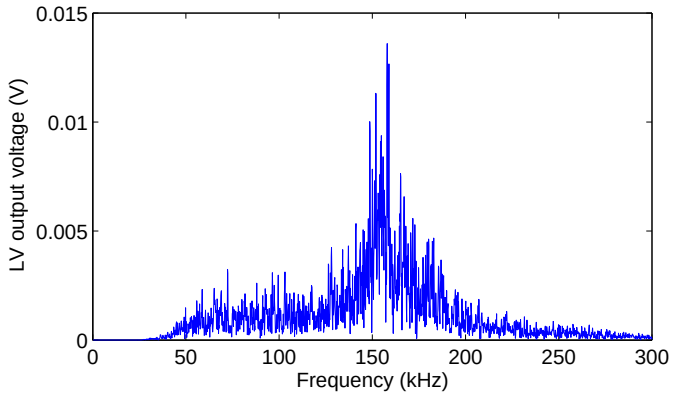


(a) Microphone Q1

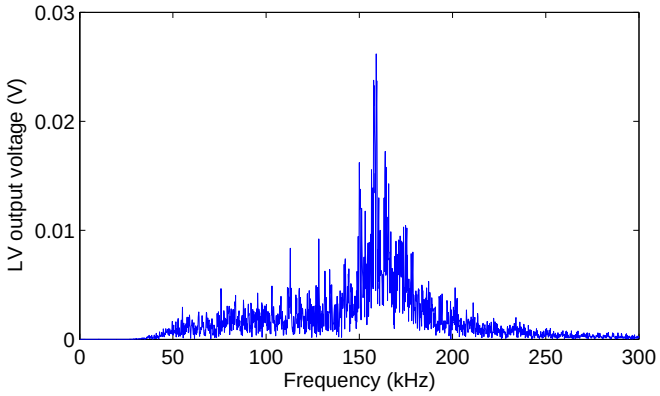


(b) Microphone Q3

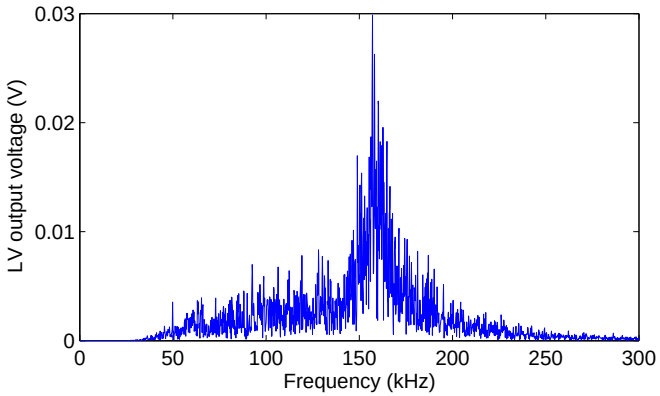


(c) Microphone Q6

Figure 6-36. FFT of the velocity measured by the laser vibrometer resulting from an acoustic impulse.

### 6.4.4 Noise Floor

The final tests are performed to characterized the minimum detectable signal of the microphones. As discussed in Section 4.2.3, the voltage amplifier is expected to give lower noise compared to the charge amplifier; this is verified experimentally.

The output referred noise PSD of the seven microphones with voltage amplifiers is given in Figure 6-37. There are many peaks at 60 $Hz$ and harmonic frequencies. There is also a region of increased noise between 30 $Hz$ and 70 $Hz$. Due to the excess spikes in the spectrum, it is unclear if this is noise generated by the microphone/amplifier system, or if it is interference. The measured PSD is closely matched between six of the microphones (I1, I2, M2, Q1, Q2, and Q3); these microphones have an average PSD at 1 $kHz$ of $1.96\times10^{-15}$ $V^2/Hz$ with a standard deviation of $0.10\times10^{-15}V^2/Hz$. Microphone M1 has a higher noise level of $2.68\times10^{-15}$ $V^2/Hz$.

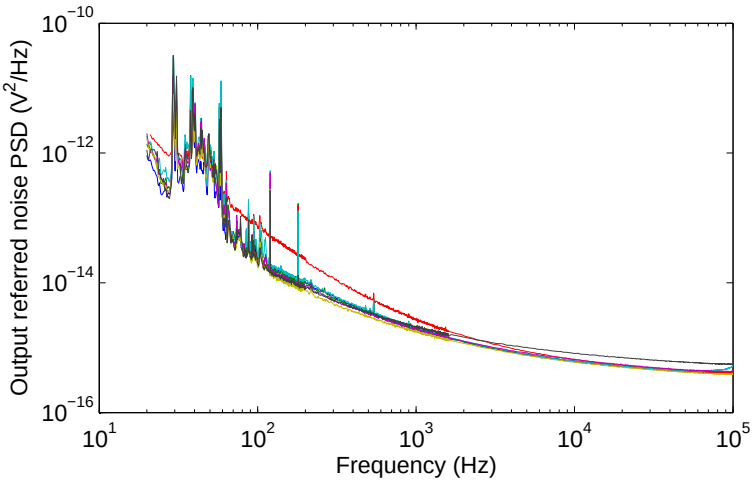


Figure 6-37. Measured output PSD noise for the voltage amplifier microphones.

The input referred noise is computed by dividing the square root of the measured PSD by the microphone sensitivity. The input referred noise for the seven voltage amplifier microphones is plotted in Figure 6-38. The input referred sound pressure noise in dB referenced to 20 $\mu Pa$ at 1 $kHz$ ranges from 21.8 $dB/\sqrt{Hz}$ to

23.7 $dB/\sqrt{Hz}$. The measured noise results for the voltage amplifier microphones are listed in Table 6-5.

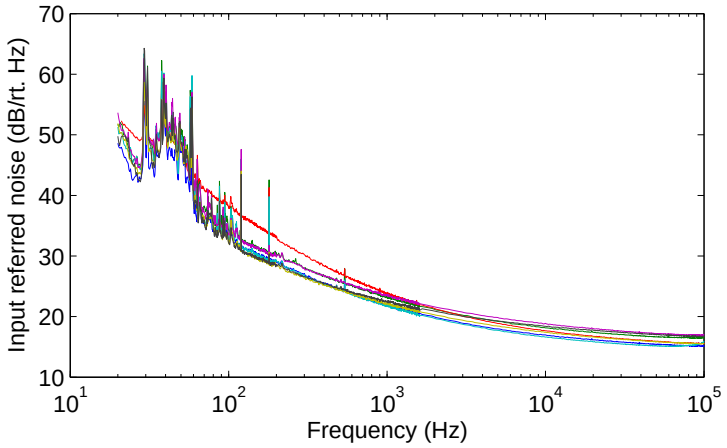


Figure 6-38. Input referred noise for the voltage amplifier microphones.

Table 6-5. Summary of the noise measurement results for microphones tested with voltage amplifiers.

| Microphone | Output noise ($V^2/Hz$) | Input noise ($dB/\sqrt{Hz}$) |
|---|---|---|
| I2 | $1.94\times10^{-15}$ | 21.8 |
| I3 | $1.91\times10^{-15}$ | 23.2 |
| M1 | $2.68\times10^{-15}$ | 23.6 |
| M2 | $2.06\times10^{-15}$ | 21.8 |
| Q1 | $1.97\times10^{-15}$ | 23.7 |
| Q2 | $1.82\times10^{-15}$ | 22.2 |
| Q3 | $2.10\times10^{-15}$ | 22.5 |

The measured output PSD noise spectrum of the charge amplifier microphones is shown in Figure 6-39. The average measured PSD at 1 $kHz$ is $7.66\times10^{-13}$ $V^2/Hz$. The input referred noise spectrum of the three microphones is plotted in Figure 6-40. The average input referred sound pressure noise at 1 $kHz$ is 41.5 $dB/\sqrt{Hz}$. The results for each of the microphones are listed in Table 6-6.

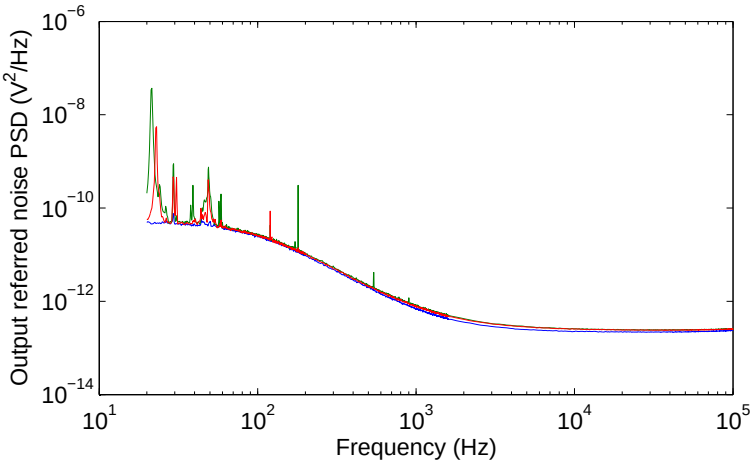


Figure 6-39. Measured output PSD noise for the charge amplifier microphones.

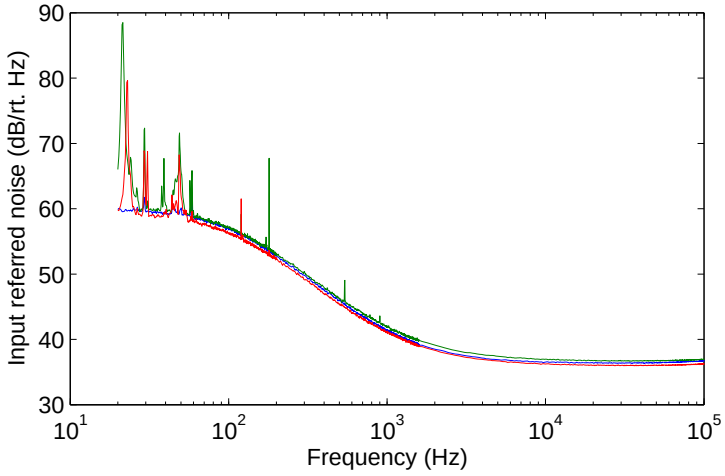


Figure 6-40. Input referred noise for the charge amplifier microphones.

Table 6-6. Summary of the noise measurement results for microphones tested with charge amplifiers.

| Microphone | Output noise $(V^2/Hz)$ | Input noise $(dB/\sqrt{Hz})$ |
|---|---|---|
| O1 | $7.09\times10^{-13}$ | 41.5 |
| O3 | $7.90\times10^{-13}$ | 41.8 |
| O6 | $8.01\times10^{-13}$ | 41.2 |

### 6.4.5 Discussion

The dual-backplate capacitive microphone has been characterized in terms of its linearity, frequency response, resonant frequency, and noise floor. While a limited number of devices have been measured, the data demonstrate the device performance. Distinct differences between the voltage amplifier and charge amplifier interface circuits have become apparent. The characterization results are given in Table 6-7. The charge amplifier degrades the noise performance and makes the microphone susceptible to vibration.

Table 6-7. Summary of the measurement results for all microphones

| Specification | Voltage amp | | Charge amp | |
|---|---|---|---|---|
| | Mean value | Standard deviation | Mean value | Standard deviation |
| Sensitivity ($\mu V/Pa$) | 166 | 14 | 368 | 18 |
| Max pressure ($dB$) | 164 | 1.6 | 166 | 1.7 |
| Noise floor ($dB/\sqrt{Hz}$) | 22.7 | 0.8 | 41.5 | 0.3 |
| Resonant frequency | - | - | 158 $kHz$ | 1 $kHz$ |

Comparing the results listed in Table 6-7 to the predictions given in Table 4-4, all measured values fall within the expected uncertainty of the estimates except for the noise floor of the microphone with the charge amplifier and the resonant frequency. The upper end of the predicted range of the charge amplifier microphone noise floor is 39.5 $dB$; while the average measured value is 41.5 $dB$. The measured output PSD of the charge amplifier is higher than predicted by a factor of 3.3. This could possibly be due to higher than expected parasitic capacitance or amplifier current noise. The lower end of the predicted resonant frequency is 161 $kHz$. This is 3 $kHz$ from the measured resonant frequency of 158 $dB$. This may be measurement error, or due to a slight compressive stress that may be present in the diaphragm. This would reduce the resonant frequency and increase the sensitivity. With the large uncertainty in the predicted microphone sensitivity, small deviations

between the measured sensitivity and the ideal predicted sensitivity have no significance. The minimum detectable signal is reported in Table 6-8 for various equivalent units. All figures except the A-weighted noise are for a 1 $Hz$ bin at 1 $kHz$.

Table 6-8. Minimum detectable signal expressed in various equivalent units.

| MDS | Value |
|---|---|
| A-weighted | 60.4 $dBA$ |
| Pressure (dB) | 22.7 $dB$ |
| Pressure (Pa) | 274 $Pa$ |
| Force | 15.1 $pN$ |
| Displacement | 75.4 $fm$ |
| Capacitance | 17.9 $zF$ |

The performance of the designed dual-backplate capacitive microphone is compared to the Brüel and Kjær 4138 condenser microphone and previous aeroacoustic microphones in Table 6-9. While the performance of the B&K microphone is not exceeded, the dual-backplate microphone exceeds the performance of all previous aeroacoustic MEMS microphones in terms of key specifications.

Table 6-9. Comparison of the designed dual-backplate capacitive microphone to the B&K 4138 condenser microphone and previous aeroacoustic MEMS microphones.

| Microphone | Radius | Max Pressure | Noise Floor | Bandwidth |
|---|---|---|---|---|
| Dissertation mic. | 230 $\mu m$ | 164 $dB$ | 22.7 $dB$ | 4 $Hz$–158 $kHz$[‡] |
| B&K 4138 [3] | 1.6 $mm$ | 168 $dB$ | 20 $dB$ | 6.5 $Hz$–140 $kHz$ |
| Arnold et al. [13] | 500 $\mu m$ | 160 $dB$ | 52 $dB$ | 10 $Hz$–100 $kHz$[†] |
| Scheeper et al. [15] | 1.95 $mm$ | 141 $dB$ | 23 $dBA$ | 251 $Hz$–20 $kHz$ |
| Horowitz et al. [112] | 900 $\mu m$ | 169 $dB$ | 48 $dB$ | 100 $Hz$–50.8 $kHz$[‡] |
| Pedersen [111] | 180 $\mu m$ | 140 $dB$ | 22 $dB$ | 50 $Hz$–75 $kHz$[‡] |

1 $Hz$ bin at 1 $kHz$. [†] Predicted bandwidth. [‡] Resonant frequency.

# CHAPTER 7
# CONCLUSIONS AND FUTURE WORK

The research goals, objectives, and key results are summarized in this chapter. The major contributions of this research are highlighted. Finally, suggestions for improvements and extensions to this work are provided.

## 7.1 Conclusions

As airlines continue to work towards reducing the noise impact of their fleets, aircraft manufacturers will continue to drive research that lowers the noise levels generated by their aircraft. To carry out this work, a unique type of microphone is needed; it should have an extremely wide operating range, while providing high fidelity. Currently, such microphones are very costly. This research sought to develop a microphone suitable for aeroacoustic measurements using MEMS technology; with the aim of a greatly reduced cost compared to traditional microphones.

Previously developed microphones for aeroacoustic applications have been studied. While great strides have been made in developing such a microphone; the literature review identifies areas of needed improvement — in particular extending the dynamic range. Existing MEMS microphones either have a sufficient noise floor or maximum pressure. However, no MEMS microphone developed to date approaches both the lower and upper end of the Brüel and Kjær 4138's dynamic range. With a noise floor of 22 $dB/\sqrt{Hz}$, a maximum pressure of 164 $dB$, and a resonant frequency of 158 $kHz$, the developed dual-backplate capacitive microphone makes a great leap forward towards the desired performance specifications; exceeding the performance of existing MEMS aeroacoustic microphones.

In addition to developing the first dual-backplate capacitive microphone for aeroacoustic measurements, other contributions of this research are as follows. The SUMMiT V MEMS foundry process at Sandia National Laboratories has been applied in a novel way to MEMS microphone design. The multi-level, planarized

polysilicon process has been leveraged to create a dual-backplate capacitive microphone. The greatest weakness of this process for the microphone is the variability it introduces into the sensitivity. However, the well controlled flatness and stress were critical for the success of this research.

The experimental characterization gives a comparison between the performance of voltage amplifier and charge amplifier interface circuits for a low-capacitance MEMS microphone. The voltage amplifier is clearly superior in terms of dynamic range, giving a noise floor 19 $dB$ lower at 1 $kHz$. Also demonstrated was the importance of good packaging. The designed package robustly contained the voltage amplifier. While the charge amplifier was external to the microphone package separated by a length of cable. This results in excessive 60 $Hz$ interference during measurements when the microphone was tested with the charge amplifier. In addition, the package did not adequately support the cables. This resulted in vibration corrupting the charge amplifier frequency response measurements.

In addition to the presented experimental characterization, a detailed theoretical background has been discussed. The single-backplate condenser and dual-backplate condenser microphones have been compared in terms of electrostatic behavior, dynamic range, and stability. Both types of microphones have been considered theoretically with a charge amplifier and a voltage amplifier. The microphone theory is applicable to the design of a capacitive microphone for arbitrary application, including audio and aeroacoustic.

## 7.2 Recommendations for Future Work

There are several areas where this work can be further developed. The designed microphone has a resonant frequency of 158 $kHz$. However, the frequency response measurements only extend up to 20 $kHz$ (25 $kHz$ for non-plane waves). A significant improvement to the microphone characterization would be to extend the range of the frequency response measurement. At a minimum, the microphone

should be characterized to at least 100 $kHz$ to qualify the microphone over the entire desired frequency range. Ideally, the frequency response can be measured over the full bandwidth of the microphone. There are several challenges to overcome to make this measurement a reality. An acoustic source is needed to generate sound over this frequency range. Typical audio drivers are limited to around 20 $kHz$. While ultrasonic drivers exist, they are typically designed for a narrow operating bandwidth. In addition to the source, an experimental setup must be developed to produce a controlled sound field. At 100 $kHz$, the wavelength of sound in air is 3.4 $mm$; thus a plane wave tube would need a cross section with a 1.7 $mm$ side length. This is impractical, as a reference microphone and a packaged MEMS microphone will not fit in this cross section. Therefore a free field measurement is likely to be the best option.

Another area for improvement is the measurement of the total harmonic distortion. For this measurement, the microphone would ideally have a pure sine wave incident pressure. Thus any harmonics generated would be due to non-linearities in the microphone. Due to limitations in the experimental setup, excessive non-linearities were produced when generating sound pressure levels approaching 160 $dB$. However, even if an ideal signal generator, amplifier, and acoustic driver were found; non-linearities would still exist due to the propagation of the high amplitude sound wave. An experimental setup may be developed to pre-distort the signal sent to the acoustic driver, such that the microphone receives a pure sine wave. R. Holman demonstrated using a feed-forward loop to pre-distort a signal to achieve a pure sine wave for a synthetic jet actuator [133]. This technique can be applied to the acoustic test setup for the THD characterization.

In order for the designed microphone to be suitable for use in the field, several improvements are necessary to the microphone die and package. First, the process flow would need to be modified to provide bond pad metallization.

This would allow for a more robust wire bond; improving yield and reducing the chance of failure after packaging. Furthermore, with more flexibility in the process flow, a design optimization could be performed potentially improving the device performance. The die could be redesigned with only one microphone per die. This has the potential to reduce the die size to 1 $mm^2$. Furthermore, interface circuitry for one microphone would be needed per package. This would greatly reduce the package size. Finally, a robust, shielded package is needed for reliability and immunity to electromagnetic interference.

There are several other experiments that can provided additional insight for the microphone behavior and implemented dual-backplate structure. The laser vibrometer may be used to measure the mode shape of the diaphragm. By positioning the laser in the center of the top backplate holes across the diameter of the diaphragm, 23 scan points may be obtained. In addition, the LV may be used to measure the response of the top backplate due to acoustic and electrical excitations. An experimental setup utilizing a shaker and a reference accelerometer may be used to determine the sensitivity of the microphone to vibration inputs. Finally, the helium PWT setup could be improved to include a method for measuring the concentration of helium in the tube. This may allow for improved repeatability and control of the experiment.

### 7.3 Recommendations for Future Microphone Designs

Based on experience in handling and packaging the microphone, several suggestions are provided for future microphone projects. These are especially applicable to projects where portions of the fabrication may possibly be carried out on individual die.

In attempts to develop a successful bond process for the polysilicon bond pads, several techniques were attempted. Several metallization strategies were tested. This involved patterning photoresist over the bond pads. There was some

difficulty in obtaining an even coating of photoresist extending to the bond pads. This was because of close proximity of the bond pads to the die edge. This issue was observed — to a lesser extent — for the backside photoresist for the DRIE. A minimum distance of 500 $\mu m$ is recommended from the die edge to features patterned on individual die. The bond pad spacing and size was made small to accommodate the number of devices on the die; 100 $um$ size pads with a 50 $\mu m$ space were used. While this is sufficient for automated bonding, it leaves little room for error for laboratory assembly. A bond pad layout with a minimum 200 $\mu m$ side length and pitch is recommended for ease in bonding. In addition, this allows alternative bonding options such as epoxy. However, these issues can be mitigated by having a robust bond pad metallization. The polysilicon bond pads proved difficult to bond to. An external company was needed to produce a reliable gold ball bond to the polysilicon pads.

Finally, it is recommended to consider the circuitry and packaging early in the design process. The noise floor achieved for this microphone was enabled via a high quality amplifier. A robust package will facilitate experimental characterization. The packaging used for this microphone was easy to use; allowing for quick transition from one device to the next. However, it did not provide sufficient shielding. The package could be improved by surrounding the microphone and wires with a metal shield. Ideally a shielded cable would enter the shielded package housing and connect to the microphone internally. However, an insulating exterior provides flexibility in the experimental setup and can help prevent ground loops.

# APPENDIX A
# LUMPED ELEMENT MODEL OF A CLAMPED CIRCULAR PLATE

In this appendix, the mechanical lumped parameters for a clamped circular plate are found. This includes the storage of potential energy represented by a lumped compliance and the storage of kinetic energy represented by a lumped mass. These results are used in Section 3.2 to develop the lumped element model of a dual-backplate condenser microphone.

## A.1 Lumped Compliance

To find the lumped compliance of the plate, the potential co-energy stored in the deflected plate is equated to the potential energy stored in a lumped spring with a deflection equal to the center deflection of the plate. For a linear spring, the potential co-energy is equal to the potential energy [21]. The potential co-energy may be generally expressed as

$$W_{PE}^{*} = \int_{0}^{F_0} w\left(F\right)\, dF. \tag{A–1}$$

The limits of the integration are from 0 to $F_0$, which is the force that corresponds to the final center deflection, $w(0)$. Rewriting in terms of uniform pressure, $p$, acting on an area, $A$, the potential co-energy is given by

$$W_{PE}^{*} = \int_{0}^{p_0} w\left(p\right) A\, dp. \tag{A–2}$$

The deflection of the plate as a function of pressure is known from Equation 3–6. It is noted that the deflection, $w$, is also a function of $r$. The potential energy stored in an infinitesimal section of the plate of area $dA$ is given by

$$dW_{PE}^{*} = \int_{0}^{p_0}\int_{0}^{A} w\left(p, r\right) dA\, dp. \tag{A–3}$$

Assuming an axisymmetric deflection, the area $dA$ can be expressed as $2\pi r\,dr$. Therefore, by integrating over $r$, the total potential co-energy is

$$W^*_{PE} = \int_0^a \int_0^{p_0} w\,(p,r)\;dp\,2\pi r\,dr. \tag{A–4}$$

Now, Equation 3–6 is substituted in for $w\,(p,r)$, which gives

$$W^*_{PE} = \int_0^a \int_0^{p_0} \frac{pa^4}{64D}\left[1-\left(\frac{r}{a}\right)^2\right]^2 dp\,2\pi r\,dr. \tag{A–5}$$

The integral over $p$ can be directly evaluated, thus Equation A–5 becomes

$$W^*_{PE} = p_0^2\,\frac{\pi a^4}{64D}\int_0^a \left[1-\left(\frac{r}{a}\right)^2\right]^2 r\,dr. \tag{A–6}$$

The integral over $r$ is equal to $a^2/6$, thus the potential co-energy is equal to

$$W^*_{PE} = p_0^2\,\frac{\pi a^4}{64D}\,\frac{a^2}{6} = p_0^2\,\frac{\pi a^6}{6\cdot 64D}. \tag{A–7}$$

From Equation 3–8, the incident pressure, $p_0$, at which the center deflection is $w(0)$, is expressed as

$$p_0 = \frac{-64D}{a^4}w(0). \tag{A–8}$$

By substituting Equation A–8 into Equation A–7, the potential co-energy becomes,

$$W^*_{PE} = \frac{(64D)^2\,w(0)^2}{a^8}\,\frac{\pi a^6}{6\cdot 64D}; \tag{A–9}$$

which is simplified to

$$W^*_{PE} = \frac{1}{2}\frac{64\pi D}{3a^2}w(0)^2. \tag{A–10}$$

As was stated earlier, for a linear spring, the potential energy is equal to the potential co-energy. The potential energy in a lumped spring is given by $W_{PE} = \frac{1}{2}k\,w(0)^2$, therefore the lumped mechanical compliance is given by $C_m =$

$\frac{1}{2}\frac{1}{W_{PE}}\,w(0)^2$. The lumped mechanical compliance of the plate, $C_{m,p}$, is [21]

$$C_{m,p} = \frac{3a^2}{64\pi D}. \tag{A–11}$$

## A.2 Lumped Mass

The lumped mass is found by comparing the kinetic energy in the distributed plate to the kinetic energy in the piston mass [21]. The kinetic energy of a mass, $m$, with a velocity, $v$, is given by $\frac{1}{2}mv^2$. For the plate with a non-uniform velocity, the kinetic energy in a infinitesimal mass is

$$dW_{KE} = \frac{1}{2}v^2\,dm. \tag{A–12}$$

Therefore, the total kinetic energy in the plate is given by

$$W_{KE} = \frac{1}{2}\int v(r)^2\,dm. \tag{A–13}$$

The velocity at the center of the diaphragm is $v(0)$ and the velocity of the diaphragm as a function of $r$ is

$$v(r) = v(0)\left[1-\left(\frac{r}{a}\right)^2\right]^2. \tag{A–14}$$

Assuming a homogenous plate with mass per unit area $\rho'$ equal to $\rho h$, where the plate has a density $\rho$ and thickness $h$, the differential mass, $dm$, is written as $\rho' 2\pi r\,dr$. Now Equation A–13 becomes

$$W_{KE} = \pi\rho' v(0)^2 \int_0^a \left[1-\left(\frac{r}{a}\right)^2\right]^4 r\,dr. \tag{A–15}$$

Evaluating the integral gives the following result for the kinetic energy in the plate,

$$W_{KE} = \frac{v(0)^2}{2}\frac{\pi a^2\rho'}{5}. \tag{A–16}$$

From Equation A–16, the lumped mechanical mass of the plate is [21]

$$M_{m,p} = \frac{\pi a^2 \rho'}{5} = \frac{\pi a^2 \rho h}{5}. \tag{A–17}$$

# APPENDIX B
# MICROPHONE FREQUENCY RESPONSE

In this appendix, the approximate frequency response of the dual backplate microphone will be derived using lumped element modeling. The equivalent circuit of the microphone is shown in Figure B-1. The expressions for the lumped elements are given in Table 3-5.

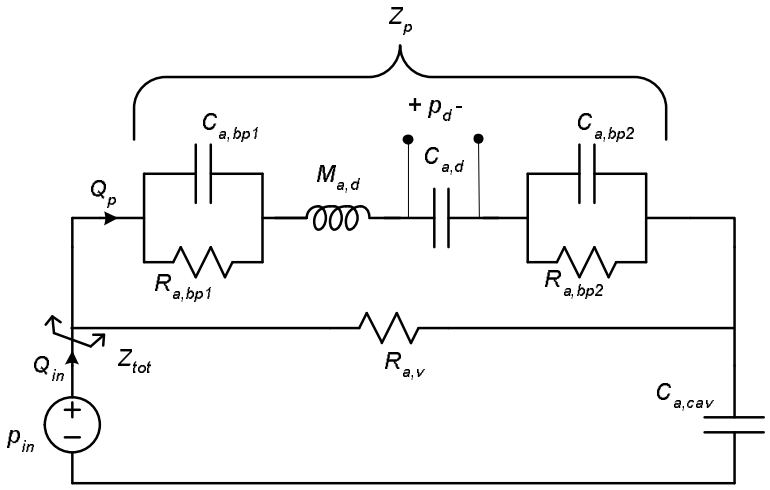


Figure B-1. Lumped element model of the dual-backplate microphone showing relevant impedances and volume velocities.

Using basic circuit analysis techniques [124], the frequency response of the microphone will be found. The electrical relation $V = IR$ is analogous to $P = QR$ in the acoustic domain, assuming an impedance analogy [21]. The quantity $p_d/p_{in}$ is found as a function of frequency. The output voltage of the microphone, as given in Equation 3–78 or Equation 3–99, is proportional to to the pressure acting on the diaphragm. This pressure is given by $p_d$ as shown in Figure B-1.

The pressure, $p_d$, is given by

$$p_d = Q_p \frac{1}{sC_{a,d}}, \tag{B–1}$$

where $Q_p$ is the volume velocity flowing through the plates of the microphone. The impedance of the compliance is given by $1/sC_{a,d}$, where $s$ is the complex

frequency in the Laplace domain [17]. The volume velocity $Q_p$ is found using a volume velocity divider relation,

$$Q_p = \frac{R_{a,v}}{Z_p + R_{a,v}} Q_{in}. \tag{B–2}$$

The total volume velocity flowing into the microphone, $Q_{in}$ is given by

$$Q_{in} = \frac{p_{in}}{Z_{tot}}, \tag{B–3}$$

where $Z_{tot}$ is the total impedance of the microphone.

To find an expression for the frequency response of the microphone, the values of the various impedances must first be found. First the impedance of the diaphragm, $Z_{a,d}$, and each backplate, $Z_{a,bp1}$ and $Z_{a,bp2}$, are found. The diaphragm impedance is the series combination of the diaphragm compliance, mass, and radiation mass. The impedance of each backplate is the parallel combination of the backplate compliance and resistance. The three impedances are as follows:

$$\begin{aligned} Z_{a,d} &= \frac{1}{sC_{a,d}} + sM_{a,d}, \\ &= \frac{s^2 M_{a,d} C_{a,d} + 1}{sC_{a,d}}; \end{aligned} \tag{B–4}$$

$$\begin{aligned} Z_{a,bp1} &= \frac{1}{C_{a,bp1}} /\!/ R_{a,bp1}, \\ &= \frac{R_{a,bp1}}{1 + R_{a,bp1} C_{a,bp1}}; \end{aligned} \tag{B–5}$$

$$\begin{aligned} Z_{a,bp2} &= \frac{1}{C_{a,bp2}} /\!/ R_{a,bp2}, \\ &= \frac{R_{a,bp2}}{1 + R_{a,bp2} C_{a,bp2}}. \end{aligned} \tag{B–6}$$

The $/\!/$ symbol is used to indicate the parallel combination of two elements.

Therefore the impedance of the series combination of the three plates is

$$Z_p = \frac{R_{a,bp1}}{1 + R_{a,bp1}C_{a,bp1}} + \frac{s^2 M_{a,d}C_{a,d} + 1}{sC_{a,d}} + \frac{R_{a,bp2}}{1 + R_{a,bp2}C_{a,bp2}}. \tag{B–7}$$

By finding a common denominator, the three terms can be combined as follows,

$$Z_p = \frac{\left\{ \begin{array}{l} sC_{a,d}R_{a,bp1}\left(1 + R_{a,bp2}C_{a,bp2}\right) + sC_{a,d}R_{a,bp2}\left(1 + R_{a,bp1}C_{a,bp1}\right) \\ + \left[s^2 M_{a,d}C_{a,d} + 1\right]\left(1 + R_{a,bp1}C_{a,bp1}\right)\left(1 + R_{a,bp2}C_{a,bp2}\right) \end{array} \right\}}{\left(1 + R_{a,bp1}C_{a,bp1}\right)\left(1 + R_{a,bp2}C_{a,bp2}\right) sC_{a,d}}. \tag{B–8}$$

The total impedance of the microphone is given by

$$Z_{tot} = \frac{R_{a,v}Z_p}{R_{a,v} + Z_p} + \frac{1}{sC_{a,cav}}, \tag{B–9}$$

which is re-written as

$$Z_{tot} = \frac{sC_{a,cav}R_{a,v}Z_p + R_{a,v} + Z_p}{sC_{a,cav}\left(R_{a,v} + Z_p\right)}. \tag{B–10}$$

By combining Equation B–2, Equation B–3, and Equation B–10, the volume velocity $Q_p$ is

$$\begin{aligned} Q_p &= p_{in}\frac{R_{a,v}}{\cancel{R_{a,v} + Z_p}}\frac{sC_{a,cav}\cancel{\left(R_{a,v} + Z_p\right)}}{sC_{a,cav}R_{a,v}Z_p + R_{a,v} + Z_p} \\ &= \frac{sC_{a,cav}R_{a,v}}{\left(1 + sC_{a,cav}R_{a,v}\right)Z_p + R_{a,v}}. \end{aligned} \tag{B–11}$$

Therefore, the frequency response of the microphone is found by substituting Equation B–11 into Equation B–1,

$$H_{mic} = \frac{sC_{a,cav}R_v}{sC_{a,d}\left(1 + sC_{a,cav}R_{a,v}\right)Z_p + sC_{a,d}R_{a,v}}. \tag{B–12}$$

The final expression for the frequency response is expressed completely in terms of lumped elements by substituting Equation B–8 into Equation B–12, however this is too long to write out here. A simplified expression is obtained by

assuming the compliance of each backplate is negligible[1] . Now, Equation B–8 becomes

$$Z_p^s = \frac{s^2\left(M_{a,rad}+M_{a,d}\right)C_{a,d} + sC_{a,d}\left(R_{a,bp1}+R_{a,bp2}\right)+1}{sC_{a,d}}. \tag{B–13}$$

Substituting Equation B–13 into Equation B–12 results in

$$H_{mic}^s = \frac{sC_{a,cav}R_{a,v}}{\left(1+sC_{a,cav}R_{a,v}\right)\left[s^2M_{a,d}C_{a,d}+sC_{a,d}\left(R_{a,bp1}+R_{a,bp2}\right)+1\right]+sC_{a,d}R_{a,v}}. \tag{B–14}$$

By expanding Equation B–14 and collecting terms by powers of $s$, the final expression for the simplified frequency response of the dual-backplate microphone is

$$H_{mic}^s = \frac{sC_{a,cav}R_{a,v}}{\left\{\begin{array}{l} s^3M_{a,d}C_{a,d}C_{a,cav}R_{a,v} \\ +s^2\Big[M_{a,d}C_{a,d}+C_{a,d}C_{a,cav}\big(R_{a,bp1}+R_{a,bp2}\big)R_{a,v}\Big] \\ +s\Big[C_{a,d}\big(R_{a,bp1}+R_{a,bp2}\big)+\big(C_{a,cav}+C_{a,d}\big)R_{a,v}\Big]+1 \end{array}\right\}}. \tag{B–15}$$

The pressure across each backplate can be found in a manner similar to Equation B–1. The diaphragm, top backplate, and bottom backplate share the same flow, thus the pressure across the top backplate is

$$p_{bp1} = Q_pZ_{bp1} \tag{B–16}$$

and the pressure across the bottom backplate is

$$p_{bp2} = Q_pZ_{bp2} \tag{B–17}$$

Discussion providing physical insight for the results obtained in Equation B–14 and Equation B–15 is given in Section 3.2.6.

[1] This assumption is discussed in Section 3.2

# APPENDIX C
# UNCERTAINTY ANALYSIS OF MICROPHONE PERFORMANCE

The uncertainty for the theoretical performance metrics is derived in this appendix. The formulations presented here utilize results obtained in Chapter 3 and Chapter 4. The sensitivity of the dual-backplate capacitive microphone is analyzed for both a charge amplifier and voltage amplifier interface circuit. Furthermore, the predictions for the resonant frequency and noise floor are explored. The final section of this appendix describes the technique used to estimate the measured sensitivity and 95 % confidence interval.

First, consider the uncertainty of a quantity $G$ which is a function of $n$ parameters, $x_1, x_2, ...x_n$, such that

$$G = f\left(x_1, x_2, ..., x_n\right). \tag{C–1}$$

Each parameter, $x_i$, is assumed to have an uncertainty such that it has a variation of $\pm U_{x_i}$ for a given confidence level. It follows that the uncertainty in $G$ is [134]

$$U_G = \sqrt{\sum_i \left(\frac{\partial G}{\partial x_i} U_{x_i}\right)^2}. \tag{C–2}$$

The previously derived expressions are analyzed according to Equation C–2 to determine the uncertainty in the theoretical microphone performance.

## C.1 Theoretical Sensitivity Uncertainty

The sensitivity for a dual-backplate capacitive microphone is derived in Section 3.2.3 and simplified results for both a microphone with a charge amplifier and a voltage amplifier are given in Section 4.2.1.

### C.1.1 Microphone with Charge Amplifier

The uncertainty analysis for the sensitivity of the microphone with a charge amplifier begins with Equation 4–9, which is re-written explicitly in terms of both

the top air gap, $g_{1_0}$, and the bottom air gap, $g_{2_0}$,

$$S_{ca} = \left\{ \frac{1}{3} \frac{V_B}{g_{1_0}} \frac{C_{1_0}}{C_f} + \frac{1}{3} \frac{V_B}{g_{2_0}} \frac{C_{2_0}}{C_f} \right\} \frac{a^4}{64D} \frac{C_{a,cav}}{C_{a,cav} + C_{a,d}}. \tag{C–3}$$

Neglecting the cavity stiffening and expressing the sensitivity in terms of only material parameters and geometry parameters, Equation C–3 becomes

$$S_{ca} = \frac{1}{3} \frac{a_d^6}{64D} \frac{V_B}{g_{1_0}^2} \frac{\epsilon_0 \pi}{C_f} + \frac{1}{3} \frac{a_d^6}{64D} \frac{V_B}{g_{2_0}^2} \frac{\epsilon_0 \pi}{C_f}, \tag{C–4}$$

neglecting differences in the top and bottom capacitor area.

Equation C–4 is the sum of two components, $S_{1_{ca}}$ and $S_{2_{ca}}$; where $S_{1_{ca}}$ is a function of $g_{1_0}$ and $S_{2_{ca}}$ is a function of $g_{2_0}$. They are identical expect for the air gap. Thus the sensitivity of Equation C–4 to changes in the various parameters is solved for by considering the first part separately. The results are then directly applied to the second part, substituting $g_{2_0}$ for $g_{1_0}$.

This analysis focuses on parameters inherent to the microphone. Thus, the uncertainty of three parameters are considered: the diaphragm radius, $a_d$, the flexural rigidity, $D$, and the air gap $g_{1_0}$. For this analysis, it is assumed that $V_B$ and $C_f$ are measured to sufficient accuracy to not affect the uncertainty of the predicted sensitivity.

However, the flexural rigidity, $D$, is a function of several parameters. Therefore uncertainty analysis must first be performed on it. Equation 3–3 gives the expression for $D$, which is a function of the modulus of elasticity, $E$, the diaphragm thickness, $h_d$, and Poisson's ratio, $\nu$. The sensitivity of $D$ to these parameters is

$$\frac{\partial D}{\partial E} = \frac{h_d^3}{12\left(1-\nu^2\right)}, \tag{C–5}$$

$$\frac{\partial D}{\partial h_d} = \frac{3Eh_d^2}{12\left(1-\nu^2\right)}, \tag{C–6}$$

and

$$\frac{\partial D}{\partial \nu} = \frac{\nu E h_d^3}{6\left(1-\nu^2\right)^2}. \tag{C–7}$$

The total uncertainty in $D$ is

$$U_D = \left(\frac{\partial D}{\partial E}U_E + \frac{\partial D}{\partial h_d}U_{h_d} + \frac{\partial D}{\partial \nu}U_\nu\right)^{\frac{1}{2}}. \tag{C–8}$$

The sensitivity of $S_{1_{ca}}$ to changes in $a_d$ is

$$\frac{\partial S_{1_{ca}}}{\partial a_d} = 2\frac{a_d^5}{64D}\frac{V_B}{g_{1_0}^2}\frac{\epsilon_0 \pi}{C_f}. \tag{C–9}$$

The sensitivity of $S_{1_{ca}}$ to variations in $D$ is

$$\frac{\partial S_{1_{ca}}}{\partial D} = -\frac{1}{3}\frac{a_d^6}{64D^2}\frac{V_B}{g_{1_0}^2}\frac{\epsilon_0 \pi}{C_f}. \tag{C–10}$$

Finally, the $S_{1_{ca}}$ varies with $g_{1_0}$ as

$$\frac{\partial S_{1_{ca}}}{\partial g_{1_0}} = -\frac{2}{3}\frac{a_d^6}{64D}\frac{V_B}{g_{1_0}^3}\frac{\epsilon_0 \pi}{C_f}. \tag{C–11}$$

The total uncertainty in $S_{ca}$, is given by

$$U_{S_{ca}} = \left(\begin{array}{l}\left(\frac{\partial S_{1_{ca}}}{\partial a_d}U_{a_d} + \frac{\partial S_{2_{ca}}}{\partial a_d}U_{a_d}\right)^2 + \left(\frac{\partial S_{1_{ca}}}{\partial D}U_D + \frac{\partial S_{2_{ca}}}{\partial D}U_D\right)^2 \\ + \left(\frac{\partial S_{1_{ca}}}{\partial g_{1_0}}U_{g_{1_0}}\right)^2 + \left(\frac{\partial S_{2_{ca}}}{\partial g_{2_0}}U_{g_{2_0}}\right)^2\end{array}\right)^{\frac{1}{2}}, \tag{C–12}$$

where the $\frac{\partial S_{2_{ca}}}{\partial x_i}$ terms are found by inspection from Equation C–9, Equation C–10, and Equation C–11.

### C.1.2 Microphone with Voltage Amplifier

The uncertainty for the microphone sensitivity with a voltage amplifier is treated in a similar manner as the previous derivation. The sensitivity for a dual-backplate capacitive microphone with a charge amplifier, given by Equation 4–10, is

re-written in terms of material and geometry parameters,

$$S_{va} = \frac{1}{3}\frac{V_B}{g_{1_0}}\frac{a_d^4}{64D}\frac{1}{1+\frac{g_{1_0}}{g_{2_0}}+\frac{C_p g_{1_0}}{\epsilon_0 \pi a_d^2}} + \frac{1}{3}\frac{V_B}{g_{2_0}}\frac{a_d^4}{64D}\frac{1}{1+\frac{g_{2_0}}{g_{1_0}}+\frac{C_p g_{2_0}}{\epsilon_0 \pi a_d^2}}. \tag{C–13}$$

Similar to Equation C–4, $S_{va}$ is the sum of two components, $S_{1_{va}}$ and $S_{2_{va}}$. Each of these components is a function of both $g_{1_0}$ and $g_{2_0}$; however, due to the similarity between them, $\frac{\partial S_{2_{va}}}{\partial x_i}$ is simply given by the expressions for $\frac{\partial S_{1_{va}}}{\partial x_i}$ with $g_{1_0}$ and $g_{2_0}$ swapped.

Beginning with $a_d$, the sensitivity of $S_{1_{va}}$ to changes in $a_d$ is

$$\frac{\partial S_{1_{va}}}{\partial a_d} = \frac{4}{3}\frac{V_B}{g_{1_0}}\frac{a_d^3}{64D}\frac{1}{1+\frac{g_{1_0}}{g_{2_0}}+\frac{C_p g_{1_0}}{\epsilon_0 \pi a_d^2}} + \frac{2}{3}\frac{V_B}{g_{1_0}}\frac{a_d^5}{64D}\frac{1}{\left(1+\frac{g_{1_0}}{g_{2_0}}+\frac{C_p g_{1_0}}{\epsilon_0 \pi a_d^2}\right)^2}. \tag{C–14}$$

The sensitivity of $S_{1_{va}}$ to $D$ is

$$\frac{\partial S_{1_{va}}}{\partial D} = -\frac{1}{3}\frac{V_B}{g_{1_0}}\frac{a_d^4}{64D^2}\frac{1}{1+\frac{g_{1_0}}{g_{2_0}}+\frac{C_p g_{1_0}}{\epsilon_0 \pi a_d^2}}. \tag{C–15}$$

The sensitivity of $S_{1_{va}}$ to $g_{1_0}$ is

$$\frac{\partial S_{1_{va}}}{\partial g_{1_0}} = -\frac{1}{3}\frac{V_B}{g_{1_0}^2}\frac{a_d^4}{64D}\frac{1}{1+\frac{g_{1_0}}{g_{2_0}}+\frac{C_p g_{1_0}}{\epsilon_0 \pi a_d^2}} - \frac{1}{3}\frac{V_B}{g_{1_0}}\frac{a_d^4}{64D}\frac{\frac{1}{g_{2_0}}+\frac{C_p}{\epsilon_0 \pi a_d^2}}{1+\frac{g_{1_0}}{g_{2_0}}+\frac{C_p g_{1_0}}{\epsilon_0 \pi a_d^2}}. \tag{C–16}$$

Finally, the sensitivity of $S_{1_{va}}$ to $g_{2_0}$

$$\frac{\partial S_{1_{va}}}{\partial g_{2_0}} = \frac{1}{3}\frac{V_B}{g_{1_0}}\frac{a_d^4}{64D}\frac{\frac{g_{1_0}}{g_{2_0}^2}}{1+\frac{g_{1_0}}{g_{2_0}}+\frac{C_p g_{1_0}}{\epsilon_0 \pi a_d^2}}. \tag{C–17}$$

Using Equation C–14, Equation C–15, Equation C–16, and Equation C–17, the total uncertainty in $S_{va}$ is

$$U_{S_{va}} = \left( \begin{array}{l} \left(\frac{\partial S_{1_{va}}}{\partial a_d}U_{a_d} + \frac{\partial S_{2_{va}}}{\partial a_d}U_{a_d}\right)^2 + \left(\frac{\partial S_{1_{va}}}{\partial D}U_D + \frac{\partial S_{2_{va}}}{\partial D}U_D\right)^2 \\ + \left(\frac{\partial S_{1_{va}}}{\partial g_{1_0}}U_{g_{1_0}} + \frac{\partial S_{2_{va}}}{\partial g_{1_0}}U_{g_{1_0}}\right)^2 + \left(\frac{\partial S_{1_{va}}}{\partial g_{2_0}}U_{g_{2_0}} + \frac{\partial S_{2_{va}}}{\partial g_{2_0}}U_{g_{2_0}}\right)^2 \end{array} \right)^{\frac{1}{2}} \tag{C–18}$$

## C.2 Theoretical Resonant Frequency Uncertainty

The resonant frequency of the dual-backplate capacitive microphone is given by Equation 3–181. For the resonant frequency uncertainty analysis, the electrostatic compliance and cavity stiffening are neglected. Thus, the resonant frequency is simplified to

$$\omega_0 = \frac{1}{\sqrt{M_{a,d}C_{a,d}}}, \tag{C–19}$$

Substituting expressions for the acoustic mass (Equation 3–138) and the acoustic compliance (Equation 3–139) into Equation C–19, the resonant frequency is re-written as

$$\omega_0 = \left(\frac{9}{80}\frac{a_d^4\rho\left(1-\nu^2\right)}{Eh_d^2}\right)^{-\frac{1}{2}}. \tag{C–20}$$

The sensitivity of $\omega_0$ to the parameters, $a_d$, $\rho$, $\nu$, $E$, and $h_d$, are as follows:

$$\frac{\partial\omega_0}{\partial a_d} = -\frac{9}{40}\frac{a_d^3\rho\left(1-\nu^2\right)}{Eh_d^2}\left(\frac{9}{80}\frac{a_d^4\rho\left(1-\nu^2\right)}{Eh_d^2}\right)^{-\frac{3}{2}}, \tag{C–21}$$

$$\frac{\partial\omega_0}{\partial \rho} = -\frac{9}{160}\frac{a_d^4\left(1-\nu^2\right)}{Eh_d^2}\left(\frac{9}{80}\frac{a_d^4\rho\left(1-\nu^2\right)}{Eh_d^2}\right)^{-\frac{3}{2}}, \tag{C–22}$$

$$\frac{\partial\omega_0}{\partial \nu} = \frac{9}{80}\frac{a_d^4\rho\nu}{Eh_d^2}\left(\frac{9}{80}\frac{a_d^4\rho\left(1-\nu^2\right)}{Eh_d^2}\right)^{-\frac{3}{2}}, \tag{C–23}$$

$$\frac{\partial\omega_0}{\partial E} = \frac{9}{160}\frac{a_d^4\rho\left(1-\nu^2\right)}{E^2h_d^2}\left(\frac{9}{80}\frac{a_d^4\rho\left(1-\nu^2\right)}{Eh_d^2}\right)^{-\frac{3}{2}}, \tag{C–24}$$

and

$$\frac{\partial\omega_0}{\partial h_d} = \frac{9}{80}\frac{a_d^4\rho\left(1-\nu^2\right)}{Eh_d^3}\left(\frac{9}{80}\frac{a_d^4\rho\left(1-\nu^2\right)}{Eh_d^2}\right)^{-\frac{3}{2}}. \tag{C–25}$$

The final expression for the resonant frequency uncertainty is

$$U_{\omega_0} = \left(\begin{array}{l}\left(\frac{\partial\omega_0}{\partial a_d}U_{a_d}\right)^2+\left(\frac{\partial\omega_0}{\partial \rho}U_{\rho}\right)^2+\left(\frac{\partial\omega_0}{\partial \nu}U_{\nu}\right)^2 \\ +\left(\frac{\partial\omega_0}{\partial E}U_{E}\right)^2+\left(\frac{\partial\omega_0}{\partial h_d}U_{h_d}\right)^2\end{array}\right)^{\frac{1}{2}}. \tag{C–26}$$

## C.3 Theoretical Noise Floor Uncertainty

The final parameter analyzed in terms of its theoretical uncertainty is the microphone noise floor. Sufficient data is not available to model the uncertainty in the predicted output referred noise floor. However, the input referred pressure noise density, $p_i$, is a function of sensitivity. Therefore, the uncertainty of the input referred noise can be estimated.

Assuming an output power spectral density of $s_{v_o}$, the input referred noise density is

$$p_i = \frac{\sqrt{S_{v_o}}}{S_{mic}}, \tag{C–27}$$

where $S_{mic}$ is the sensitivity of the microphone. The sensitivity of $p_i$ to a change in $S_{mic}$ is

$$\frac{\partial p_i}{\partial S_{mic}} = -\frac{\sqrt{s_{v_o}}}{S_{mic}^2}, \tag{C–28}$$

Therefore, the uncertainty in $p_i$ is

$$U_{p_i} = \frac{\partial p_i}{\partial S_{mic}} U_{S_{mic}}. \tag{C–29}$$

## C.4 Experimental Sensitivity Uncertainty

The sensitivity of each microphone is estimated from the measured linearity data. A typical data set for a microphone is shown in Figure C-1. The measured sensitivity is plotted versus pressure. In addition to estimating the measured sensitivity, a confidence interval for the sensitivity is desired.

Beginning with the two data points for the lowest pressures, the average sensitivity, $\overline{x}$, and sample variance, $s^2$ are computed. The upper end of the 95 % confidence interval for the variance is [135]

$$\hat{s}^2_{max} = \frac{(N-1)\, s^2}{\chi^2_{N-1;1-\alpha/2}}, \tag{C–30}$$

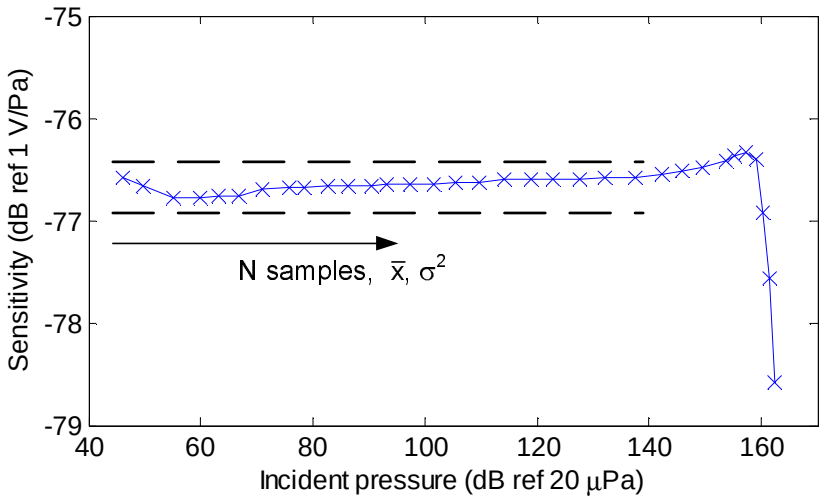


Figure C-1. Illustration of sensitivity data analysis.

where there are $N$ samples and $\chi^2_{N-1;1-\alpha/2}$ denotes the Chi-square distribution with $N-1$ degrees of freedom and a $1-\alpha$ confidence interval. For only two data points, Equation C–30 gives a large estimated variation. If the next data point falls within the range

$$\overline{x} - \hat{s}_{max} < x_i < \overline{x} + \hat{s}_{max}, \tag{C–31}$$

$N$ is increased and the above procedure is repeated. This process continues until the the next measured sensitivity falls outside the range given in Equation C–31. The sensitivity of the microphone is given by $\overline{x}$ with a 95 % confidence interval of

$$\overline{x} - \frac{st_{N-1;\alpha/2}}{N} < \overline{x} < \overline{x} + \frac{st_{N-1;\alpha/2}}{N}. \tag{C–32}$$

# APPENDIX D
# OVERVIEW OF THE SUMMiT V PROCESS

The device structure of the microphone requires three independent planar conducting layers to form the two backplates and the diaphragm. Sandia's Ultra-planar Multi-level MEMS Technology (SUMMiT V) process flow [16] is a good match for this device. It has five low-stress polysilicon layers and employs chemical mechanical polishing (CMP) to achieve ultra-flat structural layers.

Figure D-1 shows a cross section of the SUMMiT V process. The process begins with the growth of 0.63 $\mu m$ of thermal oxide and the deposition of 0.80 $\mu m$ of LPCVD silicon nitride. These layers provide isolation from the silicon substrate as well as an anchor for the polysilicon.

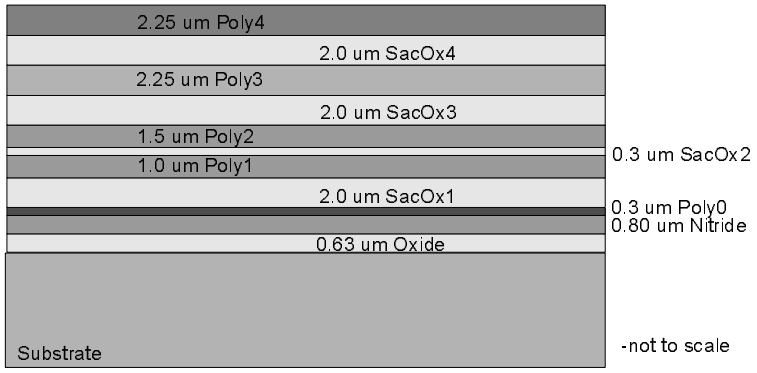


Figure D-1. Cross section of the SUMMiT V process.

The remainder of the process consists of depositing alternating layers of polysilicon and sacrificial oxide; all of the sacrificial oxide layers are deposited using LPCVD. A 0.3 $\mu m$ layer of LPCVD polysilicon, Poly0, is deposited. This is followed by SacOx1, the first layer of sacrificial oxide with a thickness of 2 $\mu m$. The next three layers are Poly1, a 1.0 $\mu m$ LPCVD polysilicon layer; SacOx2, a thin 0.3 $\mu m$ layer of oxide; and Poly2, a 1.5 $\mu m$ layer of LPCVD polysilicon. For the microphone, the entire layer of SacOx2 is removed, therefore Poly1 and Poly2 combine to form a polysilicon layer with a total thickness of 2.5 $\mu m$. This combined polysilicon layer will be referred to as Poly2. The next layer of sacrificial

oxide, SacOx3 is then deposited. This oxide layer is flattened using CMP. This allows the following layer of polysilicon to be very flat, however the thickness of the oxide is highly variable; the thicknesses and tolerances of all of the layers is given in Table D-1. Poly3, the next layer of PECVD polysilicon is deposited and has a thickness of 2.25 $\mu m$. The final sacrificial oxide layer, SacOx4, is deposited and flattened using CMP. This is followed by the final 2.25 $\mu m$ layer of PECVD polysilicon, Poly4.

Table D-1. Process data as reported by Sandia National Laboratories for the SUMMiT V process.

| Layer | Thickness | Variation |
|---|---|---|
| Poly0 | 0.29 $\mu m$ | $\pm 0.01$ $\mu m$ |
| Poly2 | 2.51 $\mu m$ | $\pm 0.003$ $\mu m$ |
| Poly3 | 2.27 $\mu m$ | $\pm 0.01$ $\mu m$ |
| Poly4 | 2.27 $\mu m$ | $\pm 0.006$ $\mu m$ |
| SacOx1 | 2.03 $\mu m$ | $\pm 0.004$ $\mu m$ |
| SacOx3 | 2.2 $\mu m$ | $\pm 0.2$ $\mu m$ |
| SacOx4 | 2.0 $\mu m$ | $\pm 0.2$ $\mu m$ |

The majority of the features of the SUMMiT V process are well suited to the dual-backplate microphone. The SUMMiT V process has three structural layers that are very flat. This prevents features from the lower layers from interfering with the upper layers. The stress in each of the polysilicon layers is well controlled and is assumed to be zero [16]. In addition, the thickness of the polysilicon layers is well controlled, thus the compliance of the polysilicon plates can be accurately predicted.

However, the SUMMiT V process does have some features that are not ideal for a dual-backplate capacitive microphone. The three structural layers are all approximately the same thickness. Therefore, assuming they have similar radii, they will have approximately the same compliance. Ideally, the backplates would be

much stiffer than the diaphragm. Furthermore, the top two sacrificial oxide layers have variable thicknesses; this will introduce significant uncertainty in the predicted microphone response. Considering these tradeoffs, the SUMMiT V process is still the best choice for the fabrication of this microphone.

REFERENCES

[1] "Aeronautics and space, noise standards: Aircraft type and airworthiness certification," *Title 14 US Code of Federal Regulations, Part 36*, 2004.

[2] T. J. Mueller, *Aeroacoustic Measurements*. Springer-Verlag Berlin Heidelberg, 2002, pp. 158–179.

[3] Brüel and Kjær, "Product data, condenser microphone cartriges – types 4133 to 4181," p. 6.

[4] D. T. Blackstock, *Fundamentals of Physical Acoustics*. John Wiley & Sons, Inc, 2000, ch. 4,14.

[5] J. Eargle, *The Microphone Handbook*. Butterworth-Heinemann, 2001.

[6] G. S. K. Wong and T. F. W. Embleton, *AIP Handbook of Condensor Microphones*, ser. Modern Acoustics and Signal Processing. New York: American Institute of Physics, 1995.

[7] G. G. Muller, R. Black, and T. E. Davis, "The diffraction produced by cylindrical and cubical obstacles and by circular and square plates," *Journal of the Acoustical Society of America*, vol. 10, no. 1, pp. 6–13, 1938.

[8] A. V. Oppenheim, R. W. Schafer, and J. R. Buck, *Discrete-time Signal Processing*, 2nd ed. Upper Saddle River, NJ: Prentice Hall, 1999.

[9] D. P. Arnold, "A MEMS-based directional acoustic array for aeroacoustic measurements," Master's thesis, University of Florida, Gainesville, FL, 2001.

[10] D. P. Arnold, T. Nishida, L. N. Cattafesta, and M. Sheplak, "A directional acoustic array using silicon micromachined piezoresistive microphones," *Journal of the Acoustical Society of America*, vol. 113, no. 1, pp. 289–298, 2003.

[11] J. R. Underbrink and R. P. Dougherty, "Array design for non-intrusive measurement of noise sources," in *National Conference on Noise Control Engineering v 2*, Inst of Noise Control Engineering. Seattle, WA: Inst of

Noise Control Engineering, 1996, pp. 757–762.

[12] S. D. Senturia, *Microsystem Design*. Kluwer Academic Publishers, 2001, ch. 1,17.

[13] D. P. Arnold, S. Gururaj, S. Bhardwaj, T. Nishida, and M. Sheplak, "A piezoresistive microphone for aeroacoustic measurements," in *Proceedings of ASME IMECE 2001, International Mechanical Engineering Congress and Exposition*. New York, NY: ASME, 2001, pp. 281–288.

[14] S. Horowitz, T. Nishida, L. Cattafesta, and M. Sheplak, "Design and characterization of a micromachined piezoelectric microphone," in *Proceedings of 11$^{th}$ AIAA/CEAS Aeroacoustics Conference & Exhibit, AIAA Paper #2005-2998*. Monterey, CA: AIAA, 2005.

[15] P. R. Scheeper, B. Nordstrand, B. L. J. O. Gullov, T. Clausen, L. Midjord, and T. Storgaard-Larsen, "A new measurement microphone based on MEMS technology," *Journal of Microelectromechanical Systems*, vol. 12, no. 6, pp. 880–891, 2003.

[16] J. J. Sniegowski and M. S. Rodgers, "Multi-layer enhancement to polysilicon surface-micromachining technology," in *Proceedings of IEDM Tech. Digest*. IEEE, 1997, pp. 903–906.

[17] A. V. Oppenheim, A. S. Willsky, and S. H. Nawab, *Signals and Systems*, 2nd ed. Upper Saddle River, NJ: Prentice Hall, 1997.

[18] Brüel and Kjær, *Microphone Handbook, vol. 1 Theory*. Nærum, Denmark: Brüel and Kjær, 1996.

[19] A. van der Ziel, *Noise in Solid State Devices and Circuits*. John Wiley & Sons, Inc., 1986.

[20] T. B. Gabrielson, "Mechanical-thermal noise in micromachined acoustic and vibration sensors," *IEEE Transactions on Electron Devices*, vol. 40, no. 5, pp. 903–909, 1993.

[21] M. Rossi, *Acoustics and Electroacoustics*. Artech House, Inc., 1988, ch. 5,6.

[22] S. Timoshenko and S. Woinowsky-Krieger, *Theory of Plates and Shells*. McGraw-Hill Book Company, 1959.

[23] R. K. Wangsness, *Electromagnetic Fields*, 2nd ed. John Wiley & Sons, 1986.

[24] N. Setter, *Piezoelectric Materials in Devices*. N. Setter, EPFL Swiss Federal Institute of Technology, 2002.

[25] A. Std 176-987, "IEEE standard on piezoelectricity," 1987.

[26] M. Royer, J. O. Holmen, M. A. Wurm, O. S. Aadland, and M. Glenn, "ZnO on Si integrated acoustic sensor," *Sensors and Actuators*, vol. 4, no. 3, pp. 357–362, 1983.

[27] S. S. Lee, R. P. Reid, and R. M. White, "Piezoelectric cantilever microphone and microspeaker," *Journal of Microelectromechanical Systems*, vol. 5, no. 4, pp. 238–242, 1996.

[28] K. Uchino, *Piezoelectric Actuators and Ultrasonic Motors*. Boston/Dordrecht/London: Kluwer Academic Publishers, 1997.

[29] M. Serridge and T. R. Licht, *Piezoelectric Accelerometer and Vibration Preamplifier Handbook*. Brüel and Kjær, 1987.

[30] M. Sheplak and J. Dugundji, "Large deflections of clamped circular plates under tension and transitions to membrane behavior," *Journal of Applied Mechanics*, vol. 65, no. 1, pp. 107–115, 1998.

[31] C. S. Smith, "Piezoresistance effect in germanium and silicon," *Physical Review*, vol. 94, no. 1, pp. 42–49, 1954.

[32] R. Schellin, M. Strecker, U. Nothelfer, and G. Schuster, "Low pressure acoustic sensors for airborne sound with piezoresistive monocrystalline silicon and electrochemically etched diaphragms," *Sensors and Actuators, A*, vol. 46, no. 1-3, pp. 156–160, 1995.

[33] R. Schellin and G. Hess, "A silicon subminiature microphone based on piezoresistive polysilicon strain gauges," *Sensors and Actuators, A*, vol. 32, no. 1-3, pp. 555–559, 1992.

[34] M. Papila, R. Haftka, T. Nishida, and M. Sheplak, "Piezoresistive microphone design pareto optimization: Tradeoff between sensitivity and noise floor," in *44th AIAA/ASME/ASCE/AHS Structures, Structural Dynamics, and Materials Conference, AIAA Paper #2003-1632*. Norfolk, VA: AIAA, 2003.

[35] ——, "Piezoresistive microphone design pareto optimization: Tradeoff between sensitivity and noise floor," *Journal of Microelectromechanical Systems*, vol. 15, no. 6, pp. 1632–1643, 2006.

[36] N. Bilaniuk, "Optical microphone transduction techniques," *Applied Acoustics*, vol. 50, no. 1, pp. 35–63, 1997.

[37] K. Kadirvel, R. Taylor, S. Horowitz, M. Sheplak, and T. Nishida, "Design and characterization of MEMS optical microphone for aeroacoustic measurement," in *Proceedings of 42nd Aerospace Sciences Meeting and Exhibit, AIAA Paper #2004-1030*. Reno, NV: AIAA, 2004.

[38] D. Garthe, J. Kobiela, and R. Kallweit, "Development of an integrated optical microphone by means of waveguide structuring on pmma," *SPIE*, pp. 618–629, 1985.

[39] J. M. Baptista, P. M. Cavaleira, and J. L. Santos, "Self-referencing intensity based q-type fibre optic sensor," *International Journal of Optoelectronics*, vol. 10, no. 2, pp. 105–113, 1995.

[40] G. He and F. W. Cuomo, "The analysis of noises in a fiber optic microphone," *Journal of the Acoustical Society of America*, vol. 92, no. 5, pp. 2521–2526, 1992.

[41] D. Hohm and R. G. Multhaupt, "Silicon-dioxide electret transducer," *Journal of the Acoustical Society of America*, vol. 75, no. 4, pp. 1297–1298, April

1984.

[42] J. Bergqvist and J. Gobet, "Capacitive microphone with a surface micromachined backplate using electroplating technology," *Journal of Microelectromechanical Systems*, vol. 3, no. 2, pp. 69–75, 1994.

[43] Q. Zou, Z. Li, and L. Liu, "Design and fabrication of silicon condenser microphone using corrugated diaphragm technique," *Journal of Microelectromechanical Systems*, vol. 5, no. 3, pp. 197–204, 1996.

[44] J. Bergqvist and F. Rudolf, "A new condenser microphone in silicon," *Sensors and Actuators, A*, vol. 21, no. 1-3, pp. 123–125, 1990.

[45] T. Bourouina, S. Spirkovitch, F. Baillieu, and C. Vauge, "A new condenser microphone with a $p^+$ silicon membrane," *Sensors and Actuators, A*, vol. 31, no. 1-3, pp. 149–152, 1992.

[46] P.-C. Hsu, C. H. Mastrangelo, and K. D. Wise, "A high sensitivity polysilicon diaphragm condenser microphone," in *Proceedings of IEEE Micro Electro Mechanical Systems (MEMS) Conference*. Piscataway, NJ: IEEE, 1998, pp. 56–63.

[47] P. Rombach, M. M*ü*llenborn, U. Klein, and K. Rasmussen, "The first low voltage, low noise differential silicon microphone, technology development and measurement results," *Sensors and Actuators, A*, vol. 95, no. 2-3, pp. 196–201, 2002.

[48] J. Bay, O. Hansen, and S. Bouwstra, "Design of a silicon microphone with differential read-out of a sealed double parallel-plate capacitor," *Sensors and Actuators, A*, vol. 53, no. 1-3, pp. 232–236, 1996.

[49] F. V. Hunt, *Electroacoustics The Analysis of Transduction, and Its Historical Background*. American Institute of Physics, 1954.

[50] H. Riegger, "unknown," *German Pat. #398195*, 1924.

[51] J. Bay, O. Hansen, and S. Bouwstra, "Micromachined double backplate differential capacitive microphone," *Journal of Micromechanics and Microengineering*, vol. 9, no. 1, pp. 30–33, 1999.

[52] P. Rombach, M. M*ü*llenborn, U. Klein, and K. Rasmussen, "The first low voltage, low noise differential condenser silicon microphone," in *Proceedings of The 14th European Conference on Solid-State Transducers, EUROSENSORS XIV*, Copenhagen, Denmark, 2000, pp. 213–216.

[53] ——, "The first low voltage, low noise differential silicon microphone, technology development and measurement results," in *Proceedings of IEEE Micro Electro Mechanical Systems (MEMS) Conference*. Lyngby, Denmark: IEEE, 2001, pp. 42–45.

[54] D. T. Martin, K. Kadirvel, J. Liu, R. M. Fox, M. Sheplak, and T. Nishida, "Surface and bulk micromachined dual back-plate condenser microphone," in *Proceedings of 18th IEEE International Conference on Micro Electro Mechanical Systems (MEMS 2005)*. Miami, FL: IEEE, 2005, pp. 319–322.

[55] P. R. Scheeper, A. G. H. van der Donk, W. Olthuis, and P. Bergveld, "A review of silicon microphones," *Sensors and Actuators, A*, vol. 44, no. 1, pp. 1–11, 1994.

[56] E. S. Kim and R. S. Muller, "IC-processed piezoelectric microphone," *IEEE Electron Device Letters*, vol. 8, no. 10, pp. 467–468, 1987.

[57] E. S. Kim, R. S. Muller, and P. R. Gray, "Integrated microphone with CMOS circuits on a single chip," in *Proceedings of 1989 International Electron Devices Meeting*. Washington, DC: IEEE, 1989, pp. 880–883.

[58] E. S. Kim, J. R. Kim, and R. S. Muller, "Improved ic-compatible piezoelectric microphone and CMOS process," in *Proceedings of 1991 International Conference on Solid-State Sensors and Actuators*. San Francisco, CA: IEEE, 1991, pp. 270–273.

[59] R. Schellin, G. Hess, W. Kuehnel, G. M. Sessler, and E. Fukada, "Silicon subminiature microphones with organic piezoelectric layers: Fabrication and acoustical behaviour," in *Proceedings of 7th International Symposium on Electrets*. Berlin, Germany: IEEE, 1992, pp. 929–934.

[60] R. P. Ried, E. S. Kim, D. M. Hong, and R. S. Muller, "Piezoelectric microphone with on-chip CMOS circuits," *Journal of Microelectromechanical Systems*, vol. 2, no. 3, pp. 111–120, 1993.

[61] S. S. Lee and R. M. White, "Piezoelectric cantilever acoustic transducer," *Journal of Micromechanics and Microengineering*, vol. 8, no. 3, pp. 230–238, 1998.

[62] S. C. Ko, Y. C. Kim, S. S. Lee, S. H. Choi, and S. R. Kim, "Micromachined piezoelectric membrane acoustic device," *Sensors and Actuator A*, vol. 103, pp. 130–134, 2003.

[63] M. Niu and E. S. Kim, "Piezoelectric bimorph microphone built on micromachined parylene diaphragm," *Journal of Microelectromechanical Systems*, vol. 12, no. 6, pp. 892–898, 2003.

[64] H. J. Zhao, T. L. Ren, J. S. Liu, L. T. Liu, and Z. J. Li, "Fabrication of high-quality pzt-based piezoelectric microphone," in *Proceedings of International Conference on Solid State Sensors and Actuators, TRANSDUCERS 2003*, vol. 1, Boston, 2003, pp. 234– 237.

[65] J. Hillenbrand and G. M. Sessler, "High-sensitivity piezoelectric microphones based on stacked cellular polymer films (L)," *Journal of the Acoustical Society of America*, vol. 116, no. 6, pp. 3267–3270, 2004.

[66] E. R. Peake, A. R. Zias, and J. V. Egan, "Solid-state digital pressure transducer," *IEEE Transactions on Electron Devices*, vol. 16, no. 10, pp. 870–876, 1967.

[67] E. Kälvesten, L. Lofdahl, and G. Stemme, "A small-size silicon microphone for measurements in turbulent gas flows," *Sensors and Actuators, A*, vol. 45, no. 2, pp. 103–108, 1994.

[68] ——, "Small piezoresistive silicon microphones specially designed for the characterization of turbulent gas flows," *Sensors and Actuators, A*, vol. 46, no. 1-3, pp. 151–155, 1995.

[69] ——, "Analytical characterization of piezoresistive square-diaphragm silicon microphone," *Sensors and Materials*, vol. 8, no. 2, pp. 113–136, 1996.

[70] M. Sheplak, K. S. Breuer, and M. A. Schmidt, "A wafer-bonded, silicon-nitride membrane microphonewith dielectrically-isolated single crystal silicon piezoresistors," in *Proceedings of 1998 Solid-State Sensor and Actuator Workshop*, Hilton Head Island, SC, 1998, pp. 23–26.

[71] M. Sheplak, M. Seiner, K. S. Breuer, and M. A. Schmidt, "A MEMS microphone for aeroacoustic measurements," in *Proceedings of 37$^{th}$ AIAA Aerospace Sciences Meeting, AIAA Paper #99-0606.* Reno, NV: AIAA, 1999.

[72] A. Naguib, E. Soupos, H. Nagib, C. Huang, and K. Najafi, "Characterization of a MEMS acoustic/pressure sensor," in *Proceedings of 37$^{th}$ AIAA Aerospace Sciences Meeting, AIAA Paper #99-0520.* Reno, NV: AIAA, 1999.

[73] ——, "A piezoresistive MEMS sensor for acoustic noise measurements," in *Proceedings of 5$^{th}$ AIAA/CEAS Aeroacoustics Conference & Exhibit, AIAA Paper #99-1992.* Bellevue, WA: AIAA, 1999.

[74] C. Huang, A. Naguib, E. Soupos, and K. Najafi, "A silicon micromachined microphone for fluid mechanics research," *Journal of Micromechanics and Microengineering*, vol. 12, no. 6, pp. 767–774, 2002.

[75] G. Li, Y. Zohar, and M. Wong, "Piezoresistive microphone with integrated amplifier realized using metal-induced laterally crystallized polycrystalline silicon," *Journal of Micromechanics and Microengineering*, vol. 14, no. 10, pp.

1352–1358, 2004.

[76] F. P. Burns, "Piezoresistive semiconductor microphone," *Journal of the Acoustical Society of America*, vol. 29, no. 2, pp. 248–253, 1957.

[77] D. C. Abeysinghe, S. Dasgupta, J. T. Boyd, and H. E. Jackson, "A novel MEMS pressure sensor fabricated on an optical fiber," *IEEE Photonics Technology Letters*, vol. 13, no. 9, pp. 993–995, 2001.

[78] W. Lee, N. A. Hall, Z. Zhou, and F. L. Degertekin, "Fabrication and characterization of a micromachined acoustic sensor with integrated optical readout," *Journal of Selected Topics in Quantum Electronics*, vol. 10, no. 3, pp. 643–651, 2004.

[79] N. A. Hall, B. Bicen, M. K. Jeelani, W. Lee, S. Qureshi, and F. L. Degertekin, "Micromachined microphones with diffraction-based optical displacement detection," *Journal of the Acoustical Society of America*, vol. 118, no. 5, pp. 3000–3009, 2005.

[80] J. A. Bucaro, N. Lagakos, B. H. Houston, J. Jarzynski, and M. Zalalutdinov, "Miniature, high performance, low-cost fiber optic microphone," *Journal of the Acoustical Society of America*, vol. 118, no. 3, pp. 1406–1413, 2005.

[81] J. H. Song and S. S. Lee, "Fiber-optic acoustic transducer utilizing a dual-core collimator combined with a reflective micromirror," *Microwave and Optical Technology Letters*, vol. 48, no. 9, pp. 1833–1836, 2006.

[82] D. Garthe, "A fiber-optic microphone," *Sensors and Actuators, A*, vol. 26, no. 1, pp. 341–345, 1991.

[83] ——, "Fiber- and integrated-optical microphones based on intensity modulation by beam deflection at a moving membrane," *Sensors and Actuators, A*, vol. 37-38, no. 2, pp. 484–488, 1993.

[84] D. S. Greywall, "Micromachined optical-interference microphone," *Sensors and Actuators, A*, vol. 75, no. 3, pp. 257–268, 1999.

[85] J. H. Song, H. M. Gu, H. J. Park, and S. S. Lee, "Optical microphone based on a reflective micromirror diaphragm," *Microwave and Optical Technology Letters*, vol. 48, no. 4, pp. 707–709, 2005.

[86] A. J. Sprenkels, R. A. Groothengel, A. J. Verloop, and P. Bergveld, "Development of an electret microphone in silicon," *Sensors and Actuators*, vol. 17, no. 3-4, pp. 509–512, 1989.

[87] J. A. Voorthuyzen, P. Bergveld, and A. J. Sprenkels, "Semiconductor-based electret sensors for sound and pressure," *IEEE Transactions on Electrical Insulation*, vol. 24, no. 2, pp. 267–276, 1989.

[88] P. Murphy, K. H*ü*bschi, N. D. Rooij, and C. Racine, "Subminiature silicon integrated electret capacitor microphone," *IEEE Transactions on Electrical Insulation*, vol. 24, no. 3, pp. 495–498, 1989.

[89] D. Hohm and G. Hess, "A subminiature condenser microphone with silicon nitride membrane and silicon backplate," *Journal of the Acoustical Society of America*, vol. 85, no. 1, pp. 476–479, 1989.

[90] J. Bergqvist, F. Rudolf, J. Maisano, F. Parodi, and M. Rossi, "A silicon condenser microphone with a highly perforated backplate," in *Proceedings of International Conference on Solid-State Sensors and Actuators*. Piscataway, NJ: IEEE, 1991, pp. 266–269.

[91] P. R. Scheeper, W. Olthuis, and P. Bergveld, "Fabrication of a subminiature silicon condenser microphone using the sacrificial layer technique," in *Proceedings of International Conference on Solid-State Sensors and Actuators*. Piscataway, NJ: IEEE, 1991, pp. 408–411.

[92] P. R. Scheeper, A. G. H. van der Donk, W. Olthuis, and P. Bergveld, "Fabrication of silicon condenser microphones using single wafer technology," *Journal of Microelectromechanical Systems*, vol. 1, no. 3, pp. 147–154, 1992.

[93] W. Kühnel and G. Hess, "A silicon condenser microphone with structured back plate and silicon nitride membrane," *Sensors and Actuators, A*, vol. 30, no. 3, pp. 251–258, 1992.

[94] J. J. Bernstein and J. T. Borenstein, "A micromachined silicon condenser microphone with on-chip amplifier," in *Proceedings of Solid-State Sensor and Actuator Workshop*. Hilton Head Island, SC: IEEE, 1996, pp. 239–243.

[95] Q. Zou, Z. Li, and L. Liu, "Theoretical and experimental studies of single-chip-processed miniature silicon condenser microphone with corrugated diaprhagm," *Sensors and Actuators, A*, vol. 63, no. 3, pp. 209–215, 1997.

[96] Y. B. Ning, A. W. Mitchell, and R. N. Tait, "Fabrication of a silicon micromachined capacitive microphone using a dry-etch process," *Sensors and Actuators, A*, vol. 53, no. 1-3, pp. 237–242, 1996.

[97] B. T. Cunningham and J. J. Bernstein, "Wide bandwidth silicon nitride membrane microphones," in *Proceedings of Conference on Micromachining and Microfabrication Process Technology III*, SPIE. Austin, TX: SPIE, 1997, pp. 56–63.

[98] M. Pedersen, W. Olthuis, and P. Bergveld, "A silicon condenser microphone with polyimide diaphragm and backplate," *Sensors and Actuators, A*, vol. 63, no. 2, pp. 97–104, 1997.

[99] ——, "An integrated silicon capacitive microphone with frequency-modulated digital output," *Sensors and Actuators, A*, vol. 69, no. 3, pp. 267–275, 1998.

[100] ——, "High performance condenser microphone with fully integrated CMOS amplifier and DC-DC voltage converter," *Journal of Microelectromechanical Systems*, vol. 7, no. 4, pp. 387–394, 1998.

[101] D. Schafer, S. Shoaf, and P. Loeppert, "Micromachined condenser microphone for hearing aid use," in *Proceedings of Solid-State Sensor and Actuator Workshop*. Hilton Head Island, SC: IEEE, 1998, pp. 27–30.

[102] A. Torkkeli, O. Rusanen, J. Saarilahti, H. Seppä, H. Sipola, and J. Hietanen, "Capacitive microphone with low-stress polysilicon membrane and high-stress polysilicon backplate," *Sensors and Actuators, A*, vol. 85, no. 1-3, pp. 116–123, 2000.

[103] X. Li, R. Lin, H. Kek, J. Miao, and Q. Zou, "Sensitivity-improved silicon condenser microphone with a novel single deeply corrugated diaphragm," *Sensors and Actuators, A*, vol. 92, no. 1-3, pp. 257–262, 2001.

[104] M. Brauer, A. Dehe, T. Bever, S. Barzen, S. Schmitt, M. Fuldner, and R. Aigner, "Silicon microphone based on surface and bulk micromachining," *Journal of Micromechanics and Microengineering*, vol. 11, no. 4, pp. 319–322, 2001.

[105] R. Kessmann, M. Klaiber, and G. Hess, "Silicon condenser microphones with corrugated silicon oxide/nitride electret membranes," *Sensors and Actuators, A*, vol. 100, no. 2-3, pp. 301–309, 2002.

[106] J. J. N. Jr. and K. J. Gabriel, "A fully-integrated CMOS-MEMS audio microphone," in *Proceedings of International Conference on Solid-State Sensors and Actuators*. Boston, MA: IEEE, 2003, pp. 230–233.

[107] S. T. Hansen, A. S. Ergun, W. Liou, B. A. Auld, and B. T. Khuri-Yakub, "Wideband micromachined capacitive microphones with radio frequency detection," *Journal of the Acoustical Society of America*, vol. 116, no. 2, pp. 828–842, 2004.

[108] P. R. Scheeper, W. Olthuis, and P. Bergveld, "The design, fabrication, and testing of corrugated silicon nitride diaphragms," *Journal of Microelectromechanical Systems*, vol. 3, no. 1, pp. 36–42, 1994.

[109] K. Acoustics, "Data sheet sp0101, sisonic silicon microphone," Tech. Rep.

[110] P. V. Loeppert and S. B. Lee, "SiSonic™ — The first commercialized MEMS microphone," in *Proceedings of Solid-State Sensor and Actuator Workshop*,

Hilton Head Island, SC, 2006, pp. 27–30.

[111] M. Pedersen, "Development of microelectromechanical systems capacitive microphone for high-frequency applications," in *Proceedings of 151st Meeting of the Acoustical Society of America*. Providence, RI: ASA, 2006.

[112] S. Horowitz, T. Nishida, L. Cattafesta, and M. Sheplak, "A micromachined piezoelectric microphone for aeroacoustics applications," in *Proceedings of Solid-State Sensor and Actuator Workshop*, Hilton Head Island, SC, 2006.

[113] J. E. Warren, A. M. Brzezinski, and J. F. Hamilton, "Capacitance-microphone static membrane deflections," *Journal of the Acoustical Society of America*, vol. 52, no. 3, pp. 711–719, 1972.

[114] ——, "Capacitance microphone dynamic membrane deflections," *Journal of the Acoustical Society of America*, vol. 54, no. 5, pp. 1201–1213, 1973.

[115] A. G. H. van der Donk, P. R. Scheeper, W. Olthuis, and P. Bergveld, "Modelling of silicon condenser microphones," *Sensors and Actuator A*, vol. 40, pp. 203–216, 1994.

[116] A. S. Sedra and K. C. Smith, *Microelectronic Circuits*, 4th ed. Oxford University Press, 1998.

[117] M. Pedersen, "A polymer condenser microphone realised on silicon containing preprocessed integrated circuits," Ph.D. dissertation, College of Engineering, University of Twente, Netherlands, 1997.

[118] J. Liu, D. T. Martin, K. Kadirvel, T. Nishida, M. Sheplak, and B. P. Mann, "Nonlinear identification of a capacitive dual-backplate MEMS microphone," in *Proceedings of 2005 ASME International Design Engineering Technical Conferences, Paper # DETC2005-84591*. ASME, 2005.

[119] L. Rade and B. Westergren, *Mathematics Handbook*. Berlin Heidelberg: Springer-Verlag, 1999.

[120] M. Pedersen, W. Olthius, and P. Bergveld, "Harmonic distortion in silicon condenser microphones," *Journal of the Acoustical Society of America*, vol. 102, no. 3, pp. 1582–1587, 1997.

[121] Z. Skvor, "On the acoustical resistance to viscous losses in the air gap of electrostatic transducers," *Acoustica*, vol. 19, pp. 295–299, 1967.

[122] D. Homentcovschi and R. N. Miles, "Modeling of viscous damping of perforated planar microstructures. applications in acoustics," *Journal of the Acoustical Society of America*, vol. 116, no. 5, pp. 2939–2947, 2004.

[123] R. W. Fox, A. T. McDonald, and P. J. Pritchard, *Introduction to Fluid Mechanics*, 6th ed. New York, NY: John Wiley & Sons, Inc., 2004, ch. 8.

[124] J. D. Irwin and C. Wu, *Basic Engineering Circuit Analysis*, 6th ed. Upper Saddle River, NJ: Prentice-Hall, 1992.

[125] S. Krylov and R. Maimon, "Pull-in dynamics of an elastic beam actuated by continuously distributed electrostatic force," *Journal of Vibration and Acoustics, Transactions of the ASME*, vol. 126, no. 3, pp. 332–342, 2004.

[126] W. R. Ashurst, C. Carraro, R. Maboudian, and W. Frey, "Fabrication of micromechanical devices from polysilicon films with smooth surfaces," *Sensors and Actuators A*, vol. 104, no. 3, pp. 213–221, 2003.

[127] H. Guckel, J. J. Sniegowski, T. R. Christenson, S. Mohney, and T. F. Kelly, "Fabrication of micromechanical devices from polysilicon films with smooth surfaces," *Sensors and Actuators*, vol. 20, pp. 117–122, 1989.

[128] G. T. Mulhern, D. S. Soane, and R. T. Howe, "Supercritical carbon dioxide drying of microstructures," in *Proceedings of International Conference on Solid-State Sensors and Actuators*. IEEE, 1993, pp. 296–299.

[129] K. R. Williams, K. Gupta, and M. Wasilik, "Etch rates for micromachining processing — part ii," *Journal of Microelectromechanical Systems*, vol. 12, no. 6, pp. 761–778, 2003.

[130] E. K. Chan, K. Garikipati, and R. W. Dutton, "Comprehensive static characterization of vertical electrostatically actuated polysilicon beams," *IEEE Design and Test of Computers*, vol. 16, no. 4, pp. 58–65, 1999.

[131] I. Chasiotis and W. G. Knauss, "The mechanical strength of polysilicon films: Part 1. the influence of fabrication governed surface conditions," *Journal of the Mechanics and Physics of Solids*, vol. 51, no. 8, pp. 1533–1550, 2003.

[132] R. Dieme, G. Bosman, M. Sheplak, and T. Nishida, "Source of excess noise in silicon piezoresistive microphones," *Journal of the Acoustical Society of America*, vol. 119, pp. 2710–2720, 2006.

[133] R. J. Holman, "An experimental investigation of flows from zero-net mass flux actuators," Ph.D. dissertation, University of Florida, Gainesville, FL, 2006.

[134] J. P. Holman, *Experimental Methods for Engineers*, 7th ed. New York, NY: McGraw Hill, 2001.

[135] J. S. Bendat and A. G. Piersol, *Random Data Analysis and Measurement Procedures*, 3rd ed. New York: John Wiley and Sons, 2000.

# BIOGRAPHICAL SKETCH

David Thomas Martin was born on November 12, 1979, in Bethlehem, Pennsylvania. He attended Doctor Phillip's High School in Orlando, FL, graduating in 1997. He then enrolled at the University of Florida where he received his bachelor's degree in electrical engineering from the University of Florida in 2001. During his final semester an undergraduate, David joined the Interdisciplinary Microsystems Group where he worked on the packaging of a piezoresistive microphone array. In August of 2001, David began his graduate studies at the University of Florida where he was awarded a fellowship from Sandia National Laboratories. In May of 2005, he earned a Master of Science degree in electrical engineering. David is currently completing his doctoral degree at the University of Florida. His research interests include microelectromechanical systems (MEMS) microphone design, packaging, and microphone characterization.